UNIVERSITY OF CALIFORNIA,
IRVINE

Atmospheric Histories of Ethane and Carbon Monoxide from Polar Firn Air and Ice Cores

DISSERTATION

submitted in partial satisfaction of the requirements
for the degree of

DOCTOR OF PHILOSOPHY

in Earth System Science

by

Kristal Robin Verhulst

Dissertation Committee:
Professor Eric S. Saltzman, Chair
Professor Michael J. Prather
Professor Donald Blake

2014

To my parents, Gregory and Jeree Verhulst,
and my sister, Jennifer,
for your love and support

"No problem can be solved from the same level of consciousness that created it."
–Albert Einstein

TABLE OF CONTENTS

Page

LIST OF FIGURES

LIST OF TABLES

ACKNOWLEDGMENTS

I would like to thank my PhD advisor, Professor Eric Saltzman. This research would not have been possible without your academic guidance. Your enthusiasm, knowledge, and dedication inspire me everyday. Thank you for opening my eyes to new research possibilities and helping me find confidence in my skills and abilities as a scientist. Thank you to my co-advisor, Dr. Murat Aydin. This dissertation would not have been possible without your training, guidance, research ideas, and support in the laboratory. Thank you to my committee members, Professor Donald Blake and Professor Michael Prather. Your comments, support, and mentorship helped make this dissertation possible. Thank you to my mentor and friend, Dr. Julie Ferguson. You inspire me everyday and your wisdom and guidance have taught me so much.

I would like to thank the entire Saltzman/Aydin research Group, past present and future, including Dr. Mike Lawler, Dr. Tom Bell, Mackenzie Grieman, Melinda Nicewonger, Jack Porter, and the numerous undergraduate researchers who helped with measurements, especially Isis Frausto-Vicencio, Elizabeth Fosse, Mihai Leonte, Michael Mori, Ricardo Jiménez, Vincent Hong, Tina Ho and Spencer Hernandez. It has been an honor and a pleasure working with you. A huge thank you to all my fellow graduate students for all your help and companionship over the years. Special thanks to my good friends Mackenzie Grieman, Alysha Coppola, Karli Ouellette, Stephanie Ho, Ashley Payne, Pasha Ameli, Tiffany Roberts-Dolu, Susan Hicks, Mike Lawler, Aaron Fellows, Tyler Sutterley, Colene Haffke, Collin Lawrence, Sasha Richey, Gergana Mouteva, Francesca Hopkins, Aimee Gibbons, and Elliot Sherman for helping make the last few years of graduate school so enjoyable. Thanks to all the past and present members of the Planeteers (aka the Clobberin' Bobblers) for many enjoyable summer softball seasons.

The firn air and ice core research presented in this dissertation would not have been possible without several key collaborators. Thank you to Murat Aydin and Todd Sowers for collection of the South Pole firn air samples, M. Drier and ICDS drillers for support during firn-air sampling and drilling in the field, and Michael Bender and Jeff Severinghaus for $\delta^{15}N$ of N_2 measurements in the firn air samples. Thank you to Don Blake, Isobel Simpson, and Simone Meinardi for ethane measurements in surface flasks, Steve Montzka for halocarbon data used to tune the firn model, Pieter Tans and Patricia Lang for firn air CO_2 data, and Paul Novelli and Kenneth Masarie for the South Pole firn CO data. Thank you to Mark Battle for help with the firn modeling work and for comparing results. Thank you to NICL, Todd Sowers and Jihong Cole-Dai for providing Antarctic ice cores. Thanks to Lee Moritz and Cyril Mc Cormick for support with method development and instrumentation. Thank you to Michael Prather, Christopher Holmes, Qi Tang, and Ivar Isaksen for help with the Chemical Transport Modeling studies.

Chapter 3 is reproduced with permission from Nature Publishing Group. This research was made possible with the generous support from several fellowships: UC Irvine Faculty Mentor Fellowship, Ralph J. and Carol M. Cicerone Fellowship, and the NASA/UCSD/Cal Space Fellowship. The firn air studies were supported by the National Science Foundation (ANT-0739598, ANT-0440602, ANT-0440509, and ARC-0520460) and NASA (NAG58935).

I would not have made it where I am today without the love and support of the following people: my parents, Greg and Jeree, my sister Jennifer, brother-in-law Shaun, my aunt and uncle, Janet and Sherman, and extended family – Jim, Judy, Charlie, Paula, Pam, Jennifer, and Chelsea. To my nieces and nephews – Samantha, Kylah Rae, Noah and (soon) Jeremy – you are a constant source of joy in my life. And finally, special thanks to David Whitten for supporting me throughout this journey and for reminding me to smile, laugh, and dance in the rain.

CURRICULUM VITAE

Kristal Robin Verhulst

EDUCATION

University of California, Irvine

Ph.D. – Earth System Science, September 2014

M.S. – Earth System Science, 2010

B.S. – Chemistry, 2008, Minor: Earth and Atmospheric Science
Honors: c*um laude*, *Phi Lambda Upsilon Honors*

SELECTED HONORS AND AWARDS

NASA/UCSD Cal Space Fellowship, Spring 2014
Ralph J. and Carol M. Cicerone Fellowship, Winter 2014
American Geophysical Union, Outstanding Student Paper, December 2012
UC Irvine Faculty Mentor Program Fellowship, 2010-2011
ESS/IGPP Symposium, Outstanding Research Presentation, December 2009
National Science Foundation, REU Fellow, Summer 2007
Lockheed Martin Aeronautics Scholarship, 2006

PUBLICATIONS

1. Verhulst, K. R., M. Aydin, and E.S. Saltzman (2013), Methyl chloride variability in the Taylor Dome ice core during the Holocene, *J. Geophys. Res.: Atmospheres,* 118, 1-11, doi:10.1002/2013JD020197.
2. Aydin, M., K. R. Verhulst, E. S. Saltzman, S. A. Montzka, D. R. Blake, Q. Tang, and M. J. Prather (2011), 20th century ethane variability from polar firn air and implications for the methane budget, *Nature,* 476, 198-201, doi:10.1038/nature10352.
3. Aydin, M., T. J. Fudge, K. R. Verhulst, M. R. Nicewonger, E. D. Waddington, E. S. Saltzman (2014), Carbonyl sulfide hydrolysis in Antarctic ice cores and an atmospheric history for the last 8,000 years, *J. Geophys. Res.: Atmospheres*, 119, doi: 10.1002/2014JD021618
4. Montzka, S.A., L. Kuijpers, M. O. Battle, M. Aydin, K. R. Verhulst, E. S. Saltzman, and D. W. Fahey (2010), Recent increases in global HFC-23 emissions, *Geophys. Res. Lett.,* 37(L02808), doi:10.1029/2009GL041195.
5. Aydin, M., S. B. Montzka, M. O. Battle, M. Williams, W. J. De Bruyn, K. R. Verhulst, et al. (2010), Post-coring entrapment of modern air in polar ice: Evidence from CFC-12 measurements in Antarctic firn air and shallow ice cores*, Atmos. Chem. Phys.,* 10, 5135–5144, doi: 10.5194/acp-10-5135-2010, doi: 10.5194/acp-10-5135-2010..
6. Saltzman, E. S., M. Aydin, K. R. Verhulst, B. Gun, and M. Williams (2009), Methyl chloride in a deep ice core from Siple Dome, Antarctica, *Geophys. Res Lett.,* 36(LO3822), doi: 10.1029/2008GLO36266.

RESEARCH EXPERIENCE

University of California, Irvine

Graduate Student Researcher, June 2008 – present
Dissertation title: "Atmospheric Histories of Ethane and Carbon Monoxide from Polar Firn Air and Ice Cores"

Undergraduate Researcher, Saltzman/Aydin Research Lab, Sept 2007- July 2008
Reconstructed a 70-kyr record of CH_3Cl using ice cores from Siple Dome and WAIS Divide, Antarctica. Senior Thesis: "Methyl chloride and methyl bromide measurements in a deep ice core from Siple Dome, West Antarctica."

NSF REU Fellow/Junior Specialist, July 2007- Sept 2007
Investigated potential causes of impurity related production of methyl halides in glacial/interglacial ice samples. Discovered methyl halide production in ice cores may be linked to influence of marine air masses and/or the temperature of the ice core site.

FIELD EXPERIENCE

Identifying Methane Emissions Hotspots, Los Angeles, CA, June 2013
Assisted in the deployment of the Keck Institute for Space Studies ethane/methane analyzer on board the UC Irvine mobile laboratory. Sampling was coordinated with a NASA DC-8 flight path.

National Ice Core Laboratory (NICL), Denver, CO, 2008-2013
Collected ice core samples for various projects during 5 yearly visits.

Desert Research Institute, Reno, NV, March 2011
Assisted with ice core analyses as a member of the WAIS-Divide Ice Core melt team. Analyzed organic acids in WAIS Divide and Summit, Greenland ice cores (ES/MS/MS).

TEACHING EXPERIENCE

Teaching Assistant, *University of California, Irvine*
The Atmosphere, ESS 5, Mar-Jun 2012, Class size: 408
Atmospheric Chemistry, ESS 142, Jan-Mar 2012, Class size: 30
Field Methods , ESS 116, Mar-June 2010, Class size: 30

Guest Lecturer, *University of California, Irvine and Fullerton College*
Oceanography, "Firn air and ice cores."
Atmospheric Chemistry (Graduate level), "Tropospheric Ozone and Control Strategies."
The Atmosphere, "Atmospheric Pollution and Urban Heat Islands."
Atmospheric Chemistry, "Urban Air Pollution and the Tropospheric Ozone Problem."

ORAL PRESENTATIONS

1. AGU Fall Meeting, "*A southern hemisphere atmospheric history of carbon monoxide from South Pole firn air,"* presenter, *December 2013.*

2. WAIS Divide Ice Core Science Meeting, "*Methyl chloride measurements in Antarctic ice cores and evidence for in situ production at West Antarctic sites,"* presenter, *September 2013.*

3. AGU Fall Meeting, "*A 50,000-year record of atmospheric methyl chloride from Antarctic ice cores"*, presenter, *December 2012.*

4. WAIS Divide Ice Core Science Meeting, La Jolla, CA, *"Ethane variability from polar firn air and ice cores: What can ethane tell us about the CH_4 budget?"* presenter, *Sept 2011.*

5. NOAA/ESRL/GMD Annual Meeting, Boulder, CO, "*A 20th century atmospheric history of ethane and implications for the methane budget,"* presenter, *May 2010.*

POSTER PRESENTATIONS

1. WAIS Divide Ice Core Science Meeting, La Jolla, CA, "*A Holocene record of atmospheric methyl chloride variability from measurements in Antarctic ice cores,"* presenter, *September 2012.*

2. AGU Fall Meeting, San Francisco, CA, abstract # C21A-0462, "*Measurements of ethane in Antarctic ice cores,"* presenter, and abstract # C21A-0464, "*Methyl chloride measurements in Antarctic ice cores covering the 70,000 years before present,"* co-author, *December 2011.*

3. ISKPPA Photochemistry Conference, La Jolla, CA, "*An atmospheric ethane history from South Pole firn air*," presenter, *February 2011.*

4. AGU Fall Meeting, San Francisco, CA, abstract # A51D-0157, "*20th century ethane variability from polar firn air and implications for the methane budget,"* presenter, *December 2010.*

5. AGU Fall Meeting, San Francisco, CA, abstract # A21C-0214, "*An atmospheric history of ethane from South Pole firn air*," presenter, *December 2009.*

6. AGU Fall Meeting, San Francisco, CA, abstract #A21B-0149, "*Ethane seasonality and incorporation into firn at Summit, Greenland*," co-author, *December 2008.*

7. AGU Fall Meeting, 2007, San Francisco, CA, abstract #A53B-1160, "*A 70ka record of methyl chloride from a Siple Dome, West Antarctica ice core*," presenter, *December 2007.*

ABSTRACT OF THE DISSERTATION

Atmospheric Histories of Ethane and Carbon Monoxide from Polar Firn Air and Ice Cores

By

Kristal Robin Verhulst

Doctor of Philosophy in Earth System Science

University of California, Irvine, 2014

Professor Eric S. Saltzman, Chair

This dissertation involves measurements of ethane and carbon monoxide in the air trapped in polar firn (porous ice) and ice cores from Greenland and Antarctica. Ethane and carbon monoxide are reactive trace gases that are involved in tropospheric ozone formation and impact the atmosphere's oxidative capacity. The major sources of these gases are from anthropogenic fossil fuel use, biofuel use, and biomass burning. Ethane fossil fuel emissions are mainly from evaporative emissions associated with the production, processing and transmission of fossil fuels. Carbon monoxide emissions are primarily due to fossil fuel combustion and atmospheric hydrocarbon oxidation. In this study, past atmospheric levels of ethane and carbon monoxide are reconstructed from polar firn air to examine man's impact on their global budgets.

Antarctic and Greenland firn air measurements show that ethane levels rose globally during the twentieth century, reached a peak in the 1980s, followed by a decline to their present-day levels. Ethane emissions reconstructions suggest that the ethane decline since 1980 was likely due to a reduction in fossil fuel emissions. The firn-air based ethane emissions histories suggest the slowdown in the atmospheric methane growth rate during the 1980s and 1990s was also due to reductions in fossil fuel emissions, possibly as a result of capture, recovery, and/or storage of

natural gas that was previously vented or flared. In order to develop longer atmospheric histories, ethane was analyzed in air extracted from bubbles in Antarctic ice cores. Both dry extraction and wet extraction procedures were utilized in this study. The results indicate that preindustrial (1000-1900 AD) ethane levels over Antarctica were 40-50% lower than today.

Carbon monoxide levels increased by roughly 40% from 1920-1980, with near zero growth after the 1990s, based on the South Pole firn air reconstructions. The rate of CO rise during the mid-twentieth century was faster than the rate of methane rise during the same period. Modeling studies show that the twentieth century CO trends at high latitudes in each hemisphere can be explained by changes in anthropogenic fossil fuel emissions. The timing of the peak and decline in the anthropogenic CO emissions reconstructions is consistent with the implementation of clean air policies in the US and Europe.

CHAPTER 1

Introduction

Human activities have had a considerable impact on the chemical composition of Earth's atmosphere since the pre-industrial era. Firn air and ice cores provide a unique archive of changes in atmospheric composition and have been used in detail to study variations in the atmospheric greenhouse gases, including methane (CH_4). The levels of atmospheric CH_4 have more than doubled since the onset of the industrial revolution due to man's activities.

Anthropogenic CH_4 sources include fossil fuel extraction, production, and use, biofuel and biomass burning, landfills and wastewater treatment facilities, rice agriculture, and ruminant animals. CH_4 also has significant natural and biogenic sources from tropical and boreal wetlands, oceans, wildfires, termites, and geologic seeps. Over long timescales, the sources of methane can be impacted by climate. However, the atmospheric budget of CH_4 is complicated, and it is difficult to predict how the natural CH_4 sources will respond in a changing climate. It is useful to study other tracers with simpler atmospheric budgets to understand changes in CH_4. In the modern atmosphere, ethane levels track the growth rate of atmospheric methane. Ethane and methane have common sources, including fossil fuels, biomass burning, and geologic emissions. Ethane has small biogenic sources, making it an ideal tracer of pre-industrial changes in methane emissions from biomass burning and geologic sources. Carbon monoxide is important because it controls the abundance of hydroxyl radical, and thus impacts the tropospheric abundance and lifetime of many gases in the atmosphere, including atmospheric methane.

In this study, ethane and carbon monoxide were measured in polar surface air, firn air, and ice cores. These measurements are used to derive atmospheric histories of these gases and understand how human activities impacted their atmospheric budgets during the last century. The firn air and ice core samples used in this research come from Summit, Greenland, the West Antarctic Ice Sheet (WAIS)-Divide, Antarctica, and the South Pole. Together, firn air records from both poles can provide an archive of the composition of gases in the atmosphere at high latitudes in each hemisphere. The South Pole is a key location for firn air studies. The South Pole firn air record provides a unique link between surface air and ice core observations, because the low temperature (-51°C) and accumulation rate (7.5 cm y^{-1}, water equivalent) provide the ideal conditions for trapping the very old air in the firn (about 90-100 years before present). The temperature and accumulation rates at WAIS-Divide, Antarctica and Summit, Greenland are similar to one another and allow reconstruction of atmospheric gases back to the 1950s.

The objective of this dissertation is to answer the following research questions: (1) How have man's activities impacted the atmosphere? (2) Are ethane and carbon monoxide levels preserved in polar firn air? (3) What do ethane and carbon monoxide levels recorded in firn air and ice cores tell us about past changes in atmospheric composition? (4) What do these variations tell us about changes in the atmospheric budgets of these gases? (5) How have their atmospheric levels varied due to human activities since the pre-industrial era?

These research goals have been accomplished through:

1) Collecting firn air samples from Summit, Greenland, WAIS Divide, and South Pole (sampling conducted by M. Aydin, T. Sowers, M. Battle, and colleagues), and collection of ice core samples during five sampling trips to the National Ice Core Laboratory in Denver, CO (2008-2013).

2) Measuring trace gas concentrations on firn air samples from South Pole, Antarctica and Summit, Greenland using gas chromatography coupled with high-resolution mass spectrometry (GC/MS). Gases measured include ethane, propane, n-butane, carbonyl sulfide, carbon disulfide, methyl chloride and methyl bromide.
3) Using a 1D firn air advection-diffusion model to simulate the diffusion of gases in the firn layers at Summit, WAIS-D and South Pole. An inversion technique was used to reconstruct atmospheric histories of trace gases based on the firn air measurements.
4) Analyzing trace gases in Antarctic ice core samples using dry and wet extraction techniques. The wet extraction technique used in this study involved the development of a new glass line and vacuum chamber for the extraction and analysis of hydrocarbon gases (ethane, propane, and n-butane). In this study, the ice core ethane data from the dry extraction chambers were used to determine the impact of can blanks on the measured ice core levels for hydrocarbon gases. Ice cores were analyzed using dry extraction were from Taylor Dome, the West Antarctic Ice Sheet (WAIS)-Divide, Siple Dome, Byrd, and Vostok. Ice cores analyzed using wet extraction technique were from WAIS-Divide and South Pole.
5) Using the UC Irvine 3D Chemical Transport Model to study how the major sources of ethane and carbon monoxide map onto the high latitude atmosphere. The data collected from these 3D modeling studies was used to interpret past changes in the atmospheric levels of ethane and carbon monoxide in terms of changes in their atmospheric emissions using simple box models of the atmosphere

Chapter 2 describes the methods used in this study, including a description of the analytical techniques and the firn air advection-diffusion model used to interpret the firn air measurements.

In Chapter 3, ethane (C_2H_6) levels were measured in firn air samples from Summit, Greenland, WAIS-Divide, and South Pole, Antarctica. The firn air measurements are used in combination with a synthesis inversion method to develop an atmospheric history of ethane at high latitudes. The ethane atmospheric histories are used to reconstruct anthropogenic fossil fuel emissions during the twentieth century. Chapter 4 presents preliminary measurements of ethane in Antarctic ice cores from WAIS Divide and South Pole during the last 1000 years. The wet extraction measurements involved the construction of a new glass line for the extraction of ethane and other insoluble gases from polar ice core samples. Ethane measurements are interpreted from the two extraction methods. Based on the wet extraction measurements, it appears likely that a pre-industrial ethane level is recorded in ice cores from these Antarctic sites. A correction is proposed for the dry extraction measurements in Antarctic and Greenland ice cores to estimate the pre-industrial ethane level.

In Chapter 5, measurements of carbon monoxide (CO) are presented from the South Pole firn air samples. The firn air measurements are used in combination with a synthesis inversion method to develop an atmospheric history of carbon monoxide for the high latitude Southern Hemisphere. The resulting CO atmospheric history is used in Chapter 6 to estimate anthropogenic CO emissions during the twentieth century. The final chapter of this dissertation discusses the current understanding of the levels of ethane and carbon monoxide in polar firn air and ice cores during the last 1000 years and possible future research directions.

The following sections provide the background information necessary to understand the various atmospheric archives that can be used to reconstruct past atmospheric composition, including surface air, firn air, and ice cores. The importance of atmospheric methane (CH_4),

ethane (C_2H_6) and carbon monoxide (CO) in tropospheric photochemistry is discussed, as well as information about their atmospheric budgets, distribution, and recent and long-term trends.

1.1 Atmospheric air archives

Surface flasks, firn air and ice cores can be used to reconstruct past changes in atmospheric composition over timescales ranging from decades, to hundreds to hundreds of thousands of years. Surface flask observations provide a snapshot of the atmosphere at a single location, at a given date and time. Flask measurements can be used to identify the long-term trends, seasonal variability, and spatial distribution of trace gases. However, the observational flask record only date back to the 1950s for CO_2, and is much shorter for other trace gases.

The air trapped in polar firn (porous ice) provides a record of smoothed atmospheric changes on decadal to centennial timescales. The firn is a compacted layer of perennial snowpack that resides in the upper ~50-120 m of the polar ice sheets. Conceptually, the firn layer can be thought of as a permeable "filter" or "sieve" through which gases from the overlying atmosphere will diffuse, resulting in a smoothed record of atmospheric changes over time. Figure 1.1 shows a schematic representation of an idealized firn column [*Battle et al.,* 2011]. The movement of gases through firn is influenced by several factors, including the open porosity (based on density of the ice), gas diffusivity, gravitational settling, pressure gradients, wind pumping, advection, formation of melt layers, and close-off fractionation of gases in the ice [*Battle et al.*, 1996; *Schwander et al.*, 1997; *Fabre et al.*, 2000; *Severinghaus and Battle*, 2006]. Figure 1.1 shows that different transport mechanisms dominate in each region of the firn (convective zone, diffusive column, lock in depth), although not all the processes shown will be present in every naturally occurring firn column. The firn layer differs from solid ice in that it is comprised of open pores (spaces) where the gases remain in contact with the overlying atmosphere. The age of

a gas at a particular depth in the firn is not a single year, but is described by a distribution of gas ages, which can be determined using a firn diffusion model [*Schwander*, 1989; *Trudinger et al.,* 1997; *Battle et al.,* 2011].

Below the porous firn layer, gases are no longer in contact with the overlying atmosphere and are trapped within the solid ice matrix. The depth where the density of ice reaches approximately 800-840 kg m^{-3} is a region known as the bubble close-off depth [*Schwander et al.*, 1997]. Below this depth, gases are locked in the ice bubbles they will age at the same rate as the surrounding ice. The exact depth of the firn-ice transition and bubble close-off is determined primarily by physical characteristics of the site, such as accumulation rate and temperature. The mean age of the air trapped in polar ice cores is always younger than the age of the surrounding ice due to diffusion in the firn layer. Firn air records provide a test for continuity and overlap between surface air observations and shallow ice core measurements, and are useful for determining how gases have changed over time. However, the preservation of an atmospheric trace gas in the firn column must first be established before reconstructing an ice core record because it provides information linking the ice core record to the modern day surface observations. Validation of firn air and ice core records as well-mixed samples of the ancient atmosphere involves comparison of measurements from several sites, with different physical properties and site characteristics.

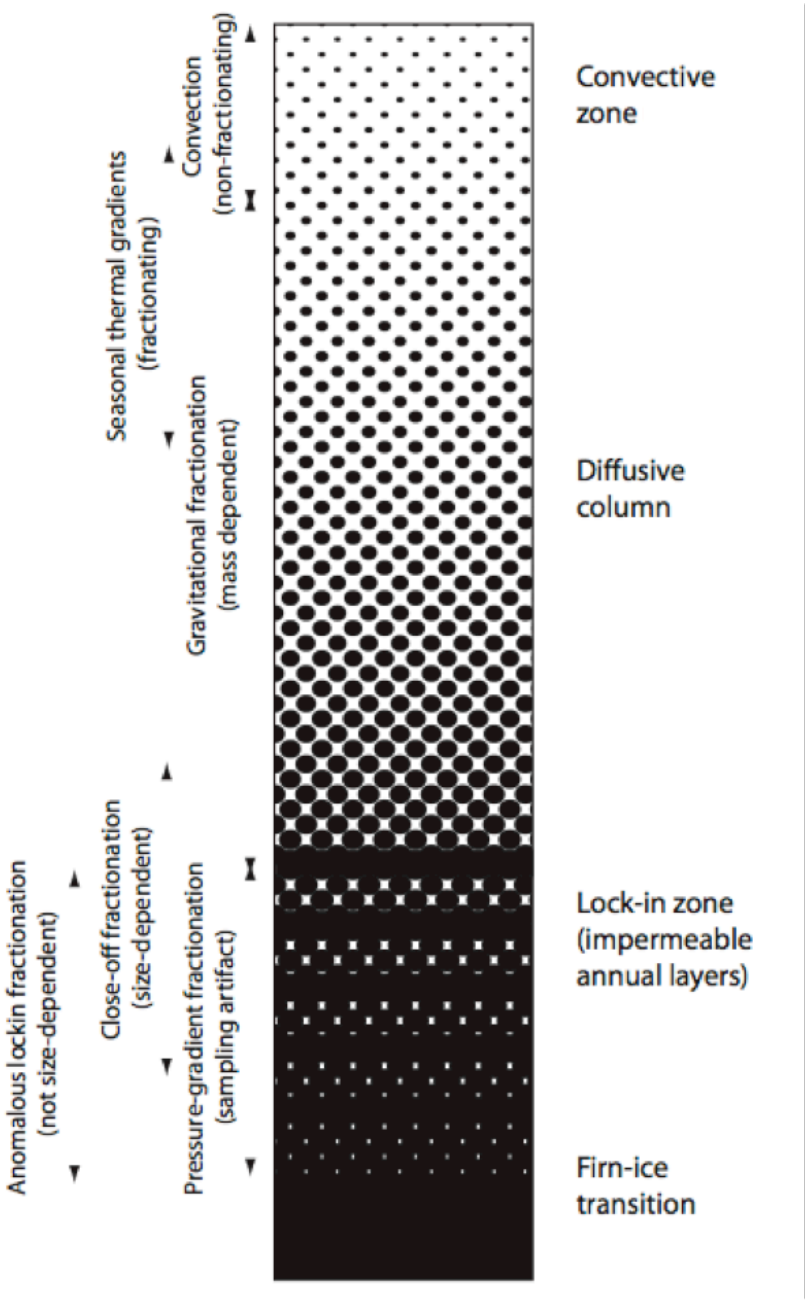

Figure 1.1: A schematic diagram of an idealized firn column from WAIS Divide (adapted from Figure 1 in *Battle et al.*, 2011). The density of ice increases with depth, while open porosity decreases with depth, indicated by the increasing area of dark shading with depth. The dominant transport mechanisms in each region are shown on the left, while the major regions of the firn column are shown on the right. The figure is not drawn to scale, and not all processes will be present in every naturally occurring firn column.

1.2 Tropospheric photochemistry of methane, ethane, and carbon monoxide

Methane is the second most important greenhouse gas that directly impacts Earth's radiative budget, with 26 times the global warming potential of carbon dioxide [*Hartmann et al.*, 2013]. Methane (CH_4), ethane (C_2H_6), and carbon monoxide (CO) exhibit considerable influence on the chemical composition of the background troposphere. In the atmosphere, destruction of these gases leads to production of tropospheric ozone, a potent greenhouse gas and atmospheric pollutant. Ozone is also important for regulating levels of hydroxyl radical, an atmospheric oxidant that determines the lifetime of many gases.

1.2.1 Reaction with tropospheric OH

The major loss pathway of these compounds is oxidation by hydroxyl radical. The hydroxyl radical (OH) is the most important atmospheric oxidant, and is responsible for controlling the lifetime and removal of many organic trace gases from the atmosphere. Production of OH occurs via ozone photolysis [*Seinfeld*, 1989]:

$$O_3 + h\upsilon \rightarrow O(^1D) + O_2 \quad (1.1)$$
$$O(^1D) + H_2O \rightarrow 2\,OH \quad (1.2)$$
$$O(^1D) + M \rightarrow O(^3P) + M \quad (1.3)$$
$$O(^3P) + O_2 \rightarrow O_3 \quad (1.4)$$

In equations 1.1-1.4, photolysis of ozone (O_3) produces excited oxygen ($O(^1D)$), which forms OH in the presence of water vapor. Equation 1.3 is a competing reaction, in which the excited oxygen is quenched and O_3 is reformed.

The role of hydrocarbons in tropospheric photochemistry and the major photochemical pathways controlling production of tropospheric ozone are described in equations 1.5-1.10:

$$RH + OH \rightarrow R^{\cdot} + H_2O \quad (1.5)$$
$$R^{\cdot} + O_2 \rightarrow RO_2 \quad (1.6)$$
$$RO_2 + NO \rightarrow NO_2 + RO \quad (1.7)$$
$$NO_2 + h\nu \rightarrow NO + O \quad (1.8)$$
$$\underline{O + O_2 + M \rightarrow O_3 + M} \quad (1.9)$$
Net: $$RH + 2O_2 + OH \rightarrow H_2O + RO + O_3 \quad (1.10)$$

The reaction of hydrocarbons (RH) with tropospheric OH produces alkyl peroxy radicals (RO_2). RO_2 radicals are precursors to tropospheric ozone formation in polluted (urban) environments in the presence of high levels of atmospheric NO_x (nitrogen oxides, NO and NO_2). Hydrocarbon oxidation can also form a wide range of ketones, aldehydes, and organic acids, which indirectly participate in tropospheric ozone formation [*Aikin et al.*, 1982; *Atkinson*, 2000].

Carbon monoxide (CO) is another reactive trace gas that plays an important role in determining tropospheric ozone and OH levels. Equations 1.11-1.16 show a simplified scheme of the reaction of CO + OH:

$$CO + OH \rightarrow CO_2 + H \quad (1.11)$$
$$H + O_2 + M \rightarrow HO_2 + M \quad (1.12)$$
$$HO_2 + NO \rightarrow NO_2 + OH \quad (1.13)$$
$$NO_2 + h\nu \rightarrow NO + O \quad (1.14)$$
$$\underline{O + O_2 + M \rightarrow O_3 + M} \quad (1.15)$$
Net: $$CO + 2O_2 + h\nu \rightarrow CO_2 + O_3 \quad (1.16)$$

Reaction of CO with OH in the troposphere generates the hydroperoxy radical (HO_2). At moderate to high NO_x (NO and NO_2) levels, HO_2 reacts with NO to form NO_2, generating tropospheric ozone, a potent atmospheric pollutant and greenhouse gas (equations 1.13-1.15). At low NO_x levels, HO_2 is a major sink for tropospheric ozone. Although CO itself is not an important greenhouse gas, it indirectly influences the abundance and lifetime of tropospheric ozone and methane (CH_4), and thus impacts earth's radiative budget.

1.2.2 Atmospheric lifetimes

The atmospheric lifetimes of CH_4, C_2H_6, and CO are determined primarily by their reaction with OH. The atmospheric lifetime of a gas with respect to OH (τ_{OH}) is determined by:

$$\tau = \frac{1}{k_{OH}[OH]} \tag{1.12}$$

where k_{OH} is the rate constant for reaction of the gas with OH, and [OH] is the concentration of OH radicals present in the atmosphere (roughly $1x10^6$ molecules cm^{-3} in the atmosphere. The actual lifetime of CH_4, C_2H_6 and CO with respect to OH is determined by their reaction rates with OH and the concentration of OH radicals. For CH_4 and C_2H_6, the rate constant for reaction with OH in the atmosphere is temperature dependent, while the reaction rate constant for CO + OH is pressure dependent [*Sander et al.*, 2006]. Hence the location where most of the methane and ethane in the atmosphere are oxidized may be different than the location where most of the CO is oxidized. The removal of hydrocarbons and CO in the atmosphere may also be dependent on the concentration of ozone, either through direct reactions with ozone or through the photochemical production of OH from ozone photolysis.

The concentration of atmospheric OH also varies significantly, both seasonally and regionally [*Spivakovsky et al.*, 2000]. The highest concentrations of OH are found in the tropics, with strong seasonality at mid-high latitudes, reflecting seasonal variations in water vapor and sunlight. The local abundance of OH is also determined by concentrations of hydrocarbons, CO, O_3, NO_x, water vapor, and the intensity of solar radiation [*Isaksen and Hov*, 1987; *Naik et al.*, 2013].

1.3 Atmospheric methane

1.3.1 Atmospheric budget

Methane is emitted primarily from fossil fuel production, transport and combustion (including natural gas, oil and coal), geologic seeps, biogenic sources (including tropical and boreal wetlands, ruminant animals, rice agriculture, and landfills), and biomass and biofuel burning (Table 1.1) [*Dlugokencky et al.*, 2011; *Etiope*, 2012; *Nisbet et al.*, 2014]. Destruction by OH is the major sink of atmospheric methane. The methane lifetime with respect to OH ($1/k_{OH}$) = 9.6 yr, while the total methane lifetime ($1/k_{total}$) = 8.4 yr [*Ehhalt et al.*, 2001]. Other methane sinks include loss to the stratosphere, and oxidation by chlorine atoms ($Cl^{\cdot}$).

1.3.2 Recent atmospheric trends

Recently, the growth rate of atmospheric methane slowed for several decades, although since 2007, atmospheric methane levels are once again on the rise [*Nisbet et al.*, 2014]. Figure 1.2 shows the global growth rate of atmospheric CH_4 based on surface flask observations from the National Oceanic Atmospheric Administration (NOAA) Carbon Cycle Group (CCG). Globally, atmospheric methane levels rose at a rate of 12 ppb y^{-1} from the mid-1980s until the 1990s. Between about 1992-2000, the growth rate slowed to about 3 ppb y^{-1}. From 1999-2006, methane levels "stagnated," at times showing near zero growth and sometimes a slight decline [*Nisbet et al.*, 2014]. In 2007, methane levels began to rise again, and have continued rising at a rate of about 6 ppb y^{-1}.

The cause of the recent slowdown of the methane growth rate is not well understood and has been the subject of considerable scientific debate [*Bousquet et al.*, 2006; *Simpson et al.,* 2006, 2012; *Aydin et al.,* 2011; *Kai et al.,* 2011; *Worton et al.,* 2012; *Nisbet et al.,* 2014]. Several

competing hypotheses have been proposed. Some studies suggested that the decline in methane growth was due to a long-term decrease in a Northern Hemisphere source, such as emissions from fossil fuels [*Bousquet et al.*, 2006; *Simpson et al.*, 2012]. However, measurements of methane isotopes ($\delta^{13}C$ and δD of CH_4) suggest that the recent decline was related to reductions in an isotopically depleted CH_4 source, such as rice agriculture [*Kai et al.*, 2011]. The alternative hypothesis presented in these studies highlight the need for a better understanding of the natural drivers over atmospheric CH_4 over long timescales.

The cause of the rise in the methane growth rate since 2007 is still uncertain. The time history and latitudinal distribution in atmospheric methane has been used to investigate global trends. The slow growth in atmospheric methane from 1992-2000 was coupled with a smaller north/south interpolar difference [*Dlugokencky*, 2003; *Dlugokencky et al.*, 2011; *Nisbet et al.*, 2014]. In 2007, Arctic methane levels rose more dramatically compared to the global trend, but have since shown equivalent growth [*Nisbet et al.*, 2014]. Since 2007, the methane growth in the southern tropics has been above the global trends, reaching >10 ppb y^{-1} in 2009 and 2010. This rise in the southern tropics may be caused by increased methane emissions through the expansion of tropical wetland area due to increased precipitation [*Nisbet et al.*, 2014]. Since 2007, the global atmospheric methane measurements have also become more depleted in $\delta^{13}C$, which is an indication that the methane growth is dominated by wetland and ruminant emissions, which are richer in ^{12}C [*Nisbet et al.*, 2014]. However, global fossil fuel emissions of methane are also suspected to be on the rise in recent years due to increased drilling and extraction activities (including shale "fracking") and leaks from natural gas systems [*Brandt et al.*, 2014].

The recent methane growth has been investigated by global modeling studies [*Bousquet et al.*, 2011; *Bergamaschi et al.*, 2013]. *Bergamaschi et al.* [2013] used observations from NOAA

ESRL's global flask sampling network, combined with retrievals of column-averaged CH_4 mole fractions from the SCIAMACHY satellite to derive global CH_4 emissions. This study suggested that CH_4 emissions were 16-20 Tg CH_4 y^{-1} higher from 2007-2010 compared to 2003–2005, with the majority of this rise located in the tropics (9-14 Tg CH_4 y^{-1}) and mid-latitude Northern Hemisphere (6-8 Tg CH_4 y^{-1}). *Bousquet et al.* [2011] showed that the increase in methane emissions in 2007 was primarily driven by changes in the tropics (~60-80%), due to emissions from natural wetlands. The remainder of the recent methane increase was suggested to be due to contributions from high northern latitudes [*Bousquet et al.,* 2011].

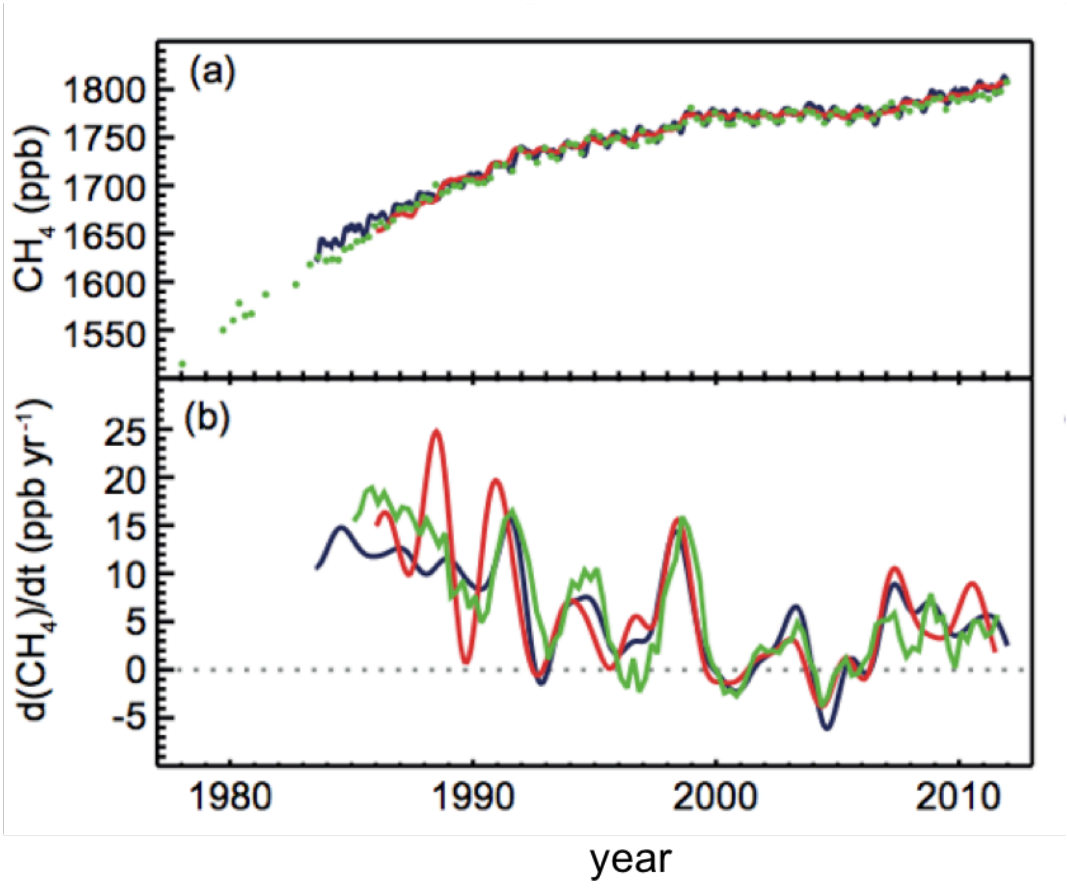

Figure 1.2: Global CH_4 mixing ratios (in ppb) and global CH_4 growth rates (in ppb y^{-1}). a) Globally averaged CH_4 dry-air mole fractions from UCI (green; four values per year, except prior to 1984, when they are of lower and varying frequency), AGAGE (red; monthly), and NOAA/ESRL/GMD (blue; quasi-weekly). b) Instantaneous growth rate for globally averaged atmospheric CH_4 using the same color code as in (a). Growth rates are calculated as the time derivative of the deseasonalized global averages [*Dlugokencky et al.*, 1994]. Figure from *Hartmann et al.*, [2013]. NOAA/ESRL data from: ftp://ftp.cmdl.noaa.gov/ccg/ch4/flask/event/.

1.3.3 Firn air and ice core records

The history of atmospheric methane during the last 2000 years shows that anthropogenic activities have led to significant increases in methane levels since the industrial revolution (Figure 1.3). The atmospheric history of methane is based on Antarctic ice core measurements [*Etheridge et al.*, 1998; *Mitchell et al.*, 2011] and surface air observations from the high latitude Southern Hemisphere [*Dlugokencky*, 2003]. Antarctic firn air and ice core measurements show that modern CH_4 levels varied between about 400-700 ppb during pre-industrial times and have more than doubled to the present day level of roughly 1780 ppb (Figure 1.3) [*Etheridge et al.*, 1998; *Mitchell et al.*, 2011]. The rise in atmospheric methane levels since the industrial revolution (circa 1700 AD) is mainly due to anthropogenic emissions (e.g. fossil fuel extraction and use, agricultural practices, landfills and wastewater treatment). Atmospheric methane levels varied around 650 and 740 ppb during the last 1000 years, between 1000-1800 AD (inset, Figure 1.3) [*Etheridge et al.*, 1998; *Mitchell et al.*, 2011]. During the last 3000 years, the CH_4 interpolar difference (IPD) was relatively constant at 41.6 ppb, despite the 115 ppb (17%) increase in the global concentration [*Mitchell et al.*, 2013]. This finding is roughly consistent with prior estimates of the CH_4 IPD based on lower-resolution ice core records [*Chappellaz et al.*, 1997; *Etheridge et al.*, 1998].

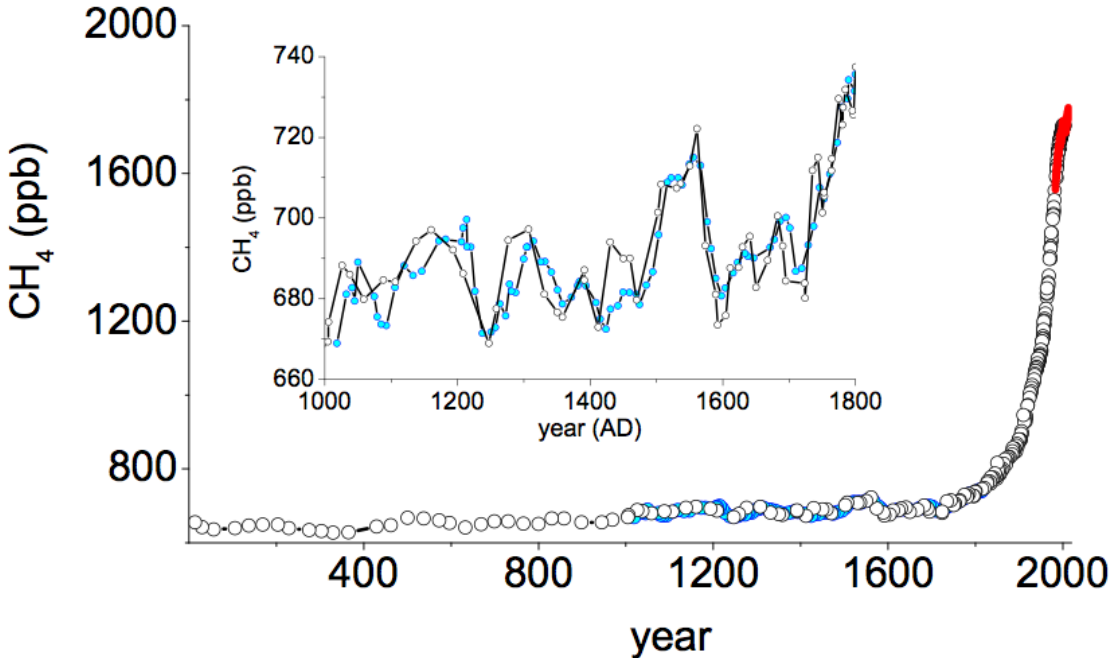

Figure 1.3: Atmospheric variations of CH_4 (in ppb) based on surface air measurements from Cape Grim, Tasmania, and firn air and ice core measurements from Law Dome, Antarctica and WAIS Divide, Antarctica. Inset: Pre-industrial CH_4 levels varied between 650 and 740 ppb from ~1000-1800 C.E. Figure adapted from *Mitchell et al.,* [2011] and *Etheridge et al.,* [1998].

1.4 Ethane

1.4.1 Atmospheric budget

Tropospheric ethane (C_2H_6) is emitted primarily from the incomplete combustion of fossil fuels, biofuels, and biomass burning [*Xiao et al.*, 2008]. Anthropogenic fossil emissions of ethane are mainly due to evaporative losses from to production, storage and use of fossil fuels. Ethane is also emitted from biomass burning. Ethane also has relatively small biogenic sources from oceans and vegetation (Table 1.1) [*Plass-Dulmer et al.*, 1995; *Rudolph*, 1995; *Clarkson et al.*, 1997; *Xiao et al.*, 2008]. The largest sources of ethane to the Southern Hemisphere include biomass burning (1 Tg yr^{-1}) and transport from the Northern Hemisphere (1.7 Tg yr^{-1}) [*Xiao et al.*, 2008]. Approximately 80% of ethane emissions originate in the Northern Hemisphere, giving

biomass burning and biogenic emissions a greater relative importance at high latitudes in the Southern Hemisphere [*Bonsang et al.*, 2008]. The range of literature estimates of global ethane sources range from about 8-18 Tg C_2H_6 yr^{-1}, revealing large uncertainties in the understanding of the evolution in ethane sources over time. Recently, the modern day global ethane emissions were re-evaluated to 13 Tg yr^{-1}, based atmospheric observations and 3D global modeling studies [*Xiao et al.*, 2008]. *Simpson et al.* [2012] observed a global decline in atmospheric ethane levels between 1984-2010, and suggested it was due to a 3 Tg y^{-1} reduction in global ethane emissions from fossil fuels (from 14.3 Tg y^{-1} to 11.3 Tg y^{-1}).

Methane and ethane are two of the most abundant hydrocarbons in the troposphere. Recent studies suggest that atmospheric ethane is important for understanding the growth rate of atmospheric methane. Methane and ethane share common fossil fuel and biomass burning sources. Fossil fuel emissions occur primarily in the Northern Hemisphere and include evaporative emissions from the production, transport, and storage of petroleum products, natural gas leaks, and to a smaller extent, vehicular exhaust [*Rudolph*, 1995; *Xiao et al.*, 2008; *Miller et al.*, 2013]. Hydrocarbon gases, such as methane and ethane, can also be emitted from natural geologic seeps. Methane also has important sources from wetlands, ruminant animals, rice agriculture, and landfills (Table 1.1). These sources are not shared with ethane and so are not discussed in further detail here.

Recent studies suggest that the ratio of methane/ethane (CH_4/C_2H_6) from fossil methane sources can provide a constraint on methane emission from fossil fuel extraction (oil and natural gas) and geologic seeps[*Etiope and Ciccioli*, 2009; *Aydin et al.*, 2011; *Simpson et al.*, 2012]. The ratio of CH_4/C_2H_6 from fossil sources is highly variable and depends on several factors, including the temperature, pressure (i.e. depth at which the reservoir is located), the age of the

reservoir, and the composition of the source material (i.e. either biogenic or thermogenic), and the surrounding rock where the reservoir is contained. Natural hydrocarbon emissions can occur due to both biogenic (microbial) and thermogenic (thermal) degradation of organic matter that has been stored for long periods of time in the subsurface of earth's crust. Generally speaking, gases emanating from seeps are mainly thermogenic in origin [*Etiope et al.*, 2008; *Etiope*, 2009]. Microbial gas is produced at shallow depths and low temperatures, while thermogenic production occurs at much greater depths and at higher temperatures [*Etiope*, 2012]. With regards to fossil fuel use, the CH_4/C_2H_6 ratio depends largely on the type of fuel responsible for the emissions. For example, CH_4/C_2H_6 emissions ratios from natural gas vary widely, depending on the whether the gas is emitted from dry-, condensate-, or oil-gas fields [*Jones et al.*, 1999; *Xiao et al.*, 2008]. Higher CH_4/C_2H_6 fossil fuel emissions ratios are seen in dry gas fields, which consist primarily of CH_4 (CH_4/C_2H_6 emissions ~20-100, on a Tg/Tg basis). The lowest emissions ratios are seen in oil fields, which contain liquefied or condensed non-methane volatile organic compounds (CH_4/C_2H_6 emissions ratio ~4-10) [*Jones et al.*, 1999; *Xiao et al.*, 2008]. The ratio of CH_4/C_2H_6 emitted from coal combustion also depends largely on the origin of the CH_4 (biogenic vs. thermogenic) [*Xiao et al.*, 2008]. The high variability in CH_4/C_2H_6 ratios from fossil fuels makes it difficult to estimate this ratio on a regional and global scale, or to determine whether this ratio has changed significantly over time. However, ethane can help to constrain the fossil and geologic sources of methane, if the ratio of these gases can be better constrained in fossil fuel vs. geologic sources.

Methane and ethane also share common biomass burning and biofuel combustion sources. *Xiao et al.* [2008] estimate that the ethane source from biofuel combustion is 2.6 Tg C_2H_6 yr^{-1}, while biomass burning contributes 2.4 Tg yr^{-1}. Approximately 40% of the biomass burning

source is thought to be emitted in the Southern Hemisphere [*Xiao et al.*, 2008]. The extent of biomass burning has changed dramatically over time as a result of changing agricultural practices, tropical deforestation, and burning of savannahs and brushlands [*Andreae and Merlet*, 2001]. *Schultz et al.* [2008] estimated that global annual emissions of C_2H_6 and CH_4 from fires roughly doubled over the last 30 years (from ~1.58 to 3.09 Tg yr^{-1} for C_2H_6 and 10.7 to 20.4 Tg yr^{-1} for CH_4 over the period 1960-1990). These estimates are based on satellite products (e.g. GFED), numerical modeling of fire occurrence, and literature reviews as part of the Reanalysis of the Tropospheric chemical composition (RETRO) project [*Schultz et al.*, 2008]. Based on these estimates, the ratio of CH_4/C_2H_6 from biomass burning emissions is about 5-10.

The major sink for tropospheric methane and ethane is reaction with hydroxyl radical ($OH^{\cdot}$). The average lifetime of tropospheric ethane is ~2 months (annual mean) [*Rudolph*, 1995; *Boissard and Bonsang*, 1996; *Poisson et al.*, 2000]. Methane and ethane are also rapidly oxidized by chlorine atoms ($Cl^{\cdot}$), which can be produced in the marine boundary layer by heterogeneous reactions involving marine aerosols [*Knipping and Dabdub*, 2003]. $Cl^{\cdot}$ atoms preferentially oxidize ethane relative to methane (about 1000 times faster), compared to their respective reaction rates with OH [*Singh and Kasting*, 1988]. *Platt et al.*, [2004] suggest that the reaction of CH_4 with $Cl^{\cdot}$ atom accounts for ~3.3% of the total methane sink, leading to a sink of ~19 Tg CH_4 yr^{-1}.

Table 1.1: Methane [(a)] and ethane [(b)] sources.

Source	Methane (Tg/yr)	Ethane (Tg/yr)
Fossil fuels	85-105	8-9.2
Biomass burning	32-39	2.4-2.8
Oceans (hydrates)	(2-9)	0.2-0.5
Vegetation/Soils	controversial	0.4-2.5
Wetlands	177-284	<0.2
Rice agriculture	33-40	<0.2
Livestock	87-94	
Freshwaters	8-73	
Landfills + Waste	67-90	--
Termites	2-22	--
Gas hydrates		--
Geologic	33-75[(a)] (42-64) [(c)]	2-4[(c)]
Total sources	526-831	~13-19

(a) IPCC 2013: *Ciais and Bala, et al.* [2013]
(b) *Xiao et al.,* [2008]
(c) *Etiope and Ciccoli* [2009]

1.4.2 Atmospheric distribution and seasonality

Ethane levels in surface air are characterized by strong seasonal variation, reflecting the wintertime accumulation and summertime drawdown due to oxidation by OH. The drawdown of ethane occurs during late August in the Northern Hemisphere and between January-March in the Southern Hemisphere. The distribution of sources and the relatively short lifetime of ethane lead to the strong latitudinal gradients observed in the troposphere. The 3D ethane surface plot in Figure 1.4 shows the global distribution of atmospheric ethane levels. Figure 1.4 represents many flask measurements, with the data smoothed by time, mixing ratio and latitude [*Helmig and Bottenheim*, 2009]. In addition, time series measurements of ethane from high latitude sites in the Northern and Southern Hemispheres have been collected from two independent labs at UC Irvine from 2000-2009 [*this study*, *Aydin et al.,* 2011; *Simpson et al.*, 2006; 2012]. These measurements show the hemispheric average ethane level between 1984-2010 was 1049±99 ppt and 277±34

ppt, for the Northern and Southern Hemispheres, respectively. Based on the surface flask data, the mean annual ethane level at high Northern latitudes was 1443±49 ppt, with a range of roughly 0.5 ppb in summer up to 2.5-3 ppb in winter [*Simpson et al.*, 2006, 2012].. The mean annual ethane level at South Pole is about 230-250 ppt, with a range from 0.5 ppb in summer up to 2.5-3 ppb in winter. Overall, the mean annual ethane level measured over Antarctica is fairly representative of the mean annual level in the remote, high latitude Southern Hemisphere [*Beyersdorf et al.*, 2010].

In populated regions, such as in the northern hemisphere, ethane increase with altitude. This reflects the fact that there are stronger boundary layer sources in these regions. However, most of the ethane measured over Antarctica is transported via high altitude, long-range transport because there are no large local sources. *Beyersdorf et al.* [2010] show ethane levels are nearly constant at 210±20 ppt in the lowest 1.5 km of the Antarctic atmosphere. Above 3 km, ethane levels increase to 280±20 ppt. The trend of increasing mixing ratios with increasing altitude is also observed for other VOCs [*Beyersdorf et al.*, 2010].

1.4.3 Recent atmospheric trends

Continuous surface air observations of ethane since 1978 show that atmospheric ethane levels declined globally by about 30% from 1984-2008 [*Simpson et al.*, 2006, 2012]. These results were later confirmed by several other independent analyses of surface air and firn air measurements [*this study,* as well as: *Helmig and Bottenheim*, 2009; *Worton et al.*, 2012; *Helmig et al.*, 2014]. *Helmig and Bottenheim* [2009] also observed a decline of ethane (-1% yr^{-1}) over Hohenpeisenberg, Germany over the last 10 years using observations from the NOAA/ESRL VOC flask sampling network. Similarly, [*Zander et al.*, 2005] observed an approximately 30% decrease in the total column abundance of ethane since the 1980s using FTIR spectroscopy

measurements at the International Scientific Station in Jungfraujoch, Switzerland. Interestingly, the continuous measurements of C_2H_6 since 1978 also show that interannual variations in ethane concentration, for the most part, coincide with the timing of changes in the methane growth rate [*Simpson et al.*, 2006, 2012]. There are few surface observations of atmospheric ethane prior to 1980.

1.4.4 Firn air and ice core records

There are no ice core records of atmospheric ethane to date. Such a record would aid in assessing the magnitude of geologic and biomass burning sources in the pre-industrial methane budget. A limited number of firn air studies of ethane and other light (C_2-C_5) VOCs have been carried out. These records suggest that these compounds are stable in firn air and not influenced by *in situ* photochemical or biological production/loss. *Swanson et al.*, [2002] measured ethane depth profiles in the shallow firn (<1.5 m) at Summit, Greenland during Spring 2004 and saw no evidence of *in situ* production. Ethane has also been measured in Antarctic firn air from South Pole and Dronning Maud Land [E. Atlas, *unpublished data, Kaspers et al.*, 2004], and North GRIP, Greenland [*Worton et al.*, 2012].

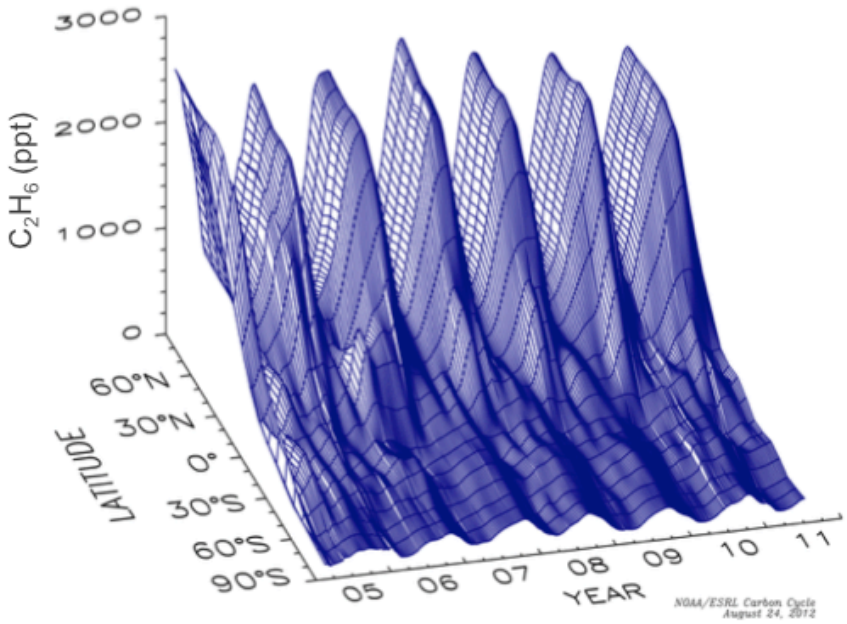

Figure 1.4: Three-dimensional representation of the latitudinal distribution of atmospheric C_2H_6 (in ppt) from 2004-2011 based on data from the NOAA/ESRL air sampling network. The surface represents many measurements, with the data smoothed by time and latitude. Figure adapted from NOAA/ESRL Carbon Cycle: http://instaar.colorado.edu/arl/Global_VOC.html.

1.5 Carbon monoxide

1.5.1 Atmospheric budget

CO is emitted from both natural and anthropogenic sources. These include direct emissions from fossil fuel combustion, biomass and biofuel burning, and minor emissions from terrestrial plants and the oceans. CO is also indirectly produced due to photochemical oxidation of CH_4 and non-methane VOCs from both anthropogenic and natural sources [*Logan et al.*, 1981; *Novelli et al.*, 1992, 1994, 1998; *Bakwin et al.*, 1994; *Duncan et al.*, 2007]. Fossil fuel emissions are linked to incomplete combustion from vehicular, residential, and industrial sources, which occur primarily in the Northern Hemisphere. CO produced indirectly via atmospheric oxidation of hydrocarbons can be classified as either a natural or fossil source depending on the origin of the CH_4 and NMVOCs. Reaction with OH is the primary loss pathway for CO (~90%), and uptake

by soils is a minor sink. The atmospheric lifetime of CO is about 1-2 months [*Kanakidou and Crutzen*, 1999]. The typical tropospheric burden of CO today is about 350 Tg y^{-1} in January and ~305 Tg y^{-1} in July [*Duncan et al.*, 2007].

1.5.2 Atmospheric distribution and seasonality

Flask observations of CO began with the 1988 NOAA Carbon Cycle cooperative air-sampling network (NOAA/ESRL) and provide information about the spatial distribution and temporal patterns of CO in the atmosphere. Figure 1.5 shows a 3D representation of the spatial and temporal patterns of CO in the marine boundary layer from 2001 to 2011, based on the NOAA Carbon Cycle Cooperative air sampling network [*Novelli and Masarie,* 2013]. The 3D surface in Figure 1.5 represents many flask measurements, with the data smoothed by time, mixing ratio and latitude. Zonally-averaged time series, representing equal areas of the earth's surface, have been extracted from this smoothed surface and used to understand long-term trends in atmospheric CO levels since the 1990s [*Novelli et al.*, 1994, 1998, 2003]. Atmospheric CO mole fractions exhibit a large interhemispheric difference, reflecting the fact that CO emissions in the Northern Hemisphere (NH), particularly fossil fuel emissions, are several-fold greater than Southern Hemisphere (SH) emissions. The mean CO level in the Northern Hemisphere is roughly 110 ppb, which is nearly twice the mean CO level in the Southern Hemisphere, roughly 60 ppb. The mean level at high Southern latitudes is approximately 75-80% of the Southern Hemisphere mean. Atmospheric CO exhibits strong seasonal variability, primarily driven by summertime loss via reaction with OH. CO removal rates vary by season and latitude, resulting in seasonal cycles that are of opposite phase in the Northern and Southern Hemispheres [*Novelli et al.*, 1994; *Novelli*, 2003]. The interannual variability in peak CO levels primarily reflects changes in biomass burning and fossil fuel emissions from year-to-year [*Novelli et al.*, 2003].

1.5.3 Recent atmospheric trends

There are relatively few systematic measurements of CO trends prior to the late 1980s. Total atmospheric column data suggest a generally increasing trend in atmospheric CO from 1950-1970 AD [*Dianov-Klokov et al.*, 1989; *Zander et al.*, 1989; *Yurganov et al.*, 1999]. Weekly CO surface flask observations began in the mid-1980s, with a few remote sites ranging from the Arctic to the South Pole [*Khalil and Rasmussen*, 1988, 1994]. These data suggested Northern Hemisphere CO levels increased around 1% per year in the during the mid-1980s. By the end of the 1980s, atmospheric CO levels were declining rapidly at about 2-3% per year [*Khalil and Rasmussen*, 1994; *Novelli et al.*, 1994]. Since the late 1980s, the latitudinal distribution, seasonality, and interannual variability of CO has been studied in detail using a globally distributed network of surface air flask observations from the NOAA Carbon Cycle flask network [*Novelli et al.*, 1992, 1994, 1998; *Novelli*, 2003; *Novelli and Masarie*, 2013]. Zonally-averaged CO mixing ratios show Northern Hemisphere CO levels decreased since the 1990s, while the Southern Hemisphere exhibits no significant long-term trend since about 1991 AD [*Novelli et al.*, 2003; *Novelli and Masarie*, 2013].

1.5.4 Firn air and ice core records

There are two prior studies on CO measurements in firn [*Assonov et al.*, 2007; *Petrenko et al.*, 2013]. *Petrenko et al.* [2013] reconstructed a CO atmospheric history for the high latitude Northern Hemisphere using firn air measurements from three Greenland sites. Their study found that Arctic CO levels were about 140-150 ppb in 1950, and rose 10-15 ppb from 1950 to the 1970s, before reaching a peak level of 160 ppb sometime between 1971-1983 AD. After the 1980s, Arctic CO levels declined about 30 ppb to the present day level (~130 ppb in 2008 AD). Firn air reconstructions from Berkner Island, Antarctica suggest that CO levels in the high

latitude Southern Hemisphere rose from about 38±7 to 52.5±1.5 ppb from 1940 to the present day [*Assonov et al.*, 2007]. The CO levels reported by *Assonov et al.* [2007] are on a volumetric scale, which corresponds to 1.08 of the NOAA/ESRL calibration scale. *Assonov et al.* [2007] estimate that the CO increase observed in the firn is somewhat larger than what is expected from the growth of atmospheric CH_4 during the 20^{th} century alone, suggesting the most likely for the CO rise during the twentieth century may be due to an increase in biomass burning emissions.

The preservation of atmospheric CO in Antarctic ice cores remains an issue of scientific debate. Several studies use Antarctic ice cores to reconstruct preindustrial CO levels [*Haan et al.*, 1996; *Haan and Raynaud*, 1998; *Ferretti et al.*, 2005; *Wang et al.*, 2010]. *Wang et al.*, [2010] measured significant variability in ice cores from South Pole and Adélie Land (D47), Antarctica, showing a CO decrease from 55 to 35 ppb from 1300-1600 AD, followed by a rise to relatively constant levels at about 50-53 ppb between 1800-1900 AD. The South Pole and D47 ice core measurements show agreement with prior CO observations from Antarctic ice cores [*Haan et al.*, 1996; *Haan and Raynaud*, 1998]. However, disagreement exists between older portions of the D47 [*Haan and Raynaud*, 1998] and Law Dome ice cores [*Ferretti et al.*, 2005]. Surprisingly, the CO level measured in 1900 AD is also larger than the annually averaged CO level over South Pole today, and is difficult to explain with reasonable changes in biomass burning [*van der Werf et al.*, 2013].

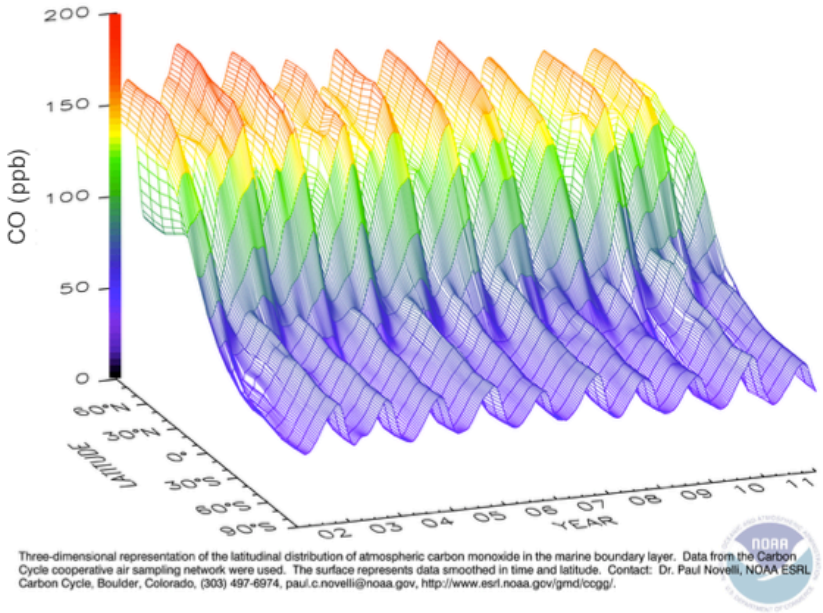

Figure 1.5: Three-dimensional representation of the latitudinal distribution of atmospheric CO (in ppb) in the marine boundary layer from 2001-2011 based on data from the NOAA Carbon Cycle cooperative air sampling network. The surface represents many measurements, with the data smoothed in time and latitude. Figure adapted from NOAA/ESRL, http://www.esrl.noaa.gov/gmd/Photo_Gallery/GMD_Figures/ccgg_figures/tn/co_surface.png.html.

1.6 Drivers of pre-industrial methane

The causes of pre-industrial atmospheric methane variations are not well understood. Globally, the spatial distribution of methane sources is quite complex, and the changes in pre-industrial methane sources are not fully constrained by the ice core records from the two poles [*Mitchell et al.*, 2013]. Several proxies have also been used to understand the observed changes in pre-industrial methane from polar ice cores, including the ^{13}C isotopes of methane [*Ferretti et al.*, 2005; *Mischler et al.*, 2009; *Sowers*, 2010; *Sapart et al.*, 2012], the methane interpolar difference (IPD) [*Mitchell et al.*, 2013], levels of carbon monoxide and its stable isotopes (^{13}C and ^{18}O) [*Ferretti et al.*, 2005; *Wang et al.*, 2010], and levels of methyl chloride [*Verhulst et al.*, 2013]. *Mitchell et al.* [2013] used the atmospheric CH_4 concentration and IPD, along with the

Eight Box Atmospheric CH_4 Model (EBAMM) to understand pre-industrial methane emissions. This study showed that a 24 Tg y^{-1} increase in CH_4 emissions is required to explain the 115 ppb CH_4 rise during the last 3000 years, with the majority of this rise coming from tropical sources. Tropical methane sources may include emissions from wetlands and/or biomass burning, however changes in the methane IPD cannot distinguish among these sources.

Relatively little is known about the drivers of global fire activity prior to the recent century. *Wang et al.* [2010] extended the ice core CO record to the latter half of the twentieth century using surface air and firn air measurements; however there is no observational CO record between around 1900-1960 AD to connect the firn air and ice core records [*Assonov et al.*, 2007]. The ice core CO record suggests there were significant variations in biomass burning during the pre-industrial period, from 1400-1900 AD, and shows agreement with biomass burning reconstructions based on charcoal influx [*Marlon et al.*, 2008; *Wang et al.*, 2010]. Methane isotopes ($\delta^{13}C$ of CH_4) measured in Antarctic ice cores suggest a very different history of biomass burning emissions, with a broad minimum in pyrogenic emissions between 1700-1900 AD [*Ferretti et al.*, 2005]. *Sapart et al.*, [2012] investigated the atmospheric methane rise during the last 2000 years using measurements of methane and its stable isotopes ($\delta^{13}CH_4$) in the NEEM and EUROCORE ice cores from Greenland. *Sapart et al.* [2012] suggested that the long-term (centennial-scale) rise in atmospheric methane levels was due to an isotopically depleted methane source, such as biogenic emissions. However, three periods within the last 2000 years were characterized by an isotopically enriched $\delta^{13}CH_4$ signature, between 0-300 AD, 900-1200 AD, and 1400-1600 AD. The methane variations during these three periods were attributed to small changes in biomass burning emissions, superimposed on a relatively constant background of pyrogenic methane emissions (around 25-30 Tg y^{-1}),

van der Werf et al. [2013] compared variations in pre-industrial fire activity from various proxies, including emissions derived from the Antarctic ice core methane isotope and carbon monoxide records and global charcoal influx [*Wang et al.*, 2010; *Marlon et al.*, 2008; *Ferretti et al.,* 2005]. *van der Werf et al.* [2013] suggest that the ice core CO record may not reflect atmospheric CO mixing ratios. The ice core CO record suggests that atmospheric CO levels over Antarctica were similar to the present day levels in 1900 AD. However, it would be extremely difficult to sustain high CO levels in 1900 AD using reasonable assumptions for biomass burning and wildfire emissions and population densities [*van der Werf et al.,* 2013]. Further investigation of past biomass burning trends is needed, either through the development of a continuous record of CO (based on surface air, firn air and ice core records), or another biomass burning tracer preserved in polar ice cores.

References

Aikin, A. C., J. R. Herman, E. J. Maier, and C. J. McQuillan (1982), Atmospheric Chemistry of Ethane and Ethylene, *J. Geophys. Res.*, *87*, 3105–3118.

Andreae, M. O., and P. Merlet (2001), Emission of trace gases and aerosols from biomass burning, *Global Biogeochem. Cycles*, *15*(4), 955–966.

Assonov, S. S., C. A. M. Brenninkmeijer, P. Jöckel, R. Mulvaney, S. Bernard, and J. Chappellaz (2007), Evidence for a CO increase in the SH during the 20th century based on firn air samples from Berkner Island, Antarctica, *Atmos. Chem. Phys.*, *7*(2), 295–308, doi:10.5194/acp-7-295-2007.

Atkinson, R. (2000), Atmospheric chemistry of VOCs and NO_x, *Atmos. Environ.*, *34*, 2063–2101.

Aydin, M., K. R. Verhulst, E. S. Saltzman, M. O. Battle, S. A. Montzka, D. R. Blake, Q. Tang, and M. J. Prather (2011), Recent decreases in fossil-fuel emissions of ethane and methane derived from firn air, *Nature*, *476*(7359), 198–201, doi:10.1038/nature10352.

Bakwin, P., P. Tans, and P. Novelli (1994), Carbon monoxide budget in the Northern Hemisphere, *Geophys. Res. Lett.*, *21*(6), 433–436.

Battle, M., M. Bender, T. Sowers, and P. Tans (1996), Atmospheric gas concentrations over the past century measured in air from firn at South Pole, *Nature*, *383*, 231–235.

Battle, M. O., J. P. Severinghaus, E. D. Sofen, D. Plotkin, A. J. Orsi, M. Aydin, S. A. Montzka, T. Sowers, and P. P. Tans (2011), Controls on the movement and composition of firn air at the West Antarctic Ice Sheet Divide, *Atmos. Chem. Phys.*, *11*(21), 11007–11021, doi:10.5194/acp-11-11007-2011.

Bergamaschi, P. et al. (2013), Atmospheric CH_4 in the first decade of the 21st century: Inverse modeling analysis using SCIAMACHY satellite retrievals and NOAA surface measurements, *J. Geophys. Res. Atmos.*, *118*(13), 7350–7369, doi:10.1002/jgrd.50480.

Beyersdorf, A. J., D. R. Blake, A. Swanson, S. Meinardi, F. S. Rowland, and D. Davis (2010), Abundances and variability of tropospheric volatile organic compounds at the South Pole and other Antarctic locations, *Atmos. Environ.*, *44*(36), 4565–4574, doi:10.1016/j.atmosenv.2010.08.025.

Boissard, C., and B. Bonsang (1996), TROPOZ II: Global distributions and budgets of methane and light hydrocarbons, *J. Atmos. Chem.*, *25*, 115–148.

Bonsang, B., A. A. Aarbaoui, and J. Sciare (2008), Diurnal variation of non-methane hydrocarbons in the subantarctic atmosphere, *Environ. Chem.*, *5*, 16–23, doi:10.1071/EN07018.

Bousquet, P. et al. (2006), Contribution of anthropogenic and natural sources to atmospheric methane variability, *Nature*, *443*(7110), 439–43, doi:10.1038/nature05132.

Bousquet, P. et al. (2011), Source attribution of the changes in atmospheric methane for 2006–2008, *Atmos. Chem. Phys.*, *11*(8), 3689–3700, doi:10.5194/acp-11-3689-2011.

Brandt, A. et al. (2014), Methane leaks from North American natural gas systems, *Science*, *343*, 733–735.

Ciais, P., C. Sabine, G. Bala, L. Bopp, V. Brovkin, J. Canadell, A. Chhabra, R. DeFries, J. Galloway, M. Heimann, C. Jones, C. Le Quéré, R.B. Myneni, S. Piao and P. Thornton (2013), *Carbon and Other Biogeochemical Cycles. In: Climate Change 2013: The Physical Science Basis. Contribution of Working Group I to the Fifth Assessment Report of the Intergovernmental Panel on Climate Change,* edited by Stocker, T.F., D. Qin, G.-K. Plattner, M. Tignor, S.K. Allen, J. Boschung, A. Nauels, Y. Xia, V. Bex and P.M. Midgley, Cambridge University Press, Cambridge, United Kingdom and New York, NY, USA.

Chappellaz, J., T. Blunier, S. Kints, A. Dallenbach, J.-M. Barnola, J. Schwander, D. Raynaud, and B. Stauffer (1997), Changes in the atmospheric CH_4 gradient between Greenland and Antarctica during the Holocene, *J. Geophys. Res.*, *102*(97), 15987–15997.

Clarkson, T., R. Martin, and J. Rudolph (1997), Ethane and propane in the southern marine troposphere, *Atmos. Environ.*, *31*(22), 3763–3771.

Dianov-Klokov, V. I., L. N. Yurganov, E. I. Grechko, and A. V. Dzhola (1989), Spectroscopic Measurements of Atmospheric Carbon Monoxide and Methane. 1: Latitudinal Distribution, *J. Atmos. Chem.*, *8*, 139–151.

Dlugokencky, E. J. (2003), Atmospheric methane levels off: Temporary pause or a new steady-state?, *Geophys. Res. Lett.*, *30*(19), 1992, doi:10.1029/2003GL018126.

Dlugokencky, E. J., P. M. Lang, and K. A. Masade (1994), The growth rate and distribution of atmospheric methane, *J. Geophys. Res.*, *99* (D8) 17021-17043.

Dlugokencky, E. J., E. G. Nisbet, R. Fisher, and D. Lowry (2011), Global atmospheric methane: budget, changes and dangers., *Philos. Trans. R. Soc. London Ser. A*, *369*(1943), 2058–72, doi:10.1098/rsta.2010.0341.

Duncan, B. N., J. A. Logan, I. Bey, I. A. Megretskaia, R. M. Yantosca, P. C. Novelli, N. B. Jones, and C. P. Rinsland (2007), Global budget of CO, 1988–1997: Source estimates and validation with a global model, *J. Geophys. Res.*, *112*(D22), 1–29, doi:10.1029/2007JD008459.

Ehhalt, D. et al. (2001), *Atmospheric chemistry and greenhouse gases. In: Climate Change 2001: The Physical Science Basis. Contribution of Working Group I to the Third Assessment Report of the Intergovernmental Panel on Climate Change*, Cambridge Univ. Press, Cambridge and New York.

Etheridge, D. M., L. P. Steele, R. J. Francey, and R. L. Langenfelds (1998), Atmospheric methane between 1000 A.D. and present: Evidence of anthropogenic emissions and climatic variability, *J Geophys Res.*, *103*(D13), 15979–15993.

Etiope, G. (2012), Climate science: Methane uncovered, *Nat. Geosci.*, *5*(6), 373–374, doi:10.1038/ngeo1483.

Etiope, G. (2009), A Global Dataset of Onshore Gas and Oil Seeps: A new Tool for Hydrocarbon Exploration, *Oil Gas Bus.*, 1–10.

Etiope, G., and P. Ciccioli (2009), Earth's degassing: A missing ethane and propane source, *Science*, *323*, 4000.

Etiope, G., K. R. Lassey, R. W. Klusman, and E. Boschi (2008), Reappraisal of the fossil methane budget and related emission from geologic sources, *Geophys. Res. Lett.*, *35*(9), L09307, doi:10.1029/2008GL033623.

Fabre, A., J.-M. Barnola, L. Arnaud, and J. Chappellaz (2000), Determination of gas diffusivity in polar firn: Comparison between experimental measurements and inverse modeling, *Geophys. Res. Lett.*, *27*(4), 557–560, doi:10.1029/1999GL010780.

Ferretti, D. F. et al. (2005), Unexpected changes to the global methane budget over the past 2000 years., *Science*, *309*(5741), 1714–7, doi:10.1126/science.1115193.

Haan, D., and D. Raynaud (1998), Ice core record of CO variations during the last two millennia: atmospheric implications and chemical interactions within the Greenland ice, *Tellus B*, 253–262.

Haan, D., P. Martinerie, and D. Raynaud (1996), Ice core data of atmospheric carbon monoxide over Antarctica and Greenland during the last 200 years, *Geophys. Res. Lett.*, *23*(17), 2235–2238.

Hartmann, D.L., A.M.G. Klein Tank, M. Rusticucci, L.V. Alexander, S. Brönnimann, Y. Charabi, F.J. Dentener, E.J. Dlugokencky, D.R. Easterling, A. Kaplan, B.J. Soden, P.W. Thorne, M. Wild and P.M. Zhai (2013), Observations: Atmosphere and Surface. In: *Climate Change 2013: The Physical Science Basis. Contribution of Working Group I to the Fifth Assessment Report of the Intergovernmental Panel on Climate Change,* edited by Stocker, T.F., D. Qin, G.-K. Plattner, M. Tignor, S.K. Allen, J. Boschung, A. Nauels, Y. Xia, V. Bex and P.M. Midgley, Cambridge University Press, Cambridge, United Kingdom and New York, NY, USA.

Helmig, D., and J. Bottenheim (2009), Volatile organic compounds in the global atmosphere, *Eos, Trans. Am. Geophys. Union*, *90*(52), 1–3.

Helmig, D. et al. (2014), Reconstruction of Northern Hemisphere 1950–2010 atmospheric non-methane hydrocarbons, *Atmos. Chem. Phys.*, *14*(3), 1463–1483, doi:10.5194/acp-14-1463-2014.

Isaksen, I., and Ø. Hov (1987), Calculation of trends in the tropospheric concentration of O_3, OH, CO, CH4, and NOx, *Tellus B*.

Jones, V. T., M. D. Matthews, and D. M. Richers (1999), Light hydrocarbons for petroleum and gas prospecting, in *Geochemical Remote Sensing of the Subsurface*, edited by G. J. S. Govett, M.Hale, Handbook of Exploration Geochemistry.

Kai, F. M., S. C. Tyler, J. T. Randerson, and D. R. Blake (2011), Reduced methane growth rate explained by decreased Northern Hemisphere microbial sources., *Nature*, *476*(7359), 194–7, doi:10.1038/nature10259.

Kanakidou, M., and P. J. Crutzen (1999), The photochemical source of carbon monoxide: Importance, uncertainties and feedbacks, *Chemosph. Glob. Chang. Sci.*, *1*(1), 91–109, doi:10.1016/S1465-9972(99)00022-7.

Kaspers, K. A. et al. (2004), Analyses of firn gas samples from Dronning Maud Land, Antarctica: Study of nonmethane hydrocarbons and methyl chloride, *J. Geophys. Res.*, *109*, D02307, doi:10.1029/2003JD003950.

Khalil, M., and R. Rasmussen (1988), Carbon monoxide in the Earth's atmosphere: indications of a global increase, *Nature*, *332*, 242–245.

Khalil, M., and R. Rasmussen (1994), Global decrease in atmospheric carbon monoxide concentration, *Nature*, *370*, 639–641.

Knipping, E. M., and D. Dabdub (2003), Impact of chlorine emissions from sea-salt aerosol on coastal urban ozone., *Environ. Sci. Technol.*, *37*(2), 275–84.

Logan, J. a., M. J. Prather, S. C. Wofsy, and M. B. McElroy (1981), Tropospheric chemistry: A global perspective, *J. Geophys. Res.*, *86*(C8), 7210, doi:10.1029/JC086iC08p07210.

Marlon, J. R., P. J. Bartlein, C. Carcaillet, D. G. Gavin, S. P. Harrison, P. E. Higuera, F. Joos, M. J. Power, and I. C. Prentice (2008), Climate and human influences on global biomass burning over the past two millennia, *Nat. Geosci.*, *1*(10), 697–702, doi:10.1038/ngeo313.

Miller, S. M. et al. (2013), Anthropogenic emissions of methane in the United States., *Proc. Natl. Acad. Sci. U. S. A.*, *110*(50), 20018–22, doi:10.1073/pnas.1314392110.

Mischler, J. A., T. A. Sowers, R. B. Alley, M. Battle, J. R. McConnell, L. Mitchell, T. Popp, E. Sofen, and M. K. Spencer (2009), Carbon and hydrogen isotopic composition of methane over the last 1000 years, *Global Biogeochem. Cycles*, *23*(GB4024), doi:10.1029/2009GB003460.

Mitchell, L., E. Brook, J. E. Lee, C. Buizert, and T. Sowers (2013), Constraints on the late holocene anthropogenic contribution to the atmospheric methane budget, *Science*, *342*(6161), 964–6, doi:10.1126/science.1238920.

Mitchell, L. E., E. J. Brook, T. Sowers, J. R. McConnell, and K. Taylor (2011), Multidecadal variability of atmospheric methane, 1000–1800 C.E., *J. Geophys. Res.*, *116*(G2), G02007, doi:10.1029/2010JG001441.

Naik, V. et al. (2013), Preindustrial to present-day changes in tropospheric hydroxyl radical and methane lifetime from the Atmospheric Chemistry and Climate Model Intercomparison Project (ACCMIP), *Atmos. Chem. Phys.*, *13*(10), 5277–5298, doi:10.5194/acp-13-5277-2013.

Nisbet, E. G., E. J. Dlugokencky, and P. Bousquet (2014), Methane on the rise-again, *Science*, *343*(6170), 493–495, doi:10.1126/science.1247828.

Novelli, P. C. (2003), Reanalysis of tropospheric CO trends: Effects of the 1997–1998 wildfires, *J. Geophys. Res.*, *108*(D15), 4464, doi:10.1029/2002JD003031.

Novelli, P. C., and K. A. Masarie (2013), Atmospheric Cycle, Carbon Monoxide Dry Air Mole Fractions from the NOAA ESRL Carbon Cooperative Global Air Sampling Network, 1988-2012, Version: 2013-06-18.

Novelli, P. C., L. P. Steele, and P. P. Tans (1992), Mixing Ratios of Carbon Monoxide in the Troposphere, *J. Geophys. Res.*, *97*(D18), 20731–20750.

Novelli, P. C., K. A. Masarie, P. P. Tans, and P. M. Lang (1994), Recent changes in atmospheric carbon monoxide, *Science*, *263*(5153), 1587–90, doi:10.1126/science.263.5153.1587.

Novelli, P. C., K. A. Masarie, and P. M. Lang (1998), Distributions and recent changes of carbon monoxide in the lower troposphere, *J. Geophys. Res.*, *103*(D15), 19015–19033.

Novelli, P. C., K. A. Masarie, P. M. Lang, B. D. Hall, R. C. Myers, and J. W. Elkins (2003), Reanalysis of tropospheric CO trends: Effects of the 1997 – 1998 wildfires, *J. Geophys. Res.*, *108*(D15), 4464, doi:10.1029/2002JD003031.

Petrenko, V. V. et al. (2013), A 60 yr record of atmospheric carbon monoxide reconstructed from Greenland firn air, *Atmos. Chem. and Phys.*, *13*, 7567–7585, doi:10.5194/acp-13-7567-2013.

Plass-Dulmer, C., R. Koppmann, M. Ratte, and J. Rudolph (1995), Light nonmethane hydrocarbons in seawater, *Global Biogeochem. Cycles*, *9*(1), 79–100.

Platt, U., W. Allan, and D. Lowe (2004), Hemispheric average Cl atom concentration from $^{13}C/^{12}C$ ratios in atmospheric methane, *Atmos. Chem. Phys.*, *4*, 2393–2399.

Poisson, N., M. Kanakidou, and P. J. Crutzen (2000), Impact of Non-Methane Hydrocarbons on Tropospheric Chemistry and the Oxidizing Power of the Global Troposphere : 3-Dimensional Modelling Results, *J. Atmos. Chem.*, *36*, 157–230.

Rudolph, J. (1995), The tropospheric distribution and budget of ethane, *J. Geophys. Res.*, *100*(D6), 11369–11381.

Sander, S. P. and R. R. Friedl, et al. (2006), *Chemical Kinetics and Photochemical Data for Use in Atmospheric Studies Evaluation Number 15.* NASA Jet Propulsion Laboratory Publication 06-2, Pasadena, CA. http://jpldataeval.jpl.nasa.gov/.

Sapart, C. J. et al. (2012), Natural and anthropogenic variations in methane sources during the past two millennia., *Nature*, *490*(7418), 85–8, doi:10.1038/nature11461.

Schultz, M. G., A. Heil, J. J. Hoelzemann, A. Spessa, K. Thonicke, J. G. Goldammer, A. C. Held, J. M. C. Pereira, and M. van het Bolscher (2008), Global wildland fire emissions from 1960 to 2000, *Global Biogeochem. Cycles*, *22*, GB2002, doi:10.1029/2007GB003031.

Schwander, J. (1989), The transformation of snow to ice and the occlusion of gases, in The Environmental Record in Glaciers and Ice Sheets, edited by H. Oeschger and C.C. Langway., pp 53-67, John Wiley, New York.

Schwander, J., T. Sowers, J.-M. Barnola, T. Blunier, A. Fuchs, and B. Malaize (1997), Age scale of the air in the summit ice: Implications for glacial-interglacial temperature change, *J. Geophys. Res.*, *102*(D16), 19483–19493.

Seinfeld, J. H. (1989), Urban Air Pollution: State of the Science, *Science*, *243*(4892), 745–752, doi:10.1126/science.243.4892.745.

Severinghaus, J., and M. Battle (2006), Fractionation of gases in polar ice during bubble close-off: New constraints from firn air Ne, Kr and Xe observations, *Earth Planet. Sci. Lett.*, *244*(1-2), 474–500, doi:10.1016/j.epsl.2006.01.032.

Simpson, I. J., F. S. Rowland, S. Meinardi, and D. R. Blake (2006), Influence of biomass burning during recent fluctuations in the slow growth of global tropospheric methane, *Geophys. Res. Lett.*, *33*(L22808), 1–5, doi:10.1029/2006GL027330.

Simpson, I. J., M. Andersen, S. Meinardi, L. Bruhwiler, N. J. Blake, D. Helmig, F. S. Rowland, and D. R. Blake (2012), Long-term decline of global atmospheric ethane concentrations and implications for methane, *Nature*, *488*, 490–494, doi:10.1038/nature11342.

Singh, H., and J. Kasting (1988), Chlorine-hydrocarbon photochemistry in the marine troposphere and lower stratosphere, *J. Atmos. Chem.*, *7*, 261–285.

Sowers, T. (2010), Atmospheric methane isotope records covering the Holocene period, *Quat. Sci. Rev.*, *29*, 213–221, doi:10.1016/j.quascirev.2009.05.023.

Spivakovsky, C. M. et al. (2000), Three-dimensional climatological distribution of tropospheric OH: Update and evaluation, *J. Geophys. Res.*, *105*(D7), 8931, doi:10.1029/1999JD901006.

Swanson, A., N. Blake, J. Dibb, M. Albert, D. R. Blake, and F. S. Rowland (2002), Photochemically induced production of CH_3Br, CH_3I, C_2H_5I , ethene, and propene within surface snow at Summit, Greenland, *Atmos. Environ.*, *36*, 2671–2682.

Trudinger, C., I. Enting, D. M. Etheridge, R. J. Francey, V. A. Levchenko, L. P. Steele, D. Raynaud, and L. Arnaud (1997), Modeling air movement and bubble trapping in firn, *J. Geophys. Res.*, *102*(D6), 6747–6763.

Verhulst, K. R., M. Aydin, and E. S. Saltzman (2013), Methyl chloride variability in the Taylor Dome ice core during the Holocene, *J. Geophys. Res. Atmos.*, *118*(21), 12,218–12,228, doi:10.1002/2013JD020197.

Wang, Z., J. Chappellaz, K. Park, and J. E. Mak (2010), Large variations in Southern Hemisphere biomass burning during the last 650 years, *Science*, *330*(6011), 1663–6, doi:10.1126/science.1197257.

van der Werf, G. R., W. Peters, T. T. van Leeuwen, and L. Giglio (2013), What could have caused pre-industrial biomass burning emissions to exceed current rates?, *Clim. Past*, *9*(1), 289–306, doi:10.5194/cp-9-289-2013.

Worton, D. R. et al. (2012), Evidence from firn air for recent decreases in non-methane hydrocarbons and a 20th century increase in nitrogen oxides in the northern hemisphere, *Atmos. Env.*, *54*, 592–602, doi:10.1016/j.atmosenv.2012.02.084.

Xiao, Y., J. A. Logan, D. J. Jacob, R. C. Hudman, R. Yantosca, and D. R. Blake (2008), Global budget of ethane and regional constraints on U.S. sources, *J. Geophys. Res.*, *113*(D21), D21306, doi:10.1029/2007JD009415.

Yurganov, L. N., E. I. Grechko, and A. V. Dzhola (1999), Zvenigorod carbon monoxide total column time series: 27 yr of measurements, *Chemosph. Glob. Chang. Sci.*, *1*, 127–136.

Zander, R., P. Demoulin, D. H. Ehhalt, U. Schmidt, and C. P. Rinsland (1989), Secular increase in total column abundance of carbon monoxide above central Europe since 1950, *J. Geophys. Res.*, *94*(89), 11021–11028.

Zander, R., E. Mahieu, P. Demoulin, P. Duchatelet, C. Servais, G. Roland, Delbouille, M. De Maziere, and C. P. Rinsland (2005), Evolution of a dozen non-CO_2 greenhouse gases above Central Europe since the mid-1980s, *Environ. Sci.*, *2*(2-3), 295–303.

CHAPTER 2

Experimental Methods

2.1 Introduction

This chapter discusses the analytical methods used in this study, including descriptions of: 1) the gas chromatography/mass spectrometry analytical methods, 2) the dry and wet techniques used to extract ethane from ice core samples, and 3) firn air sites, sampling, and modeling techniques used to reconstruct the atmospheric histories of ethane and carbon monoxide.

2.2 Gas chromatography/mass spectrometry techniques

2.2.1 Sample preparation

Firn air, surface air, and ice core samples were analyzed using an Agilent 5890 gas chromatograph (GC) and high-resolution mass spectrometer (MS - Waters Autospec Ultima). Figure 2.1 shows a diagram of the custom inlet used to collect and cryogenically condense the gas sample before injection into the GC/MS system. During collection, the gas sample flows at 10 ml/min through a mass flow controller (MFC) and two redirecting valves (Valco 1 and Valco 2) via 1/8" stainless steel tubing [*Aydin et al.,* 2007]. The three main stages of sample preparation are loading, refocusing, and injection.

During the loading stage, the sample flows through Trap 1, which consists of a 1/8" stainless steel/glass bead u-trap immersed in liquid nitrogen. The target gases (analytes) condense on the glass beads when the liquid N_2 dewar is raised, while the major constituents of air (e.g. N_2, O_2,

Ar) flow through the trap and are collected in the 300-cm^3 calibrated volume downstream of Trap 1. This collection chamber is evacuated before sample collection begins, and thus serves two purposes: 1) to measure the size of the gas sample and 2) to provide a pressure gradient to pull the sample through the glass bead trap (Trap 1). The size of the gas sample is calculated using the initial and final pressure measurements taken before and after sample collection using a capacitance manometer (Baratron, MKS Instruments). Next, the volume is isolated and evacuated and the process is repeated, so sample remaining in the line is collected. After the sample is loaded onto Trap 1, approximately 30 cm^3 (volume at STP) of an isotope-labeled standard (discussed below) is loaded on to the glass bead trap and collected using the same procedure as the sample.

The second stage of sample collection involves thermal desorption of the sample and isotope standard. These are transferred to Trap 2 (the refocusing trap) in a stream of He carrier gas. Trap 2 is a fused silica loop encased in a 1/32" stainless steel loop immersed in liquid nitrogen. During the refocusing stage, the sample and isotope move from Trap 1 to Trap 2 and those compounds that are more volatile than the target analytes are removed, allowing for a cleaner injection. After the sample is transferred and refocused, it is thermally desorbed into the carrier gas stream for injection into the GC column for chromatographic separation.

During the injection stage, the liquid N_2 dewar on trap 2 is dropped, and the loop is electrically heated. The chromatographic column consists of a 5 m long DB5 pre-column (0.32 mm ID and a 0.25 μm film thickness; Agilent J&W) and a 55 m long DB1 analytical column (0.32 mm ID and 0.25 μm film thickness), connected via a multi-port redirecting valve (Valco 2, Figure 1). After the target gases reach the analytical column (approximately 8.5 minutes after injection), Valco-2 is switched out of line so that any impurities left behind on the pre-column

are carried to waste and are not injected into the analytical column. The chromatographic separation of gases is carried out using the temperature ramp shown in Table 2.1.

Table 2.1: Temperature program for the Agilent 5890 gas chromatograph [*Aydin et al.*, 2007].

Stage	$T_{initial}$	T_{final}	T program
1	40°C	-50°C	pre-cool
2	-50°C	-50°C	Isothermal for 3 min at begin injection
3	-50°C	-40°C	5°C/min
4	-40°C	-30°C	15°C/min
5	-30°C	120°C	30°C/min
6	120°C	120°C	Isothermal for 17 min (includes back flush)

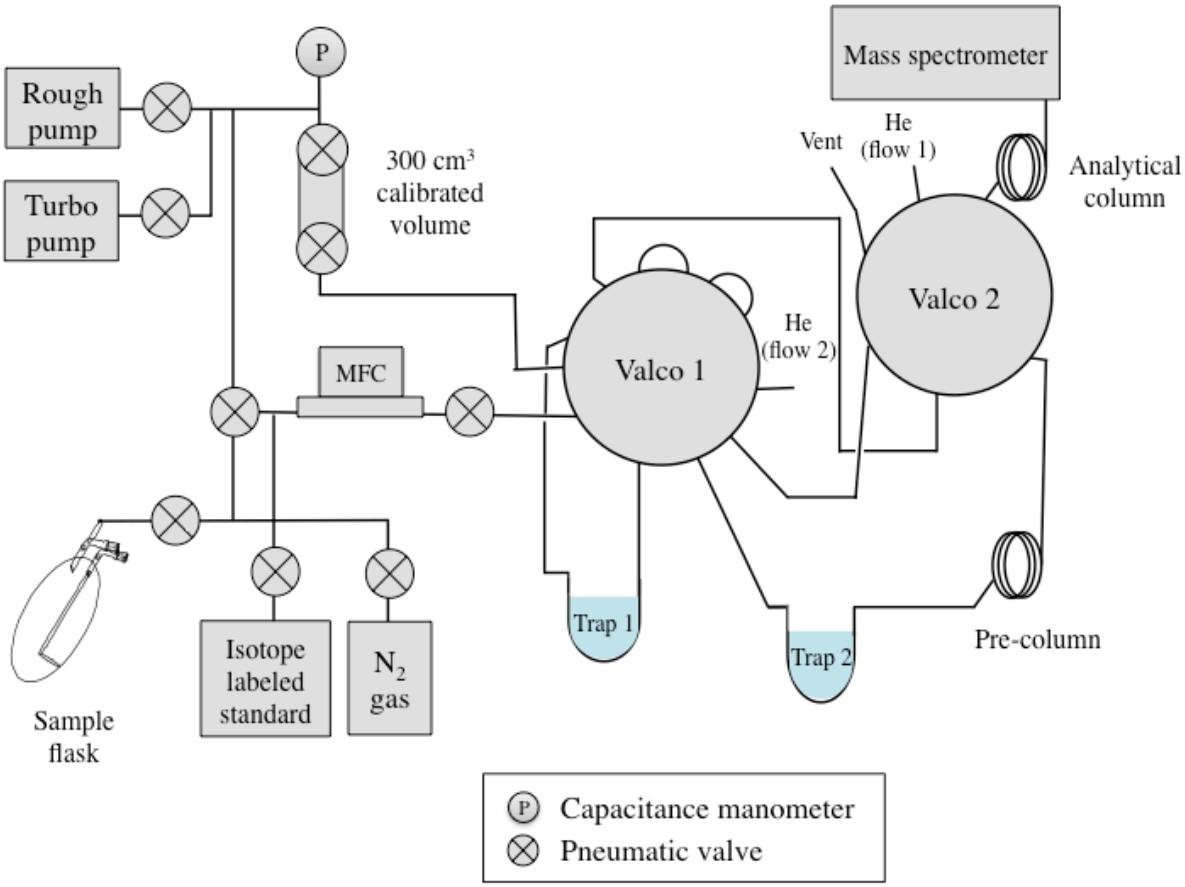

Figure 2.1: Simplified schematic showing the valve configuration for the custom automated inlet and GC/MS system used in this study.

2.2.2 Isotope-labeled internal standard

An isotopically-labeled internal standard is added to each sample before analysis to monitor instrument response and to account for changes in instrument sensitivity. The internal standard consists of a mixture of eight isotopically-labeled gases, including: ^{13}C-ethane, ^{13}C-propane, ^{13}C -butane, ^{13}C-carbonyl sulfide, D3-methyl chloride (CD_3Cl), D3-methyl bromide (CD_3Br), D3-acetonitrile (CD_3CN), ^{13}C-carbon disulfide. In this study, the ^{13}C-labeled ethane peak was used to help quantify the ^{12}C (unlabeled) C_2H_6 peak. The internal standard diluted to ambient (ppt) levels using humidified N_2 in a 34.0 L stainless-steel tank air-sampling cylinder (Essex Cryogenics of Missouri, Inc, part no. 80C-0008-8). The diluted standard is made from a primary

standard, which consists of a ppb-level mixture of the same eight isotopically-labeled gases stored in an Aculife-treated aluminum cylinder (Scott Gases).

2.2.3 Calibration standards

System calibrations were performed roughly every 3 months using UCI standards as reference gases. There are three UCI primary calibration standards used in this study (referred to as M8, M10, and M11). The primary gas standards are prepared from commercial-grade pure compounds [*Aydin et al.*, 2007]. Working calibration standards are prepared for calibration of the GC/MS system on a routine basis (monthly or quarterly). The working standards were prepared by diluting the primary (ppb-level) unlabeled standard with humidified N_2 gas in an electropolished stainless steel flask. These are prepared as needed and used the same day. Figure 2.2 shows a calibration curve for ethane from January 2012, which was used for some of the ice core measurements shown in Chapter 4.

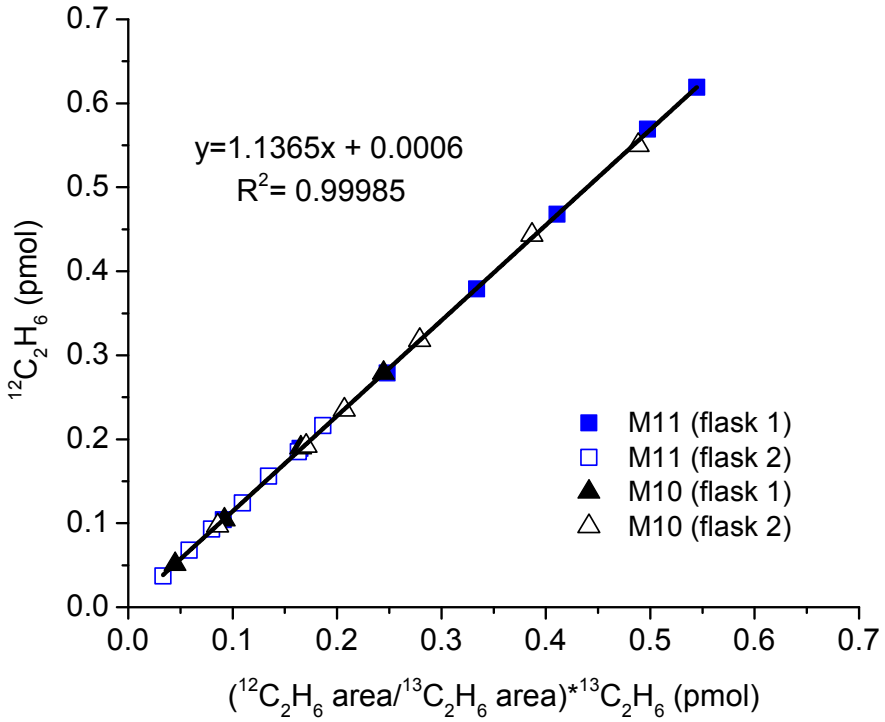

Figure 2.2: Ethane calibration curve for flasks made from two primary standard tanks (M10 and M11). File: CAL primary 30Jan2012.

2.2.4 Mass spectrometric detection

The Micromass Autospec Ultima was used with an electron impact ionization (EI) source in positive ion mode. The instrument has a dual focusing electro-magnetic analyzer, allowing for high mass resolution. During analysis, two ethane peaks are detected: C_2H_6 and $^{13}C_2H_6$ at masses of 30.0470 amu and 31.0503 amu, respectively. The total run time is 15 minutes. Data collection involves 9 time functions, collecting various masses for several target analytes (Table 2.2). Mass calibration of the instrument was performed daily. This involves the injection approximately 0.1 µl of deuterium-labeled dodecane into a reservoir upstream of the source, connected by a capillary tube. A different lock mass is used for each time function, near the mass of the analytes detected within that function. Data was acquired for each analyte mass for 80 ms, with a programmed delay of 5 ms when switching between masses. The ethane peak has a large signal to noise ratio and is easily detected above the background and noise. During this study, the Autospec was operated with a mass resolution >6000 (M/ΔM at 5%). A sample chromatogram showing the ^{12}C ethane, propane, and n-butane peaks from an ice core sample is shown in Figure 2.3.

Table 2.2: Masses and retention times of analytes detected by GC/MS.

Function	Analyte	Mass (amu)	Retention Time (min)	Lock Mass
1	$^{12}C_2H_6$	30.0470	6.22	31.9898
1	$^{13}C_2H_6$	31.0503	6.22	
2	C_3H_8	44.0626	8.64	62.0980
2	$^{13}C_3H_8$	45.0660	8.64	
2	$CO^{32}S$	59.9670	8.41	
2	$CO^{34}S$	61.9628	8.41	
2	$^{13}CO^{32}S$	60.9703	8.41	
3	CFC-12	84.9657	9.24	80.1400
4	$CH_3{}^{35}Cl$	49.9923	10.18	50.0980
4	$CH_3{}^{37}Cl$	51.9894	10.18	
4	CD_3Cl	53.0112	10.14	
5	C_4H_{10}	58.0783	11.71	62.0980
5	$^{13}C_4H_{10}$	59.0816	11.71	
6	$CH_3{}^{79}Br$	93.9418	12.15	96.1680
6	$CH_3{}^{81}Br$	95.9398	12.15	
6	CD_3Br	96.9606	12.10	
7	CS_2	41.0265	13.35	46.0700
7	$^{13}CS_2$	44.0454	13.28	
9	CH_3CN	75.9441	14.17	80.1400
9	$^{13}CH_3CN$	76.9475	14.16	

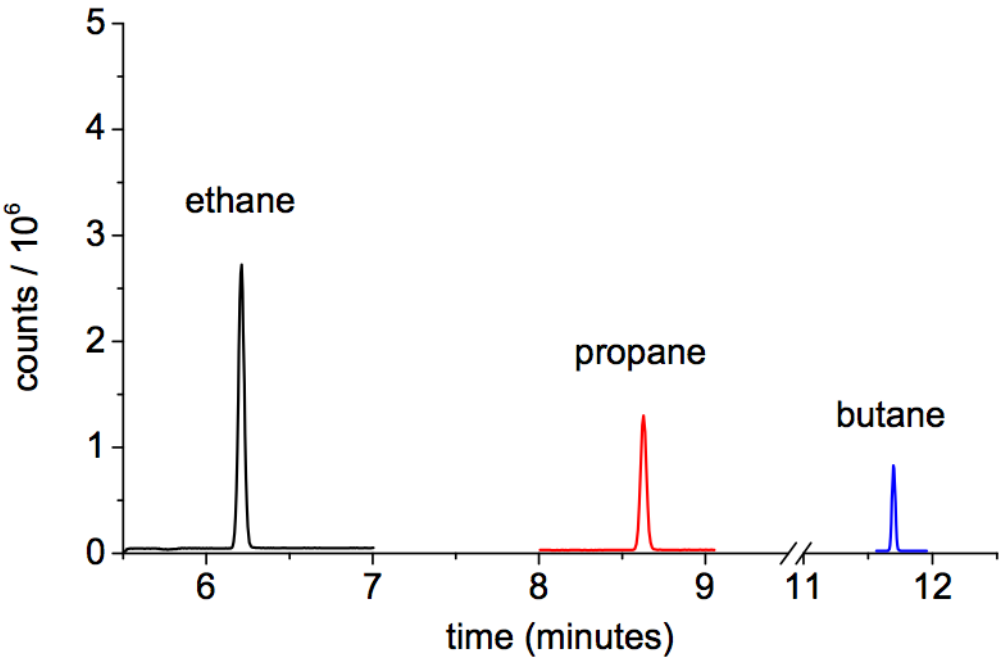

Figure 2.3: Sample chromatogram from an ice core analyzed using the Agilent 5890 GC/Autospec Ultima MS. Peaks are shown for ethane (C_2H_6), propane (C_3H_8), and n-butane (C_4H_{10}).

2.3 Ice core gas extraction methods

2.3.1 Dry extraction apparatus

A diagram of the vacuum line and extraction apparatus is shown in Figure 2.4. Air was extracted from the ice core bubbles using a dry-extraction "ice grater" device. This technique was developed to extract carbon dioxide and methane by *Etheridge et al.*, 1988; *Sowers and Jubenville*, 2000] and was later adapted for use with parts per trillion level trace gases such as methyl chloride, methyl bromide, and carbonyl sulfide [*Aydin et al.*, 2007; *Saltzman et al.*, 2008]. The dry extraction chambers consist of a stainless steel tube for the chamber, which is sealed with an 8" stainless steel conflat flange. A ¾" OD stainless steel tube and Swagelok valve were welded to the upper flange. The vacuum seal was created with a 6.743" copper gasket that was pressed tightly between the two conflat flanges (torque setting 19.8 N m).

Eight different extraction chambers were used in this study. They were constructed in two series (Table 2.3). Series 1 chambers (cans 1-4) were designed and fabricated in the UCI machine shop. These cans were used in earlier measurements of light alkanes in Greenland ice cores [*Aydin et al.*, 2007]. Can 1 was made from 316 stainless steel and a straight tube, with 8" conflat flanges welded to each end and a custom made cutter design. The blades consist of six industrial cutters (Accutec/Cuisipro, Canada) cutters tack welded together onto a steel frame. The blade design consists of 14 rows of 1/2" cutters, alternating with either 6 or 7 blades across the width. Cans 2-4 from series 1 were made with grade 304 stainless steel. The chamber tube was rolled from a flat sheet of stainless steel with a heliarc seam weld, and conflat flanges were welded to either end. Can series 2 (cans 5-8) was designed and fabricated beginning in 2008 at the UCI Machine Shop and Electron Beam Engineering, Inc. (Anaheim, CA) using low carbon steel (austenitic stainless steel type 316L), with clean, electron beam welds and a new Accutec

industrial cutter design with wider cutting surfaces. Cans 1 and 5 have the lowest ethane blanks of all 8 cans used in this study (see Chapter 4).

Table 2.3: Dry extraction chamber materials and design.

Can #	# of flanges	Accutec cutter design	Can material	Welds	Chamber design
1	2	6 mounted cutters	304 SS	Heliarc	Single tube
2	2	6 mounted cutters	304 SS	Heliarc	Flat sheet, bent and welded
3	2	6 mounted cutters	304 SS	Heliarc	Flat sheet, bent and welded
4	2	6 mounted cutters	304 SS	Heliarc	Flat sheet, bent and welded
5	1	Single sheet	316L SS*	electron beam	Single tube
6	1	Single sheet	316L SS	electron beam	Single tube
7	1	Single sheet	316L SS	electron beam	Single tube
8	1	Single sheet	316L SS	electron beam	Single tube

*The lid of can 5 is 316LN SS (Kurt Lesker part no. F0800N000NLN).

2.3.2 Dry extraction procedure

The outer few millimeters of the ice core samples were manually removed with a scalpel at -40°C to eliminate potentially contaminated surfaces. The ice core samples (~400-600 g; 10-15 cm long) were then loaded into the vacuum chamber cooled to -50°C. Samples were mechanically shredded across a stainless steel grater to release gases trapped in ice core bubbles. The gases were collected in a stainless steel tube immersed in liquid He (4K), which acts as a cryogenic pump to collect the bulk gas sample. The tube is sealed with a ¼" Swagelok valve, allowing the sample to be transferred for analysis by GC/MS. An aliquot (~15-60 mL STP) of dry N_2 gas was placed over the ice sample before and after shredding to provide a background measurement for trace gas contamination during extraction and analysis. The average of the two nitrogen blanks is subtracted from the ice core sample.

2.3.3 Wet extraction apparatus

The wet extraction (or melt-refreeze) method has been used in earlier studies to extract noble gases and methane from polar ice cores [*Brook et al.*, 2000; *Severinghaus et al.,* 2003; *Grachev et al.*, 2007]. The first wet extraction tests conducted in this study utilized a glass vessel that terminated in a glass/stainless steel transition, based on a design from these earlier studies. However, several tests suggested that the ethane blank was sensitive to interactions with water vapor on the steel surfaces. This led to the construction of an all glass vessel, sealed with an Indium wire. The design for both vacuum chambers is described below, as well as vacuum line modifications. The final configuration for the glass vacuum line is shown in Figure 2.4.

Glass chamber with glass/stainless steel transition: The first generation glass chamber consisted of two pieces, a lower glass vessel that terminated in a glass/stainless steel transition and a 4-5/8" conflat flange (Larson Electronic Glass, Redwood City, CA, part no. SPD-300-F5-OAL). The lid consists of an upper stainless steel 4-5/8" conflat flange with a ¼" valve stem and ball valve to isolate the flask (304 SS). The vacuum seal was created with a 3.598" copper gasket that was pressed tightly between the two flanges using a torque of approximately 19.8 Nm. Samples were melted by submersing the lower half of the flask in a warm water for about 30 min, followed by rapid refreeze in an ethanol/dry ice bath cooled to approximately -60°C. The top of the flask was heated to 30 °C to prevent water vapor from collecting on the surface of the flask and potentially transferring it to the GC column. The ice core blanks were measured by placing a small aliquot of dry N_2 gas over the solid ice and then successively melting and re-freezing the sample and collecting the gas in a stainless steel cold finger immersed in liquid He (4K).

All glass chamber: The second-generation melter consisted on a 1.485 L glass flask, sealed

with an o-ring. The all glass extraction vessel consists of two separate pieces to allow for loading the ice core sample. The lower part of the chamber consists of a cylindrical glass tube (ID: 3") with a rounded bottom to hold the ice. The upper lid contains a valve stem and straight-line glass shut-off valve with a standard cap and polytetrafluoroethylene (PTFE) o-ring (Glass Expansion, LTD, part no: K2B3-08). Both the glass cap (top of chamber) and the glass tube (bottom of chamber) are terminated with flattened glass flanges. A vacuum seal is created using an o-ring. Tests were conducted with o-rings made from various materials (e.g. Viton®, Teflon, and Indium wire) in order to minimize the system blank. The results from these tests showed that the best vacuum seal with minimal outgassing was obtained using a 1/16" indium wire. The final construction of the glass vessel utilized a 1/16" indium wire o-ring squeezed between the two flat faces of the extraction vessel to create a vacuum seal. The glass flanges are pinched using an external, machined Delrin clamp with six ¼" threaded holes and stainless steel bolts. The indium wire provides a clean, leak-tight seal with negligible ethane outgassing. However, the two ends of the glass must be flat to form a good seal with the indium wire and there must be an overlapping, tapered edge on the wire in order to create an even seal. By using indium wire, we were also able to ensure that the vacuum seal would not be compromised to due to changes in the temperature of the glass vessel. The procedure for the all-glass melter was modified from that described earlier in order to: 1) decrease the time for the experiment and 2) limit the time that the gases were exposed to liquid water. This procedure used is described in detail in section 2.3.4.

Glass vacuum line: The glass shut-off valve on the lid of the all-glass chamber is used to connect the vessel to a vacuum line with an oil-free pumping system, consisting of a molecular drag pump (Adixen Alcatel Drytel, model:1025) backed with a diaphragm pump (Pfeiffer, model: MVP 070-3). The glass bead trap dries the gas stream leaving the melter before collection

in a ¼" stainless steel cold finger immersed in liquid He. Several vacuum line modifications were made to improve the ethane system blanks. For this reason, melter samples analyzed during summer 2011 underwent a slightly different procedure than samples analyzed during spring 2012. The 2011 samples had more exposure to steel components on the vacuum line and were opened to a Baratron gauge before the sample was collected. Samples analyzed in 2012 were also preceded by a "pre-melt/exploding" N_2 blank, as described in Chapter 4.

2.3.4 Wet extraction procedure

Approximately 200-400 g samples were loaded into the glass vessel. The outer 3-5 mm of the ice core is removed with a scalpel at -30° C to eliminate potentially contaminated surfaces. Samples were weighed to the nearest 1 g and placed in the pre-cooled all-glass vacuum chamber to near –40° C using a dry ice-ethanol bath. The exact dimensions of the ice core samples used varied slightly depending on available ice core samples. All samples weighed less than 400 g because larger samples will have the potential to break the vessel due to the expansion of ice when the sample melt water is refrozen. After the sample is loaded, the chamber was sealed using an o-ring made from 1/16" indium wire. Before use, the indium wire is cleaned by immersing in a 5% H_2SO_4 bath for several seconds to remove the oxidized layer on the outer surface. The bottom of the vessel is kept at -40° C until it is time to melt the sample. The glass vessel is flushed with clean N_2 and evacuated several times to remove any remaining modern air in the chamber. The vessel is then checked for leaks in the 1 mTorr range using a Pirani pressure gauge on the vacuum line. The sample is left pumping for about 30 min before analysis. The Pirani gauge can be isolated from the glass portion of the extraction line while the sample is analyzed. PTFE fittings are used to connect various pieces of the vacuum line. The background of the vacuum line can be confirmed analytically with a N_2 blank before the sample is extracted.

When the vacuum line was first constructed, this procedure was used check for potential leaks or outgassing from the PTFE fittings.

When the sample was ready to be extracted, the glass vacuum chamber was isolated from the pump using the gas expansion valve on the top flange. The sample began melting as soon as the cold bath (-40° C, dry ice-ethanol) was replaced with a tepid water bath (30°C). Before the sample was fully melted - when there is a small chunk of ice left - the warm water was replaced by a cold ice water bath (~0-2° C) and the gas expansion valve on the chamber was opened to start the extraction of the gas sample. The ice water bath prevents the ice core water inside the vessel from warming during extraction. As the gas leaves the vessel, it flows through a glass bead cold trap at (-40° C, dry ice-ethanol mixture) to dry the gas stream. The cold trap consists of a 5/8" glass tube filled with 4 mm glass beads and is attached to the vacuum line via Teflon Swagelok fittings. Downstream of the cold traps, the sample is collected for 2 minutes in a stainless steel cold finger immersed in liquid He (4K). The cold finger is then isolated and allowed to warm to room temperature. The collected gases are analyzed using an automated gas preparation inlet and GC/MS (see section 2.2). During the first melt cycle (i.e. the sample melt), we extract about 98-99% of the ice core ethane, a conservative estimate based on the solubility of ethane in 0°C water. A more detailed discussion of the ethane solubility correction is given in Chapter 4. Degassed ice core water from individual ice core samples was used to perform additional ice core blank tests (see Chapter 4).

Cleaning procedures: During development of this method, variations in blanks were observed due to the procedures used to clean the melt vessel and the glass bead trap. Ethane, propane, and n-butane levels in the "pre-melt" N_2 blanks were monitored to check the cleanliness of the extraction chambers. When anomalous blanks were observed in the vessel or extraction

line, the glass components of the vessel and glass line were washed in a 1 M KOH bath, rinsed with MilliQ water, and baked overnight in a vacuum oven at 100°C. All glass parts and ice core samples were handled using poly-vinyl liners.

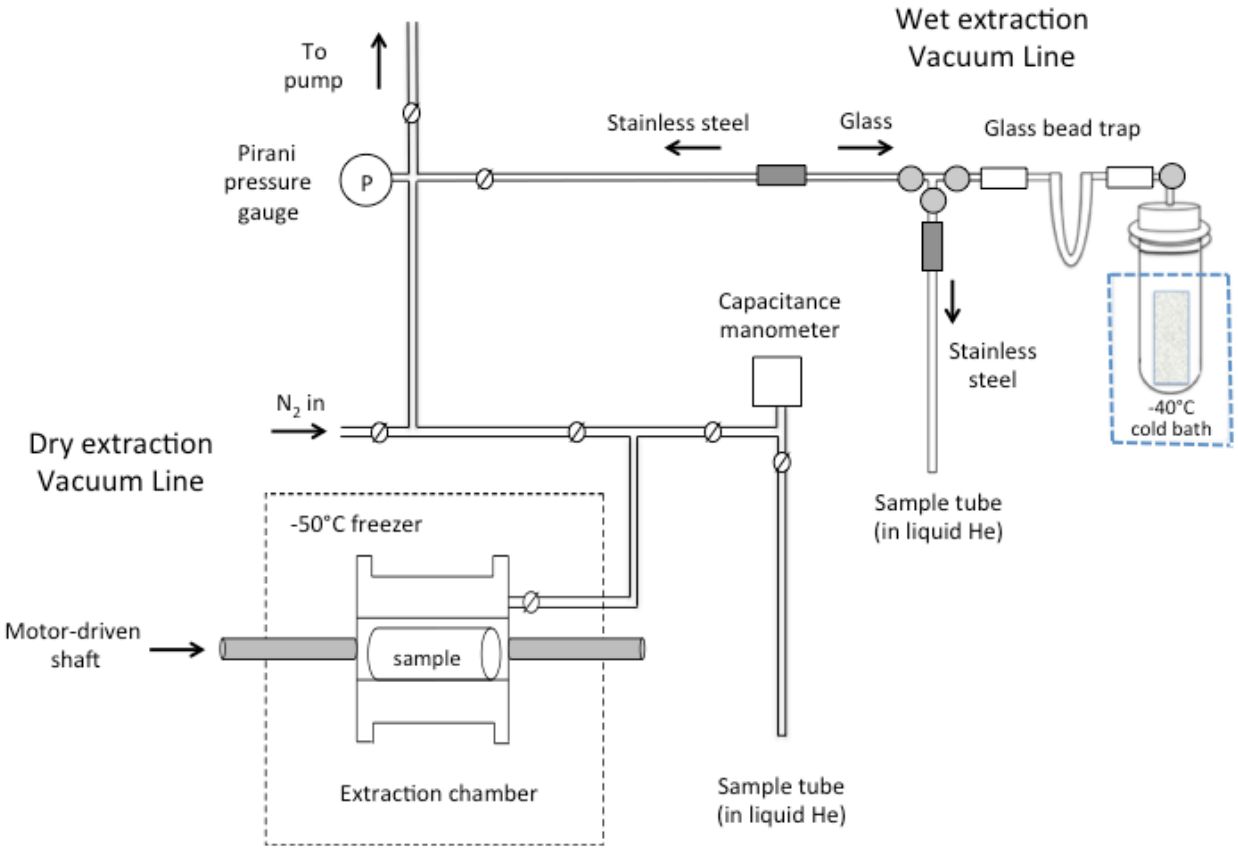

Figure 2.4: Vacuum line set up for dry and wet-extraction ice core measurements. Dry extraction vacuum line (*from left to right*): Ice core samples (400-500 g) are shredded under vacuum, in a stainless steel vessel at -50°C. Gases released during this process are cryogenically focused into a ¼" stainless steel tube immersed in liquid He. Wet extraction vacuum line (*from right to left)*: the two-piece glass extraction vessel with cold bath is attached to the glass vacuum line, which consists of a glass bead trap, glass tee. The vessel consists of a cylindrical glass tube with a rounded bottom and a glass cap with a glass valve with a PTFE tip. The glass bead trap dries the gas stream leaving the glass vacuum chamber before collection in a ¼" stainless steel extraction tube immersed in liquid He. The flow of the gas stream is controlled via three glass valves with PTFE tips, located on the glass tee. The stainless steel extraction tube is connected to the glass line via a glass/stainless steel transition.

2.4 Firn air methods

2.4.1 Firn air sites

This study utilizes firn air measurements from three sites: (1) South Pole (collected in 2008/2009), (2) WAIS Divide (2004/2005), Antarctica and (3) Summit Greenland (2006). The physical characteristics (temperature, pressure, accumulation rate) at each site are listed in Table 2.4. The firn air sampling methods used at WAIS Divide, Antarctica and Summit, Greenland are covered in detail in prior studies [*Battle et al.*, 2011; *Petrenko et al.*, 2013]. The firn air sampling methods used to collect samples from the South Pole are described here. Details on the firn air sampling at Summit Greenland and WAIS Divide, Antarctica are given by *Petrenko et al.,* [2013] and *Battle et al.,* [2011], respectively.

Table 2.4: Site characteristics at Summit, Greenland[a], WAIS Divide[b], Antarctica, and the South Pole[c].

	Summit	WAIS Divide [b]	South Pole
Temperature (°C)	-31*	-31*	-51
Pressure (bar)	0.665	0.78	0.681
Accumulation rate (cm yr^{-1}, water eq)	23	22	7.5
Elevation (m)	3207	1759	2835
Firn close-off depth (m)	71	66.5	117

a) *Schwander et al.*, [1997]
b) *Orsi et al.*, [2012] and *Mitchell et al.*, [2011]
c) *Ferris et al.*, [2011]
* We use T=-31°C in the WAIS-D firn model. *Orsi et al.*, [2012] report T=-28.5°C for WAIS-D and -29.5°C for Summit, Greenland.

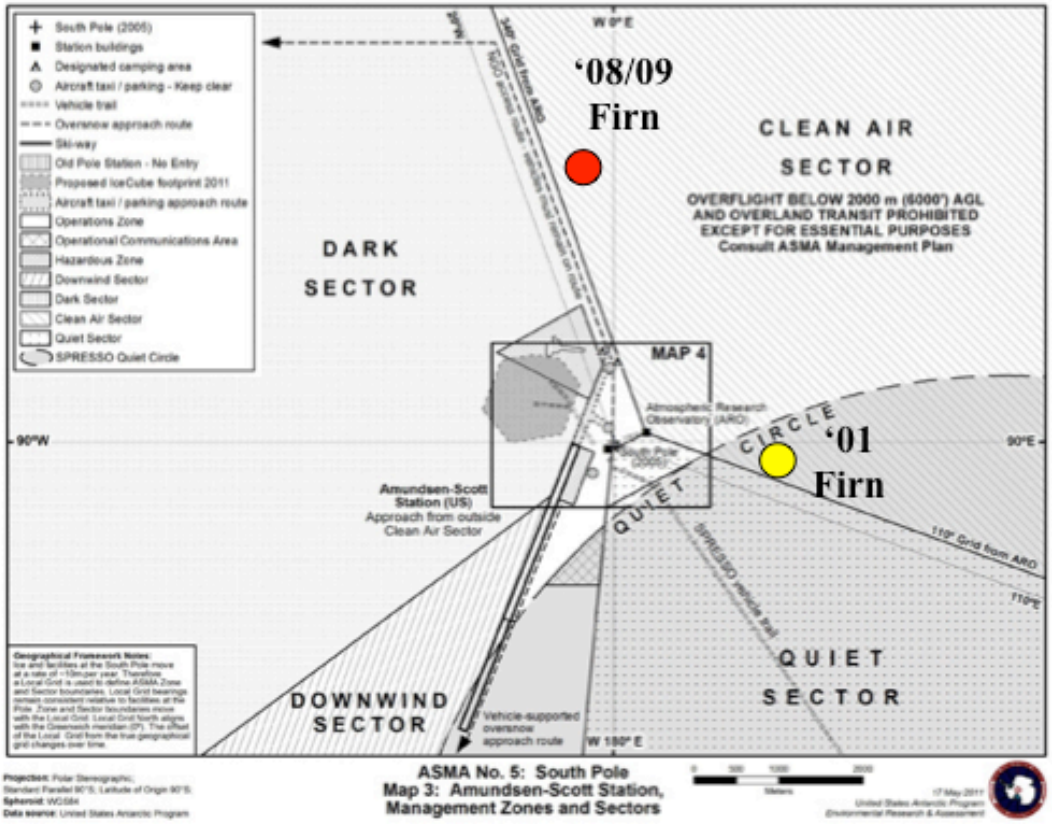

Figure 2.5: Location of the 2008/2009 firn air sampling site in the Clean Air Sector (red circle). The site of the 2001 firn air sampling is marked for comparison (yellow circle). Adapted from: http://www.southpole.aq/maps/.

2.4.2 South Pole firn air sampling techniques

Firn air samples were collected from South Pole, Antarctica during the 2008/2009 field season. Drilling took place near South Pole Station, at the edge of the Clean-Air Sector (Figure 2.5) using the 3" ECLIPSE drill. The firn air was sampled from two adjacent holes drilled at approximately 16 depths ranging from the surface to about 120 m depth, near the bubble close-off region. Firn air samples were collected by M. Aydin (UC Irvine) and T. Sowers (Penn. State Univ.).

A diagram of the firn air sampling apparatus is shown in Figure 2.6. The firn air sampling procedure involves drilling to the sampling depth and lowering the sampling apparatus into the borehole, leaving a small headspace for pumping firn air. The firn bladder was inflated to seal

the borehole [*Battle et al.*, 1996]. Firn air was drawn through an inlet tube using a metal bellows pump. CO_2 levels in the firn air were monitored using a closed-path NDIR instrument (LICOR). Sampling began after the measured CO_2 level stabilized, indicating no contamination from surface air leaks.

UCI, NOAA/CCGG, NOAA/HATS, and PSU flasks were filled from the two firn holes. This study utilizes flasks from UCI (for ethane analyses) and NOAA/CCGG (for carbon monoxide analyses). These flasks consist of a 2.5 L borosilicate glass chamber, equipped with a glass valve with a PTFE tip (Gas Expansion, LTD). In total, 80 UCI flasks and 36 NOAA/CCGG flasks were filled. The NOAA/CCGG flasks were filled with the sample flow directed through an $MgClO_4$ drier and pressurized to 6 psi. The $MgClO_4$ drier was bypassed while filling the UCI flasks, which were pressurized to >10 psi. For this reason, the NOAA/CCGG flasks are considered "dry" and the UCI flasks are considered "wet."

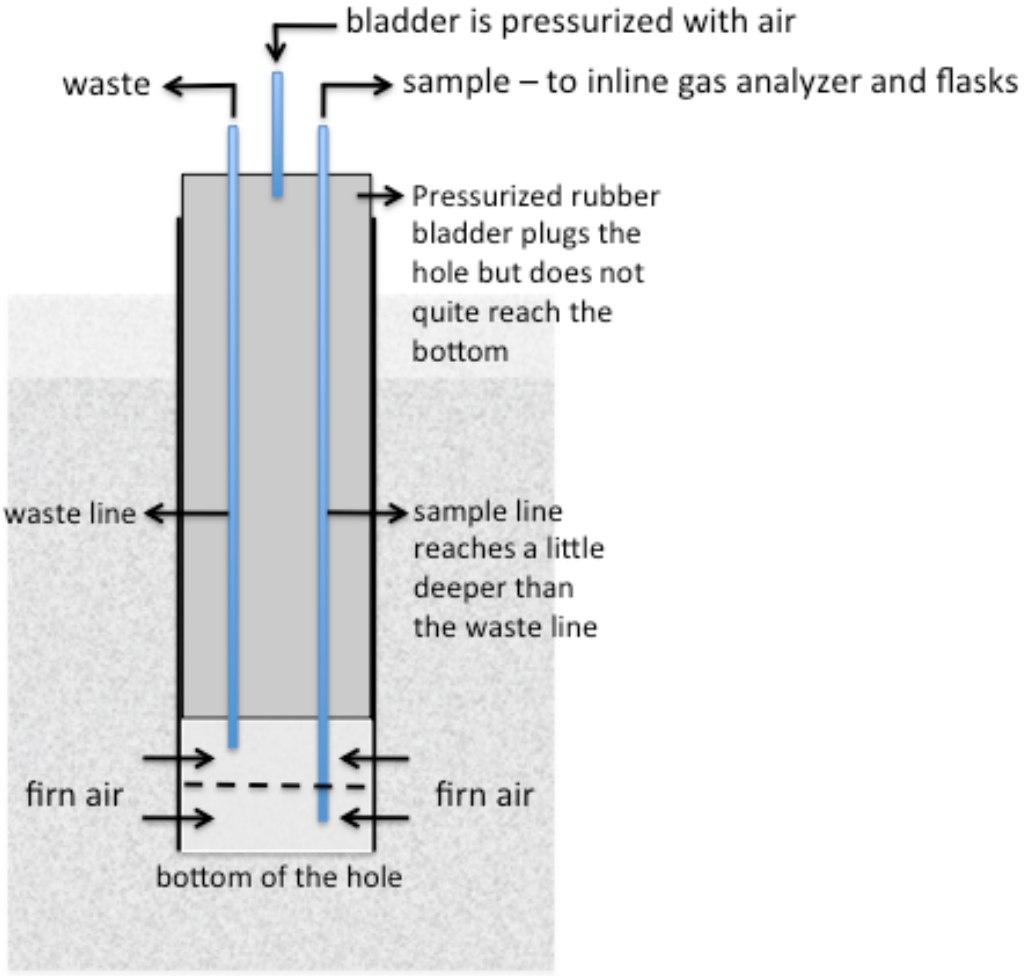

Figure 2.6: Diagram of the sampling apparatus used to collect the South Pole 08/09 firn air samples. (Credit: M. Aydin).

2.4.3 Description of the firn air model

In this study, a 1D firn air advection-diffusion model is used to infer atmospheric histories for ethane and carbon monoxide. This model is based on *Trudinger et al.* [1997]. The model consists of 350 horizontal layers of equal mass, using a coordinate system that is fixed relative to the snow surface. The gas flux across a layer within the firn column (J_z) is calculated as follows:

$$J_z = -D_z * \left[\frac{dC}{dz} - \frac{MgC}{RT}\right] + v_z C \quad (2.1)$$

where z is depth, D_z is a tunable diffusivity function that varies with depth as described below, C is the concentration of the gas tracer of interest, M is molecular weight of the tracer (relative to air), R is the gas constant, and T is temperature (in K), and v_z is the vertical velocity at depth z based on the accumulation rate at the site (in units of m y^{-1}). The first term represents gas transport due to diffusion and gravitational separation. In this study, gravitational effects were turned off in the model, and the firn air measurements of each gas were corrected for gravity using measurements of $\delta^{15}N$ of N_2 in the firn column (see Chapter 5). The second term is due to downward advection, which results from the steady accumulation of snow.

The diffusion profile is defined as:

$$D_z = k_D * s_{open} * D_o \tag{2.2}$$

where D_o is the molecular diffusion coefficient of the gas in air, the depth profile of open porosity (s_{open}), and a depth-dependent empirical "tuning coefficient" (k_D). D_o is calculated based on the site temperature and pressure [*Wilke and Lee,* 1955]. The tuning coefficient k_D is manually adjusted to achieve agreement between the modeled and measured depth profiles for a gas with a known atmospheric history.

The change in concentration of a gas tracer within each layer of the firn is calculated as a function of time from the flux divergence. The second term accounts for the change in open porosity with depth:

$$\frac{dC}{dt} = -\frac{d}{dz}J_z - \frac{1}{f_z}\left(\frac{df}{dz}\right)J_z \tag{2.3}$$

where C is the tracer concentration, J_z is the flux divergence (equation 2.1), and f_z is the fraction of the open porosity at depth z. As an upper boundary condition in the model, the gas concentration in layer 1 is set equal to the gas concentration at the surface. The lower model

boundary lies below the diffusive zone. At that boundary gas is moved purely by advection, at a rate equal to the snow accumulation rate.

The depth profiles of density and open and closed porosity are based on measurements or calculated using empirical models developed by *Herron and Langway,* [1980] and *Schwander* [1989] (see Table A1). The porosity profile in the firn column is defined as:

$$s_{z,total} = 1 - \left(\frac{\rho_z}{\rho_0}\right) \tag{2.4}$$

$$s_{z,closed} = s_{z,total} * e^{\left(75*\left(\frac{\rho_z}{\rho_{close-off}}-1\right)\right)} \tag{2.5}$$

$$s_{z,open} = s_{z,total} - s_{z,closed} \tag{2.6}$$

where ρ_z is the density of ice at depth z, ρ_0 is the density of solid ice at the site, [*Severinghaus and Battle*, 2006], $\rho_{close-off}$ is the density of ice at close off.

The firn air advection-diffusion model is run in forward mode with a 1-year surface "pulse" of the trace gas of interest (concentration=1). The output of the model is a matrix containing the time-dependent concentration of the tracer as a function depth in the firn at 1-year intervals. This matrix can be used to map a concentration time-history into a depth profile for the firn air site as follows:

$$\begin{bmatrix} f_{age_1,z_1} & \cdots & f_{age_m,z_1} \\ \cdots & \cdots & \cdots \\ f_{age_1,z_n} & \cdots & f_{age_m,z_n} \end{bmatrix} \times \begin{bmatrix} C_{t_1} \\ \cdots \\ C_{t_m} \end{bmatrix} = \begin{bmatrix} C_{z_1} \\ \cdots \\ C_{z_n} \end{bmatrix} \tag{2.7}$$

where $f_{age,z}$ is the tracer concentration normalized to the total concentration at depth z, C_t is the atmospheric history of the tracer at time=t, C_z is the predicted concentration of the tracer as a function of depth in the firn column, m is the number of model years, and n is the number of

model layers. A plot of the age distributions (Green's functions) for South Pole is shown is Chapter 5.

2.4.4 Model inputs, tuning and validation

The firn model requires several inputs, including: (1) the depth profile for a gas with a known atmospheric history (e.g. CO_2, CFC-12, or CH_3CCl_3), (2) the tuned diffusivity-depth profile for this gas, (3) the free air diffusion coefficient of the gas, and (4) the open porosity and density profiles of the firn column (measured or modeled). The diffusivity profile in the firn is tuned based on the measurement depth profile for a gas with a known atmospheric history, such as CO_2.

In this study, the diffusion profiles for South Pole and WAIS Divide were tuned iteratively using the CO_2 atmospheric history. The CO_2 atmospheric history is well-known for the Southern Hemisphere, based on NOAA/ESRL atmospheric observations, the firn air measurements from the site of interest, and the Law Dome ice core record [*Etheridge et al.*, 1996]. We start with a function of decreasing density with depth and tune the diffusion profile (piecewise segments) to achieve agreement with the modeled and measured CO_2 depth profile. The CO_2 measurements in this study were provided by P. Lang (NOAA/ESRL/CCG, Carbon Cycle Group). Halocarbon measurements (CH_3CCl_3, CFC-12, HCFC-22, HFC-23, and HFC-134a) were also used for tuning and validation and were provided by S. Montzka (NOAA/ESRL/HATS, Halocarbons and Atmospheric Trace Species).

The diffusion profile is validated using another gas with a known atmospheric history (e.g. CH_4 and CFC-12) and comparing the model result to the measured depth profile of that gas. For South Pole and WAIS Divide, CO_2 and CFC-12 were used as tuning compounds, and the tuned diffusion profiles were tested using halocarbon measurements (HCFC-22, HFC-134a).

Atmospheric histories were derived for Summit, Greenland using similar methods, using the CH_3CCl_3 and CFC-12 as the tuning compounds. For Summit, Greenland, halocarbon gases were used rather than CO_2, as there is no equivalent long-term atmospheric record of CO_2 for the Northern Hemisphere.

2.4.6 Deriving atmospheric histories

In order to derive an atmospheric history for a gas with an unknown atmospheric history from a firn air depth profile, an inverse method was used. An initial guess for the atmospheric history is specified, and the Green's functions from the 1D advection-diffusion model are used to calculate a firn depth profile for the tracer using equation (2.7). A cost function is used to quantify the goodness of fit between the modeled and measured depth profiles in the firn. The Matlab minimization function "fminunc" is used to search for an atmospheric history that minimizes the cost function. Additional details related to the inversion method and cost function are discussed in Chapters 3 and 5.

References

Aydin, M., M. B. Williams, and E. S. Saltzman (2007), Feasibility of reconstructing paleoatmospheric records of selected alkanes, methyl halides, and sulfur gases from Greenland ice cores, *J. Geophys. Res.*, *112*(D7), 1–9, doi:10.1029/2006JD008027.

Aydin, M., K. R. Verhulst, E. S. Saltzman, M. O. Battle, S. A. Montzka, D. R. Blake, Q. Tang, and M. J. Prather (2011), Recent decreases in fossil-fuel emissions of ethane and methane derived from firn air, *Nature*, *476* (7359), 198–201, doi:10.1038/nature10352.

Battle, M., M. Bender, T. Sowers, and P. Tans (1996), Atmospheric gas concentrations over the past century measured in air from firn at South Pole, *Nature*, *383*, 231–235.

Battle, M. O., J. P. Severinghaus, E. D. Sofen, D. Plotkin, A. J. Orsi, M. Aydin, S. A. Montzka, T. Sowers, and P. P. Tans (2011), Controls on the movement and composition of firn air at the West Antarctic Ice Sheet Divide, *Atmos. Chem. Phys.*, *11*(21), 11007–11021, doi:10.5194/acp-11-11007-2011.

Brook, E. J., S. Harder, J. Severinghaus, E. J. Steig, and C. M. Sucher (2000), On the origin and timing of rapid changes in atmospheric methane during the last glacial period, *Glob. Biogeochem. Cyc.*, *14*(2), 559–572.

Etheridge, D. M., L. P. Steele, R. L. Langenfelds, R. J. Francey, J.-M. Barnola, and V. I. Morgan (1996), Natural and anthropogenic changes in atmospheric CO_2 over the last 1000 years from air in Antarctic ice and firn, *J. Geophys. Res.*, *101*(D2), 4115–4128.

Etheridge, D. M., G. I. Pearman, and F. de Silva (1988), Atmospheric trace-gas variations as revealed by air trapped in an ice core from Law Dome, Antarctica, *Annals of Glaciology*, 10, 28-33.

Ferris, D. G., J. Cole-Dai, A. R. Reyes, and D. M. Budner (2011), South Pole ice core record of explosive volcanic eruptions in the first and second millennia A.D. and evidence of a large eruption in the tropics around 535 A.D., *J. Geophys. Res.*, *116*(D17), D17308, doi:10.1029/2011JD015916.

Grachev, A. M., E. J. Brook, and J. P. Severinghaus (2007), Abrupt changes in atmospheric methane at the MIS 5b–5a transition, *Geophys. Res. Lett.*, *34*(20), L20703, doi:10.1029/2007GL029799.

Herron, M. M. and C. C. Langway, (1980), Firn densification: An empirical model, *J. Glaciology*, 25 (93), 373-385.

Mitchell, L. E., E. J. Brook, T. Sowers, J. R. McConnell, and K. Taylor (2011), Multidecadal variability of atmospheric methane, 1000–1800 C.E., *J. Geophys. Res.*, *116*(G2), G02007, doi:10.1029/2010JG001441.

Montzka, S. A., M. Aydin, M. Battle, J. H. Butler, E. S. Saltzman, B. D. Hall, A. D. Clarke, D. Mondeel, and J. W. Elkins (2004), A 350-year atmospheric history for carbonyl sulfide inferred from Antarctic firn air and air trapped in ice, *J. Geophys. Res.*, *109*(D22), D22302, doi:10.1029/2004JD004686.

Orsi, A. J., B. D. Cornuelle, and J. P. Severinghaus (2012), Little Ice Age cold interval in West Antarctica: Evidence from borehole temperature at the West Antarctic Ice Sheet (WAIS) Divide, *Geophys. Res. Lett.*, *39*, L09710, doi:10.1029/2012GL051260.

Petrenko, V. V., P. Martinerie, P. Novelli, et al. (2013), A 60 yr record of atmospheric carbon monoxide reconstructed from Greenland firn air, *Atmos*. *Chem*. *Phys*., *13*, 7567–7585, doi:10.5194/acp-13- 7567-2013.

Rommelaere, V., L. Arnaud, and J.-M. Barnola (1997), Reconstructing recent atmospheric trace gas concentrations from polar firn and bubble ice data by inverse methods, *J. Geophys. Res.*, *102*(D25), 30069–30083.

Saltzman, E. S., M. Aydin, C. Tatum, and M. B. Williams (2008), 2,000-year record of atmospheric methyl bromide from a South Pole ice core, *J. Geophys. Res.*, *113*(D5), D05304.

Schwander, J., T. Sowers, J.-M. Barnola, T. Blunier, A. Fuchs, and B. Malaize (1997), Age scale of the air in the summit ice: Implications for glacial-interglacial temperature change, *J. Geophys. Res.,*102(D16) 19483-19493.

Schwander, J. (1989), The transformation of snow to ice and the occlusion of gases, in The Environmental Record in Glaciers and Ice Sheets, edited by H. Oeschger and C.C. Langway., pp 53-67, John Wiley, New York.

Severinghaus, J., A. Grachev, B. Luz, N. Caillon (2003), A method for precise measurement of argon 40/36 and krypton/argon ratios in trapped air in polar ice with applications to past firn thickness and abrupt climate change in Greenland and at Siple Dome, Antarctica, *Geochimica et Cosmochimica Acta*, 67 (3), 325-343

Severinghaus, J., and M. Battle (2006), Fractionation of gases in polar ice during bubble close-off: New constraints from firn air Ne, Kr and Xe observations, *Earth Planet. Sci. Lett.*, *244*(1-2), 474–500, doi:10.1016/j.epsl.2006.01.032.

Sowers, T., Jubenville, J. (2000), A modified technique for liberating occluded gases from ice cores, *J. Geophys. Res.*, 105 (D23), 29155-29164.

Trudinger, C., I. Enting, D. M. Etheridge, R. J. Francey, V. A. Levchenko, L. P. Steele, D. Raynaud, and L. Arnaud (1997), Modeling air movement and bubble trapping in firn, *J. Geophys. Res.*, *102*(D6), 6747–6763.

Wilke , C. R., and C. Y. Lee (1955), Estimation of diffusion coeficients for gases and vapours, *Ind. Eng. Chem*, 47, 1253-1257.

CHAPTER 3

Recent decreases in fossil-fuel emissions of ethane and methane derived from firn air

3.1 Introduction

Methane and ethane are the most abundant hydrocarbons in the atmosphere and they affect both atmospheric chemistry and climate. Both gases are emitted from fossil fuels and biomass burning, whereas methane (CH_4) alone has large sources from wetlands, agriculture, landfills and waste water. In this study, ethane was measured in firn air samples collected at Summit, Greenland), and at the West Antarctic Ice Sheet – Divide (WAIS-D) and at the South Pole in Antarctica. Atmospheric ethane histories were developed for each site using a one-dimensional firn air diffusion model and an inversion method. A two-box model was then used to estimate top-down ethane emissions histories for fossil fuel and biomass burning sources. The firn-air derived emissions histories are compared alongside bottom-up ethane emissions inventories and are used to investigate atmospheric methane emissions during the twentieth century.

3.2 Measurements and Methods

3.2.1 Firn-air measurements, modeling and inversion

At all three sites, multiple flasks (see section 3.5) from the same depth were filled sequentially, using established methods [*Battle et al.*, 1996]. All flasks were analyzed at the University of California, Irvine, using ~100 cm^3 STP samples on a gas chromatography-mass

spectrometry (GC-MS) system designed for trace gas analysis on small air samples [*Aydin et al.*, 2007]. Summit and South Pole flasks were analyzed at least twice. We used a one-dimensional firn-air model and a synthesis inversion method to derive atmospheric histories of the annual-mean, high-latitude, tropospheric abundances of ethane from the firn-air measurements (see section 3.5).

3.2.2 Two-box model

The Northern and Southern hemispheres are represented as equal mass boxes of 2.2×10^9 Tg (exchange time 1 year). Ethane is lost through $OH^{\bullet}$ oxidation (1/2.6 $months^{-1}$) and transport into the stratosphere (1/35 yr^{-1}), yielding a present day lifetime of 2.3 months. The annual-mean $OH^{\bullet}$ loss frequency varies over the past 100 years based on the methane feedback on tropospheric $OH^{\bullet}$: −0.32% in $OH^{\bullet}$ for every +1% in methane [*Ehhalt et al.*, 2001]. The $OH^{\bullet}$ changes differently in Northern and Southern hemispheres: −0.305% and −0.335%, respectively, based on simulations with the UCI-CTM [*Hsu and Prather*, 2005; *Prather et al.*, 2008]. We adopt a methane increase of 900 ppb to 1,790 ppb since 1900 [*MacFarling Meure et al.*, 2006]. Fossil-fuel, biofuel and biomass-burning sources in the model Northern Hemisphere are adopted from previous work [*Xiao et al.,* 2008], and represent 93%, 81% and 58%, respectively, of the total emissions. The fossil-fuel emission histories for various biomass-burning scenarios are developed by an inverse optimization algorithm (see section 3.5).

3.2.3 Three-dimensional model

The UCI-CTM's simulation of ethane with realistic distribution of sources [*Tang and Prather*, 2010] is used to relate the northern and southern tropospheric mean abundances to the annual-mean abundance over the ice sheets, and thus provide a correction to the two-box model histories for the firn-air modeling (see section 3.5).

3.3 Results and Discussion

3.3.1 Ethane atmospheric histories

We measured ethane in firn air collected at Summit (in Greenland), at the West Antarctic Ice Sheet – Divide, WAIS-D (in Antarctica), and at the South Pole. A synthesis inversion method was used to develop atmospheric histories of ethane for each site, using a one-dimensional firn air diffusion model (Figure 3.1) (see section 3.2). The mean temperatures and the ice accumulation rates are very similar at Summit (−31 °C, 20 cm yr^{-1}) and at WAIS-D (−31 °C, 22 cm yr^{-1}), resulting in similar gas age distributions in the firn and atmospheric histories constrained for the past 50–60 years [*Faïn and Ferrari*, 2008; *Aydin et al.*, 2010]. South Pole is considerably colder (−51 °C), with a lower ice accumulation rate (~8 cm yr^{-1}) and a deeper firn column. As a result, atmospheric histories based on South Pole firn air measurements are constrained for the past 80–90 years [*Battle et al.*, 1996]. The ethane atmospheric histories based on the WAIS-D and South Pole firn air measurements display the same trends for the period since 1950 (Figure 3.1).

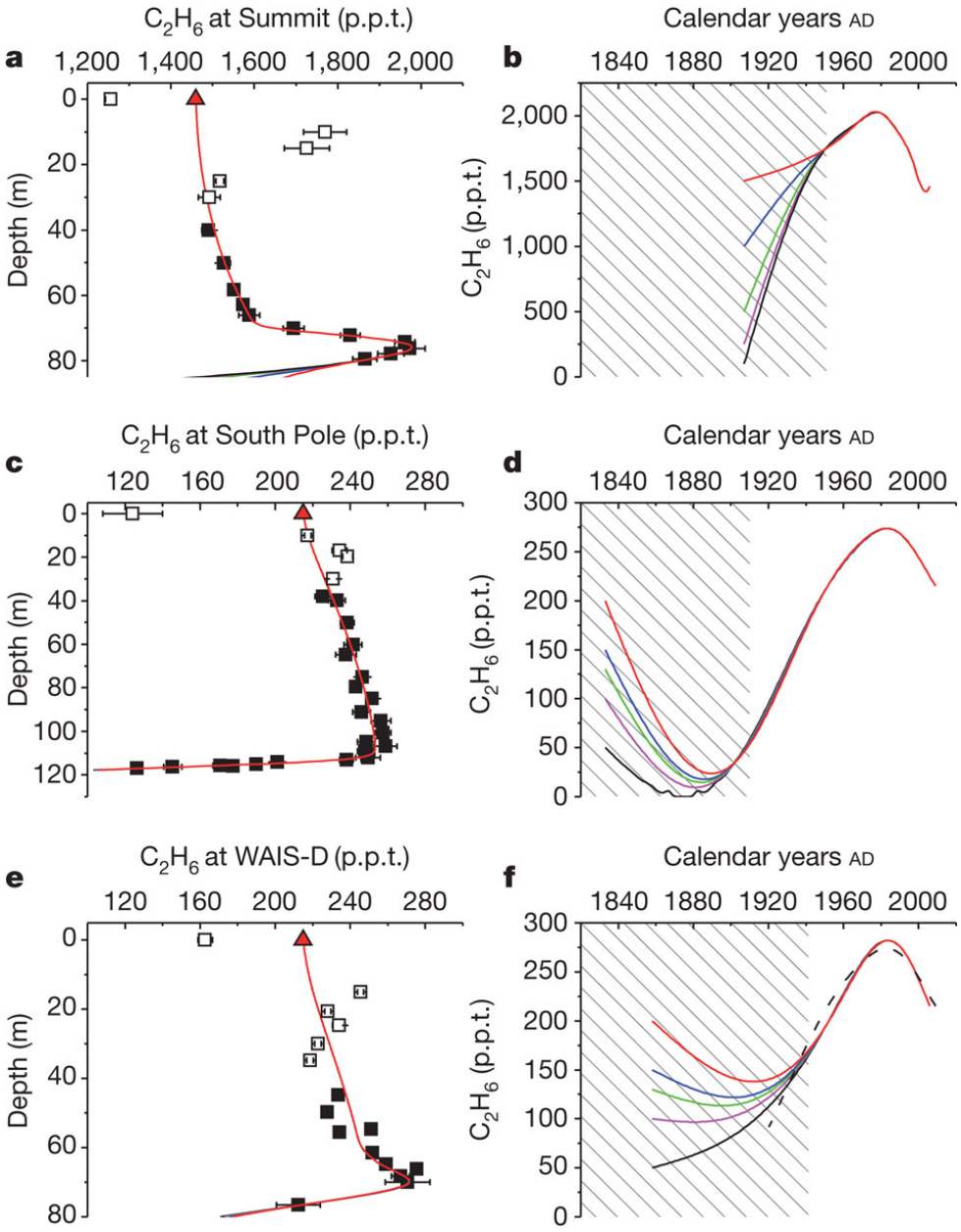

Figure 3.1: Firn air results for Summit (a, b), South Pole (c, d) and WAIS-Divide (e, f). Filled and open squares in a, c and e show measurements with estimated uncertainties (error bars, ±2 s.e.). Solid lines in a, c and e show modeled firn profiles for the three respective sites, with the five different atmospheric histories (solid lines) shown in b, d and f. These five atmospheric histories were obtained by inverse modeling of the measurements with five different boundary conditions at t=0 that are identified by different colors, each representing a different pre-industrial mixing ratio for ethane. The data points in the top 35 m (Summit and South Pole) and 40 m (WAIS-D) of the firn are subject to the effects of seasonal variations in surface ethane levels (see section 3.5) and are ignored during inverse modeling (open squares in a, c and e). The inversions were forced with contemporary annual-mean surface mixing ratios of 1,460 ppt at Summit and 215 ppt at South Pole and WAIS-D (red triangles in a, c and e) (see section 3.5). The South Pole atmospheric history is overlaid on the independently derived WAIS-D atmospheric histories for comparison (dashed line in f). The inversions are sensitive to assumptions about the pre-industrial ethane levels before 1950, 1940 and 1910 at Summit, WAIS-D and South Pole, respectively (shaded areas), implying that only the inversion results for the later years are valid atmospheric histories.

Mean annual ethane levels measured over Summit and South Pole are consistent with those at other high-latitude sites, indicating that the measurements in polar firn air provide a reasonable sampling of the ethane mixing ratios in high latitudes (see section 3.5). Together, the three atmospheric histories show ethane levels peaking in the HNL and HSL atmospheres in the early 1980s, followed by a decline over the 20 years that followed. The South Pole site contains sufficiently old air to constrain the ramp-up period during the early to mid twentieth century (Figure 3.1). On the basis of these atmospheric histories, HSL annual-mean ethane levels increased fivefold between 1910 and 1980 (from about 60 ppt to 280 ppt), and declined more than 10% (to less than 250 ppt) by 2000. In the HNL, ethane increased from ~1.7 ppb in 1950 to ~2.0 ppb in 1980, and declined 25% to ~1.5 ppb in 2000.

3.3.2 Ethane emissions histories

To infer the causes of the atmospheric ethane variations in terms of changes in large-scale sources, we must relate high-latitude ethane levels to hemispheric averages. We used the modern atmospheric ethane distribution [*Simpson et al.*, 2006; *Xiao et al.*, 2008] and sensitivity tests with the UCI Chemical Transport Model (UCI-CTM) [*Hsu and Prather*, 2005; *Prather et al.*, 2008] to derive ratios relating the response of the HNL and HSL to changes in hemispheric mean ethane levels (see section 3.5). Next, we used a simple two-box model (see section 3.2) representing the troposphere in the Northern and Southern hemispheres to simulate variations in mean atmospheric ethane levels over the past century resulting from various scenarios for fossil-fuel, biomass-burning, and biofuel emissions. Fossil-fuel and biofuel emissions are concentrated in the northern mid-latitudes, and biomass burning in the tropics. As a result, these sources contribute to hemispheric ethane levels with different efficiencies (see sections 3.2 and 3.5).

The two-box model was used to infer the fossil-fuel ethane emission histories needed to achieve agreement with the firn-air-derived atmospheric ethane histories from Summit and South Pole, under various assumptions about biomass-burning emissions (Figure 3.2, see Section 3.5). The results show clearly that ethane variability over decadal timescales during the twentieth century was dominated by changes in the fossil-fuel ethane source. When biomass-burning and fossil-fuel ethane emissions are both allowed to vary after 1950, the model yields a biomass-burning source of less than 1 Tg yr^{-1} in 1950, rising to ~3 Tg yr^{-1} by 2000, followed by a drop to 2 Tg yr^{-1}. The model results show a large change in fossil-fuel ethane emissions in the first half of the twentieth century, peaking at 14–16 Tg yr^{-1} in the late 1950s. Fossil-fuel emissions are then constant for about 20 years, followed by a 45% drop over the next 30 years. The model yields 8–10 Tg yr^{-1} for fossil-fuel ethane emissions at the end of the twentieth century, consistent with the modern ethane budget inferred from atmospheric ethane levels [*Xiao et al.*, 2008; *Pozzer et al.*, 2010].

3.3.3 Comparison to bottom-up methane inventories

Fossil-fuel emissions are also a significant source of methane into the atmosphere, and the observed decline in the growth rate of atmospheric methane [*Dlugokencky*, 2003; *Simpson et al.*, 2006] parallels the decline in atmospheric ethane levels during 1980–2000. This evidence suggests that the decline in methane growth rates was caused by a gradual reduction in fossil-fuel emissions, which was already underway when continuous direct atmospheric measurements of methane started in 1984 and 1985 [*Dlugokencky*, 2003; *Simpson et al.*, 2006]. The stabilization of atmospheric ethane in recent years [*Simpson et al.*, 2006] suggests that fossil-fuel emissions are now steady (see section 3.5). Thus, the recent increases in atmospheric methane levels are

probably not derived from increased fossil-fuel emissions and must be due to other sources, as previously suggested [*Rigby et al.*, 2008; *Dlugokencky et al.*, 2009].

The ethane-based biomass-burning emission history agrees well with independent estimates [*Schultz et al.*, 2008; *Xiao et al.*, 2008]. However, our fossil-fuel emissions history is quite different from bottom-up methane emission inventories [*Stern and Kaufmann*, 1996; *van Aardenne et al.*, 2001] (Figure 3.3). Most notably, the ethane-based fossil-fuel emissions display a steep ramp-up after 1920 and a sharp decline after 1980, whereas the bottom-up methane fossil-fuel emission inventories display a generally increasing trend through the entire twentieth century, with the sharpest increases occurring between 1950 and 1980. Hydrocarbons are emitted from a variety of fossil-fuel sources, each exhibiting a different range of methane/ethane emission ratio (MER). For example, coal and natural gas emissions are methane-rich (MER = 5–100) with respect to emission ratios measured near oil-storage and oil-processing facilities (MER = 3–5) [*Xiao et al.*, 2008]. It is possible that the global-average MER (the ratio of total methane to total ethane emissions from all fossil-fuel sources combined) changed over time as the relative emission strengths of the different fossil-fuel sources varied during the twentieth century, but the apparent differences between the ethane-based fossil-fuel emission histories and inventory-based methane emissions (Figure 3.3) cannot be reconciled with such considerations. Inconsistencies are already apparent in mid-century, when the ratio of bottom-up methane emissions to ethane-based fossil-fuel emissions imply an MER of 2–3 (Figure 3.3). It is highly unlikely that the global-average MER during the 1950s could be lower than point sources with the lowest MERs, especially considering that both coal and natural gas were sources of significant hydrocarbon emissions during that period. This suggests the bottom-up methane inventories underestimate fossil-fuel emissions at mid-century.

The ethane-based estimates of fossil-fuel emissions show a decline during the 1980s, while the methane-inventory-based estimates of fossil-fuel emissions show an increase (Figure 3.3). Opposing trends in the fossil-fuel emissions of ethane and methane are highly unlikely, because this requires ethane to be selectively removed from both newly introduced and existing hydrocarbon sources while the residual methane is released to the atmosphere. Natural gas is used in the production of feedstock ethane in plastics manufacturing. However, it seems implausible that methane, which is economically the most valuable component of natural gas, would simply be vented back into the atmosphere after ethane had been removed from natural gas. In fact, the amount of feedstock ethane produced from natural gas is inversely related to the price of natural gas [*Remer and Jorgens*, 1978] and probably declined as natural gas became progressively more valuable during the second half of the twentieth century. We conclude that the discrepancy between the ethane-based fossil-fuel emission histories and the fossil-fuel emission histories from the bottom-up methane inventories cannot be explained by realistic changes in global-average MER during the twentieth century.

The decline in fossil-fuel emissions, as calculated from our firn-air ethane records, coincides with a period of rapid expansion in natural gas production during the second half of the twentieth century [*Barns and Edmonds*, 1990; *Gilardoni*, 2008]. We speculate that the rising economic value of natural gas during the late twentieth century [*Gilardoni*, 2008] and the development of cleaner technologies led to sharp reductions in the release of light hydrocarbons into the atmosphere. Emissions linked specifically to the growing natural gas industry must have been more than offset by large reductions in the venting of light hydrocarbons, including methane and ethane, associated with production and processing of petroleum. These changes appear to be underestimated in the bottom-up methane inventories. We estimate that the total decline in fossil-

fuel emissions of ethane was 5–6 Tg yr^{-1} during 1980–2000. Attributing this decline entirely to decreases in fossil-fuel emission sources with the lowest MER (3–5) implies a 15–30 Tg yr^{-1} drop in fossil-fuel emissions of methane. Distributing the decline among different fossil-fuel sources would yield a larger change in methane emissions from fossil fuels. An independent inversion analysis of methane observations suggests that a 20 Tg yr^{-1} drop in fossil-fuel methane emissions during the 1990s contributed to the decline in methane growth rates [*Bousquet et al.*, 2006]. Our results are consistent with such a decline, but provide additional evidence that the drop in fossil-fuel emissions started sooner, by about a decade. The decline in fossil-fuel emissions during the 1990s accounts for less than 60% of the total reduction during 1980–2000 in the two-box model results for ethane, suggesting that the reduction in fossil-fuel methane emissions could be ~40% larger than the previous estimate [*Bousquet et al.*, 2006] of 20 Tg yr^{-1}.

Given that we do not have comparable observations from lower latitudes, it is possible that a shift in the location of fossil-fuel emissions towards lower latitudes within the Northern Hemisphere contributed to the observed ethane decline during 1980–2000. However, we estimate this effect to be relatively small on the basis of sensitivity tests with the UCI-CTM, which show that possible changes in the location of the emission reductions for ethane could add about 20% to the magnitude of emission reductions calculated above (see section 3.5).

It is also possible that the late twentieth century decline in ethane could have been caused by a decrease in the atmospheric lifetime of ethane, but we estimate the likelihood for such changes to be low. Assuming fixed emissions, a 5–6 Tg yr^{-1} increase in ethane loss (roughly one-third of the peak budget) would be required to account for the observed ethane decline. A change of this magnitude due to increases in $OH^{\bullet}$ concentrations during the late twentieth century is unlikely [*Prinn*, 2005; *Montzka et al.*, 2011]; however, atmospheric levels of chlorine atoms ($Cl^{\bullet}$) might

have increased, because of increasing tropospheric NO*x*, increasing tropospheric ozone and increasing acidity of aerosols [*Lawler et al.*, 2009; *Thornton et al.*, 2010]. A $Cl^{\bullet}$ sink of the magnitude required to explain the ethane decline would have a minor effect on the methane budget (~3%), because the relative reactivity of $Cl^{\bullet}$ versus $OH^{\bullet}$ (kCl/kOH) is considerably smaller for methane than it is for ethane. Accounting for the ethane decline would require an increase of roughly 1.1×10^4 $Cl^{\bullet}$ cm^{-3} over the entire marine boundary layer, or a much larger increase if just the polluted boundary layer is considered. Estimates for the clean marine boundary layer are in the range 10^3–10^4 $Cl^{\bullet}$ cm^{-3}. It is not possible to assess whether a change of the required magnitude is viable with the limited observational data available at present [*Allan et al.*, 2007; *Lawler et al.*, 2009].

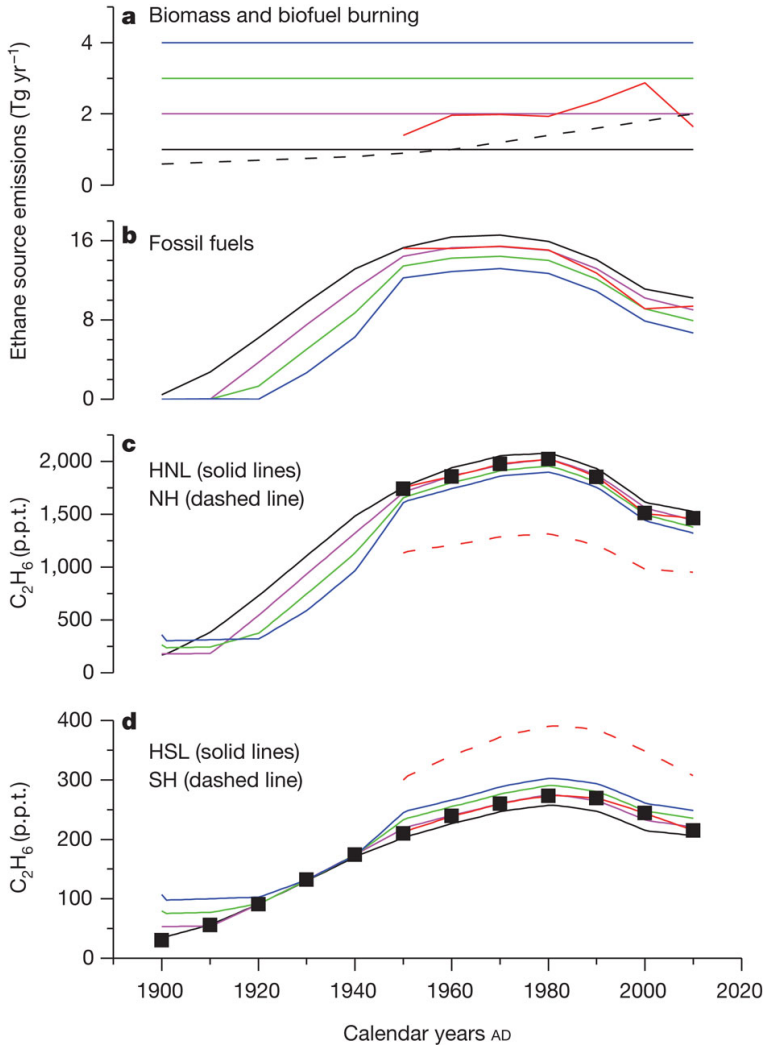

Figure 3.2: Historical global ethane emissions and the resulting atmospheric histories derived with the two-box model. Historical global ethane emissions (a, b) and the resulting atmospheric histories (c, d) are derived with the two-box model to be consistent with the site-specific atmospheric histories based on firn-air results (Figure 3.1). Fossil-fuel emission histories were developed by considering five different biomass-burning cases. In the first four cases, biomass-burning emissions are fixed at 1, 2, 3 and 4 Tg yr^{-1} (black, purple, green and blue lines, respectively; a–d), and the fossil-fuel emissions are varied to minimize the χ^2 value of the fit to the firn-air-based ethane atmospheric histories (black squares in c and d) from both the high northern latitudes and high southern latitudes (HNL and HSL) during 1950–2000, and from HSL only during 1900–1940. We included 2010 in the box model optimizations by assuming the atmospheric ethane levels remained constant at the mixing ratios used as surface tie-points used in firn inversions (Figure 3.1). As a fifth case, the fit to the atmospheric histories is optimized by allowing both the fossil-fuel and the biomass-burning emissions to vary (thick red lines). Variable biomass burning is considered only for the period since 1950, because atmospheric histories from both hemispheres are needed to constrain the partitioning between fossil-fuel and biomass-burning emissions. Emissions from biofuel burning are fixed at the historical estimates (dashed black line; a) in all five cases [*van Aardenne et al.*, 2001]. The atmospheric lifetime of ethane (see section 3.2) is also the same in all five cases. The hemispheric-average atmospheric histories are also shown for the fifth case (dashed red lines; c and d), in which fossil-fuel and biomass-burning emissions are both varied. Ethane levels in HNL and HSL are obtained from Northern and Southern hemispheric (NH and SH) levels using the following ratios for fossil-fuel, biofuels and biomass-burning emissions: HNL/NH: 1.6, 1.4, 1.0; HSL/SH: 0.7, 0.7, 0.7. Values differ from 1.0 owing to the latitudinal distribution of each type of emission (see section 3.5).

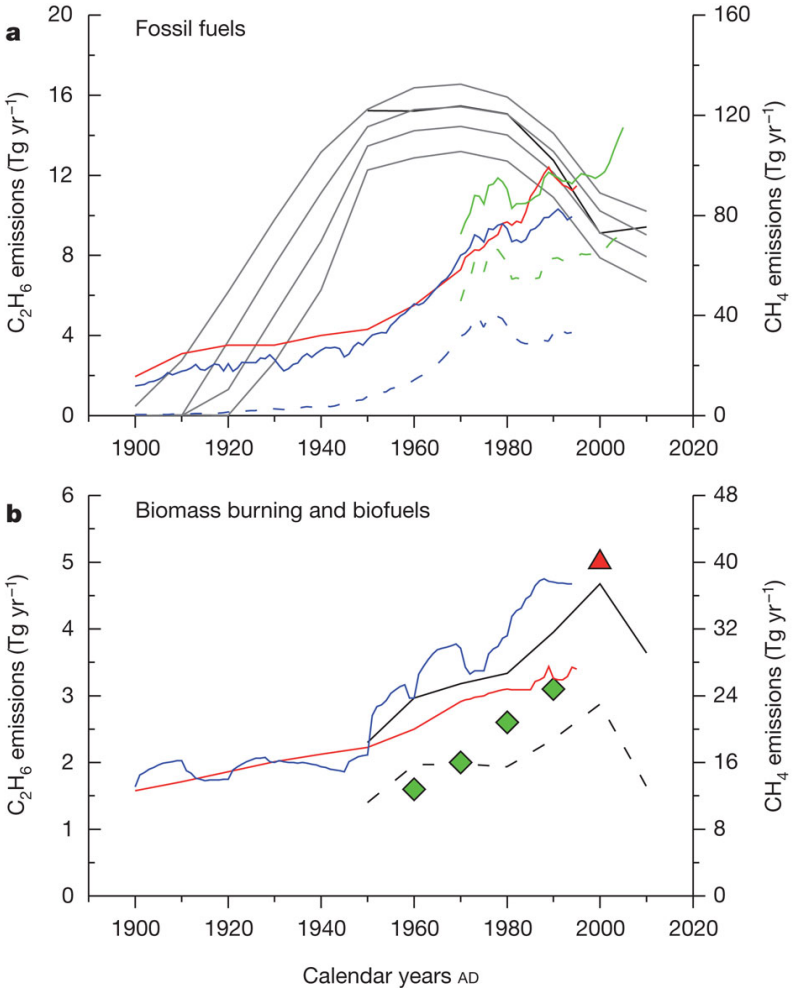

Figure 3.3: Comparison of top-down and bottom-up global ethane emissions. a, Ethane-based fossil-fuel emission histories (left *y*-axis) for fixed biomass burning (solid grey lines) and variable biomass burning (solid black line) cases, compared with bottom-up methane emission estimates from fossil fuels (colored lines, right *y*-axis) based on the following sums of emissions: blue, gas flaring, gas supply and coal mining [*Stern and Kaufmann*, 1996]; red, fossil-fuel consumption, fossil-fuel production and industrial [*van Aardenne et al.*, 2001]; green, oil, gas and solid fuels (data from http://edgar.jrc.ec.europa.eu/). The oil and gas only methane emissions from EDGAR4.1 (see URL in previous sentence; green dashed line) and gas flaring and gas supply methane emissions from [*Stern and Kaufmann*, 1996] (blue dashed line) are also shown. The trends in the ethane-based histories are relatively insensitive to assumptions about biomass burning. None of the bottom-up methane fossil-fuel emission inventories display a persistent decline during 1980–2000 that would be consistent with the ethane-based emission histories. The scales of the left and right *y*-axes are set at a ratio of 8 because it suits the presentation well and is consistent with b. b, Ethane emissions (left *y*-axis) from biomass burning (dashed black line) and biomass-burning+biofuels (solid black line) for the variable biomass-burning case in the two-box model compared with methane emissions (right *y*-axis) attributed to the total burning product from [*Stern and Kaufmann*, 1996] (blue line) [*Stern and Kaufmann*, 1996] and with EDGAR-HYDE 1.4 (red line) [*van Aardenne et al.*, 2001]. The scales of the left and right *y*-axes are set at a ratio of 8, which is a measurement-based estimate of methane/ethane emission ratio (MER) from biomass burning [*Andreae and Merlet*, 2001]. Our results and the bottom-up methane inventories are consistent in how hydrocarbon emissions from biomass burning changed over time and suggest an MER of 8 on a Tg per Tg basis, in agreement with the earlier estimates [*Andreae and Merlet*, 2001]. Our estimate of ethane biomass-burning emissions from the variable biomass-burning case is also in good agreement with some independent estimates of historical ethane emissions from biomass burning [*Schultz et al.*, 2008] (green diamonds, left *y*-axis) and a total burning emissions estimate (biomass burning+biofuels) for present day [*Xiao et al.*, 2008] (red triangle, left *y*-axis).

3.5 Supplementary Information

3.5.1 Flask sampling at different firn sites

For the Summit campaign, we analyzed two flasks from each of the 16 firn sampling depths from a single hole. The South Pole data are based on the analysis of 67 flasks at 29 firn sampling depths from two separate holes, with triplicate sampling at some depths. The WAIS-D data are based on the analysis of 23 flasks filled at 16 firn sampling depths from two holes, with duplicate sampling at some depths.

3.5.2 Ethane measurements in surface air collected at high latitude sites from the northern and southern hemispheres

We measured ethane in paired surface air flasks collected by NOAA-ESRL at selected sites with the same analytical system used in the analyses of firn air samples. Three of the sites are in the high southern latitudes (HSL – defined here as south of 30°S): Cape Grim, Australia (40.7°S, 144.7°E), Palmer station, Antarctica (64.8°S, 64.0°W), and South Pole, Antarctica. These measurements (UCI-A) compare well to an independent set of ethane data from the South Pole [*Simpson et al.*, 2006] (UCI-B), collected and measured by the Blake-Rowland laboratory at UCI (Figure 3.4, *top panel*). The timing and the amplitude of seasonal ethane variations are similar at the different sites within the UCI-A measurements and show agreement between the UCI-A and UCI-B data sets. This indicates that atmospheric ethane is fairly well-mixed between 41°S and 90°S. In addition, UCI-A and UCI-B data display agreement with time series data from mid-latitude sites between 30°S and 47°S [*Blake*, 2010] (Figure 3.4, *middle and bottom panels*). We conclude that the annual mean ethane levels at the South Pole are representative of the mean ethane mixing ratios in the mid to high southern latitudes (HSL).

In the northern hemisphere, Summit data were measured in NOAA/ESRL flasks (UCI-A data, 2006-2008) and in UCI flasks from the Blake-Rowland laboratory at UCI (UCI-B data, 1999-2004). The two data sets display similar seasonal amplitude and annual mean levels (Figure 3.5). Additionally, both the UCI-A and UCI-B data sets compare well with time series measurements from other high northern latitude sites [*Blake*, 2010] (HNL – defined here as north of 30°N) (Figure 3.5). We conclude that the annual mean ethane mixing ratio at Summit, Greenland is representative of the mean ethane levels in the HNL.

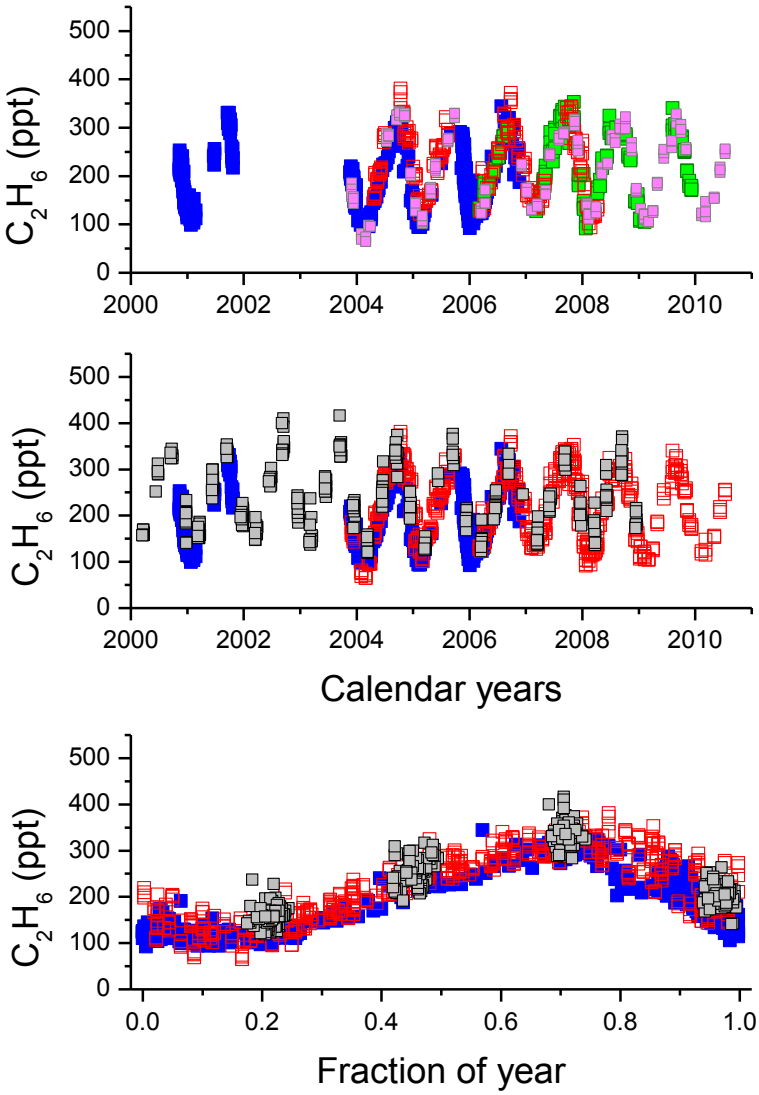

Figure 3.4: Ethane surface air measurements from high southern latitudes (HSL). Panel A – UCI-A time-series measurements in surface air from Cape Grim, Australia (purple squares), Palmer station, Antarctica (red squares), and South Pole, Antarctica (green squares) and UCI-B data from South Pole, Antarctica (blue squares). Panel B – The UCI-A (red squares) and the UCI-B (blue squares) data are compared with time series measurements from various HSL sites (gray squares). The HSL data shown here are a filtered version of the original HSL data [*Blake*, 2010]. 20 out of a total of 365 data points (5.5%) were excluded because they were outliers. A measurement is designated an outlier if it is not within ±2σ (standard deviation) of the mean (all sites) for the month of the year that particular measurement was made. Panel C – The data in the panel B are shown versus fraction of the year (Jan 1st = 0.0, Dec 31st = 1.0).

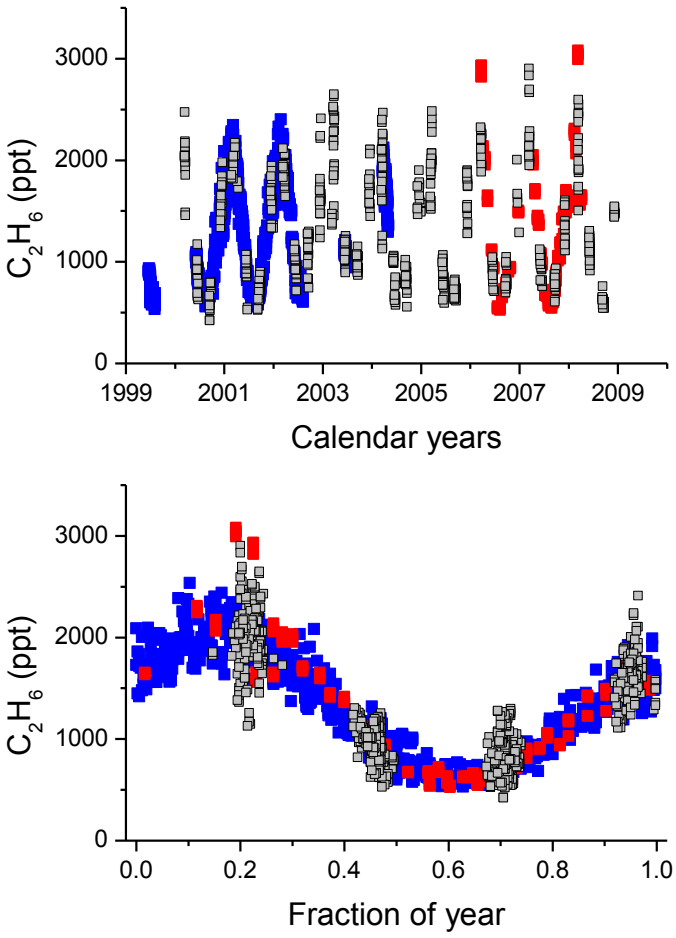

Figure 3.5: Ethane surface air measurements from high northern latitudes (HNL). *Panel A* – The UCI-A data from Summit, Greenland (red squares), the UCI-B measurements from Summit, Greenland (blue squares), and time series measurements from various HNL sites (gray squares). The HNL data shown here are a filtered version of the original HNL data [*Blake*, 2010]. 27 out of a total of 761 measurements (3.5%) were excluded because they were outliers. A measurement is designated an outlier if it is not within ±2σ (standard deviation) of the mean (all sites) for the month of the year that particular measurement was made. *Panel B* – The data in panel A are shown versus fraction of the year (Jan 1st = 0.0, Dec 31st = 1.0).

3.5.3 Estimating the relationship between high latitude ethane and mean hemispheric mixing ratios for biomass and biofuel burning and fossil fuel sources

We used the modern atmospheric ethane distribution [*Simpson et al.*, 2006; *Xiao et al.*, 2008] and sensitivity tests with the UCI Chemical Transport Model (UCI-CTM) [*Hsu and Prather*, 2005; *Prather et al.*, 2008] to derive ratios relating the response of levels in the HNL and HSL relative to hemispheric mean ethane levels from perturbations in ethane emissions from different sources. Flask network measurements show that in the modern atmosphere the mean ethane mixing ratios in the HNL are 1.5 times higher than the northern hemispheric average [*Simpson et al.*, 2006]. UCI-CTM simulations [*Tang and Prather*, 2010] show that the responses of HNL and NH mean levels to a perturbation in ethane emissions from biomass burning are similar (HNL/NH response ratio is 1). In other words, if the mean NH mixing ratio increases by 1 ppt due to an increase in the biomass burning ethane emissions, HNL levels also increase by 1 ppt. For FF and BF ethane emissions, we used the ratio of these sources in the NH to the total global burden [*Xiao et al.*, 2008] (1.145) as an indicator of the heavier influence of fossil emissions at HNL and calculated 1.6 and 1.4 for response ratios for HNL/NH as response ratios, respectively (Table 3.1).

Mean ethane levels in the HSL are 30% lower than the southern hemispheric average [*Simpson et al.*, 2006]. The UCI-CTM runs [*Tang and Prather*, 2010] suggest that mean HSL ethane levels are equally sensitive to changes in fossil fuel or burning based emissions, suggesting a HSL/SH response ratio of 0.7 for the three types of emissions (Table 3.1).

3.5.4 Firn air modeling and inversion to develop atmospheric histories

The UCI firn model is a one-dimensional model with a fixed snow accumulation rate and a

vertically varying diffusivity that is constant with time [*Aydin et al.*, 2010]. The diffusivity is tuned for South Pole and WAIS-D, using CO_2 and CFC-12 profiles measured at the NOAA/ESRL-GMD laboratory and the known atmospheric histories of these gases. For the Summit site, the diffusivity was tuned with firn air measurements of CFC-12 and CH_3CCl_3, and then validated with HCFC-22 and HFC-134a. These compounds were measured at the NOAA/ESRL-GMD laboratory. The diffusivity profiles were adapted to ethane based on the ratio of the molecular diffusivities of ethane to the compounds used for tuning. Molecular diffusivities were calculated based on an empirical relationship [*Wilke and Lee*, 1955] (Table 3.2).

A synthesis inversion method was used to obtain atmospheric histories from the firn air ethane measurements using the firn air model. The UCI firn model is forced with atmospheric histories that represent annual mean ethane levels. Ethane levels in the atmosphere display large seasonal variations (Figure 3.5) that can propagate into the shallower depths of firn, which are ventilated on sub-annual time scales. This gives rise to a damped sinusoidal seasonal variability, which is evident in the upper portion of the firn profiles at all sites (Figure 3.1). To eliminate the impact of these seasonal variations, data from the top 40 m at WAIS-D, and the top 35 m at Summit and South Pole are ignored in the inversions. These visually determined cut-off depths are consistent with penetration depths determined by running a flat atmospheric history with realistic seasonality in the Bowdoin firn model [*Mischler et al.*, 2009] (Figure 3.6). We also considered whether it is possible to introduce a bias in firn air measurements due to seasonally varying wind pumping (Figure 3.7). The results show that any biases in annual mean levels resulting from these effects are small.

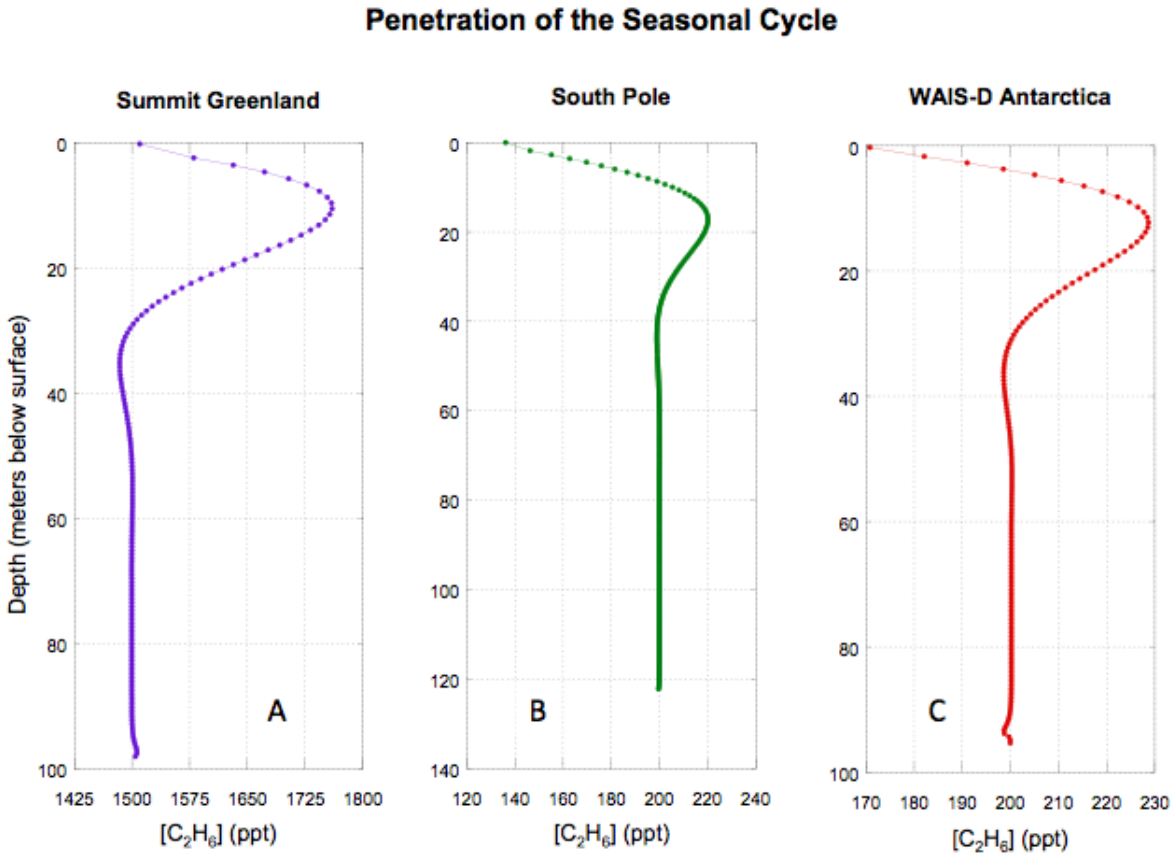

Figure 3.6: Penetration of ethane seasonal variability into the firn. Firn profiles for Summit (panel A), South Pole (panel B), and WAIS-D (panel C) when the Bowdoin firn model is forced with realistic seasonality superimposed on a constant annual mean mixing ratio of 1,500 ppt, 200 ppt, and 200 ppt for Summit, South Pole, and WAIS-D, respectively. These plots justify the exclusion of shallow data from the firn air inversion, which was conducted with a model without seasonality.

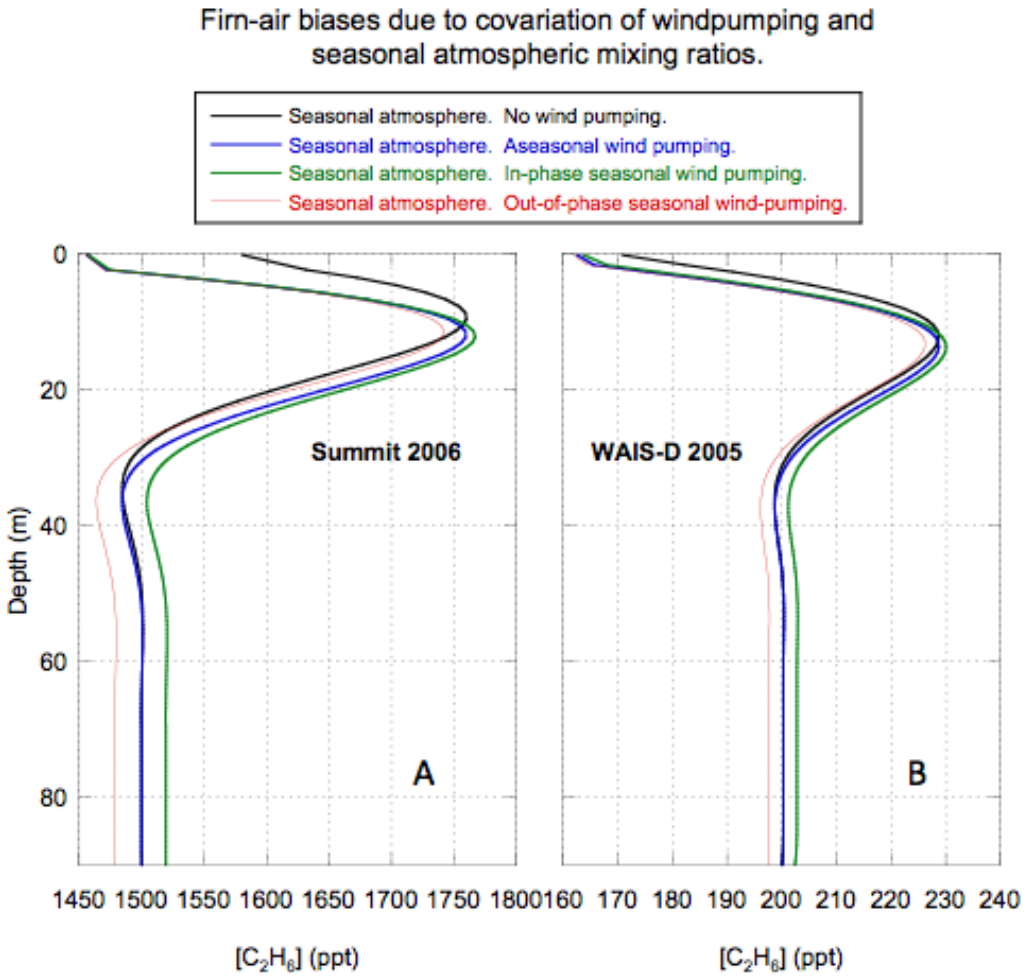

Figure 3.7: Impact of wind-pumping on ethane levels in firn air. The figure is the same as Figure 3.6 (black lines) with three additional model runs for Summit (panel A) and WAIS-D (panel B) sites, representing three different cases of wind pumping parameterized as eddy-diffusivity: 1) constant eddy- diffusivity (blue), 2) seasonal eddy-diffusivity in phase (green), and out of phase (red) with ethane seasonality. For the in-phase (out-of-phase) simulations, wind pumping is at 100% of the annual mean level when atmospheric ethane levels are highest (lowest) and at 0% when the ethane mixing ratios are at a minimum (maximum). Results for South Pole are not appreciably different from those at WAIS-D. This modeling exercise indicates that even with very conservative assumptions, the maximum biases in deep firn due to rectification of atmospheric seasonality are smaller than the uncertainty in the firn air measurements themselves. Note: the shallowest values in the plots give the mixing ratios in the shallowest box (not the free atmosphere at the surface).

Table 3.1: Estimated responses in HNL and HSL mixing ratios for a unit change in the mean hemispheric mixing ratio. For example, a HNL/NH response of 1.6 ppt : 1.0 ppt is equivalent to a response ratio of 1.6.

	HNL : NH	HSL:SH
Fossil fuel use	1.6 ppt : 1.0 ppt	0.7 ppt : 1.0 ppt
Biofuel burning	1.4 ppt : 1.0 ppt	0.7 ppt : 1.0 ppt
Biomass burning	1.0 ppt : 1.0 ppt	0.7 ppt : 1.0 ppt

Table 3.2: Ratio of ethane diffusivity to that of the tuning compounds at different sites.

	Summit	South Pole	WAIS Divide
D_{C2H6}/D_{CO2}	--	0.938	0.932
D_{C2H6}/D_{CFC-12}	1.667	1.674	1.659
$D_{C2H6}/D_{CH3CCl3}$	2.026	--	--

To develop the ethane atmospheric histories, we optimized the "goodness of fit" between the modeled and measured firn air concentrations, using the MATLAB minimization algorithm "fminunc" with the internal parameter "tolerance" set to 10^{-8}. This routine was used to minimize the cost function. The cost function (f) was calculated from the sum of the reduced chi-square statistic (χ^2) and a smoothness criterion (S):

$$f = \frac{1}{4}\chi^2 + S \tag{3.1}$$

where

$$\chi^2 = \sum_{i=1}^{n} \frac{\left(\frac{(calculated-observed)^2}{\sigma^2}\right)}{(n-1)} \tag{3.2}$$

In equation (3.2), σ is the standard error at each depth, determined from the pooled standard deviation of replicate flask pairs and triplicates (where available) and n is degrees of freedom (number of sampling depths). We calculate a σ value of 12.5 ppt for Summit, 2.1 ppt for South Pole, and 5.8 ppt for WAIS-D.

The smoothness criterion (S) in equation (3.1) is based on the second time derivative of the atmospheric history (C) and describes the "roughness" of the modeled atmospheric concentrations [*Rommelaere et al.*, 1997]:

$$S = \alpha * \left(\frac{\partial^2 C}{\partial t^2}\right) \tag{3.3}$$

The relative importance of the smoothness parameter in the cost function is adjusted by a weighing factor (α). We conducted inversions with a range of α values to find the smallest value that produced a continuous, smooth atmospheric history for each of the firn air sites while providing a good fit to the data (Figures 3.8-3.10). The α is 10^{-4} for the Summit, and 0.1 for the

South Pole firn histories later used in box model inversions. The inversions for the Antarctic sites require markedly higher α values than the Summit inversion. The primary reason behind the difference is the lower mean ethane levels measured at the two Antarctic sites, which results in greater fractional scatter. At low α values, the inversion achieves better statistical fits by producing high- frequency variations to replicate variations that could be scatter in the data. This is particularly true at the WAIS-D site.

We initialize the inversions by prescribing a linear atmospheric history between a start date (1830, 1850, and 1910 for South Pole, WAIS Divide, and Summit, respectively) and when the firn studies were conducted (2008, 2005, and 2006 for South Pole, WAIS Divide, and Summit, respectively). The start dates were chosen to satisfy the condition that air from these dates makes up less than 0.1% of the air drawn from the deepest sampling depth (volume fraction) at each of the firn measurement sites. We determined the contemporary ethane levels, using the surface air measurements shown in Figure 3.4. The annual mean ethane mixing ratio in 2005 and 2008 over Antarctica was 215 ppt. The annual mean ethane mixing ratio over Greenland in 2006 was 1,460 ppt. The surface ethane levels are not allowed to vary during the inversions. For each site, multiple runs were made with a range of ethane mixing ratios for the start date. The early portions of the resulting atmospheric histories are sensitive to the assumption about the initial ethane level (Figures 3.8-3.10) because those years are not well constrained by firn air measurements. The results discussed in this paper refer only to those portions of the calculated atmospheric histories that are independent of the ethane level chosen as a starting point.

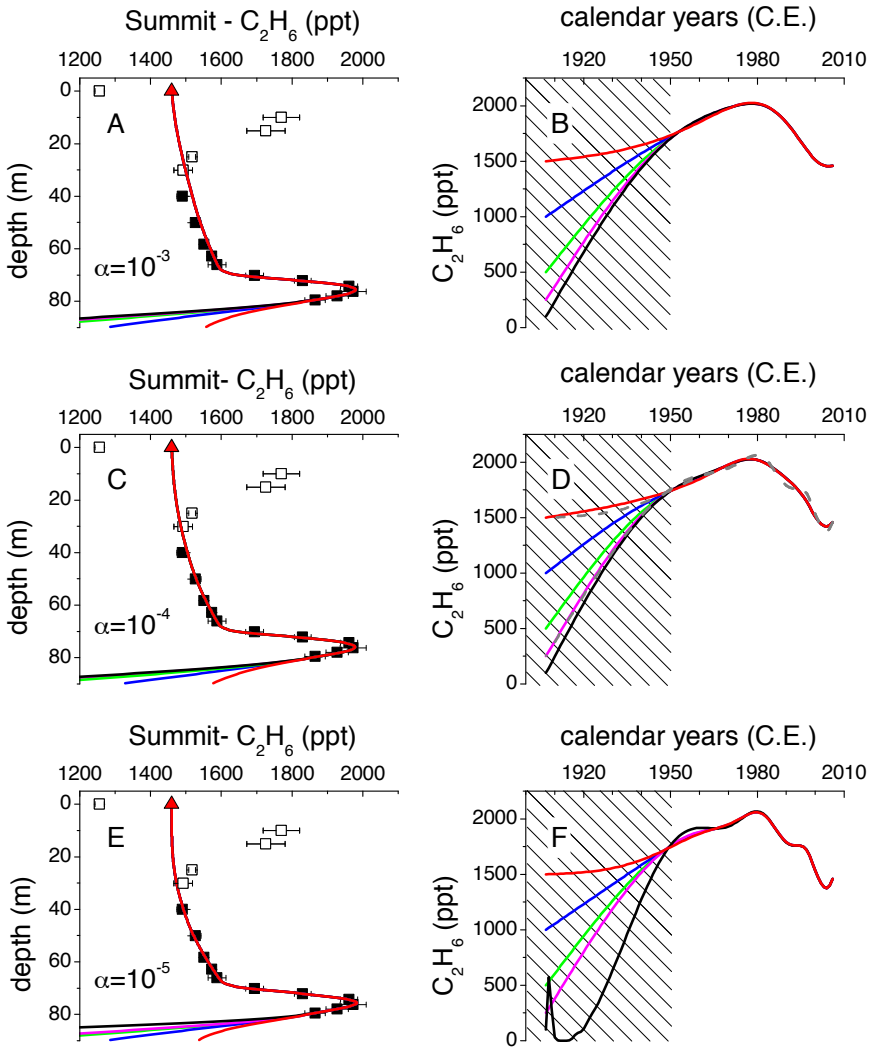

Figure 3.8: Summit firn air inversions with different smoothing factors. Ethane mixing ratios (±2 s.e.) in firn air at Summit, Greenland (black squares – panels A, C, and E) and the atmospheric histories developed based on these measurements (solid lines – panels B, D, and F) for smoothing parameter $\alpha=10^{-3}$, 10^{-4}, and 10^{-5} (in order from top to bottom) as smoothing parameters. The solid lines in panels A, C, and E are the modeled firn profiles for the three respective α values, with the five different atmospheric histories shown in panels B, D, and F. The atmospheric histories were obtained by inverse modeling of the measurements with five different boundary conditions at t_0 that are identified by different colors, each representing a different preindustrial mixing ratio for ethane. Data from depths affected by seasonal variations at the surface (open squares – panels A, C, and E) are ignored during the inversion. Ethane mixing ratio at the surface in 2006 was fixed at 1,460 ppt (red triangle – panels A, C, and E) in all inversions. We used the $\alpha=10^{-4}$ case in our analysis of the changes in the ethane budget despite the fact that $\alpha=10^{-5}$ results in a better statistical fit to the shallowest data point. We chose not to interpret the higher frequency variations shown in the $\alpha=10^{-5}$ inversion (panel F) because they cannot be validated with data from additional sites from Greenland. Overlaid in the panel D are two solutions with $\alpha=10^{-5}$ for direct comparison (gray dashed lines – same as purple and red lines in panel F), which clearly demonstrates the ethane peak in the atmosphere and the magnitudes of the overall increase and drop before and after peak do not change significantly between $\alpha=10^{-4}$ and $\alpha=10^{-5}$. For $\alpha=10^{-3}$ or larger values, the goodness of fit progressively deteriorates. The inversions are sensitive to assumptions about the preindustrial ethane levels prior to 1950 at Summit (shaded area), implying only the inversion results for later years are valid atmospheric histories.

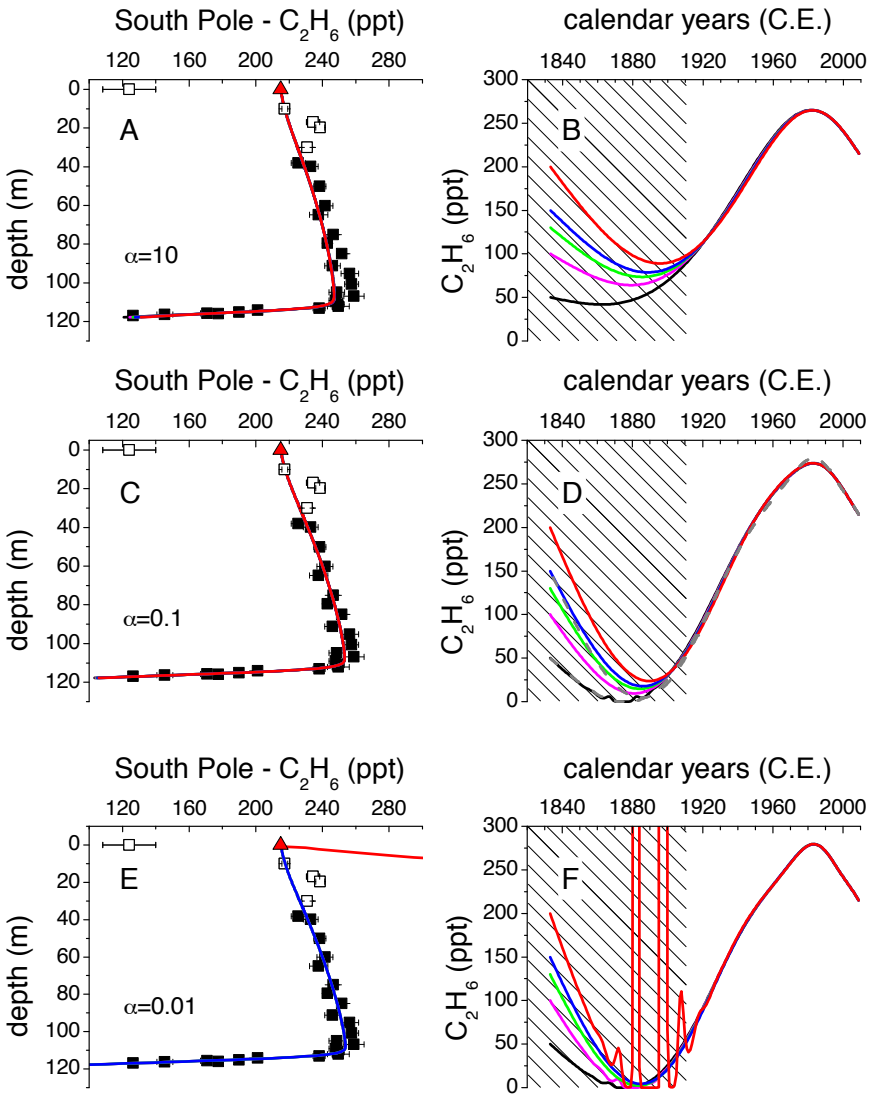

Figure 3.9: South Pole firn air inversions with different smoothing factors. Ethane mixing ratios (±2 s.e.) in firn air at South Pole, Antarctica (black squares – panels A, C, and E) and the atmospheric histories developed based on these measurements (solid lines – panels B, D, and F) for smoothing parameter α=10, 0.1, and 0.01 (in order from top to bottom) as smoothing parameters. The solid lines in panels A, C, and E are the modeled firn profiles for the three respective α values, with the five different atmospheric histories shown in panels B, D, and F. The atmospheric histories were obtained by inverse modeling of the measurements with five different boundary conditions at t_0 that are identified by different colors, each representing a different preindustrial mixing ratio for ethane. Data from depths affected by seasonal variations at the surface (open squares – panels A, C, and E) are ignored during the inversion. Ethane mixing ratio at the surface in 2009 was fixed at 215 ppt (red triangles – panels A, C, and E) in all inversions. We used the α=0.1 case in our analysis of the changes in the ethane budget because with larger α values, the goodness of fit deteriorates and the inversion cannot match the peak ethane levels observed in the firn. α values lower than 0.1 do not improve goodness of fit and can result in non-convergent solutions depending on the initial condition as shown in panel F. Overlaid in panel D are two of the solutions with α=0.01 for direct comparison (gray dashed lines – same as black and green lines in panel F). Neither the timing of the peak ethane levels nor the magnitudes of changes before and after the peak are affected by an order of magnitude change in α. The inversions are sensitive to assumptions about the preindustrial ethane levels prior to 1910 at South Pole (shaded area), implying only the inversion results for later years are valid atmospheric histories.

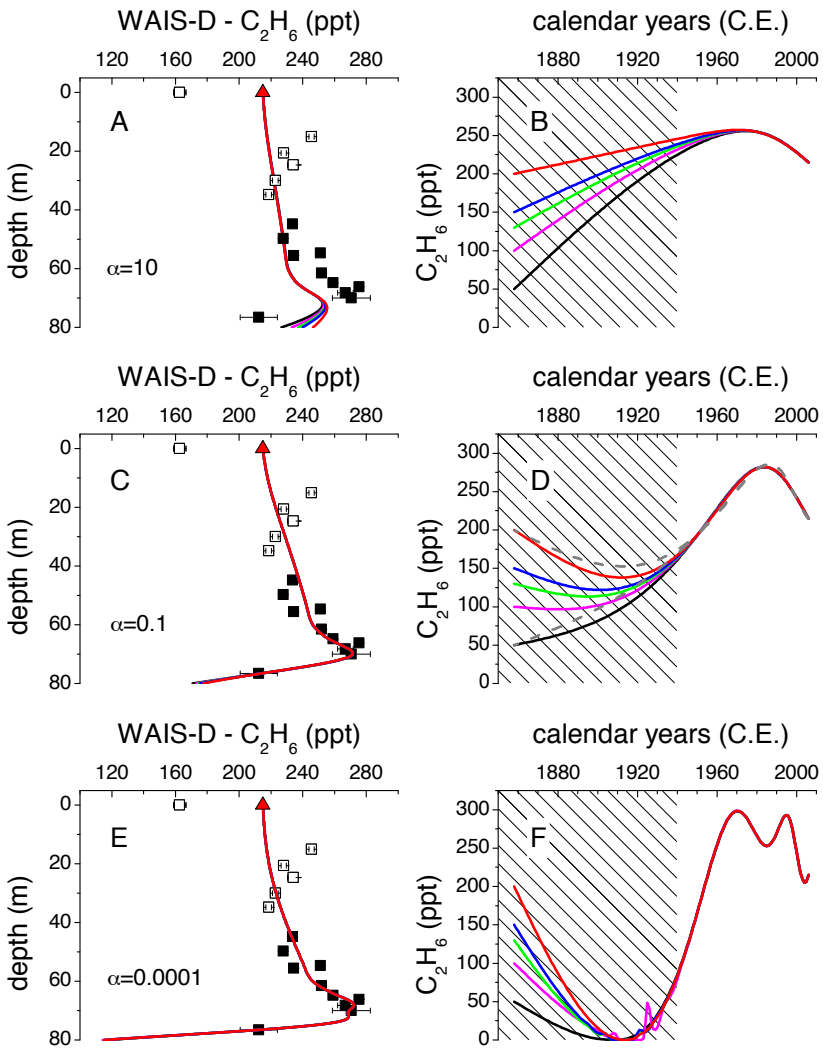

Figure 3.10: WAIS-D firn air inversions with different smoothing factors. Ethane mixing ratios (±2 s.e. when available or ±1σ) in firn air at WAIS-D, Antarctica (black squares – panels A, C, and E) and the atmospheric histories developed based on these measurements (solid lines – panels B, D, and F) for smoothing parameter α=10, 0.1, and 0.0001 (in order from top to bottom) as smoothing parameters. The solid lines in panels A, C, and E are the modeled firn profiles for the three respective α values, with the five different atmospheric histories shown in panels B, D, and E. The atmospheric histories were obtained by inverse modeling of the measurements with five different boundary conditions at t_0 that are identified by different colors, each representing a different preindustrial mixing ratio for ethane. Data from depths affected by seasonal variations at the surface (open squares – panels A, C, and E) are ignored during the inversion. Overlaid in panel D are two solutions with α=0.01 (gray dashed lines). Ethane mixing ratio at the surface in 2005 was fixed at 215 ppt (red triangles – panels A, C, and E) in all inversions. When the results are viewed in progression from α=0.1 to α=0.0001, it becomes clear that at lower values of α, the inversion is trying to fit to the scatter in the data (particularly near 65 m) by first shifting the timing of the peak and then creating a double peak while providing marginal improvement to the fit of the shallower data points. Similar to the Summit and South Pole results, higher α values result in an underestimation of the peak ethane levels observed in the firn. The inversions are sensitive to assumptions about the preindustrial ethane levels prior to 1940 at WAIS-D (shaded area), implying only the inversion results for later years are valid atmospheric histories.

3.5.5 Sensitivity of atmospheric histories to uncertainty in the molecular diffusion coefficient of ethane

We explored the impact of the uncertainty in the diffusion coefficient of ethane by conducting two separate inversions for each site, changing the diffusivity of ethane by +5% and -5%. The results demonstrate that the major features of the atmospheric histories are insensitive to small changes in the diffusivity of ethane (Figures 3.11-3.13). For the three different diffusivities tested here, the magnitude and the timing of the ethane peak in the atmospheric histories remained well within the range explored with different BB scenarios in the box model inversions.

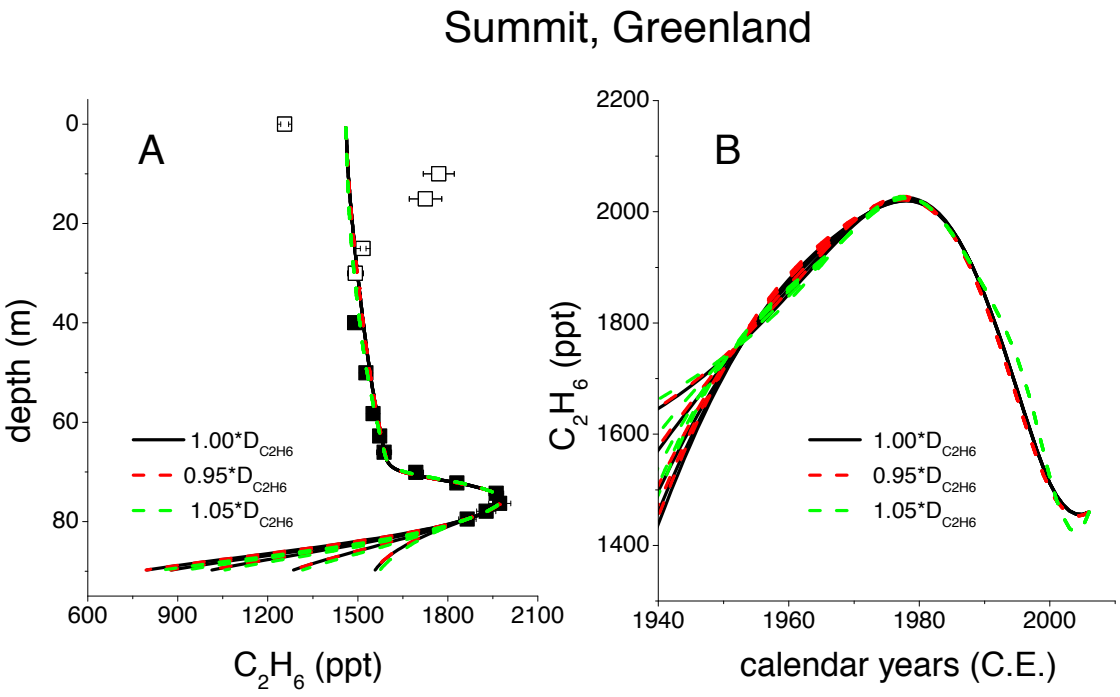

Figure 3.11: Summit firn air inversions with different ethane diffusion coefficients. The ethane measurements (±2 s.e.) are the same as in Fig. 3.8 (black and open squares – panel A). The Summit atmospheric history (black line – panel B) is compared with atmospheric histories based on inversions using +5% (dashed green line – panel B) and -5% (dashed red line – panel B) of the calculated diffusivity for ethane (Table 3.2). The firn profiles for the atmospheric histories based on three different diffusivities are indistinguishable (black, dashed red, and dashed green lines – panel A). The sensitivity test for $0.95*D_{C2H6}$ was conducted with $\alpha=10^{-3}$ because at $\alpha=10^{-4}$ the inversion does not converge for one of the five starting conditions.

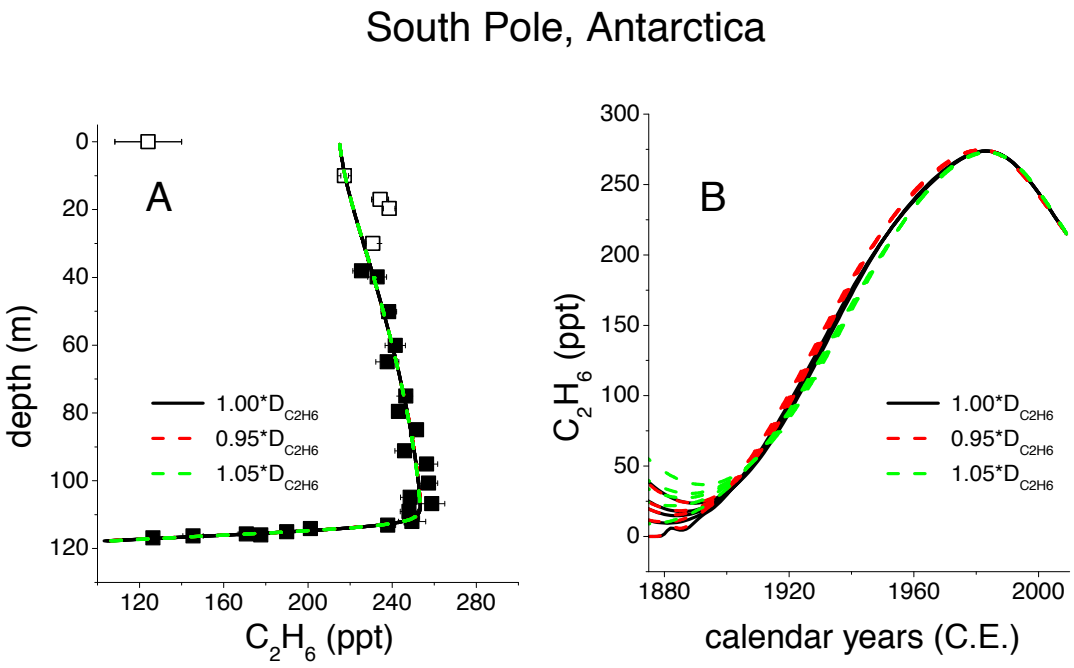

Figure 3.12: South Pole firn air inversions with different ethane diffusion coefficients. The ethane measurements (±2 s.e.) are the same as in Fig. 3.9 (black and open squares – panel A). The South Pole atmospheric history (black line – panel B) is compared with atmospheric histories based on inversions using +5% (dashed green line – panel B) and -5% (dashed red line – panel B) of the calculated diffusivity for ethane (Table 3.2). The firn profiles for the atmospheric histories based on three different diffusivities are indistinguishable (black, dashed red, and dashed green lines – panel A). The sensitivity test for $0.95*D_{C2H6}$ was conducted with $\alpha = 0.2$ because at $\alpha = 0.1$ the inversion does not converge for all starting conditions.

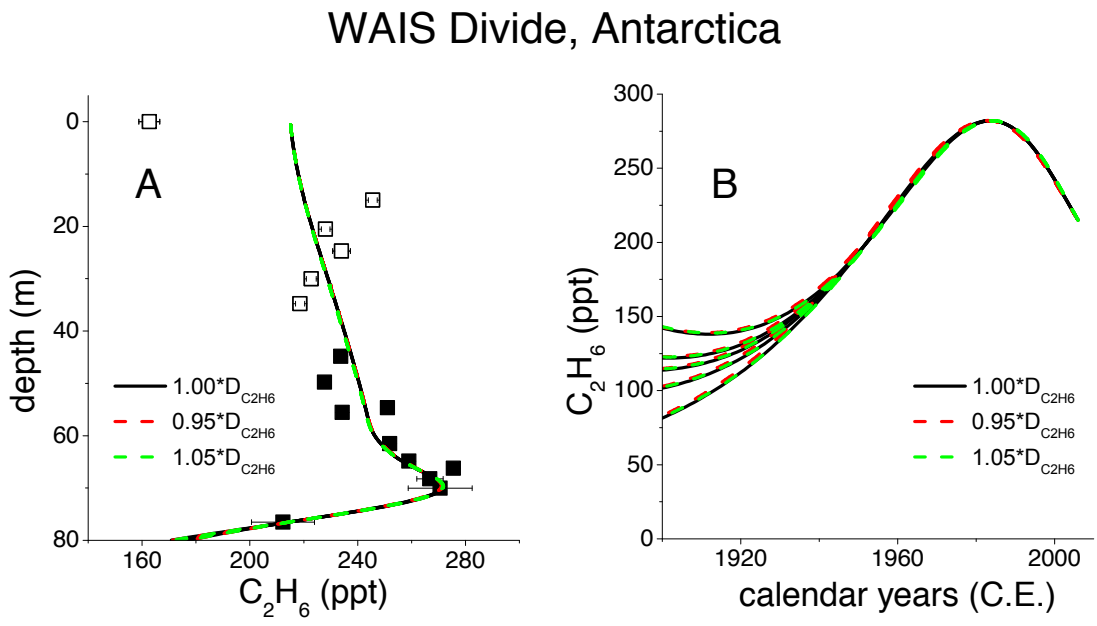

Figure 3.13: WAIS-D firn air inversions with different ethane diffusion coefficients. The ethane measurements (±2 s.e.) are the same as in Fig. 3.10 (black and open squares – panel A). The comparison of the WAIS-D atmospheric history (black line – panel B) with atmospheric histories based on inversions using +5% (dashed green line – panel B) and -5% (dashed red line – panel B) of the calculated diffusivity for ethane (Table 3.2). The firn profiles for the atmospheric histories based on three different diffusivities are indistinguishable (black, dashed red, and dashed green lines – panel A). These sensitivity tests were conducted with α =0.1.

3.5.6 Developing fossil fuel emission histories for various biomass burning scenarios

We calculated ethane fossil fuel emissions over time from the derived atmospheric histories of ethane for both fixed and variable BB emissions scenarios. Modeled ethane emissions were prescribed (in Tg y^{-1}) and the mass balance equations were solved to calculate the ethane mixing ratios (in ppt) for the HNL and HSL. The box model result was then compared with the firn-air based atmospheric histories at Summit and South Pole. We choose not to use the WAIS-D-derived atmospheric history for the 2-box inversion because 1) the turn around in the atmosphere is defined by only one data point and there is larger scatter in shallow firn data, and 2) the South Pole atmospheric history constrains a longer time period (Figure 3.1). The firn-air based atmospheric histories do not extend to 2010, however, we included 2010 in the box model optimizations by assuming the atmospheric ethane levels remained constant at the mixing ratios used as surface tie- points used in firn inversions. The annual mean ethane mixing ratio in 2005 and 2008 over Antarctica was 215 ppt, and over Greenland in 2006 was 1,460 ppt as explained above.

We used the MATLAB function "fminsearch" for the fixed BB emissions scenarios and the MATLAB function "fminunc" for the variable one, with tolerances set to 10^{-4}. The algorithms minimize the same total chi-square statistic, without normalization (equation 3.4a). For the 1950-2010 period, we first calculated the chi-square separately for HNL and HSL by summing the squared difference between observed and predicted hemispheric mixing ratios discretely for every decade, using equation (3.2) without normalization. The HNL and HSL chi-squares are summed to give equal weight to each hemisphere in the minimization during this period (equation 3.4b). The 1900-1940 period is constrained by the firn air record from South Pole only. The total chi-square during this period is equal to two times the chi-square of HSL (equation

3.4c), which assures that the algorithm searches equally hard to fit to the South Pole data for this time period.

$$\chi^2_{total} = \chi^2_A + \chi^2_B \quad (3.4a)$$

$$\chi^2_A = [\chi^2_{HNL} + \chi^2_{HSL}]_{1950-2000} \quad (3.4b)$$

$$\chi^2_B = [2 * \chi^2_{HSL}]_{1900-1940} \quad (3.4c)$$

We considered four fixed BB emissions cases at emissions of 1, 2, 3, and 4 Tg/y. We also considered one case where both BB and FF ethane emissions were allowed to vary. In all the cases, the FF emission history was set at 5 Tg/y between 1900-1930 and to 15 Tg/y between 1940-2010 as a starting condition for the minimization algorithm. In the variable biomass burning case, BB emissions were set at 1 Tg/y for all years as a starting condition.

3.5.7 Sensitivity of fossil fuel emission histories to location of ethane emissions in the northern hemisphere

Using the UCI CTM calculations for the QUANTIFY project [*Hoor et al.*, 2009], we examined the sensitivity of the Greenland annual mean ethane levels to our gridded FF and BF emissions in North America and Europe (NA-EU) versus Asia (AS – Japan, China, S and SE Asia). For the same absolute change in emissions, the relative impact on Greenland ethane is 171 and 73 ppt/Tg (2.4:1) for NA-EU and AS, respectively. These sensitivities are calculated as a tropospheric mean for the four model pixels that are geographically closest to the exact location of Summit.

Based on our firn air measurements, ethane levels at Summit, Greenland peaked at ~2,020 ppt in 1980 and dropped to ~1,510 ppt in 2000 (510 ppt drop). Scaling the base case (present day) in the UCI-CTM to match the lifetime and emission budgets of previous work [*Xiao et al.*,

2008], we calculate total FF+BF emissions of 11.7 Tg/y and an annual mean ethane level of 1,342 ppt at Summit. Given the sensitivities listed above, a 3.7 Tg/y increase in emissions distributed based on the current contributions of NA, EU and AS to fossil fuel ethane emissions [*Xiao et al.*, 2008] results in a 510 ppt increase in the modeled ethane levels over Summit. This amounts to 2.5 Tg/y increase in NA-EU (2/3 of the total change) and 1.2 Tg/y of increase in AS (1/3 of the total change), and a total FF+BF emissions of 15.4 Tg/y. If we change the emissions in the NA-EU region only, a 510 ppt change at Summit can be achieved by adding 3.0 Tg/y of emissions to the base case (19% lower than 3.7 Tg/y, FF+BF emissions of 14.7 Tg/y).

Fossil fuel ethane emissions in AS are estimated at 2.0 Tg/y in previous work [*Xiao et al.*, 2008], albeit for a geographically broader Asia, which includes the Russian Arctic. By comparison, the UCI-CTM has 2.2 Tg/y of emissions in AS (without Russia) in the base case simulation. Estimates of fossil fuel CO_2 emissions indicate that fossil fuel use in AS roughly doubled during 1980-2000 [*Boden et al.*, 2011]. If ethane emissions also doubled, this would imply about a 1 Tg/y increase in fossil fuel ethane emissions in AS. The sensitivities listed above indicate that relocating 1 Tg/y of emission sources from NA-EU to AS results in a 98 ppt drop in Summit mixing ratios, or a drop that is only 19% (98 ppt/510 ppt) less than what we infer otherwise, practically having the same impact on the results as the scenario presented in the paragraph above. It should be noted that FF use in AS has continued to increase through the first decade of the 21st century [*Boden et al.*, 2011]. Interestingly, the surface ethane measurements [*Simpson et al.*, 2006] do not show any indication of diverging trends in ethane mixing ratios between the tropics and high latitudes of either hemisphere between 1996-2005, suggesting these developments have not yet caused a measureable change in the global distribution of ethane.

3.6 Conclusions

- The firn air results show atmospheric ethane levels rose globally from the early twentieth century until the 1980s. After 1980, the ethane trend reversed, and levels began declining globally over the next 20 years. Results from the 2-box model suggest that ethane variability during the 20th century was primarily driven by changes in fossil fuels emissions.
- The box model results suggest ethane fossil fuel emissions peaked in the 1960s and 1970s at 14–16 Tg yr^{-1} and dropped to 8–10 Tg yr^{-1} by the end of the twentieth century. The peak and decline in ethane fossil-fuel sources is likely related to changes in emissions of light alkanes associated with oil/gas production and use.
- The top-down ethane fossil-fuel emissions histories developed in this study are used to infer changes in atmospheric methane, since methane and ethane share common sources. The ethane emissions histories imply that the fossil-fuel source of methane also began to decline in the 1980s, and may have contributed to the late twentieth century slow-down in the growth rate of atmospheric methane.

References

van Aardenne, J. A., F. J. Dentener, J. G. J. Olivier, C. G. M. Klein Goldewijk, and J. Lelieveld (2001), A 1 x 1 degree resolution dataset of historical anthropogenic trace gas emissions for the period 1890-1990, *Global Biogeochem. Cycles*, *15*(4), 909–928.

Allan, W., H. Struthers, and D. C. Lowe (2007), Methane carbon isotope effects caused by atomic chlorine in the marine boundary layer: Global model results compared with Southern Hemisphere measurements, *J. Geophys. Res.*, *112*(D4), D04306, doi:10.1029/2006JD007369.

Andreae, M. O., and P. Merlet (2001), Emission of trace gases and aerosols from biomass burning, *Global Biogeochem. Cycles*, *15*(4), 955–966.

Aydin, M., M. B. Williams, and E. S. Saltzman (2007), Feasibility of reconstructing paleoatmospheric records of selected alkanes, methyl halides, and sulfur gases from Greenland ice cores, *J. Geophys. Res.*, *112*(D7), 1–9, doi:10.1029/2006JD008027.

Aydin, M. et al. (2010), Post-coring entrapment of modern air in some shallow ice cores collected near the firn-ice transition: evidence from CFC-12 measurements in Antarctic firn air and ice cores, *Atmos. Chem. Phys.*, *10*(11), 5135–5144, doi:10.5194/acp-10-5135-2010.

Barns, D. W., and J. A. Edmonds (1990), *An Evaluation of the Relationship Between the Production and Use of Energy and Atmospheric Methane Emissions*, TR047, DOE/NBB-0088P, National Technical Information Service, US Dept of Commerce, Springfield.

Battle, M., M. Bender, T. Sowers, and P. Tans (1996), Atmospheric gas concentrations over the past century measured in air from firn at South Pole, *Nature*, *383*, 231–235.

Blake, D. R. (2010), *Methane, Nonmethane Hydrocarbons, Alkyl Nitrates, and Chlorinated Carbon Compounds including 3 Chlorofluorocarbons (CFC-11, CFC- 12, and CFC-113) in Whole-air Samples*, Carbon Dioxide Information Analysis Center, Oak Ridge National Laboratory, U.S. Department of Energy, Oak Ridge Tenn., U.S.A.

Boden, T. A., G. Marland, and R. J. Andres (2011), *Global, Regional, and National Fossil Fuel CO_2 Emissions*, Carbon Dioxide Information Analysis Center, Oak Ridge National Laboratory, U.S. Department of Energy, Oak Ridge Tenn., U.S.A.

Bousquet, P. et al. (2006), Contribution of anthropogenic and natural sources to atmospheric methane variability, *Nature*, *443*(7110), 439–43, doi:10.1038/nature05132.

Dlugokencky, E. J. (2003), Atmospheric methane levels off: Temporary pause or a new steady-state?, *Geophys. Res. Lett.*, *30*(19), 1992, doi:10.1029/2003GL018126.

Dlugokencky, E. J. et al. (2009), Observational constraints on recent increases in the atmospheric CH_4 burden, *Geophys. Res. Lett.*, *36*(18), L18803, doi:10.1029/2009GL039780.

Ehhalt, D. et al. (2001), *Atmospheric chemistry and greenhouse gases. In: Climate Change 2001: The Physical Science Basis. Contribution of Working Group I to the Third Assessment Report of the Intergovernmental Panel on Climate Change*, Cambridge Univ. Press, Cambridge and New York.

Faïn, X., and C. Ferrari (2008), Mercury in the snow and firn at Summit Station, Central Greenland, and implications for the study of past atmospheric mercury levels, *Atmos. Chem. and Phys.*, *8*, 3441–3457.

Gilardoni, A. (2008), *The world market for natural gas: Implications for Europe*, (Springer 2008).

Hoor, P. et al. (2009), The impact of traffic emissions on atmospheric ozone and OH: results from QUANTIFY, *Atmos. Chem. Phys.*, *9*, 3113–3136.

Hsu, J., and M. J. Prather (2005), Diagnosing the stratosphere-to-troposphere flux of ozone in a chemistry transport model, *J. Geophys. Res.*, *110*(D19), D19305, doi:10.1029/2005JD006045.

Lawler, M. J., B. D. Finley, W. C. Keene, A. A. P. Pszenny, K. A. Read, R. von Glasow, and E. S. Saltzman (2009), Pollution‐enhanced reactive chlorine chemistry in the eastern tropical Atlantic boundary layer, *Geophys. Res. Lett.*, *36*(8), L08810, doi:10.1029/2008GL036666.

MacFarling Meure, C., D. Etheridge, C. Trudinger, P. Steele, R. Langenfelds, T. van Ommen, A. Smith, and J. Elkins (2006), Law Dome CO_2, CH_4 and N_2O ice core records extended to 2000 years BP, *Geophys. Res. Lett.*, *33*(14), L14810, doi:10.1029/2006GL026152.

Mischler, J. A., T. A. Sowers, R. B. Alley, M. Battle, J. R. McConnell, L. Mitchell, T. Popp, E. Sofen, and M. K. Spencer (2009), Carbon and hydrogen isotopic composition of methane over the last 1000 years, *Global Biogeochem. Cycles*, *23*(GB4024), doi:10.1029/2009GB003460.

Montzka, S. A., M. Krol, E. Dlugokencky, B. Hall, P. Jöckel, and J. Lelieveld (2011), Supp Info: mall interannual variability of global atmospheric hydroxyl, *Science*, *331*(6013), 67–9, doi:10.1126/science.1197640.

Pozzer, A., J. Pollmann, D. Taraborrelli, P. Jöckel, D. Helmig, P. Tans, J. Hueber, and J. Lelieveld (2010), Observed and simulated global distribution and budget of atmospheric C_2-C_5 alkanes, *Atmos. Chem. Phys.*, *10*(9), 4403–4422, doi:10.5194/acp-10-4403-2010.

Prather, M. J., X. Zhu, S. E. Strahan, S. D. Steenrod, and J. M. Rodriguez (2008), Quantifying errors in trace species transport modeling., *Proc. Natl. Acad. Sci. U.S.A.*, *105*(50), 19617–21, doi:10.1073/pnas.0806541106.

Prinn, R. G. (2005), Evidence for variability of atmospheric hydroxyl radicals over the past quarter century, *Geophys. Res. Lett.*, *32*(7), L07809, doi:10.1029/2004GL022228.

Remer, D., and C. Jorgens (1978), Ethylene Economics and production forecasting in a changing, *Eng. Process Econ.*, *3*, 267–278.

Rigby, M. et al. (2008), Renewed growth of atmospheric methane, *Geophys. Res. Lett.*, *35*(22), L22805, doi:10.1029/2008GL036037.

Rommelaere, V., L. Arnaud, and J.-M. Barnola (1997), Reconstructing recent atmospheric trace gas concentrations from polar firn and bubble ice data by inverse methods, *J. Geophys. Res.*, *102*(D25), 30069–30083.

Schultz, M. G., A. Heil, J. J. Hoelzemann, A. Spessa, K. Thonicke, J. G. Goldammer, A. C. Held, J. M. C. Pereira, and M. van het Bolscher (2008), Global wildland fire emissions from 1960 to 2000, *Global Biogeochem. Cycles*, *22*, GB2002, doi:10.1029/2007GB003031.

Simpson, I. J., F. S. Rowland, S. Meinardi, and D. R. Blake (2006), Influence of biomass burning during recent fluctuations in the slow growth of global tropospheric methane, *Geophys. Res. Lett.*, *33*(L22808), 1–5, doi:10.1029/2006GL027330.

Stern, D. I., and R. K. Kaufmann (1996), Estimates of global anthropogenic methane emissions 1860-1993, *Chemosphere*, *33*(1), 159–176.

Tang, Q., and M. J. Prather (2010), Correlating tropospheric column ozone with tropopause folds: the Aura-OMI satellite data, *Atmos. Chem. Phys.*, *10*(19), 9681–9688, doi:10.5194/acp-10-9681-2010.

Thornton, J. A. et al. (2010), A large atomic chlorine source inferred from mid-continental reactive nitrogen chemistry, *Nature*, *464*, 271–274, doi:doi:10.1038/nature08905.

Wilke, C. R., and C. Y. Lee (1955), Estimation of diffusion coefficients for gases and vapours, *Ind. Eng. Chem.*, *47*, 1253–1257.

Xiao, Y., J. A. Logan, D. J. Jacob, R. C. Hudman, R. Yantosca, and D. R. Blake (2008), Global budget of ethane and regional constraints on U.S. sources, *J. Geophys. Res.*, *113*(D21), D21306, doi:10.1029/2007JD009415.

CHAPTER 4

Measurements of ethane in Antarctic ice cores

4.1 Introduction

This study presents ethane measurements in air extracted from ice cores from the West Antarctic Ice Sheet (WAIS) Divide, Antarctica and the South Pole and examines the feasibility of reconstructing paleoatmospheric ethane levels from ice core air bubbles. Such a measurement would allow us to reconstruct the history of atmospheric ethane over long time scales and better constrain the modern day atmospheric budgets of ethane and methane. Ice core samples were analyzed using a dry (mechanical shredding) method and a wet extraction (melting) method. Results from the wet extraction method suggest that paleoatmospheric ethane is preserved in Antarctic ice. The samples analyzed here provide a first estimate of preindustrial atmospheric ethane levels over Antarctica.

4.2 Methods

The ice core sites, samples, and chronologies, and the dry and wet extraction methods are summarized here. The instrumentation and laboratory procedures used to analyze ethane in this project are described in more detail in Chapter 2.

4.2.1 Ice core site, samples, and chronology

We analyzed samples from a shallow ice core dry-drilled at the West Antarctic Ice Sheet (WAIS) Divide, Antarctica (WDC-05A). The WDC-05A core was drilled to 298 m using a 10

cm electromechanical drill during the 2005/2006 Antarctic field season. The WDC-05A site is about 1.3 km northwest of the main borehole of the deep WAIS-Divide ice core (WDC-06A), which is located near the flow divide at the center of West Antarctica (79.467°S, 112.085°W, 1759 m elevation) [*Mitchell et al.*, 2011]. WAIS-Divide has a modern annual accumulation rate of about 22 cm yr^{-1} (water equivalent), with a mean annual air temperature of −28.5°C [*Orsi et al.*, 2012]. Overall, quality of the WDC-05A ice cores was excellent. The use of dry-drilled ice cores in this study eliminates the possibility of complications with the ice core signal related to the use of drilling fluids, which are usually composed of saturated hydrocarbons and can become trapped in microfractures within the ice. In prior studies, such drilling fluids have been suggested to generate trace gas artifacts [*Haan et al.*, 1996].

WAIS-Divide ice core samples analyzed in this study were dated using the WDC05A:2 chronology [*Mitchell et al.*, 2011]. At the lock-in depth (approximately 66.5 m), the mean age of C_2H_6 in the open porosity is about 9.2 years, based on the ratio of diffusivities of CO_2 and C_2H_6 at WAIS-Divide (D_{C2H6}/D_{CO2} = 0.932, see Chapter 3, Table 3.2), and given a mean CO_2 age of 9.9 years [*Mitchell et al.*, 2011]. At the close-off depth, the age of the ice is 215 years, making the delta age (D_{age}) for C_2H_6 equal to 204.4 years (compared to 205.1 years for CO_2). A constant D_{age} was subtracted from the WDC05A:2 ice chronology with depth, assuming temperature and accumulation at the WDC05A site have remained relatively constant in the last 1000 years [*Mitchell et al.*, 2011]. The gas age of the deepest WDC05A ice cores is about 1000 AD. The estimated uncertainty of the chronology is ±10 years, based on a detailed comparison of methane records from the WDC05A and Law Dome, Antarctica (L. Mitchell, personal communication, 2014).

A small number of samples were also analyzed from a shallow ice core from South Pole

(SP04C5). The South Pole ice core was drilled during the 2004-2005 austral summer to 182 m depth using an electromechanical drill [*Ferris et al.*, 2011]. The ice core site is located 4.7 km west of the Amundsen-Scott South Pole Station (89°57.5'S, 17°40'W). The modern annual snow accumulation rate at South pole is roughly 20 cm y^{-1} (about 7.5 cm water equivalent) and the mean annual air temperature is about -51°C. The age-depth relationship for the SPO4C5 ice core is based on annual layer counting using the annual cycles in Mg^{2+} and Na^{+} concentrations. The ice age in the deepest samples from this core is 1828 years BP (before present=2004). At the lock-in depth (approximately 117 m, see Chapter 3), the mean age of C_2H_6 in the open porosity is about 100 years, based on the ratio of diffusivities of CO_2 and C_2H_6 at South Pole (D_{C2H6}/D_{CO2} = 0.938, see Chapter 3, Table 3.2), and given a mean CO_2 age 78 years (Chapter 3). At this depth, the age of the ice is 1096 years, making the delta age (D_{age}) for C_2H_6 equal to 1002 years (compared to 992 years for CO_2). A constant D_{age} was subtracted from the SPO4C5 ice chronology with depth, assuming temperature and accumulation rate. The gas age of the deepest SPO4C5 ice cores is about 1200 AD.

4.2.2 Dry extraction method

Seventy-four WDC-05A ice core samples were analyzed by dry extraction [*Aydin et al.*, 2007, 2008; *Saltzman et al.*, 2008]. The dry extraction technique involves mechanical shredding of an ice core sample at -50° C in a stainless steel (SS) vacuum chamber equipped with a custom-made cutter (i.e. cheese grater) design. Ice core samples weighed 400-500 g and were ~15 cm long. Two different stainless steel vacuum chamber designs were used for dry extraction. Series 1 chambers were fabricated from series 316 stainless steel with heliarc welding [*Aydin et al.*, 2007]. Series 2 chambers were fabricated from series 316L low carbon stainless steel with electron beam welding (2008, UCI Machine Shop and Electron Beam Engineering, Inc.,

Anaheim, CA). Details of the dry extraction procedure are given in Chapter 2.

Of the 74 samples analyzed from the WDC-05A core, 6 measurements were impacted by leaks and/or contamination (e.g. due to post-coring entrapment) [*Aydin et al.*, 2010]. Three of these samples were located close to the firn-ice transition, at 71.5, 74.7, and 76.82 m. Three additional samples showed evidence of contamination, indicated by CFC-12 measurements. The CFC-12 levels for the three samples at 92.325 m, 126.93 m, and 133.3 m was 9 ppt, 595 ppt, and 7 ppt, respectively. Two additional measurements were excluded at outliers at 139.4 m and 255.6 m). Ethane measurements from the remaining 66 ice core measurements samples are shown in Figure 4.1.

Dry extraction blanks involve isolating a small aliquot of clean, dry N_2 gas over the ice core sample before and after mechanical shredding, as used in prior studies [*Aydin et al.*, 2007]. The N_2 gas is isolated in the chamber for the same amount of time as the sample shred (23 min) and gas extraction (4 min). During the blank the chamber is kept stationary. The average of the two clean N_2 blanks is used to correct the total ethane measured in the sample.

4.2.3 Wet extraction method

Eighteen WAIS-Divide (WDC-05A) and four South Pole (SP 04-5) ice core samples were analyzed by wet extraction using the extraction setup described in Chapter 2. Wet extraction has previously been used for the extraction and analysis of low solubility gases such as methane, as well as noble gases, and O_2 [*Bender et al.*, 1997; *Brook et al.*, 2000; *Severinghaus and Grachev*, 2003; *Mitchell et al.*, 2011]. In this study ice core samples roughly 15-20 cm long and 200-400 g were analyzed. The outer ~5 mm of the ice core is removed with a scalpel at about -30° C to eliminate potentially contaminated surfaces. Samples were weighed to the nearest 1 g and placed in a pre-cooled 3” ID cylindrical, all-glass vacuum chamber pre-cooled to near -40° C using a

dry ice-ethanol bath. The chamber is sealed using a 1/16" OD indium wire o-ring.

The bottom of the glass extraction vessel is kept at -40° C while it is flushed with clean N_2 and evacuated several times to remove any modern air from the chamber. The vessel is then checked for leaks in the 1-mTorr range using a Pirani pressure gauge on the vacuum line. The sample is left pumping for a total of about 30 min before analysis. The background of the vacuum line is confirmed analytically with a clean-N_2 blank before the sample extraction. When the sample is ready to be extracted, the glass vacuum chamber is isolated from the pump using the glass shut-off valve on the top flange. The sample is allowed to melt by replacing the cold (-40°C, dry ice-ethanol) bath with lukewarm water (30-40°C). Before the sample is fully melted, the warm water is replaced by a cold (0°C) ice water bath to prevent warming of the ice core melt water inside the vessel during extraction. The valve on top of the vessel is then opened to start the extraction. As the gas leaves the vessel, it flows through a glass bead cold trap at -40° C (dry ice-ethanol mixture) to dry the gas stream. The cold trap consists of a 5/8" glass tube filled with 4 mm glass beads and is attached to the vacuum line using ½" PTFE Swagelok fittings. Downstream of the cold traps, the sample is collected for 2 minutes in a stainless steel cold finger immersed in liquid He (4K). The cold finger is then isolated and allowed to warm to room temperature. The cold finger is then attached to an automated gas preparation inlet, where the gas sample is prepared for injection into the GC/MS system [Chapter 2].

The melter analyses were conducted during summer 2011 (11 samples) and spring 2012 (7 samples). The 2011 samples were exposed to a Baratron gauge that was subsequently shown to increase blank levels. This was eliminated for the 2012 samples. Blank procedures also varied between the two periods, as described below. To quantify the ethane level in the ice core bubbles, the measured ethane signal must be corrected for the ethane system blank. Various

methods were used to quantify the ethane system blank on each sample associated with wet extractions, as described below.

Dry N_2 blank: A pre-sample dry N_2 blank was performed before the sample was melted for all eleven samples analyzed in 2011. In this procedure, a small amount of N_2 gas was isolated over the solid ice core sample at -40°C for about 25-30 minutes, similar to the amount of time it takes to melt the ice core sample. Dry N_2 blanks were not performed on samples analyzed in 2012.

"Exploding" N_2 blank: A pre-sample, "exploding" N_2 blank was performed before the sample was melted for two of the samples analyzed in 2011, and six of the samples analyzed in 2012. In this procedure, N_2 was isolated over the frozen ice core sample in the glass vessel. Next, the cold alcohol bath was replaced with a hot water bath (60° C) in order to break up the sample by thermal shock. As soon as a droplet of liquid water was observed in the chamber (about 5 min), the hot water bath was replaced with a cold (0° C) ice water bath and the N_2 gas was extracted from the chamber. The N_2 gas was isolated in the chamber for a total of 4-7 minutes, followed by a 2-minute extraction. The primary goal of this procedure was to break the sample into small pieces, thus increasing the ice surface area it would melt more rapidly during the sample extraction step. The average exploding N_2 blank for samples analyzed in this study was 0.086 ± 0.027 pmol C_2H_6 (mean±1σ).

N_2 melt blanks: For all samples, at least one N_2 blank was performed using the degassed ice core sample water, after the ice core ethane sample was extracted from the ice core bubbles. First, the ice core water was refrozen using a -40° C ethanol/dry ice bath. The sample was refrozen from the bottom, and with the vessel open to the pump in order to exclude gases upon refreeze. After the sample was fully frozen, the blank procedure was initiated by placing clean N_2 over the frozen ice. Next, the flask was isolated and the sample was melted using the same procedure as

the sample. The N_2 was left over the melted ice core water for the exact time it took to melt the sample (~20-30 min). Finally, the N_2 blank was extracted and analyzed using the same procedures as the sample. The average melt N_2 blank after the sample is roughly 0.124±0.026 pmol ethane (±1σ). The ethane measured in the N_2 melt blank is subtracted from the sample. It is assumed that the ethane signal in the N_2 melt blank reflects the ethane introduced due to melting of the sample.

Multiple N_2 blanks were conducted on nine out of eleven WAIS-Divide samples analyzed in 2011. After the first N_2 melt blank, the sample melt water was refrozen under vacuum at -40°C. When the sample was completely refrozen, N_2 was placed over the frozen ice in the headspace in the vessel. The ice core water sample was melted in a similar fashion to the first N_2 melt blank for the same amount of time it took to melt the sample. For three of the nine samples, a third N_2 melt blank was measured using the same procedure. These blanks can be used to check the reproducibility of the N_2 melt blank after the sample is extracted. The results from these blanks can also be used to determine if there is significant production of ethane associated with the number of times the sample is melted. For 2011 samples, there is no difference in the average N_2 blank based on 1st and 2nd melt N_2 blank, and a small decrease in the 3rd melt N_2 blank (Table A3).

4.2.4 Ethane mixing ratios and solubility correction for wet extraction analyses

In this study, ethane mixing ratios are reported in parts per trillion (ppt = pmol mol^{-1}). The ethane level in the ice core bubbles is calculated using the following equation:

$$Ethane\ (ppt) = \frac{m_{total\ ethane} - m_{blank\ ethane}}{m_{total\ air}} \quad (4.1)$$

where $m_{total\ ethane}$ and $m_{total\ air}$ are the total pmol of ethane and moles of air, respectively, present in the ice core bubbles, and $m_{blank\ ethane}$ is the pmol of ethane measured in the N_2 blank

taken after the sample is extracted. Ethane is more soluble than air (O_2 and N_2). Therefore, the measured mixing ratio of ethane in the headspace over the sample melt water is expected to be slightly lower than the original molar mixing ratio of the air in the bubbles trapped in the ice core sample. The corrections for the solubility of ethane and air in water were also quantified, as described below.

After the blank is subtracted from the sample, the remaining moles of ethane can be corrected for solubility in water, assuming that the gas in the vessel is in equilibrium with the melted ice core water at 0°C. A similar correction can also be applied to the air content of the sample, to correct for solubility of oxygen and nitrogen. Henry's law solubility constants for ethane, propane, butane, nitrogen and oxygen are given in Table 4.1 [*Wilhelm et al.*, 1977; *Sander*, 1999]. The solubility corrections for ethane and air in water at 0°C can be determined as follows:

$$m_{total} = m_g + m_l \tag{4.2}$$

$$\frac{m_l}{m_g} = \alpha \left(\frac{V_w}{V_a}\right) \tag{4.3}$$

where m_{total} is the sum of the moles of a compound present in the vessel headspace (m_g) and the moles of a compound dissolved in the water (m_l), and α is the Ostwald coefficient or dimensionless Henry's law constant at 0°C. Substituting equation (4.3) in equation (4.2):

$$m_{total} = m_g * \left(1 + \alpha \frac{V_l}{V_g}\right) \tag{4.4}$$

where m_{total} is proportional to the ratio of the volume of water present in the vessel (V_l) to the volume of air present in the vessel (V_g). In this calculation, we assume the solubility of ethane and air in solid ice is negligible compared to the solubility in water. In other words, we assume the initial ethane concentration in the melt water is zero (i.e. no ethane was dissolved in the ice initially, before the bubbles were released).

The solubility correction is a minor component of the overall uncertainty in a measurement. If the headspace and sample melt water are assumed to be in equilibrium, the correction factor for ethane using equations (4.1-4.4) is approximately 1.3%, based on V_w=280 mL of melt water in a 1485 cm^3 glass vessel at 0°C. However, during the extraction of the gas sample, the water in the vessel is actually exposed to vacuum when the valve on the cold finger is opened, rather than sitting at equilibrium. Therefore, more of the dissolved gases are actually released from the water than would be at equilibrium at 0°C. For this reason, we consider 1.3% the upper limit to the actual correction required on the ethane data. Ethane mixing ratios reported in this study are reported as blank corrected measurements only.

Table 4.1: Henry's Law constants for selected gases at 273.15 K [*Sander*, 1999]. The ethane solubility correction is determined using Henry's Law constants for C_2H_6 and the weighted average of O_2 and N_2 for air.

Compound	**$k°_H$ @ 293.15 K**	**d $ln(k_H)/d(1/T)$**	**$k_H(T)$* @ 273.15 K**
	M/atm	K	M/atm
Oxygen (O_2)	0.0013	1500	0.0019
Nitrogen (N_2)	0.00065	1300	0.0009
Methane (CH_4)	0.0014	1700	0.0021
Ethane (C_2H_6)	0.0018	2400	0.0033
Propane (C_3H_8)	0.0015	2700	0.0029
n-butane (C_4H_{10})	0.0012	3100	0.0026

***** The temperature dependent solution for the Henry's Law constant is:

$$k_H(T) = k°H * \exp([d(\ln(k_H))/d(1/T)] [(1/T) - 1/(298.15\ K)]$$

where $d(\ln(k_H))/d(1/T)$ is the temperature dependence parameter for Henry's Law constant, and k°H is the Henry's law constant for solubility of the compound in water at 298.15 K.

4.3 Results and Discussion

4.3.1 Dry extraction results

The average ethane level measured by dry extraction is 703.4±258.6 ppt (mean±1σ, n=66). Ethane levels show significant scatter, with the lowest measurements around 250-300 ppt (Figure 4.1). Ethane levels measured in duplicate samples from the same depths (at 84.8, 159.2, 222.3, and 266.6 m) show poor precision. Ethane levels measured in N_2 blanks taken before and after the sample is shredded are small, roughly 0.08 pmol ethane, or about 7% of the ethane signal measured in the ice core air bubbles.

Ethane levels are significantly correlated with propane and n-butane in the dry extraction results (Figure 4.3). The ethane:propane ratio is roughly 3:1 and the ethane:butane ratio is roughly 4.5:1. The extraction chamber construction appears to impact the hydrocarbon blanks measured for the WDC-05A ice cores. Ethane blanks were smaller for stainless steel chambers from can series 2. The average ethane blank measured in chambers from can series 1 is 0.08±0.03 pmol, while the average in can series 2 is 0.05±0.02 pmol (mean±1σ). The lowest ethane, propane and n-butane mixing ratios were measured in cans 1 and 5 relative to the other chambers (Figures 4.2 and 4.3).

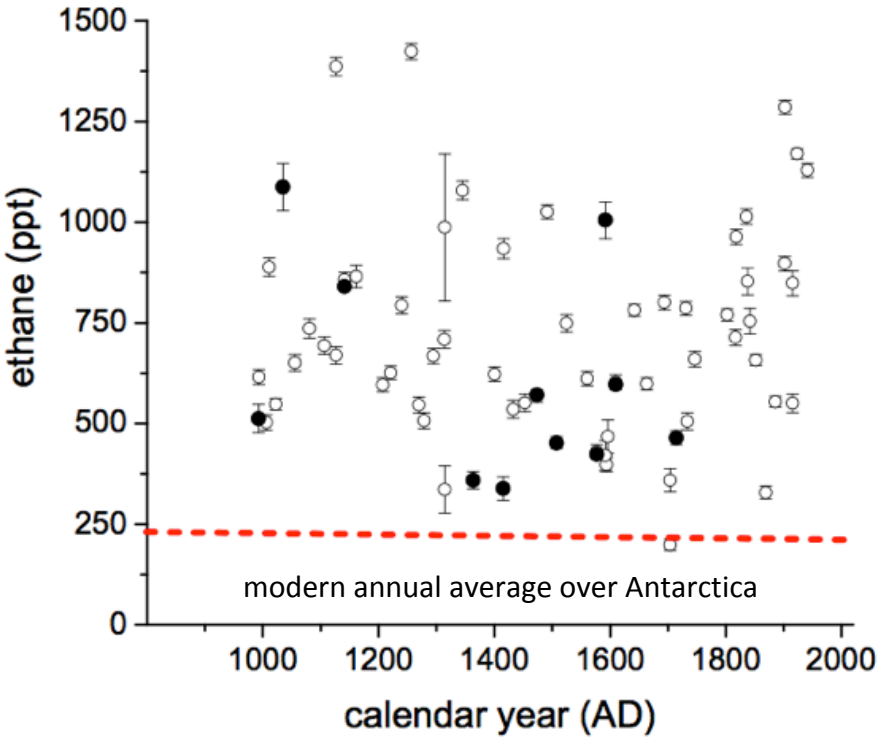

Figure 4.1: Dry-extraction ethane measurements from a shallow WAIS-Divide ice core. Samples have gas ages covering the last 1,000 years before present. Mean ethane level measured in the samples is 703.4±258.6 ppt (±1σ, n=66). Error bars are based on ±1σ of the measured ethane blank measured in can series 1 or can series 2. The dashed red line indicates the present-day, annually averaged atmospheric ethane level over Antarctica (230-250 ppt)

The present-day, annually averaged atmospheric ethane level over South Pole Antarctica in 2009 was 226 ppt, based on measurements from the NOAA/ESRL network. The average ethane level measured using dry extraction is roughly 3-fold higher, however, the lowest ethane measurements are similar to modern day levels (Figure 4.1). We expect ethane levels in the pre-industrial atmosphere to be significantly lower than at present because of much lower fossil fuel emissions (see Chapter 3). The low alkane blanks and poor precision of the measurements suggest the alkane production process is occurring during the analysis of the sample that is not captured in the pre- and post-shred blanks. The ice core propane, and n-butane levels measured by dry extraction are also elevated relative to the modern Antarctic atmosphere (Table 4.3). The

elevated alkane levels suggest they are produced either: 1) by sample handling, 2) extraction and analysis, or 3) *in situ* within the ice.

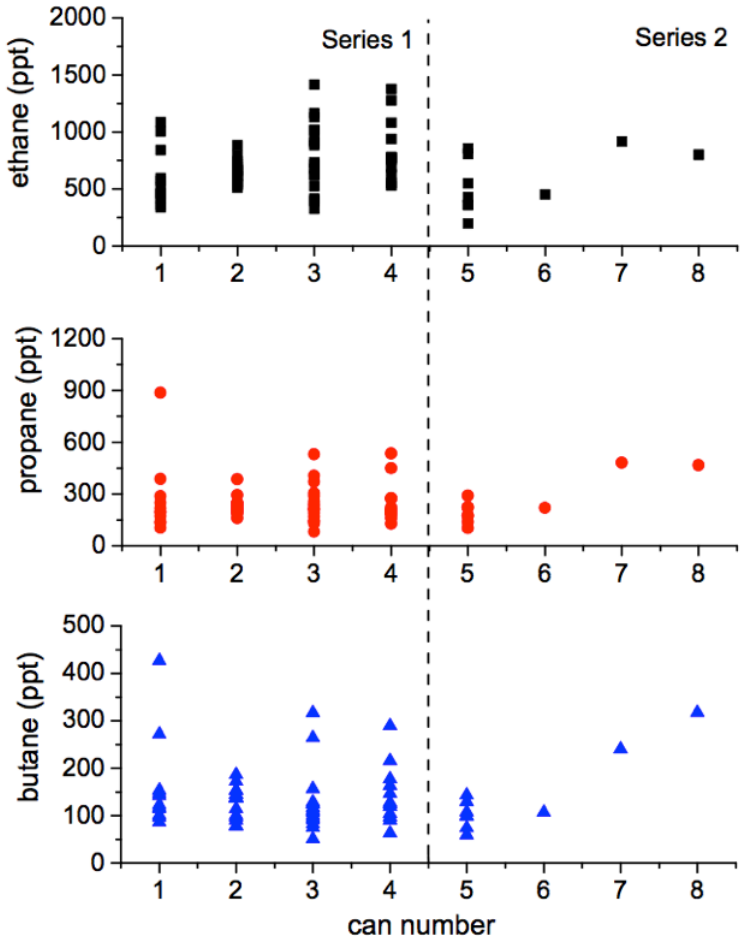

Figure 4.2: Ethane (a), propane (b), and n-butane (c) mixing ratios measured in WAIS-Divide ice core air using different stainless steel vacuum chambers. Dashed vertical line is used to distinguish between the two can series designed for the dry extraction procedure. Series 2 vacuum chambers (cans 5-8) were constructed using low-carbon steel, and clean electron-beam welds (Electron Beam Engineering, Inc., Anaheim, CA), in an effort to reduce can blanks for the light alkanes.

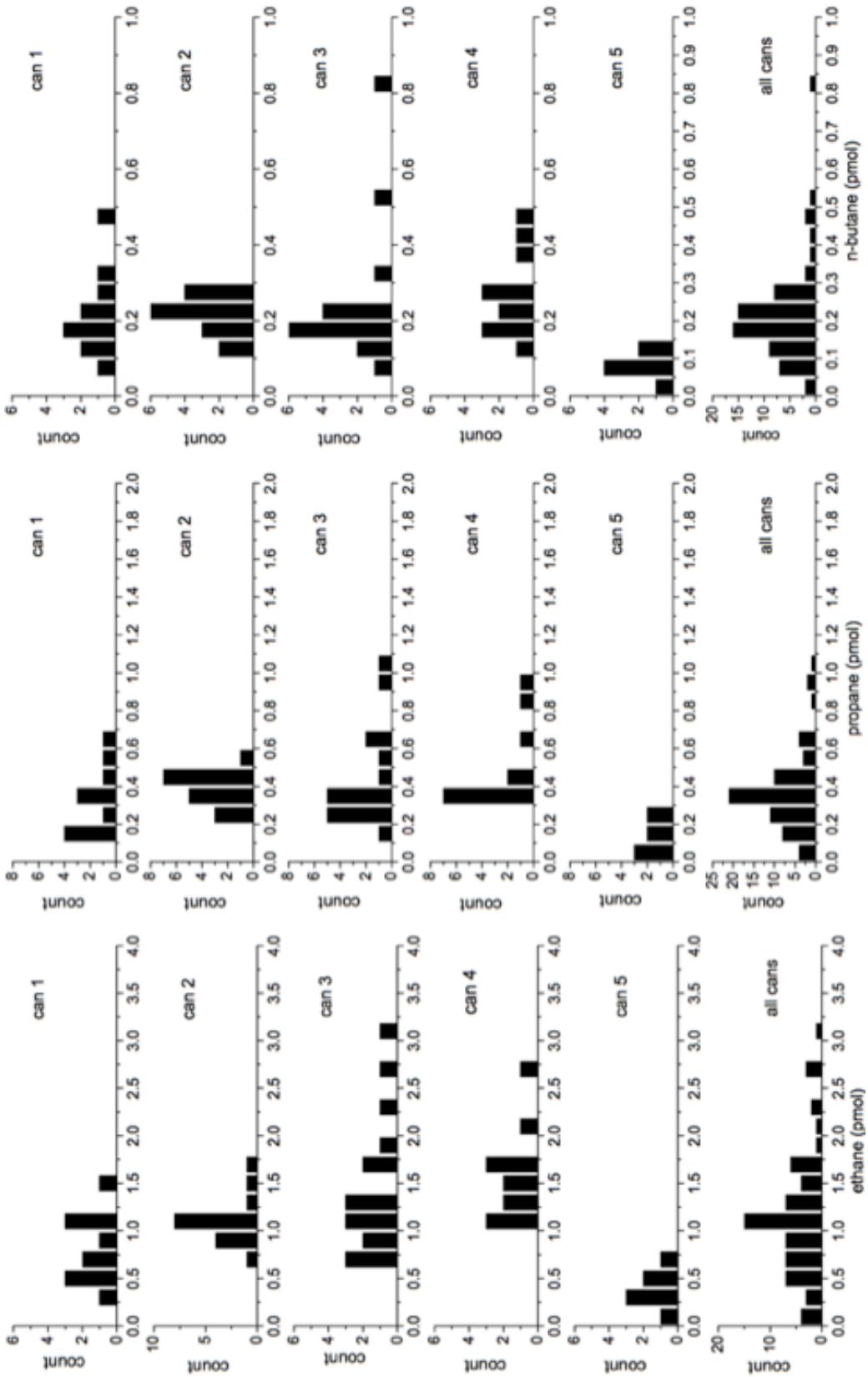

Figure 4.3: Histograms showing pmol of ethane (left) propane, (middle), and n-butane (right) measured in WAIS Divide ice core air using individual stainless steel vacuum chambers (cans 1-5). Bin sizes are 0.2, 0.1, and 0.05 pmol for ethane, propane, and n-butane, respectively.

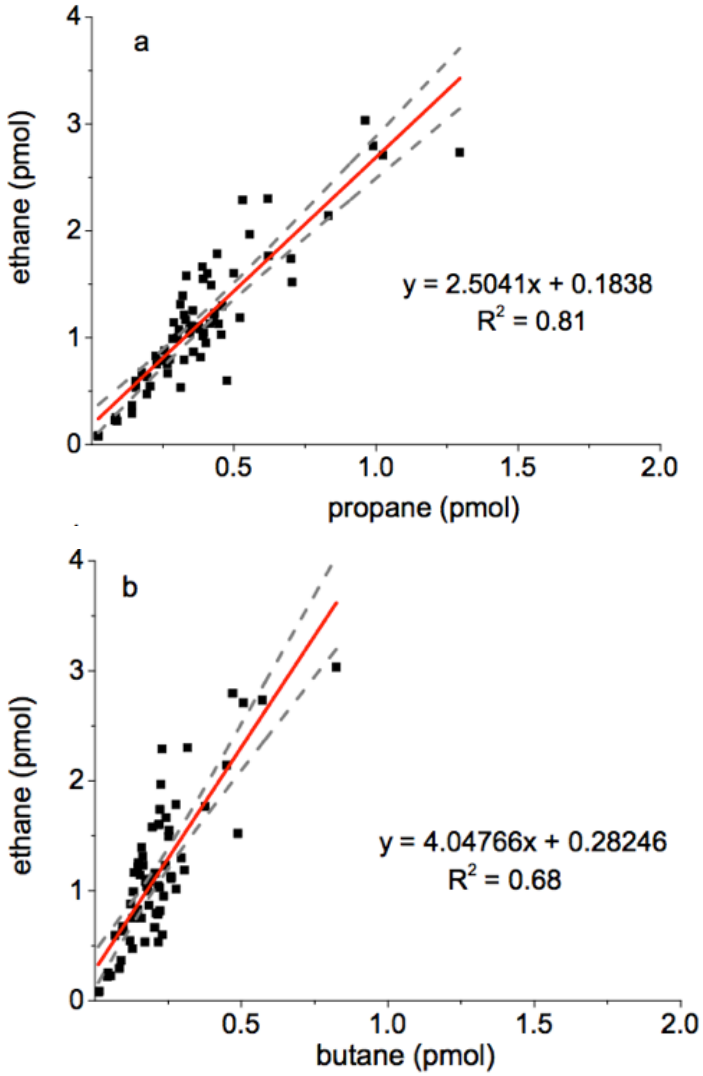

Figure 4.4: Dry-extraction results for ethane, propane and n-butane. a) Ethane plotted versus propane measured in WAIS-Divide ice core samples, after correcting for the average of the blank before and after the sample. b) Ethane plotted versus n-butane measured in WAIS-Divide ice core samples, after correcting for the average of the blank before and after the sample. Both panels – Least squares linear regression (red line) shown with 95% confidence interval (dashed grey lines).

4.3.2 Wet extraction results

Figure 4.5 shows the wet extraction results fro ethane in WAIS-Divide and South Pole ice cores. Ethane mixing ratios were quantified by subtracting the mean N_2 blank taken after the ice core gas sample was extracted. The blanks from 2011 and 2012 samples were treated separately. The average ethane level from the WAIS-Divide samples was 157.3±48.9 ppt (±1σ, n=11) and 118.9±43.3 ppt (±1σ, n=7) for samples analyzed in 2011 and 2012, respectively. More analyses

of duplicate samples are needed to validate the measurement reproducibility. Analysis of three WAIS-Divide samples from near 236 m depth suggest that the ethane measurement is reproducible, possibly to <5% of the measured ethane level (Table 4.2). Three measurements of ethane in South Pole ice cores analyzed in 2012 have a mean level of 140.5±31.2 ppt in samples with gas ages ranging from 1200-1600 AD. The ethane levels measured in both ice cores are lower than the modern day atmospheric ethane level over Antarctica (about 250 ppt). The South Pole ethane measurements roughly agree with the WAIS-Divide measurements in samples with overlapping gas ages (Figure 4.6).

Propane and n-butane mixing ratios were determined in the WAIS-Divide samples using the same methods that were applied for ethane. Propane and n-butane levels measured in the ice core samples ranged from roughly 50-130 ppt and 10-80 ppt, respectively (Figure 4.6). For propane and n-butane, the mean level measured in the ice core samples was nearly twice their modern day levels at the South Pole, which are roughly 40 and 20 ppt for propane and butane, respectively (Table 4.3).

There is some correlation between ethane:propane and ethane:butane in the samples and blanks for WAIS-Divide ice (Figure 4.8). The ratio for ethane:propane is roughly 2:1 in both samples and blanks. For ethane:butane, the ratio is 3.5:1 for samples and 2.7:1 for blanks (Table 4.3). The hydrocarbon ratios measured in ice core air are low compared to the modern atmosphere, suggesting that the propane and n-butane levels may not represent an atmospheric signal.

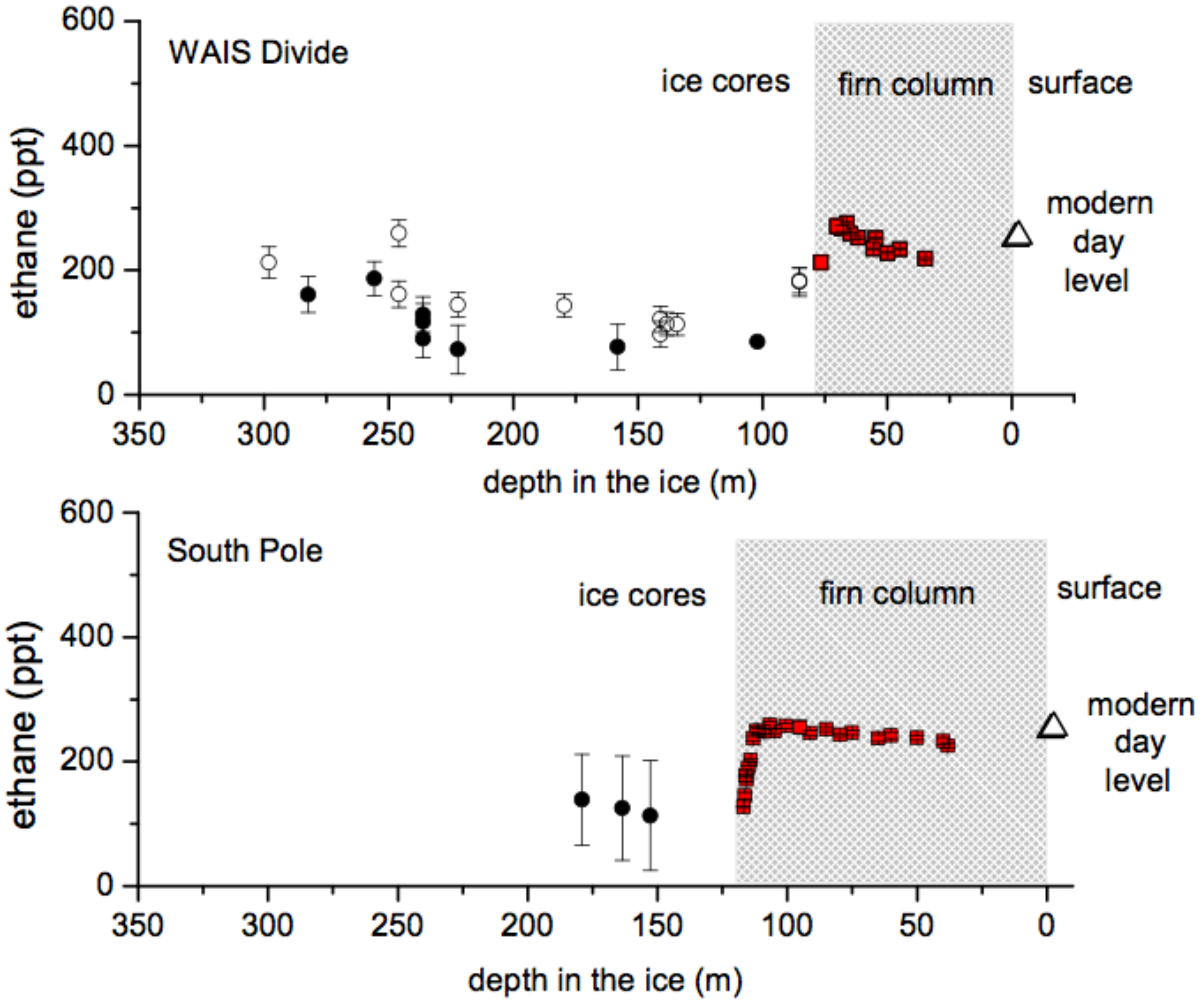

Figure 4.5: Depth profile of ethane levels measured in WAIS-Divide and South Pole firn air and ice core bubbles using a wet extraction technique. WAIS-Divide ice core measurements are shown for samples analyzed in 2011 (unfilled circles) and 2012 (filled circles). Three South Pole measurements at 152.8, 163.6 and 179.1 m depth have ethane levels of 113.2, 125.3, and 138.8 ppt, in agreement with the South Pole firn. WAIS-Divide firn air samples (red squares, top panel) were collected during the 2004/2005-field season and the South Pole firn air samples were collected during the 2008/2009-field season (red squares, bottom panel). Errors for the wet extraction measurements are calculated as ±1σ of the ethane blank for 2011 and 2012 samples. Errors are not shown for the firn air samples because the measurement uncertainty is smaller than the data marker. At present, the ethane level over Antarctica is roughly 250 ppt (triangle). Firn air measurements are discussed in detail in Chapter 3.

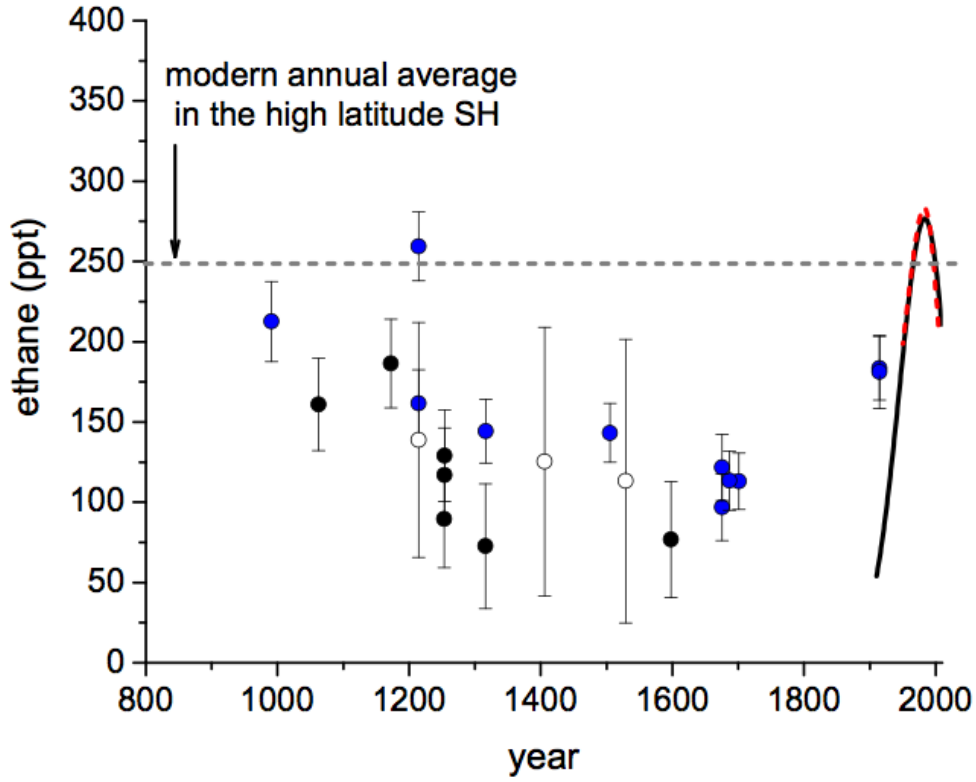

Figure 4.6: Ethane levels measured in ice core samples from WAIS-Divide (filled symbols) and South Pole (unfilled symbols) using a wet extraction technique. The dashed line indicates the modern atmospheric level of ethane over Antarctica in 2009, based on measurements from the NOAA/ESRL network (226.1 ppt). Error bars on the represent ±1σ of the wet extraction blanks for WAIS-Divide and South Pole. The variance in the WAIS-Divide blanks from 2011 and 2012 samples were estimated separately.

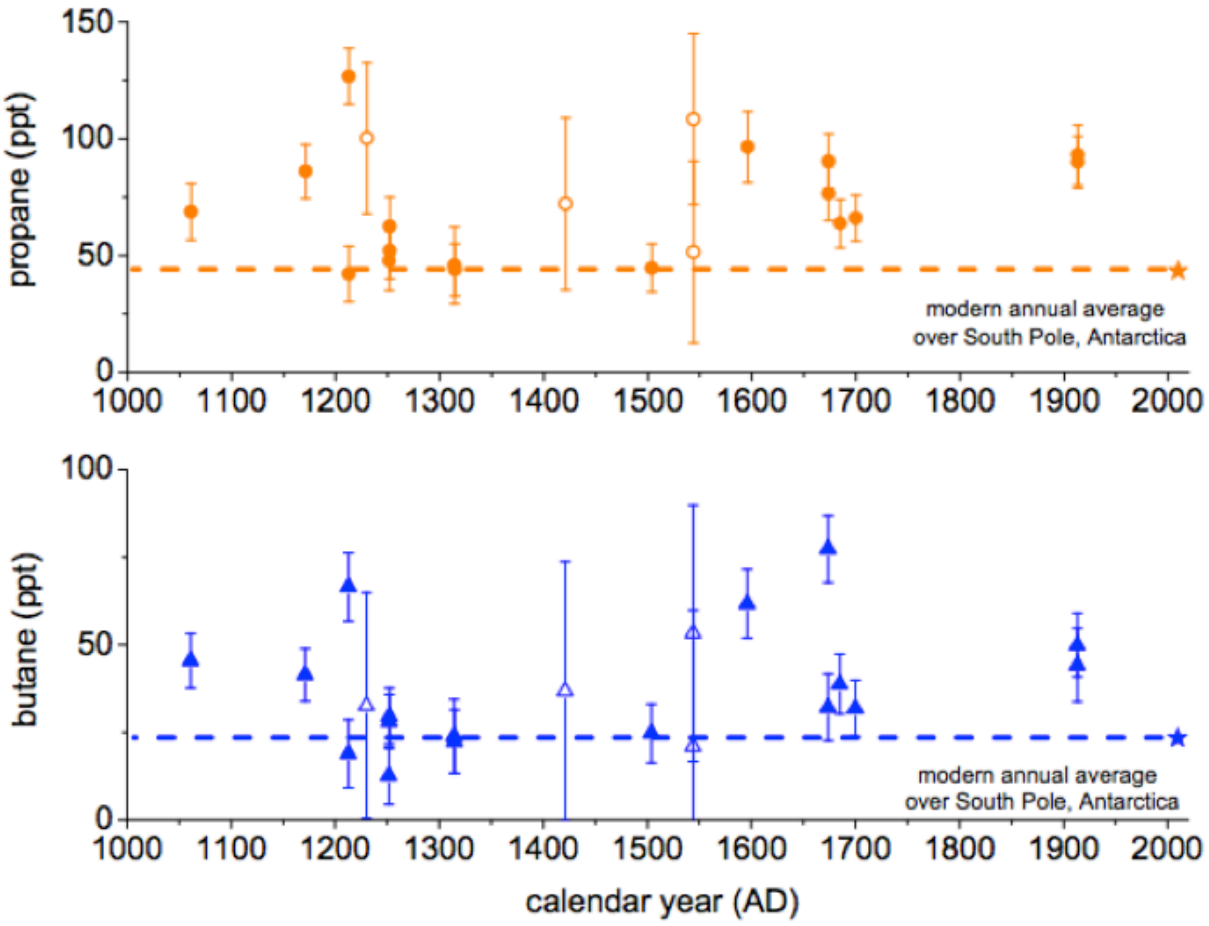

Figure 4.7: Propane and n-butane levels measured in ice core samples from WAIS-Divide (filled symbols) and South Pole (unfilled symbols) using a wet extraction technique. The dashed line in each panel indicates the modern atmospheric level of each gas over Antarctica in 2009, based on measurements from the NOAA/ESRL network (43.4 and 23.3 ppt for propane and n-butane respectively, Table 4.3). Error bars on the wet extraction samples represent ±1σ of the wet extraction blanks for WAIS-Divide and South Pole. The variance in the WAIS-Divide blanks from 2011 and 2012 samples were estimated separately.

Table 4.2: Wet extraction results for three samples measured near 236 m.

BD	Size	Time Exploding N_2 blank	Time Sample	Time N_2 melt blank	Ethane Exploding N_2 blank	Ethane Sample (uncorr)	Ethane N_2 melt blank	Ethane Sample (corrected for mean blank)
m	**g**	**min**	**min**	**min**	**pmol**	**pmol**	**pmol**	**ppt**
236.34	250.1	7	27	28	0.075469	0.223647	0.079123	129.3
236.16	257.3	--	32	32		0.277371	0.121734	130.6
236.16	252.9	4	29.5	29.5	0.072715	0.258823	0.117603	122.2

Table 4.3: Comparison of annually averaged ethane, propane, and n-butane mixing ratios (ppt) in surface flask samples from Antarctica and in WAIS-Divide ice cores (this study) and GISP ice cores [*Aydin et al.,* 2007]. Ethane:propane and ethane:butane ratios are rounded to the nearest whole number. GISP samples were analyzed by *Aydin et al.,* [2007].

	ethane	propane	n-butane	ethane: propane	ethane: n-butane
Surface air*	ppt	ppt	ppt		
Halley Station*	185	31	5	6 : 1	37 : 1
Neumayer*	380	84	50	5 : 1	8 : 1
Scott Base*	288				
South Pole 2004*	196	20	10	10 : 1	20 : 1
South Pole 2006*	205	29	9	7 : 1	23 : 1
South Pole 2009**	226.1	43.4	23.3		
Average	246.7 ± 75	41.5 ± 25	19.5 ± 18.4	7	19

Ice cores	ethane: propane	ethane: n-butane
Dry extraction (GISP2 D)	1:1 (0.28)	1.5:1 (0.23)
Dry extraction (GISP2 B)	4.5:1 (0.48)	--
Dry extraction (WAIS-D)	2.5:1 (0.81)	4:1 (0.67)
Wet extraction (sample)	1.8:1 (0.78)	3.5:1 (0.77)
Wet extraction (blank)	1.9:1 (0.6)	2.7:1 (0.46)

* Surface air data from Table 5 in *Beyersdorf et al.*, [2010].
** Surface flask measurements from NOAA/ESRL

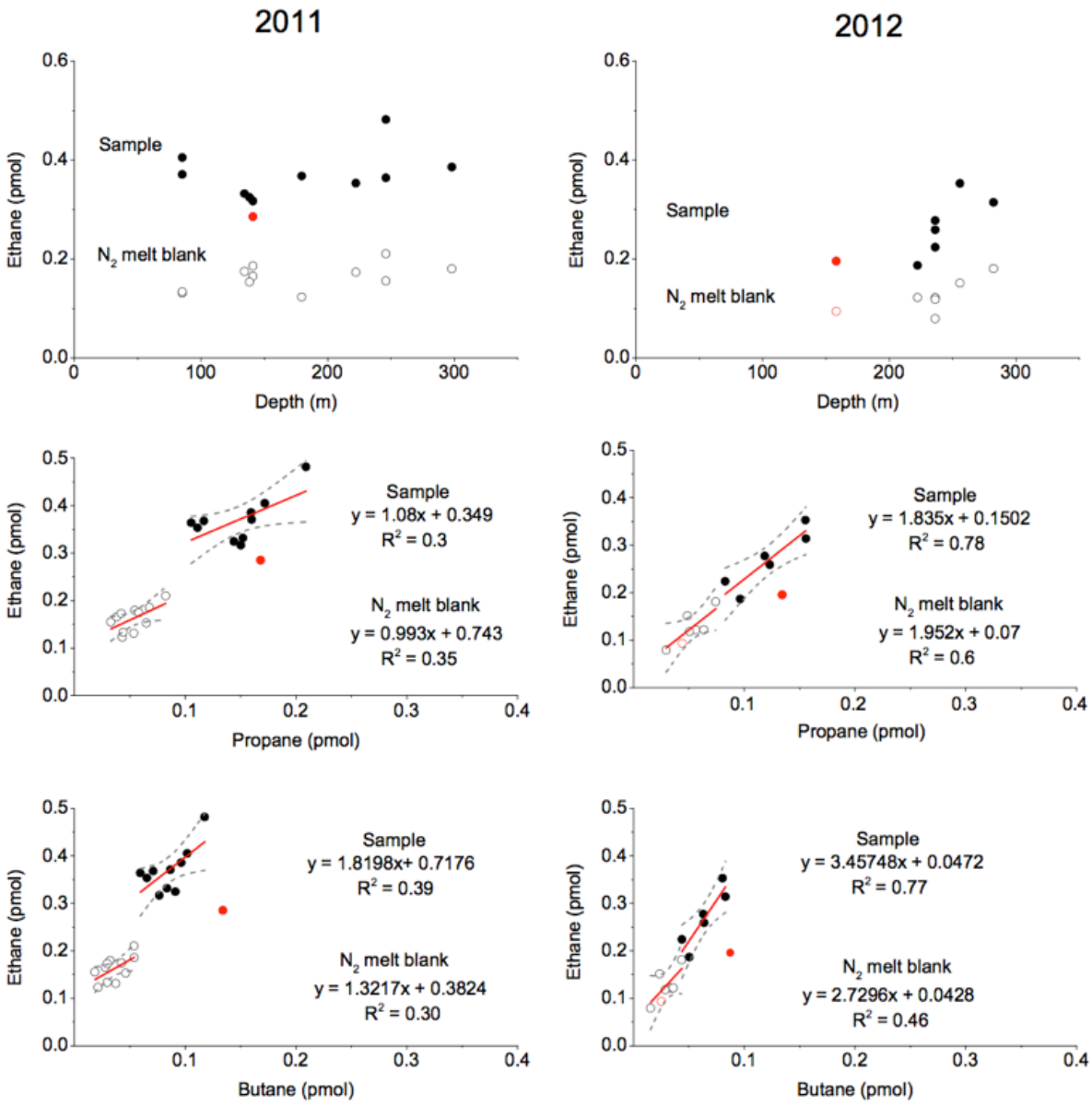

Figure 4.8: Ice core ethane data (in pmol) for samples analyzed using the wet extraction technique in 2011 (left) and 2012 (right). *Top panels* – Ethane signal (in moles) for WAIS-Divide uncorrected ice core samples (filled circles, labeled raw signal) and clean N_2 blanks (open circles). *Middle panels* – Correlation between ethane and propane in WAIS-Divide ice core samples and clean N_2 blanks. *Bottom panels* – Correlation between ethane and butane. Solid red and dashed grey lines represent linear least squares fit to the data and 95% CI. Red points indicate samples excluded from the regression analyses.

The largest uncertainty in the ethane ice core measurement is the blank, which is roughly 50% of the ethane ice core signal (Figure 4.8). The ice core blank is intended to account for any background ethane that introduced due to the sample processing and extraction. The blank can result from a variety of factors, including desorption of contaminants from the walls of the glass vacuum chamber, extraction line, or analytical system; leaks from the vacuum line fittings or the seal on the vacuum chamber; and degassing from the ½" PTFE fitting or valve tip seals. Alternatively, the ethane blank could result from *in situ* production of ethane in the ice core melt water.

Blank analysis on the sample pre-concentration line suggests that the majority of the analytical blank is on the extraction side. Multiple blanks on refrozen ice core water do not show a trend, suggesting that the blank does not result from the ice core water itself. Therefore, the large ethane blank most likely results from the walls of the glass vacuum line, and/or the vessel. There is no statistical difference between the average ethane mixing ratio measured in samples analyzed in 2011 and 2012 (Student's t-test, p= 0.0822, Figure A1). However, ethane blanks were slightly lower in 2012 samples (0.12±0.03 pmol ethane in 2012 compared to 0.16±0.02 pmol in 2011). The reduction in the blank was likely due to removal of a capacitance manometer (Baratron) and steel tubing on the vacuum line. For this reason, we have higher confidence in the results from 2012. This degree of confidence in the measured ethane level is reflected in the smaller measurement uncertainty in the 2012 samples.

There is no correlation between the blank-corrected ethane in the sample and the post-melt blank (Figure 4.8 and 4.9). These results suggest that there is little to no ethane production in the melt water, or the production is small compared to the size of the ethane signal in the system blank. Multiple N_2 blanks measured on samples in 2011 show no trend in the ethane blank based

on the number of times the sample is melted (Table A3). The "exploding" N_2 blanks from 2012 samples have a mean level of 0.09±0.03 pmol ethane (mean±2*s.e.), while the average melt N_2 blank after the sample is 0.12±0.03 pmol ethane (Table A3). The small difference between the pre- and post-melt blanks may arise due to desorption from the walls of the vacuum chamber, or may reflect the amount of time the N_2 gas and liquid water are isolated in the vessel (~5-10 min vs. 20-30 min). The average "uncorrected" ethane level measured in the sample was 0.26±0.05 pmol.

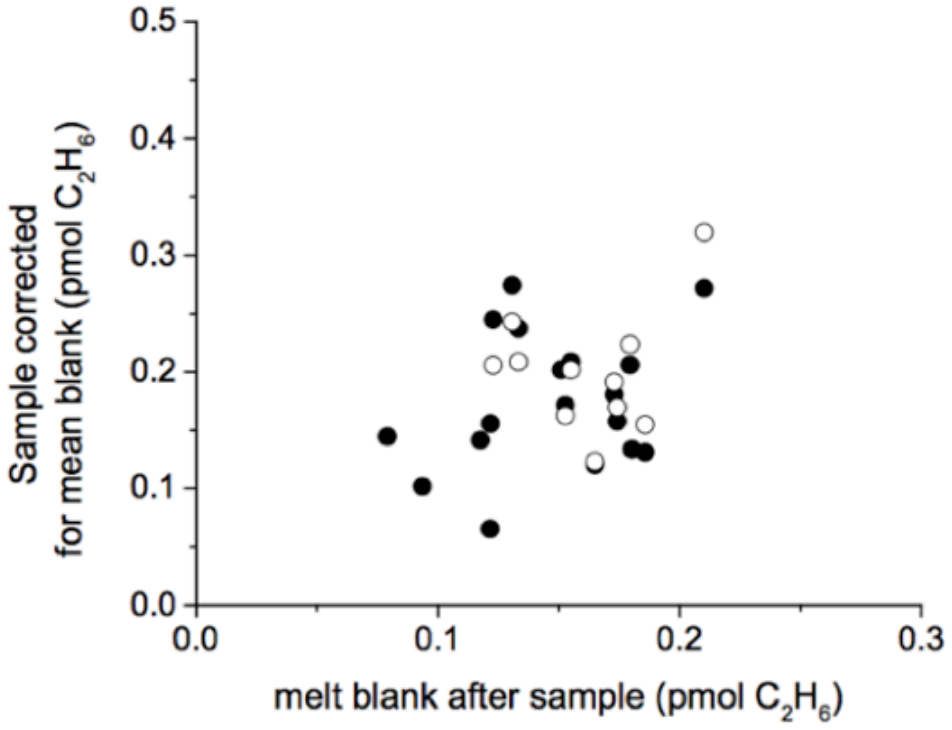

Figure 4.9: Ethane measurements from WAIS-Divide ice cores, after correcting for the mean blank measured after the sample. Ethane measurements are plotted versus the individual melt blanks from the same ice core sample. Data are shown for samples analyzed in 2011 (open circles) and 2012 (filled circles).

4.3.3 Comparison of the wet and dry extraction blanks

Surprisingly, the blanks from WAIS-Divide ice core samples are similar for samples analyzed dry and wet extraction. For dry extraction, N_2 blanks taken before and after the sample was shredded have a mean ethane level of 0.08±0.03 pmol and 0.09±0.03 pmol, respectively (mean±2*s.e.). For wet extraction, "exploding" N_2 blanks taken before the sample was melted had a mean level of 0.09±0.03 pmol ethane, while blanks taken after the sample was melted were slightly larger, with a mean level of 0.12±0.03 pmol ethane.

The reason for the similarity between the wet and dry extraction blanks is unknown. However, we find that the representativeness of the blank and the reproducibility of the wet extraction measurements are both improved in the samples analyzed by wet extraction (Table 4.2). The representativeness of the ice core blank is critical for the interpretation of ethane ice core gas records. For dry extraction, the N_2 blank is roughly 7% of the ethane signal measured in the sample (i.e. blank + ice core bubbles), while the wet extraction blank is roughly 50% of the sample. This suggests that the "*true*" ethane blank is not captured by the stationary N_2 blanks taken before and after the dry extraction shredding process.

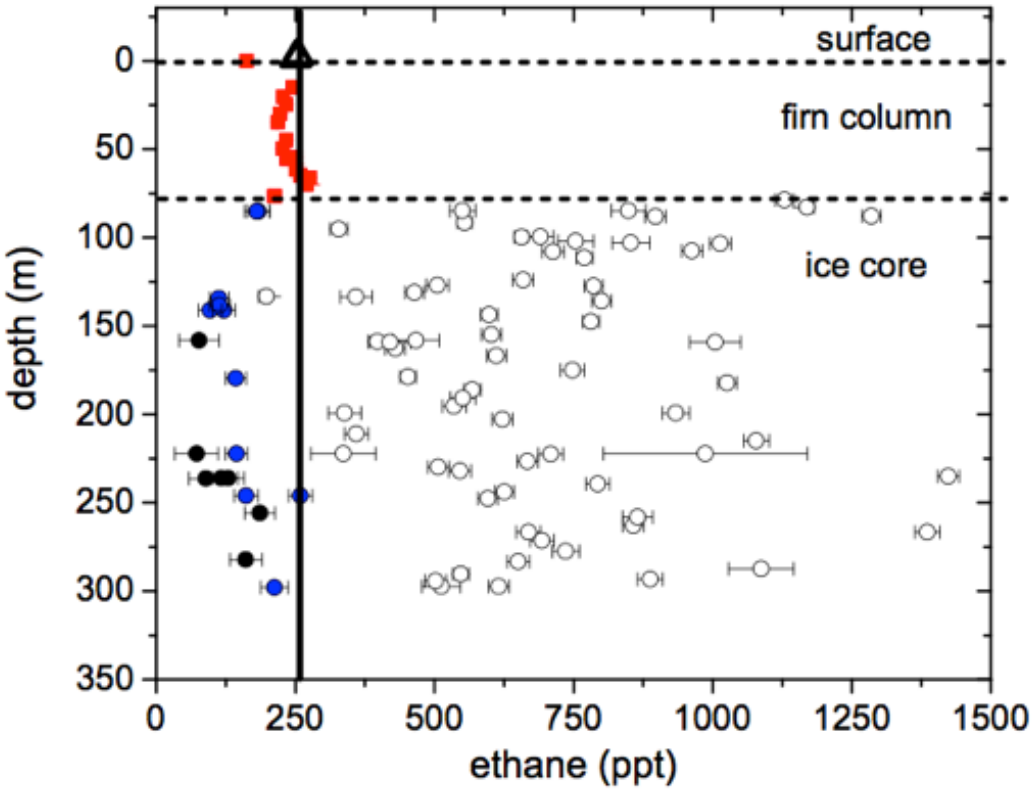

Figure 4.10**:** Ethane levels measured in WAIS-Divide firn air (Chapter 3) and ice core bubbles using the wet and dry extraction techniques (this study). Ethane dry extraction ice core measurements are shown as open circles (also shown in Figure 4.1). Ice core dry extraction errors bars are calculated using ±1σ of the ethane blank from can series 1 and can series 2. Ethane wet extraction measurements from 2011 (blue circles) and 2012 (black circles). Ice core errors bars are calculated as ±1σ of the ethane blank for wet extraction samples analyzed in 2011 and 2012. WAIS-Divide firn air samples (red squares) were collected during the 2004/2005 firn air sampling campaign (Chapter 3). Modern day ethane level over Antarctica is roughly 250 ppt (solid vertical black line). Error bars are only shown where the measurement uncertainty is larger than the data marker. Errors in the WAIS-Divide firn air measurements are estimated to be is ±11.7 ppt (±2*s.e of the measured level, not shown).

4.3.4 Comparison of the wet and dry extraction blanks

The wet-extraction ethane measurements are significantly lower than dry-extraction measurements from the same depth (Student's t-test, $p<0.0001$, Figure 4.10). Based on a comparison of nearby measurements, the dry extraction data are roughly 0.5-1 ppb elevated relative to the wet extraction data. The alkane ratios for WAIS-Divide samples are slightly lower for the wet extraction samples compared to dry extraction samples. For dry extraction the ethane:propane ratio was roughly 3:1 while the ethane:n-butane ratio was roughly 4:1. For wet

extraction samples the ethane:propane ratio was roughly 2:1 and the ethane:n-butane ratio was 3-3.5:1. The lower wet extraction ratios likely reflect the reduced ethane blank during extraction. The levels of propane and n-butane measured with both extraction methods clearly do not reflect atmospheric mixing ratios. The alkane ratios observed in both methods are lower than the ratios expected for the modern atmosphere (Table 4.3). In 2004 and 2006, the annually averaged ratios of ethane:propane and ethane:butane were roughly 7:1 and 22:1 [*Beyersdorf et al.*, 2010]. Prior Greenland ice core analyses were completed using the dry extraction procedure using stainless steel chambers from can series 1 [*Aydin et al.*, 2007]. The Greenland results also show some evidence of correlation between the alkanes, although the correlation coefficients are not as significant as those observed for the WAIS-Divide samples (Table 4.3).

Overall, the levels of ethane are significantly higher in the shred samples, suggesting significant ethane production due to the mechanical process of shredding the ice. The direct comparison of the wet and dry extraction data supports this hypothesis. Several studies have shown evidence for mechanically stimulated outgassing of metals in ultra-high vacuum systems due to friction, strain, or flexing of stainless steel surfaces in ultra high vacuum chambers [*Řepa and Rott*, 1997; *Higaki et al.*, 2006]. *Řepa and Rott*, [1997] show displacement of dissolved gases due to mechanical defomation, and that the release of gas was temperature dependent, but occurred only if the limit of elasticity was reached. *Higaki et al.*, [2006] show the release or production of methane that was not adsorbed on the surfaces (or dissolved in the bulk) due to the friction of ice on steel. These studies imply that such processes may have occurred in our stainless steel vacuum chambers, which resulted in the elevated ethane levels we observed in the dry extraction samples. The lower ethane levels measured during the wet extraction procedure suggest that ethane is not produced in situ in the ice, which supports this hypothesis.

The dry extraction measurements also show significant scatter. The cause of the scatter is unknown, but could be related to differences in the wear of the materials, related to the frictional force produced by two sliding bodies. The Blok-Archard and Archard wear equations provide a simple model to describe sliding wear, based on the points of frictional contact due to the material roughness (theory of asperity contact) [*Fischer*, 1988]. Therefore, we can assume that the wear of the stainless steel cutters (and thus the production of ethane), may be related to several factors, including 1) the hardness of the cutter material and/or density of the ice core sample, 2) the load (i.e. weight of the ice core sample), and/or 3) the degree to which the stainless steel cutters are flexed by the mechanical shredding process.

4.3.5 Comparison of firn air and ice core measurements

The shallowest wet extraction measurements from WAIS-Divide have ethane levels of 183 ppt and 181 ppt at 85.2 m. This is roughly 30 ppt lower than the deepest firn air measurement from WAIS-Divide, 212±11.7 ppt at 76.5 m (Figure 4.5). The wet extraction measurements are all lower than the modern day. In contrast, the dry extraction data are clearly elevated relative to the firn and the modern atmosphere (roughly 250 ppt ethane over Antarctica, Figure 4.10).

The WAIS-Divide firn air record constrains the atmospheric ethane level to roughly 200 ppt in 1950 AD (Figure 4.6). The mean ethane level measured by wet extraction is about 90 ppt lower (118.9.4 ± 43.3 ppt in air ranging in age from 1000-1600 AD, Figure 4.6). The consistency between the WAIS-Divide firn air an ice core measurements implies that an atmospheric ethane signal may be preserved in the ice. Unfortunately, there is no temporal overlap to directly compare the WAIS-Divide ice core and firn air records. The South Pole firn air record provides a better constraint on the atmospheric ethane level in the early twentieth century (see Chapter 3).

Three measurements of ethane in South Pole ice cores analyzed in 2012 have a mean level of 140.5±31.2 ppt in samples with gas ages ranging from 1200-1600 AD. This is similar to the ethane level measured in South Pole firn air samples (Figure 4.5). However, there is no direct overlap with which to compare the ethane firn air and ice core records from the South Pole. The South Pole firn air reconstructions suggest atmospheric ethane levels were roughly 50-100 ppt in 1920 AD (Figure 4.6). Shallow ice core measurements from WAIS-Divide have ethane levels roughly 100 ppt higher than these firn air reconstructions from the same time period (circa 1915 AD). The reason the ice core data do not show strong agreement with the firn air reconstructions is not known. The data suggest that the issue is not related to the ice core analytical procedure because 1) the WAIS-Divide and South Pole ice core results agree with one another within their respective uncertainties, and 2) the ethane levels measured in both ice cores are lower than present day, as suggested by the firn air results. Instead, this problem could result from issues with the dating of the firn air and ice core samples. More ethane measurements are required to investigate the preservation of atmospheric ethane in Antarctic ice, preferably in cores and firn air samples with overlapping gas ages.

Propane and n-butane levels measured in the wet extraction samples are also shown in Figure 4.7. The propane and n-butane data measured by wet extraction are preliminary and have not been corrected for solubility. In 2009 AD, atmospheric levels of propane and n-butane at South Pole, Antarctica were roughly 43 and 23 ppt, respectively. Most of the propane and n-butane levels measured in WAIS-Divide and South Pole ice core samples are elevated relative to their modern day levels over Antarctica (Figure 4.7). Dry extraction measurements of propane and n-butane are higher than wet extraction data. These data suggest that is not yet possible to reconstruct an atmospheric propane or n-butane signal from Antarctic ice cores using either

technique described in this study. Firn air measurements of propane and n-butane suggest the levels of these gases may be preserved in Greenland and Antarctic firn air [*Worton et al.*, 2012; *Helmig et al.*, 2014]. Unfortunately, there are no other published records propane and n-butane in Antarctic ice cores with which to compare these results. While possibility remains that atmospheric propane and n-butane levels are also preserved in the ice, the mixing ratios measured here do not appear to reflect atmospheric levels.

4.3.6 Hypothetical correction for the ethane dry extraction ice core measurements

In a prior study, ethane was analyzed in Greenland ice cores by dry extraction and suggested ethane levels were around 1.5 ppb from 1700-1900 AD, similar to the modern day ethane level at high northern latitudes [*Aydin et al.*, 2007]. The new WAIS-Divide results suggest these Greenland ice core measurements were also be affected by can blanks. In this section, we speculate about a method for correcting the Greenland ice core data based on the wet and dry extraction results from WAIS-Divide samples. The goal of this exercise is to determine whether a preindustrial ethane gradient can be estimated based on the available ice core data.

The ethane dry extraction measurements are clearly elevated relative to the wet extraction measurements (Figure 4.11). However, there are not enough overlapping measurements to compare individual wet/dry extraction samples. For this reason we use the difference in the mean ethane levels measured in WAIS-Divide samples to estimate the correction. The 4 highest ethane levels (>1 pmol measured in the WAIS-Divide samples were excluded from the correction because the WAIS-Divide results from Can 1 are not normally distributed (lower panel, Figure 4.11). Both the WAIS-Divide and Greenland ice core measurements employed the use of Cans 1 and 2, and both data sets clearly show can dependence of the ethane measurements (Figure 4.3 and Figure A2). For this reason, we only use can 1 results to correct the dry extraction

measurements. The WDC-05A ice core was dry-drilled, eliminating the potential for ethane production due to drilling fluid contamination. The n-butyl acetate drilling fluid used to drill the GISP2 D ice cores showed enhanced ethane levels relative to the dry-drilled GISP2 B ice cores [*Aydin et al.*, 2007]. For this reason, the ethane correction was only applied to dry-drilled Greenland (GISP2 B) ethane measurements.

The correction to the dry extraction data is applied as follows:

$$Ethane\ Corrected\ (ppt) = \frac{m_{dry} - \overline{m}_{(WAIS\ dry-WAIS\ wet)}}{m_{air}} \quad (4.5)$$

where $\overline{m}_{(dry-wet)}$ = 0.61-0.17= 0.49 pmol (Figure 4.11), m_{dry} is the ethane level measured in individual dry extraction samples, m_{air} is the moles of air measured in the dry extraction sample.

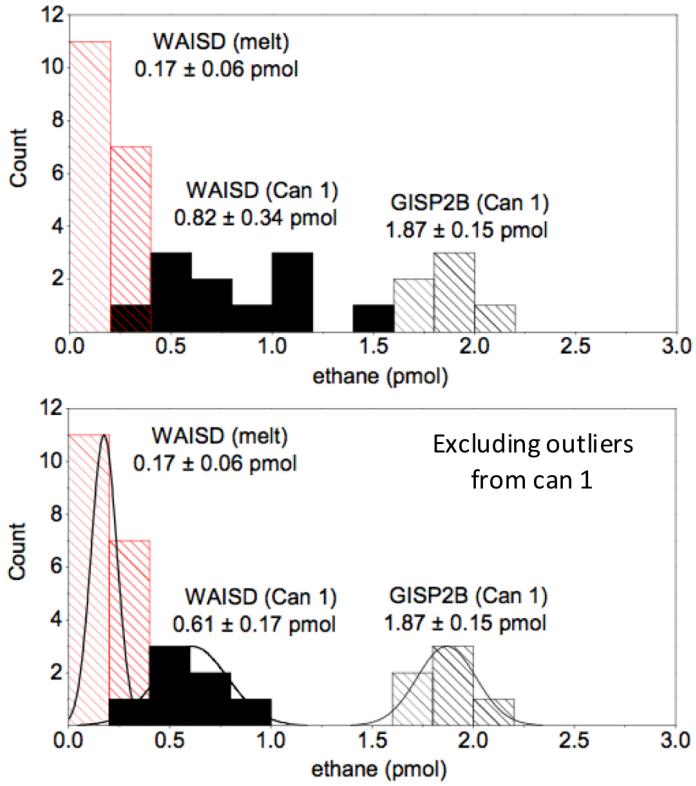

Figure 4.11: Histograms of ethane measurements (in pmol) from WAIS-Divide and Greenland ice cores. In both panels, WAIS-Divide (WDC-05A) ice core measurements are shown for wet extraction samples (hatched red bars) and dry extraction samples for can 1 (solid black bars). Greenland ice core measurements from the dry-drilled GISP 2B ice cores analyzed in can 1 are shown by the hatched black bars [*Aydin et al.*, 2007]. The lower panel shows the WAIS-Divide results from can 1 after excluding 4 outliers with ethane levels >1 pmol. The data in the lower panel were used to correct the ethane dry extraction results (see Figure 4.12).

Figure 4.12 shows the "corrected" Antarctic ice core results based on the comparison of the two extraction methods. After correction, the dry extraction measurements from can 1 have ethane levels in the same range as the wet extraction measurements from WAIS-Divide (Figure 4.12). The agreement between the "corrected" dry extraction data and wet extraction measurements is surprising, especially considering the large errors assumed in the correction. Some of the corrected WAIS-D data are below 0 ppt. Although those corrected data points clearly cannot represent an atmospheric level, the errors bars are large and agree within the uncertainties of the wet extraction measurements. Though speculative, the agreement shown by the corrected Antarctic data shows that it may be useful to apply a similar correction to ethane data from Greenland ice cores.

Aydin et al., [2007] analyzed ethane levels in samples from the dry-drilled Greenland GISP2 B ice core. The correction described in equation (4.5) was applied to the seven GISP2 B samples that were analyzed in can 1 (the same vacuum chamber used in this study). The gas ages for these GISP2 B samples were calculated using a mean ethane gas age of 8 years, a close-off depth of 72 m, and the GISP2 D ice age-depth scale based on annual layer counting [*Aydin et al*., 2007; *Meese et al.,* 1994; *Schwander et al., 1997*]. The ice age scale for the GISP2 B core was calculated by applying a +5 year offset to the ice ages of the GISP2 D core at the same depth, based on a comparison of various major ions in the two cores [*Aydin et al.,* 2007].

The corrected GISP2 B samples have ethane levels ranging from roughly 0.7-0.95 ppb, for samples with gas ages between 1700-1900 AD (triangles, Figure 4.12). This is 30-50% lower than the ethane level in the high latitude Northern Hemisphere today. If true, the correction to the Greenland data suggests that ethane levels in the Northern Hemisphere nearly doubled since the pre-industrial period. This result needs to be validated with wet extraction measurements on

Greenland ice cores, but could have important implications for the global pre-industrial ethane budget.

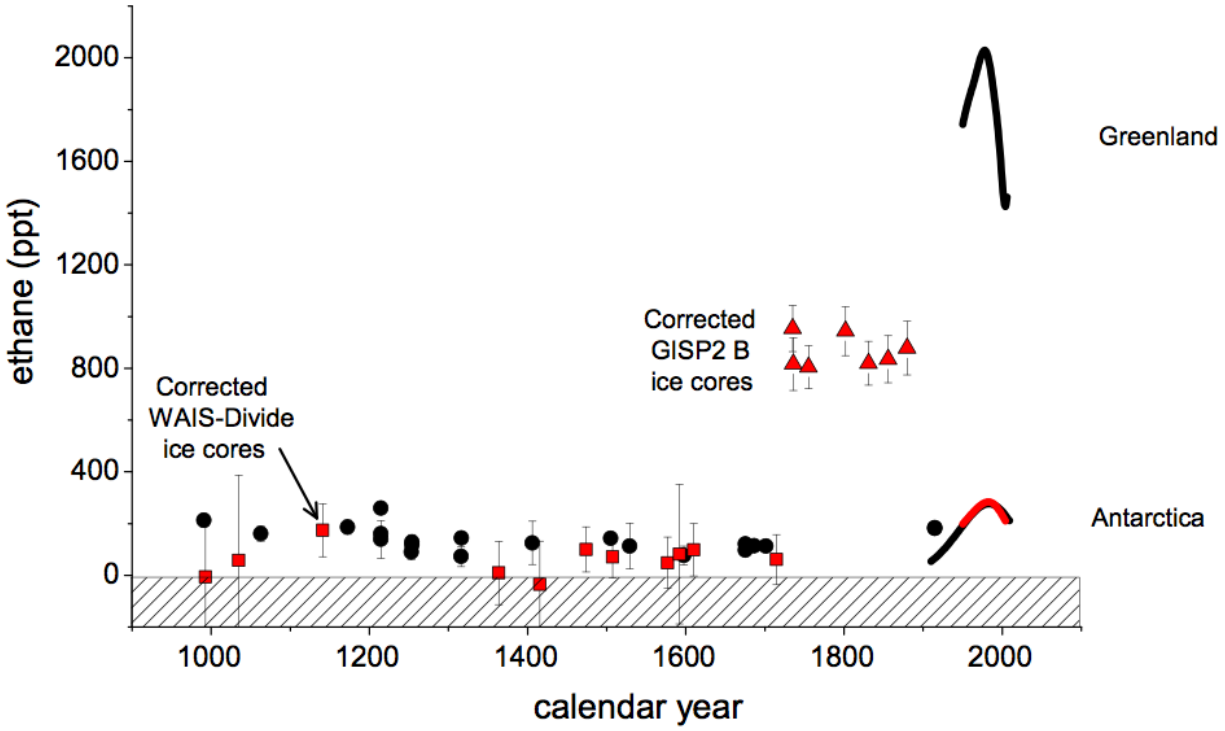

Figure 4.12: Ethane measurements from Greenland ice cores [Aydin et al., 2007], Antarctic ice cores (this study), and firn air (Chapter 3). The upper portion of the figure shows ethane results from Greenland firn air and ice cores, while the lower portion of the figure shows the results for Antarctica. The atmospheric ethane reconstruction from Summit, Greenland is shown from 1950-2006 AD (black line) along with the "corrected" Greenland ice core measurements from the dry-drilled GISP2B ice cores covering the period 1700-1900 AD (red triangles) [*Aydin et al.*, 2007]. Ice core measurements from WAIS-Divide, Antarctica are shown from the wet extraction technique (black circles) and corrected dry-extraction measurements from can 1 only (red squares). Errors for the "corrected" dry extraction measurements were determined based on propagation of errors ($\pm\sqrt{{\sigma_1}^2 + {\sigma_2}^2 + {\sigma_3}^2}$, where σ_1 is the error in the ethane dry extraction that is being corrected, σ_2 is the variance in the ethane levels measured by wet extraction, and σ_3 is the variance in the ethane levels measured by wet extraction. Atmospheric ethane reconstructions from Antarctic firn air are also shown. The South Pole firn air reconstruction shows ethane levels from 1910-2008 AD (black line), while the WAIS-Divide firn air reconstruction shows ethane levels from 1950-2005 AD (red line). Wet extraction results were quantified by subtracting the N_2 blank taken after the ice core gas sample was extracted. Error bars on the wet extraction samples represent $\pm 1\sigma$ of the ethane blanks. Ethane blanks from 2011 and 2012 were treated separately. The Greenland and Antarctic firn air results discussed in detail in Chapter 3.

4.4. Conclusions

- A new glass vacuum line and wet extraction chamber were designed and used to measure ethane levels in Antarctic ice core samples. Based on comparison of dry and wet extraction methods, it is highly likely ethane, propane, and n-butane levels measured in Antarctic ice cores by dry extraction are impacted by production related to the mechanical shredding procedure. The dry extraction pre- and post- shred blanks do not appear to capture this production.
- The average ethane level measured in the WAIS-Divide wet extraction samples is about 140 ± 50 ppt. This is roughly 40-50% lower than the modern day level over Antarctica (250 ppt = parts per trillion). South Pole and WAIS-Divide ice core wet extraction measurements agree within their uncertainties, in ice core samples with gas ages ranging from 1000-1900 AD. Direct comparison of firn air and ice core depth profiles for the wet extraction data suggest it may be possible to reconstruct paleo atmospheric ethane levels from Antarctic ice core air bubbles.
- The Antarctic ice core data suggest that the analytical artifact from the dry extraction procedure impacted prior measurements of ethane in Greenland ice cores [*Aydin et al.*, 2007]. Ethane levels measured in Greenland (GISP2 B) dry extraction measurements from can 1 were corrected to 0.75-1 ppb between 1700-1900 AD. This is 30-50% lower than the ethane level in the high latitude Northern Hemisphere today.
- A challenge remains in reducing the magnitude and variability of the ethane blank in Antarctic ice cores, which is roughly 50% of the ethane signal in the ancient air sample. Blank analysis on the sample pre-concentration line suggests that the majority of the analytical blank is on the extraction side. Multiple blanks on refrozen ice core water do

not show a trend, suggesting that the blank does not result from the ice core water itself. Therefore, the large ethane blank most likely results from the walls of the glass vacuum line, and/or the vessel.

- The shallow ice core measurements from WAIS-Divide and South Pole agree well with the firn air depth profiles from Chapter 3. However, the time histories of ethane based on firn air and ice core measurements show some disagreement between the youngest ice core measurements in WAIS-Divide ice, and the oldest part of the atmospheric reconstruction from the South Pole firn air samples. This suggests there may be problems with the dating of the firn air and/or ice core records. More analyses of ethane in shallow ice cores with gas ages circa 1850-1900 AD are needed to validate the firn air and ice core reconstructions.
- Ethane levels measured in dry and wet extraction samples are correlated with propane and n-butane levels measured in the same samples. Potential mechanisms involving hydrocarbon production in ice are not well understood, in part due to our limited knowledge of the chemistry of the individual ice core samples. Comparisons of the data to trace chemical measurements in the ice may provide further insight into the cause of the elevated propane and n-butane levels observed in the Antarctic cores.

References

Aydin, M., M. B. Williams, and E. S. Saltzman (2007), Feasibility of reconstructing paleoatmospheric records of selected alkanes, methyl halides, and sulfur gases from Greenland ice cores, *J. Geophys. Res.*, *112*(D7), 1–9, doi:10.1029/2006JD008027.

Aydin, M., M. B. Williams, C. Tatum, and E. S. Saltzman (2008), Carbonyl sulfide in air extracted from a South Pole ice core: a 2000 year record, *Atmos. Chem. Phys.*, *8*(24), 7533–7542, doi:10.5194/acp-8-7533-2008.

Aydin, M. et al. (2010), Post-coring entrapment of modern air in some shallow ice cores collected near the firn-ice transition: evidence from CFC-12 measurements in Antarctic firn air and ice cores, *Atmos. Chem. Phys.*, *10*(11), 5135–5144, doi:10.5194/acp-10-5135-2010.

Bender, M., T. Sowers, and E. Brook (1997), Gases in ice cores, *Proc. Natl. Acad. Sci. U. S. A.*, *94*(16), 8343–9.

Beyersdorf, A. J., D. R. Blake, A. Swanson, S. Meinardi, F. S. Rowland, and D. Davis (2010), Abundances and variability of tropospheric volatile organic compounds at the South Pole and other Antarctic locations, *Atmos. Environ.*, *44*(36), 4565–4574, doi:10.1016/j.atmosenv.2010.08.025.

Brook, E. J., S. Harder, J. Severinghaus, E. J. Steig, and C. M. Sucher (2000), On the origin and timing of rapid changes in atmospheric methane during the last glacial period, *Glob. Biogeochem Cyc.*, *14*(2), 559–572.

Ferris, D. G., J. Cole-Dai, A. R. Reyes, and D. M. Budner (2011), South Pole ice core record of explosive volcanic eruptions in the first and second millennia A.D. and evidence of a large eruption in the tropics around 535 A.D., *J. Geophys. Res.*, *116*(D17), D17308, doi:10.1029/2011JD015916.

Fischer, T. E. (1988), Tribochemistry, *Ann. Rev. Mater. Sci*, *18*, 303–323.

Haan, D., P. Martinerie, and D. Raynaud (1996), Ice core data of atmospheric carbon monoxide over Antarctica and Greenland during the last 200 years CO levels observed in Antarctic ice exhibit no significant of methane hydrocarbons, *Geophys. Res. Lett.*, *23*(17), 2235–2238.

Helmig, D., V. Petrenko, P. Martinerie, E. Witrant, T. Röckmann, A. Zuiderweg, R. Holzinger, J. Hueber, C. Thompson, J. W. C. White, W. Sturges, A. Baker, T. Blunier, D. Etheridge, M. Rubino, and P. Tans (2014), Reconstruction of Northern Hemisphere 1950–2010 atmospheric non-methane hydrocarbons, *Atmos. Chem. Phys.*, *14*(3), 1463–1483, doi:10.5194/acp-14-1463-2014.

Higaki, S., Y. Oya, and Y. Makide (2006), Emission of Methane from Stainless Steel Surface Investigated by Using Tritium as a Radioactive Tracer, *Chem. Lett.*, *35*(3), 292–293, doi:10.1246/cl.2006.292.

Meese, D. A., A. J. Gow, P. Grootes, P. A. Mayewski, M. Ram, M. Stuiver, K. C. Taylor, E. D. Waddington, and G. A. Zielinski (1994), The accumulation record from the GISP2 core as an indicator of climate change through the Holocene, Science, 266(5191), 1680–1682.

Mitchell, L. E., E. J. Brook, T. Sowers, J. R. McConnell, and K. Taylor (2011), Multidecadal variability of atmospheric methane, 1000–1800 C.E., *J. Geophys. Res.*, *116*(G2), G02007, doi:10.1029/2010JG001441.

Orsi, A. J., B. D. Cornuelle, and J. P. Severinghaus (2012), Little Ice Age cold interval in West Antarctica: Evidence from borehole temperature at the West Antarctic Ice Sheet (WAIS) Divide, *Geophys. Res. Lett.*, *39*(9), n/a–n/a, doi:10.1029/2012GL051260.

Řepa, P., and M. Rott (1997), Outgassing of metals stimulated by friction, *Vacuum*, *48*(7-9), 775–778.

Saltzman, E. S., M. Aydin, C. Tatum, and M. B. Williams (2008), 2,000-year record of atmospheric methyl bromide from a South Pole ice core, *J. Geophys. Res.*, *113*(D5), D05304, doi:10.1029/2007JD008919.

Sander, R. (1999), *Compilation of Henry's law constants for inorganic and organic species of potential importance in environmental chemistry*, Germany.

Severinghaus, J., and A. Grachev (2003), A method for precise measurement of argon 40/36 and krypton/argon ratios in trapped air in polar ice with applications to past firn thickness and abrupt climate change in Greenland and at Siple Dome, Antarctica, *Geochim. Cosmochim. Acta*, *67*(3), 325–343.

Schwander, J., T. Sowers, J.-M. Barnola, T. Blunier, A. Fuchs, and B. Malaize (1997), Age scale of the air in the summit ice: Implication for glacial-interglacial temperature change, *J. Geophys. Res.*, 102(D16), 19483 – 19493.

Verhulst, K. R., M. Aydin, and E. S. Saltzman (2013), Methyl chloride variability in the Taylor Dome ice core during the Holocene, *J. Geophys. Res. Atmos.*, *118*(21), 12,218–12,228, doi:10.1002/2013JD020197.

Wilhelm, E., R. Battino, and R. Wilcock (1977), Low-Pressure Solubility of Gases in Liquid Water, *Chem. Rev.*, *77*(2), 219–262.

Worton, D. et al. (2012), Evidence from firn air for recent decreases in non-methane hydrocarbons and a 20th century increase in nitrogen oxides in the northern hemisphere, *Atmos. Environ.*, *54*, 592–602, doi:10.1016/j.atmosenv.2012.02.084.

CHAPTER 5

A southern hemisphere atmospheric history of carbon monoxide during the 20th century

5.1. Introduction

This study presents a twentieth century atmospheric history of carbon monoxide in the Southern Hemisphere using firn air samples collected from South Pole, Antarctica during the 2008/2009 field season. A one-dimensional firn air diffusion model is used to constrain atmospheric CO levels in the high latitude Southern Hemisphere during the 20th century. The implications of the South Pole CO ice core record are discussed.

5.2. Methods

5.2.1 Firn air data and sample quality control

Forty-five flasks were used for CO analysis. Thirty-six of these samples were from *"dry"* NOAA/CCG flasks that were filled with the sample flow directed through an $MgClO_4$ drier and pressurized to 6 psi. The $MgClO_4$ drier was bypassed while filling the remaining nine flasks (UCI flasks), which were pressurized to >10 psi. There was no observable difference between the "wet" UCI flasks and the "dry" NOAA/CCGG flasks, which were filled through the $MgClO_4$ drier. CO analysis in the South Pole 08/09 flasks was completed using a fast-response vacuum ultraviolet resonance fluorescence technique (VURF, instruments from Aero-Laser GmbH,

Garmisch-Partenkirchen, Germany) [*Gerbig et al.*, 1999]. The CO mole fractions reported here are tied to the WMO 2004 scale. The analytical precision of the measurements is roughly 1 ppb.

The sample quality control criteria involved checking flasks for contamination using measurements of other trace gases in the firn air flasks. For example, gases such as CO_2 and CH_4 have well-known atmospheric histories and so can be used to check for sample contamination and vacuum leaks. Ten South Pole flasks had higher than expected CO_2 concentrations compared to the well-known CO_2 firn depth profile at South Pole [*Battle et al.*, 1996], indicating an equipment leak and/or flask contamination during sampling. Three flasks filled from the deep firn (116.9 m) showed elevated COS and CS_2 levels, suggesting contamination due to leaks or outgassing of and/or outgassing of rubber components of the firn bladder or seals when vacuum was pulled on the hole. The average difference in CO levels measured in the remaining replicate flasks from various depths is 0.5 ppb (n=8 flask pairs). The CO firn depth profile from South Pole is shown in Figure 5.1. Contaminated samples are indicated by open squares in Figure A3.

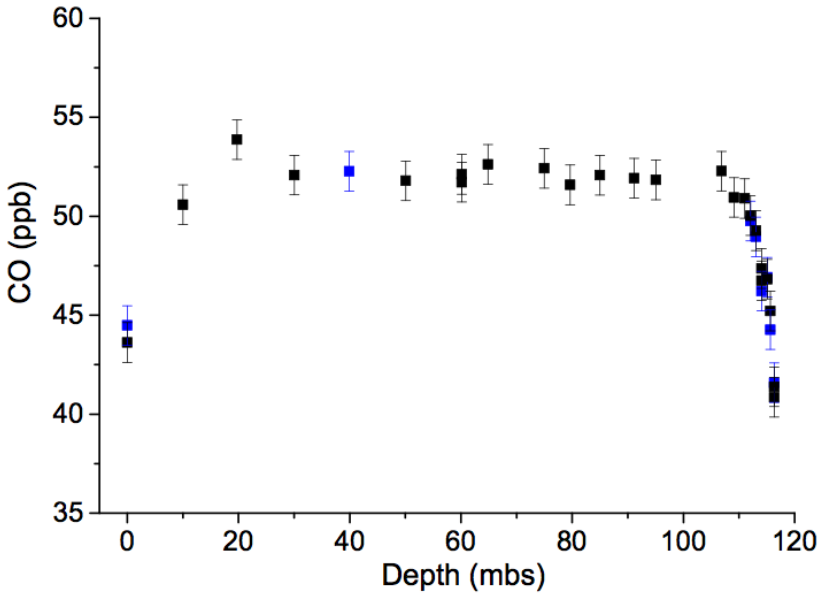

Figure 5.1: Depth profile of carbon monoxide measurements from the South Pole firn. Glass flasks were filled from NOAA/ESRL/CCG (black squares) and UCI (blue squares).

5.2.2 Corrections to the firn data

A small correction for gravitational enrichment in the firn was applied to account for the difference between the molecular weight of CO (28 kg/mol) and that of air (29 kg/mol). The rate of gravitational enrichment in the firn roughly follows the barometric relationship (equation 5.1) [*Craig et al.*, 1988; *Bender et al.*, 1994]. The gravitational correction is calculated using a fit to the depth-averaged profile of $\delta^{15}N$ of N_2 versus depth in the firn at South Pole (M. Bender and J. Severinghaus, *personal communication*). The depth profile of $\delta^{15}N$ of N_2 is shown in Figure 5.2 and reflects the processes controlling gas transport in the firn. The linearity of the $\delta^{15}N$ profile at South Pole indicates a porous ice column in which gas transport is primarily dominated by molecular diffusion, while the increase in $\delta^{15}N$ of N_2 with depth in the firn is due to gravitational enrichment of the heavier isotope. At the base of the firn (approximately 111 m), the $\delta^{15}N$ of N_2 is relatively constant, indicating the depth of the lock in zone, where relatively denser winter layers hinder vertical movement of gases [*Butler et al.*, 1999]. The correction is applied as follows:

$$[CO]_{gcorr} = [CO] - [CO]\frac{(M_{CO}-M_{air})\,(z*m+b\,)}{1000} \tag{5.1}$$

where $[CO]_{gcorr}$ is the gravitationally corrected CO mole fraction (in ppb), [CO] is the uncorrected mole fraction of CO measured in the firn (in ppb), M_{CO} and M_{air} are the molecular weights of CO and the average molecular weight of air, respectively, z is the depth in the firn, and m and b are the slope and intercept of a linear fit to the $\delta^{15}N$ measured depth profile. In the lock-in zone, below 111 m in the South Pole firn, we use a constant $\delta^{15}N$ correction (0.61) with depth.

A second, larger correction was applied to the data to account for a 2.9 ppb offset observed between surface flasks filled through the firn equipment and flasks filled directly at South Pole

Observatory on the same date (Table 5.1). The cause of the offset is unknown, but it is assumed to reflect a blank in the sampling tube and equipment. The final depth averaged CO data set, after all corrections, is given in Table A9.

Table 5.1: Comparison of surface flasks filled through the firn air system during the on 1/1/2009 during the South Pole 08/09 field campaign and NOAA flask observations from a nearby monitoring station at South Pole Observatory during the same morning. All CO data are on the WMO 2004 scale.

Time	Flask #	Flask type	Fill method	CO (ppb)	Average CO (ppb)
10:41	UCI-08-06	UCI glass	"wet" thru bladder	44.5	
10:41	6572-66	NOAA CCGG	"dry" thru bladder	43.6	44.1
05:12	4507-99	NOAA CCGG	Direct fill	42.3	
05:12	4508-99	NOAA CCGG	Direct fill	41.6	
05:17	2935-99	NOAA CCGG	Direct fill	40.4	
05:17	2936-99	NOAA CCGG	Direct fill	40.3	41.1
				Offset ± 2*SE (ppb)	2.9 ± 1.3

5.2.3 Firn air diffusion model tuning and validation

The 1D UCI firn diffusion model was used to reconstruct atmospheric CO levels from the South Pole firn air measurements. The UCI firn diffusion model has a depth resolution of 0.7 cm at the surface and 0.3 cm at the bottom of the firn and is integrated with a variable time step Runge-Kutta algorithm [*Aydin et al.*, 2004; *Montzka et al.*, 2004]. The model was run for 177 years and the output was stored at yearly intervals. The model inputs are the density profile for the firn site and the diffusivity coefficient of the gas of interest. The density of the firn at South Pole was calculated based on an empirical model [*Herron and Langway*, 1980]. The diffusion coefficients used in this study were obtained from empirical fits to experimental data given by *Wilke and Lee*, [1955] for the temperature and pressure at South Pole. These data give a $D_{CO}/D_{CO2} = 1.33$. The model produces a set of gas age distributions (Green's functions) as a function of depth in the firn. The age distributions for CO in the South Pole firn are shown in Figure 5.3.

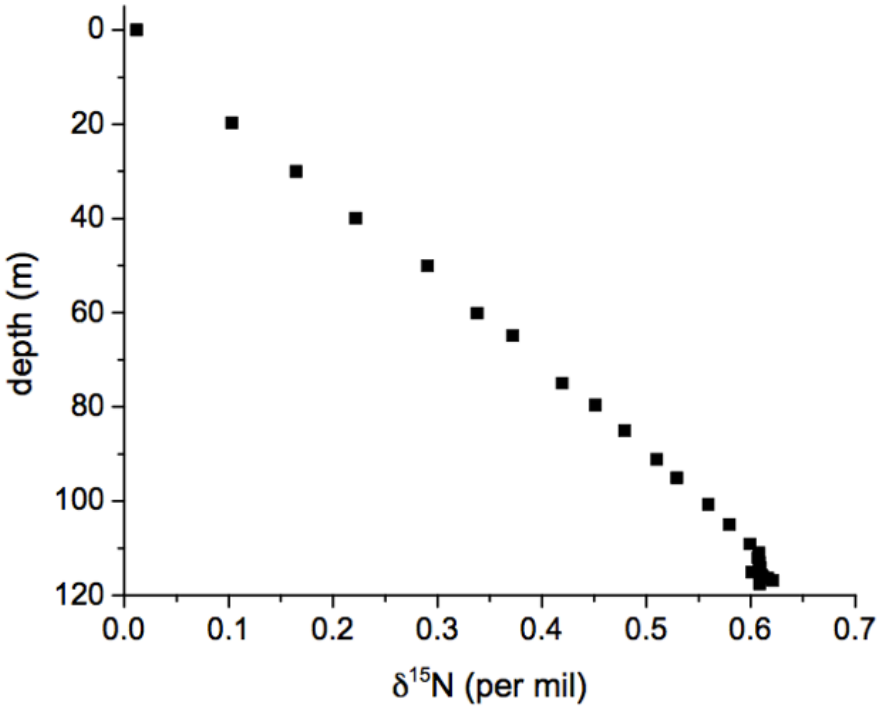

Figure 5.2: Profile of depth averaged $\delta^{15}N$ of N_2 plotted versus depth in the South Pole firn. Measurements were conducted on flasks collected during the South Pole 08/09 firn sampling campaign,

The firn diffusivity profile was tuned for South Pole using CO_2 measurements from the South Pole firn air flasks [Chapter 2, and *Aydin et al.*, 2011]. The atmospheric history of CO_2 was used as a surface boundary condition [*Etheridge et al.*, 1996]. The model was run iteratively, adjusting the diffusivity versus depth profile manually to achieve agreement with the measured CO_2 depth profile. This tuning process results in a depth profile that agrees with the measurements, with a chi square near unity.

The firn diffusion profile is validated using CH_4 and CFC-12 measurements in the South Pole flasks (NOAA/ESRL). Both gases have well-known atmospheric histories [*Etheridge et al.*, 1998, S. Montzka, personal communication]. The validation process involves running the firn model with the tuned diffusivity profile described above and the diffusion coefficient of the

"test" gas (in this case, either the CFC-12 or CH_4). Next, we use the gas age distributions produced by the firn model (Figure 5.3), along with the known atmospheric history of the test gas to obtain a depth profile of predicted mole fractions versus depth in the South Pole firn. The model depth profile for the firn is then compared with the observational depth profile for the test gas.

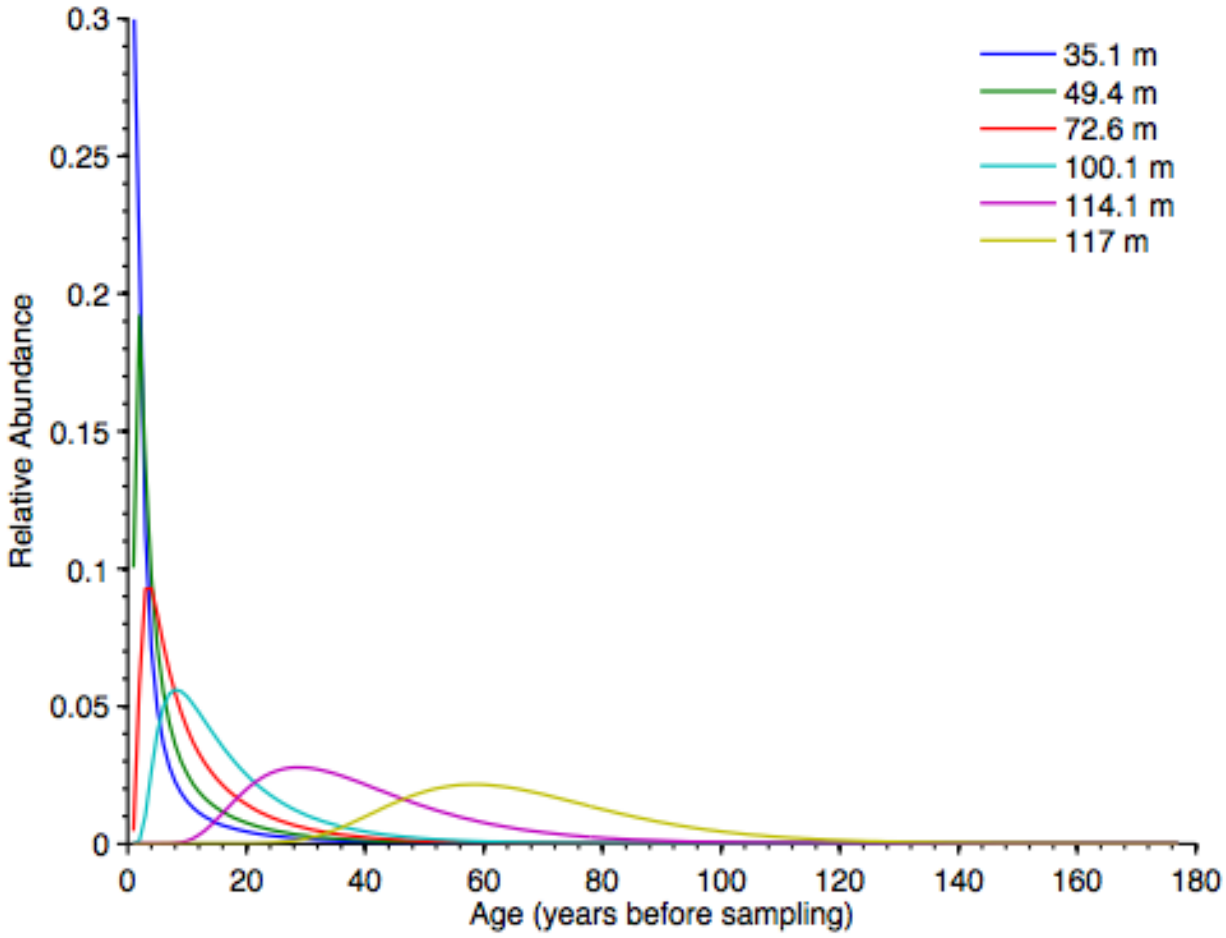

Figure 5.3: Carbon monoxide age distributions at specified depths in the South Pole firn from the 1D firn air advection diffusion model.

5.2.4 Inverse modeling used to infer the atmospheric CO history

The atmospheric history is iteratively adjusted to minimize a cost function, using the MATLAB minimization algorithm "fminunc" (tol= 10^{-12}). The cost function (f) was defined as:

$$f = \chi^2_{red} + S \tag{5.2}$$

where χ^2_{red} is the reduced chi-square statistic and S is a smoothness term. The reduced chi square statistic is:

$$\chi^2_{red} = \sum_{i=1}^{n} \frac{\left(\frac{(CO_{model} - CO_{obs})^2}{\sigma^2}\right)}{n-1} \tag{5.3}$$

where n is the degrees of freedom (number of sampling depths) and σ is the analytical uncertainty of the firn air CO measurements (1 ppb). The smoothness term (S) describes the "roughness" or amplitude of high frequency variations of the modeled atmospheric concentrations [*Rommelaere et al.*, 1997] and is defined as follows:

$$S = \alpha \times \sum \left(\frac{\partial^2 C}{\partial t^2}\right)^2 \tag{5.4}$$

where α is a weighting term and is multiplied by the squared sum of the second time derivative of the atmospheric history. For CO, we use a range of alpha values from 1 to 40.

5.3 Results and Discussion

5.3.1 CO levels in the high latitude Southern Hemisphere

We analyzed monthly CO surface flask observations at the four sites closest to the South Pole firn air sampling site, including South Pole Observatory (89.98° S, 24.8° W), Syowa Station, Antarctica (69° S, 39.575° E), Palmer Station, Antarctica (64.92° S, 64° W), and Cape Grim Observatory, Australia (40.683° S 144.69° E). Atmospheric CO levels at all the high southern latitudes exhibit strong seasonal variability (Figure 5.4). The annually averaged CO level at

South Pole is similar to other sites south of 40 °S. The mean annual CO levels at these sites varies by 2.6 ppb, with the lowest levels observed over South Pole, Antarctica and the highest levels over Cape Grim Observatory. The three Antarctic sites appear to have slightly reduced winter peaks (about 3-5 ppb) relative to Cape Grim (Figure 5.4). Mean CO levels at high southern latitudes are ~15-20% lower than the SH average [*Novelli and Masarie*, 2013].

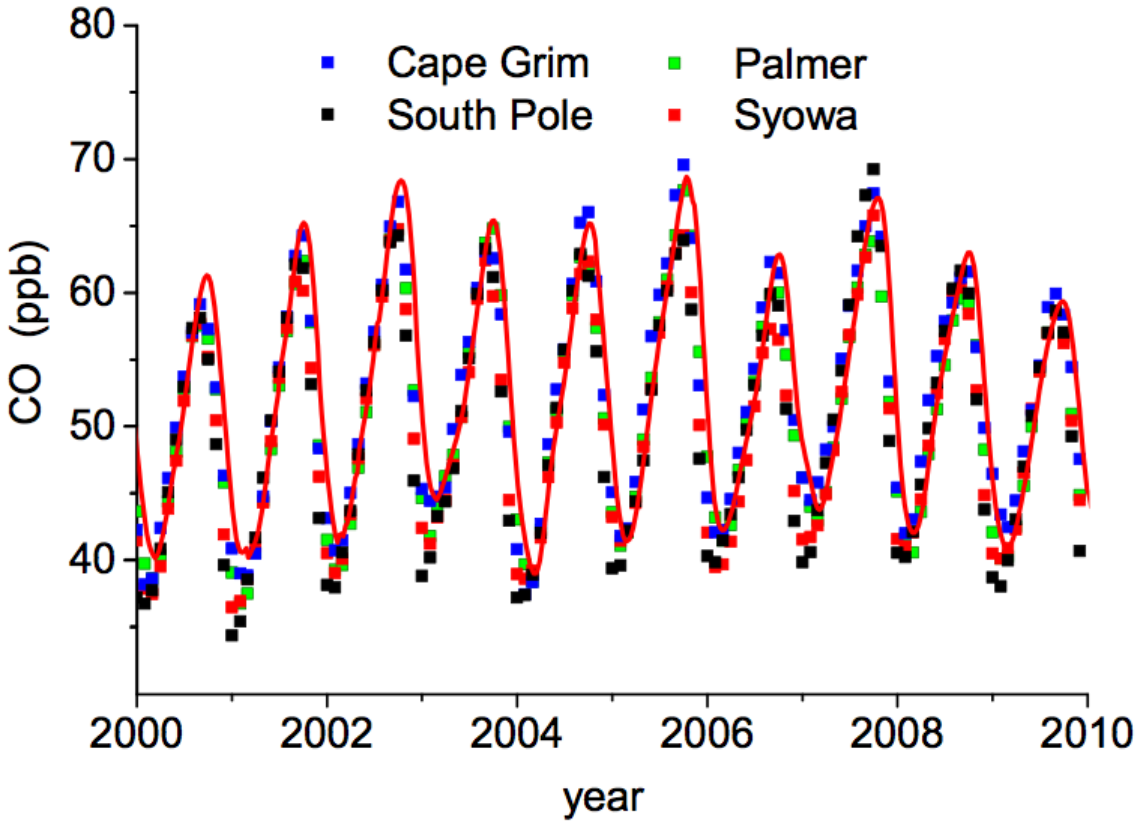

Figure 5.4: Comparison of monthly surface CO levels at four sites in the high latitude Southern Hemisphere: Cape Grim Observatory, Australia (40.683° S 144.69° E), Syowa Station, Antarctica (69° S, 39.575° E), Palmer Station, Antarctica (64.92 ° S, 64° W), and the South Pole Observatory (89.98° S, 24.8° W). The red line indicates the zonal mean in the high Southern Latitudes based on zonally averaged flask data from 30-90 °S [*Novelli and Masarie*, 2013].

5.3.2 CO atmospheric history based on Antarctic firn measurements

Figure 5.5 shows the corrected, depth-averaged CO measurements from the South Pole firn air flasks and the atmospheric CO history derived from these measurements. Carbon monoxide

levels in the firn increase from about 38 ppb in the deepest firn sample at 116.34 m to 49 ppb at 107 m, and remain constant at about 49-50 ppb at shallower depths. In the reconstructions of atmospheric CO, the model inversion was initialized using a modern mean annual CO surface mixing ratio of 50.6 ppb at South Pole in the year 2008. The surface CO mixing ratio in the year 2008 is allowed to vary after the first model iteration. The solid lines in Figure 5.5a represent the modeled CO firn profiles determined using the five different atmospheric histories shown in Figure 5.5b. The five atmospheric histories shown in Figure 5.5 were obtained using the inverse method described earlier with five different boundary conditions at time t=0. The various colored lines represent a different pre-industrial CO mixing ratio fixed in the model year 1830 AD. The firn inversion method is sensitive to assumptions about the pre-industrial CO level at South Pole prior to about 1910 AD because air from older years has a relatively small impact on the mean age in the deepest South Pole firn air sample. For this reason, we only consider inversion results for later years to represent a valid atmospheric CO history, as indicated by the shaded area in the Figure 5.5.

The firn air reconstructions suggest that CO levels in the high latitude Southern Hemisphere increased by roughly 40% between 1920-1980 AD, from about 30 ppb to 50 ppb. At the South Pole, it appears that atmospheric CO levels rose significantly faster during the fist half of the twentieth century compared to the last 20-30 years, when there is no significant trend (Figure 5.5). The lack of a trend in CO levels at high Southern latitudes during the last ~20 years has been shown previously using measurements of CO in annually averaged surface flask data from 1990-2010 AD (Figure 5.5) [*Novelli and Masarie*, 2013].

Seasonal CO variability is evident in the upper 35 m of the South Pole firn depth profile (Figure 5.5). The seasonality of gases in the firn results from the ventilation of air in the shallow

section of the firn, which occurs on sub-annual timescales. Model simulations indicate that the depth of penetration of the seasonal signal at the South Pole is roughly 35 m [*Aydin et al.*, 2011]. For this reason, CO data from shallower depths are excluded from the cost function during inverse modeling (see Section 5.2).

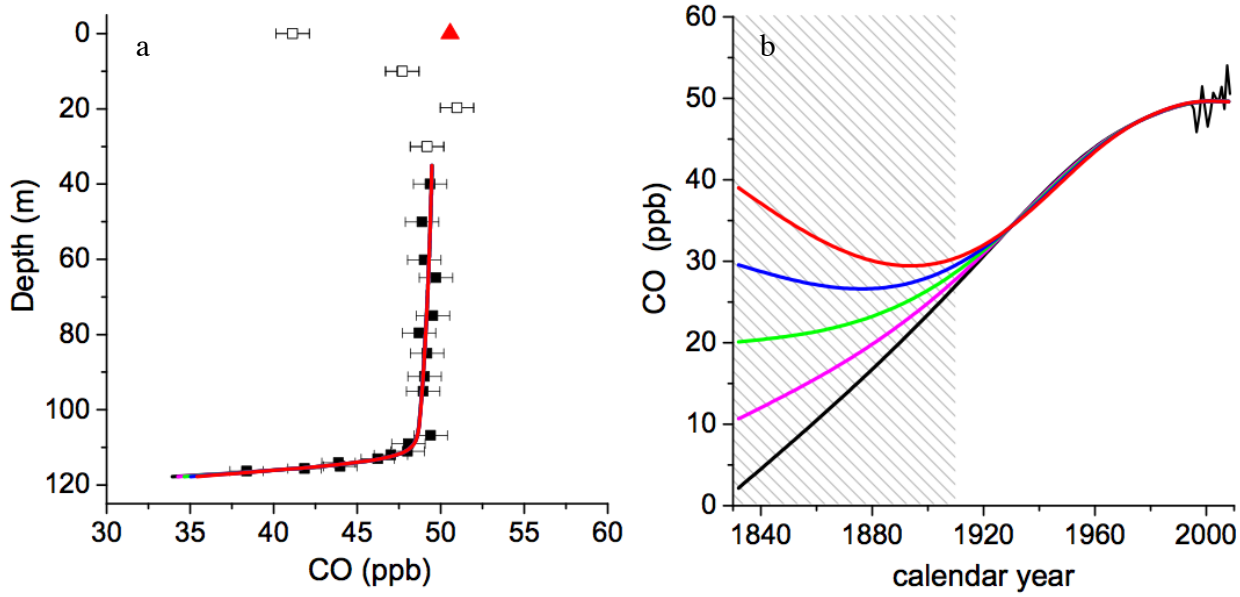

Figure 5.5: Carbon monoxide measurements in the firn at South Pole and atmospheric histories derived from the measurements. a) Depth profile of CO measured in the South Pole firn. Filled and open squares show CO measurements with estimated uncertainties (±1 ppb). Solid lines represent the modeled CO firn profiles (solid lines) using the five different atmospheric histories shown in the right panel. Measurements in the top 35 m of the South Pole firn (open squares) are subject to the effects of seasonal variations in surface CO levels and are excluded from the cost function during inverse modeling (see text). Red triangle represents the annual average of monthly CO surface observations from South Pole (1/2008 – 12/2008), based on the NOAA/CCG flask network. b) Atmospheric CO histories derived from the South Pole measurements (left panel). The five atmospheric histories shown were obtained by inverse modeling of the CO firn depth profile from South Pole using five different boundary conditions are time t=0. Different colored lines represent a different pre-industrial CO mixing ratio fixed in the model year 1830 AD and the weight of the smoothness parameter was the same in all inverse simulations (α=30). The firn inversion method is sensitive to assumptions about the pre-industrial CO level at South Pole prior to 1910 AD. Shaded area indicates years where a valid atmospheric history can be reconstructed from the South Pole firn. Black line from 1993-2008 AD represents the annual average of monthly surface CO levels measured in NOAA Carbon Cycle flasks filled at South Pole Observatory [*Novelli and Masarie*, 2013].

Atmospheric CO levels have also been reconstructed using firn air from Berkner Island, Antarctica [*Assonov et al.*, 2007]. The agreement between the South Pole and Berkner Island CO reconstructions is remarkable, especially considering that the data were obtained from different boreholes, the firn air was extracted using different equipment, the CO levels were measured in two different laboratories, and the atmospheric CO levels were reconstructed using two different firn air models (Figure 5.6). The CO reconstructions from Berkner Island shown in Figure 5.6 were scaled by a factor of 1.08 to transform them onto the NOAA calibration scale for comparison alongside the South Pole firn air data [*Assonov et al.*, 2007]. Differences in the timing and rate of the CO increase predicted from the two sites between 1950-1980 are small. Both the South Pole and Berkner Island CO reconstructions predict a similar atmospheric CO level around 1950 AD (about 39 ppb for Berkner Island and 41 ppb for South Pole). The South Pole firn air record provides new information about the early twentieth century atmospheric CO level, constraining CO levels to around 30 ppb in 1920 AD. This is 25-30% lower than the CO level predicted in the 1950s based on the Berkner Island firn air record.

There is some uncertainty in the South Pole atmospheric CO reconstruction due to the uncertainty in the blank correction applied to the CO firn depth profile (see Section 5.2). A second suite of atmospheric CO histories was developed using the CO firn data without the blank correction (see Section 5.2). The CO histories based on the uncorrected firn data are very similar to those shown in Figure 5.6, except they are offset by +3 ppb (see Appendix, Figure A4).

5.3.3 CO atmospheric history based on South Pole firn air and ice core measurements

Prior CO measurements in Antarctic ice cores suggest that preindustrial CO levels over Antarctica were 50-53 ppb between 1800-1900 AD, similar to modern day levels [*Haan and Raynaud*, 1998; *Wang et al.*, 2010]. The CO measurements in South Pole ice cores from the late

1800's are considerably higher than the deepest South Pole firn air measurement (38 ppb at 116.3 m) [*Wang et al.*, 2010]. This raises a question as to whether it is possible to construct a CO atmospheric history that is compatible with both the ice core and firn air measurements.

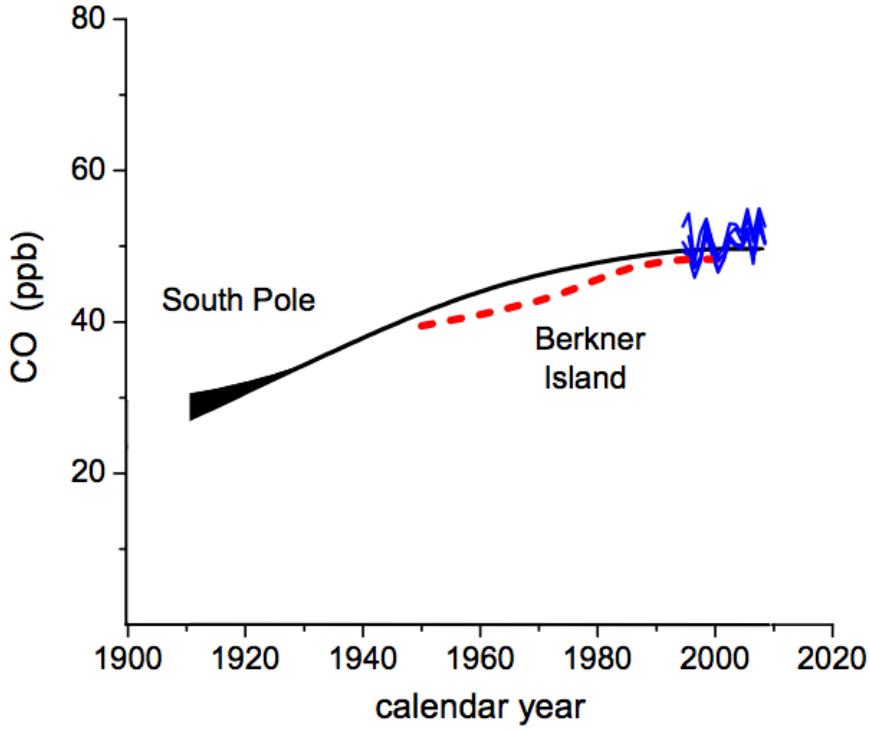

Figure 5.6: Comparison of 20th century atmospheric carbon monoxide histories based on Antarctic firn air and surface air observations. Atmospheric CO levels reconstructed from the corrected South Pole firn data (thick black line, identical to the colored lines in Figure 5.5). Dashed red line shows an independent atmospheric CO reconstruction derived from Berkner Island firn air samples [*Assonov et al.,* 2007]. The Berkner Island CO reconstruction was multiplied by 1.08 to account for the difference between the two laboratory calibration scales, as reported in *Assonov et al.,* [2007]. Berkner Island firn air samples constrain the Antarctic CO history to approximately 1950 AD. Solid blue lines shows annually averaged CO concentrations at four high southern latitude sites in the NOAA global flask sampling network (see Figure 5.4).

We carried out inversions using "firn air + ice core" scenarios with CO levels fixed at 53 ppb between 1830-1900 AD based on the mean of the Antarctic ice core data (Figure 5.7). The inversions were carried out using similar methods to the "firn air only" scenarios (see Section 5.2). Only one model result fits both the deepest firn air and shallowest ice core measurements within their uncertainties (blue line, α=1, Figure 5.7). This scenario requires CO levels to decrease rapidly from 53 ppb near 1900 AD, with a minimum around 32 ppb around 1935 AD, followed by a rapid increase back up to 50 ppb in 1980 (blue line, Figure 5.7). There are potentially other mathematical solutions that can explain both the firn air and ice core data (e.g. red line, Figure 5.7). However, we do not consider those scenarios realistic in terms of changes in atmospheric CO levels. Interestingly, inclusion of the ice core data in the inversion does not significantly alter the atmospheric CO histories after approximately 1940 (Figure 5.7). Unfortunately, there is no temporal overlap between the firn air reconstructions and the ice core measurements with which to directly compare measurements. The latest ice core data are from 1900 AD, while the oldest firn air measurements only constrain atmospheric CO levels for years after 1910 AD.

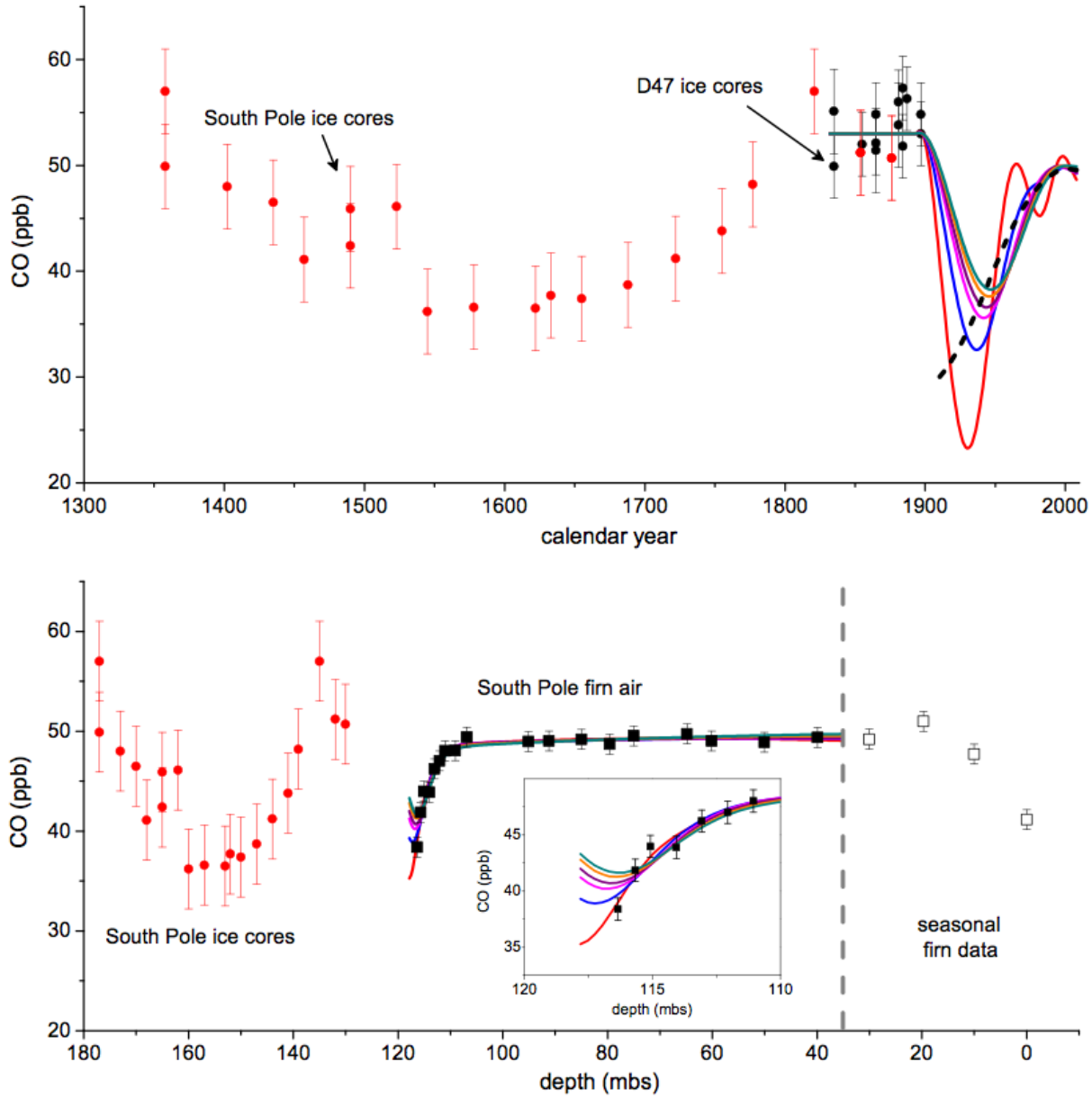

Figure 5.7: "Alternative" CO atmospheric histories derived using South Pole blank corrected firn air and ice core measurements. *Top panel* – Dashed black line represents the CO atmospheric history derived from the South Pole firn air measurements (blank corrected) alone from 1910-2010 AD. Solid lines represent modeled CO mixing ratios constrained by Antarctic ice core data using different weighting of the function "smoothness" (α), where: α=0.1 (red line), α=1 (blue line) α=5 (magenta line), α=10 (purple line), α=20 (orange line) α=30 (cyan line). CO levels from 1830-1900 AD were constrained using the mean CO mixing ratio measured in the South Pole (black circles) and D47 (red circles) ice cores [*Wang et al.,* 2010]. CO mixing ratios were unconstrained for all other model years. *Bottom panel* – Modeled and measured CO mixing ratios in the firn at South Pole. Measured CO mole fractions are represented by filled and open squares. The solid colored lines show the modeled CO mixing ratios in the firn. The dashed vertical line indicates the depth at which seasonal influences no longer impact the South Pole firn air measurements. The open squares show the CO measurements near the surface in the firn at the South Pole. These data are influenced by seasonal variations and were excluded from the model inversion method. *Inset, bottom panel* – Modeled and measured CO levels in the South Pole firn from 110 to 120 m.

5.3.4 Comparison of CO and CH_4 records

The atmospheric CH_4 and CO trends suggest that a substantial part of the South Pole CO atmospheric history can be explained by changes in atmospheric CH_4 levels alone (Figure 5.8). This is not surprising given that oxidation of atmospheric CH_4 contributes about 25-30% of the global CO source. However, the rate of atmospheric CO growth appears to be faster than the rate of CH_4 growth between 1940-1980 (Figure 5.8), suggesting that an additional CO source is required. In Chapter 6, atmospheric models are used to explore the cause of the rise and subsequent leveling-off of atmospheric CO levels during the twentieth century.

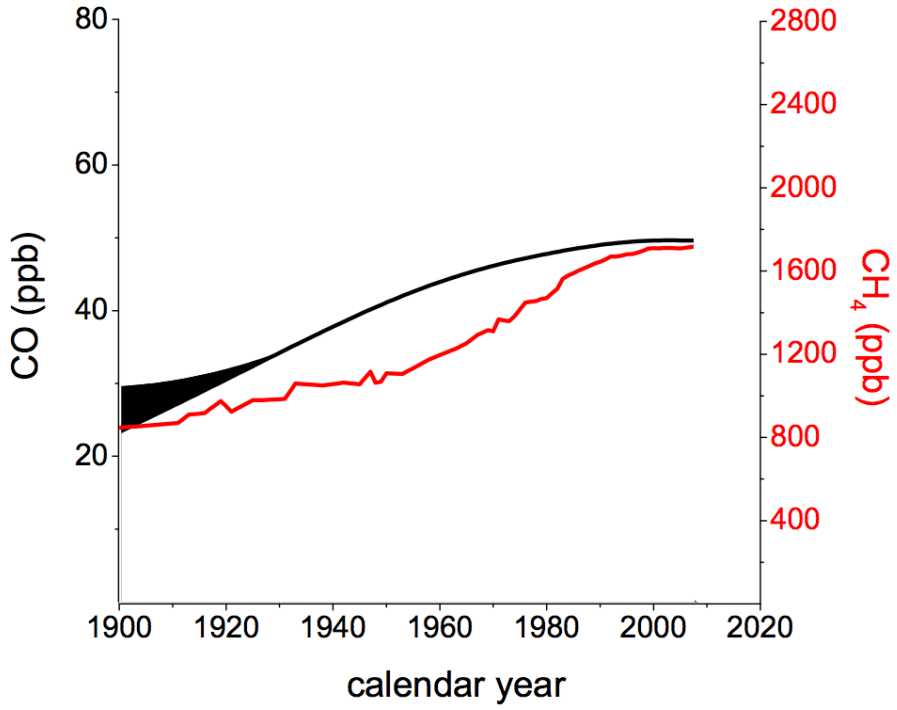

Figure 5.8: Comparison of 20th century atmospheric carbon monoxide and methane histories. The Southern Hemisphere carbon monoxide history from South Pole (black band, left y-axis) is plotted with the atmospheric methane history (red line, right y-axis) based on NOAA flask measurements, and firn air and ice core measurements from Law Dome, Antarctica [*Etheridge et al.*, 1998]. The width of the band reflects the uncertainty in the CO atmospheric history given various starting conditions for the model initialization in 1830 AD (see text).

5.4 Conclusions

- The South Pole CO reconstructions suggest that CO levels in the high latitude Southern Hemisphere increased by roughly 40% between 1920-1980, from about 30 ppb to 50 ppb. Atmospheric CO levels at South Pole rose significantly faster during the fist half of the twentieth century compared to the last 20-30 years, when there is no significant trend.
- The South Pole atmospheric CO reconstructions show good agreement with annually averaged surface flask data from 1990-2008. The firn air CO histories also show remarkable agreement with prior reconstructions from Berkner Island [*Assonov et al.*, 2007].
- Only one model result fits both the deepest firn air and shallowest ice core measurements, within their uncertainties. This scenario requires CO levels to decrease rapidly from 53 ppb near 1900, with a minimum around 32 ppb around 1935, followed by a rapid increase back up to 50 ppb in 1980. Inclusion of the ice core data in the inversion does not significantly alter the atmospheric CO histories after approximately 1940.
- Together, the atmospheric CH_4 and CO trends suggest that a substantial part of the South Pole CO trend can be explained by changes in atmospheric CH_4 levels. However, the rate of atmospheric CO growth appears to be faster than the rate of CH_4 growth between 1940-1980, suggesting that additional CO emissions are required to explain the rate of the CO levels between 1940-1980.

References

Assonov, S. S., C. A. M. Brenninkmeijer, P. Jöckel, R. Mulvaney, S. Bernard, and J. Chappellaz (2007), Evidence for a CO increase in the SH during the 20th century based on firn air samples from Berkner Island, Antarctica, *Atmos. Chem. Phys.*, *7*(2), 295–308, doi:10.5194/acp-7-295-2007.

Aydin, M., E. S. Saltzman, W. J. De Bruyn, S. A. Montzka, J. H. Butler, and M. O. Battle (2004), Atmospheric variability of methyl chloride during the last 300 years from an Antarctic ice core and firn air, *Geophys. Res. Lett.*, *31*(2), L02109, doi:10.1029/2003GL018750.

Aydin, M., K. R. Verhulst, E. S. Saltzman, M. O. Battle, S. A. Montzka, D. R. Blake, Q. Tang, and M. J. Prather (2011), Recent decreases in fossil-fuel emissions of ethane and methane derived from firn air, *Nature*, *476*(7359), 198–201, doi:10.1038/nature10352.

Battle, M., M. Bender, T. Sowers, and P. Tans (1996), Atmospheric gas concentrations over the past century measured in air from firn at South Pole, *Nature*, *383*, 231–235.

Bender, M., T. Sowers, J.-M. Barnola, and J. Chappellez (1994), Changes in the O_2/N_2 ratio of the atmosphere during recent decades reflected in the composition of air in the firn at Vostok Station, Antarctica, *Geophys. Res. Lett.*, *21*(3), 189–192.

Butler, J. H., M. Battle, M. L. Bender, S. A. Montzka, A. D. Clarke, E. S. Saltzman, C. M. Sucher, J. P. Severinghaus, and J. W. Elkins (1999), A record of atmospheric halocarbons during the twentieth century from polar firn air, *Nature*, *399*, 749–755.

Craig, H., Y. Horibe, and T. Sowers (1988), Gravitational separation of gases and isotopes in polar ice caps, *Science*, *242*(4886), 1675–1678, doi:10.1126/science.242.4886.1675.

Etheridge, D. M., L. P. Steele, R. L. Langenfelds, R. J. Francey, J.-M. Barnola, and V. I. Morgan (1996), Natural and anthropogenic changes in atmospheric CO_2 over the last 1000 years from air in Antarctic ice and firn, *J Geophys Res.*, *101*(D2), 4115–4128.

Etheridge, D. M., L. P. Steele, R. J. Francey, and R. L. Langenfelds (1998), Atmospheric methane between 1000 A.D. and present: Evidence of anthropogenic emissions and climatic variability, *J Geophys Res.*, *103*(D13), 15979–15993.

Gerbig, C., S. Schmitgen, D. Kley, A. Volz-thomas, K. Dewey, and D. Haaks (1999), An improved fast-respinse vacuum-UV resonance fluorescence CO instrument, *J. Geophys. Res.*, *104*(D1), 1699–1704.

Haan, D., and D. Raynaud (1998), Ice core record of CO variations during the last two millennia: atmospheric implications and chemical interactions within the Greenland ice, *Tellus B*, 253–262.

Herron, B. M. M., and C. C. Langway (1980), Firn Densification: An Empirical Model, *J. Glaciol.*, *25*(93), 373–385.

Montzka, S. A., M. Aydin, M. Battle, J. H. Butler, E. S. Saltzman, B. D. Hall, A. D. Clarke, D. Mondeel, and J. W. Elkins (2004), A 350-year atmospheric history for carbonyl sulfide inferred from Antarctic firn air and air trapped in ice, *J. Geophys. Res.*, *109*(D22), D22302, doi:10.1029/2004JD004686.

Novelli, P. C., and K. A. Masarie (2013), Atmospheric Cycle, Carbon Monoxide Dry Air Mole Fractions from the NOAA ESRL Carbon Cooperative Global Air Sampling Network, 1988-2012, Version: 2013-06-18.

Rommelaere, V., L. Arnaud, and J.-M. Barnola (1997), Reconstructing recent atmospheric trace gas concentrations from polar firn and bubble ice data by inverse methods, *J. Geophys. Res.*, *102*(D25), 30069–30083.

Wang, Z., J. Chappellaz, K. Park, and J. E. Mak (2010), Large variations in Southern Hemisphere biomass burning during the last 650 years, *Science*, *330*(6011), 1663–6, doi:10.1126/science.1197257.

Wilke, C. R., and C. Y. Lee (1955), Estimation of diffusion coefficients for gases and vapours, *Ind. Eng. Chem.*, *47*, 1253–1257.

CHAPTER 6

Top-down historical atmospheric carbon monoxide emissions inventory during the 20th century

6.1. Introduction

In this chapter, the observed changes in atmospheric CO levels derived from firn air and surface air data are explored in terms of changes in major CO sources and sinks. The modern day CO budget is explored using the UCI Chemical Transport Model and a simple box model of the troposphere. The box model is used to reconstruct atmospheric CO emissions from anthropogenic fossil fuel and biomass burning sources. CO emissions are derived for the Southern Hemisphere and the global atmosphere based on the South Pole atmospheric history in Chapter 5. The results are compared alongside global emissions from the Atmospheric Chemistry and Climate Modeling Intercomparison Project (ACCMIP) inventory [*Lamarque et al.,* 2010]. The CO emissions histories derived from the box model calculation are compared with the CO atmospheric history for the high latitude Northern Hemisphere, based on Greenland firn air reconstructions from *Petrenko et al.* [2013].

6.2 Methods

Modeling studies were conducted to derive emissions histories consistent with the CO reconstructions based on the South Pole firn air data discussed in Chapter 5. A combination of field observations and simulations using a 3D chemical transport model and a simple box model

of the atmosphere was used to develop the CO emissions histories during the twentieth century. The UCI Chemical Transport Model (UCI CTM) was used to understand the relative impact of a particular source on high latitude CO levels, and to relate the response in tropospheric CO levels in each hemisphere to the high latitudes. A description of the box model and CTM simulations is given here. In the following sections, we define the high latitude Northern Hemisphere as HNH (60-90°N) and the high latitude Southern Hemisphere as HSH (60-90°S).

6.2.1 Greenland and Antarctic firn air records

In this study we use information about historical CO trends to interpret CO emissions during the twentieth century. Together, the Greenland and Antarctic CO reconstructions suggest that atmospheric CO levels rose globally between 1950-1970 [Chapter 5 - this study, and *Petrenko et al.,* 2013]. The South Pole firn air record constrains the CO rise much earlier (to the early 1900s), although a change in CO levels in the high latitude Southern Hemisphere (HSH – 60-90°S) is not necessarily indicative of a global CO trend prior to 1950. After the 1980s, the Greenland and Antarctic CO trends appear to be decoupled. CO levels in the Arctic declined by approximately 21 ppb between 1980-2006, from about 158 ppb to 137 ppb [*Petrenko et al.,* 2013]. During the same period, the firn air and surface flask data show CO levels stabilized over Antarctica and the HSH [this study, and *Novelli et al.*, 2003].

6.2.2 CO box model description

The two-box model was used in this study to simulate the atmospheric abundance of CO in each hemisphere. The simple, two-box model simulates the atmospheric CO abundance in each hemisphere based on prescribed, time-varying emissions histories. The mass balance equation for the CO burden in each hemisphere (CO_N, CO_S) is given by:

$$\frac{dCO_N}{dt} = f_N\left(S_{ff} + S_{bb} + S_{oc} + P_{CH_4\ Oxid} + P_{BVOC\ Oxid}\right) - (k_{CO,OH} + k_{soil} + k_{strat}) * CO_N - k_{IHT}(CO_N - CO_S) \quad (6.1)$$

$$\frac{dCO_S}{dt} = (1 - f_N)\left(S_a + S_{bb} + S_{oc} + P_{CH_4\ Oxid} + P_{BVOC\ Oxid}\right) - (k_{CO,OH} + k_{soil} + k_{strat}) * CO_S - k_{IHT}(CO_S - CO_N) \quad (6.2)$$

where S_a, S_{bb}, and S_{oc} represent direct fluxes of CO from anthropogenic, biomass burning, and oceanic sources. Anthropogenic CO sources include direct fossil emissions, anthropogenic biofuel emissions, and CO produced indirectly from oxidation of anthropogenic NMVOCs in the atmosphere. $P_{CH_4\ Oxid}$ represents the time-dependent CO production from oxidation of atmospheric CH_4 (see equation 6.3 below), and $P_{BVOC\ Oxid}$ represents CO produced from oxidation of biogenic VOCs (BVOCs). $k_{CO,OH}$, k_{soil}, and k_{strat} are the first-order loss rate constants for reaction of CO+OH, loss to soils, and loss to the stratosphere. We use $k_{CO,OH} = {}^{1}/_{0.1315\ y}$, this is inverse lifetime against tropospheric OH, based on *Kanakidou and Crutzen* [1999]. For CO loss to soils, we use $k_{soil} = {}^{1}/_{1.644\ y}$, which is roughly 8% of the total loss, although there is likely significant uncertainty associated with this estimate. For CO loss to the stratosphere, we use $k_{strat} = {}^{1}/_{2.466\ y}$. We use an inverse time constant of $k_{IHT} = {}^{1}/_{1\ y}$, for interhemispheric transport. CO emissions from the global oceans were assumed to be constant and fixed at 20 Tg y^{-1}. Direct biogenic emissions of CO are small and likely account for 4% or less of the total CO budget. Therefore, these emissions were not included in the box model calculations.

In equations (6.1-6.2), f_N is the fraction of the source in the northern hemisphere and is different for each source (Table 6.1). For example, anthropogenic CO emissions from fossil fuel and biofuel use are concentrated in the northern mid-latitudes (f_N=0.95), while biomass burning

emissions are split more evenly between the two hemispheres (f_N=0.58). The box model solution is integrated using Matlab's ode45 solver, with variable time step and tolerance set at $1e^{-5}$.

Methane oxidative source: In the box model, the production of CO from oxidation of atmospheric methane ($P_{CH_4\ oxid_{(t)}}$) is time-dependent and is calculated as follows:

$$P_{CH_4\ oxid_{(t)}} = \lambda \times \left(\frac{k_1}{k_2}\right) \times CH_{4_{(t)}} \times F_{(t)} \tag{6.3}$$

where k_1 is present-day, inverse lifetime for CH_4 for the tropospheric reaction of CH_4+OH $\left(k_1 = {}^{1}/_{9.6\ y}\right)$, k_2 is the inverse lifetime for the tropospheric reaction of CO+OH $\left(k_2 = {}^{1}/_{0.1315\ y}\right)$, $CH_{4_{(t)}}$ is the atmospheric CH_4 burden in model year t, λ is the dimensionless yield of CO from CH_4 oxidation. In this study, changes in atmospheric CH_4 are prescribed based on the atmospheric history of CH_4 from the Law Dome ice core and NOAA surface observations [*Etheridge et al.*, 1998], assuming a molar yield (λ) of 0.95 for the conversion of atmospheric CH_4 to CO [*Duncan et al.*, 2007]. There is also seasonality in the atmospheric CH_4 signal, however this was not included as part of the calculation in equation (6.3) due to the coarse resolution of the box model solution at decadal time slices. Overall, the production of CO from CH_4 oxidation is about 30% of the total tropospheric source. $F_{(t)}$ represents the time-dependent dimensionless fractional change in $\left({}^{k_1}/_{k_2}\right)$, and is prescribed based on ACCMIP estimates for the global OH change from pre-industrial to modern [*Naik et al.* 2013], as shown in equation (6.4):

$$F_{(t)} = \begin{cases} 1.0 \pm 0.05 & in\ 2000\ AD \\ 1.04 \pm 0.1 & in\ 1980\ AD \\ 1.02 \pm 0.1 & in\ 1900\ AD \end{cases} \tag{6.4}$$

Naik et al. [2013] does not report OH changes or uncertainties after 2000. Therefore, in equation (6.4), we assume there is no additional OH change or uncertainty between model years 2000 and

2010. In the box model calculation, we assume an equal source of CO from CH_4 oxidation in both hemispheres, although there is evidence for higher oxidation of CH_4 in the Northern Hemisphere [*Spivakovsky et al.,* 2000].

Uncertainty in OH: There is some uncertainty associated with our knowledge of the abundance of atmospheric OH during the last century. *Naik et al.* [2013] estimated the air-mass weighted tropospheric mean OH abundance at three time slices from the pre-industrial (1850), in 1980 and in 2000, based on the comparison of sixteen 3D chemical transport models in the Atmospheric Chemistry and Climate Modeling Intercomparison Project (ACCMIP) and suggested that the uncertainty in atmospheric OH from preindustrial to modern is roughly 5-10%. Changes in OH abundance will impact the atmospheric lifetimes of CH_4 and CO. Therefore, the uncertainty in OH also impacts the amount of CO produced by oxidation of atmospheric CH_4, as shown in equation (6.3-6.4). To account for the uncertainty in CO+OH, the lifetime of CO ($\tau_{CO,OH}$) is also scaled as a percent change relative to the first model year (1900) using $F_{(t)}$, as follows:

$$\tau_{CO,OH} = \left(\frac{1}{k_{CO,OH}}\right) * F_{(t)} \quad (6.5)$$

In the atmosphere, the reaction of CO+OH is determined by the abundance of [CO] and [OH], and the bimolecular reaction rate constant $\left(k_{CO,OH}\right)$, which is pressure dependent. The pressure dependence of $k_{CO,OH}$ is not considered in this simple box model calculation.

VOC oxidative source: CO is also produced from the oxidation of anthropogenic and biogenic volatile organic compounds (differentiated in this study as NMVOCs and BVOCs). The losses of soluble intermediates for anthropogenic NMVOCs are expected to be small based on prior modeling studies [e.g. *Bergamaschi et al.*, 2000; *Duncan et al.*, 2007]. For this reason, we consider anthropogenic CO emissions as the sum of fossil fuel and NMVOC oxidative

emissions, assuming the molar CO yield from oxidation of anthropogenic NMVOCs is 1.0, using a ratio of $(28\ g\ CO\ mol^{-1})/(12\ g\ C\ mol^{-1})$. There is some evidence that the levels of anthropogenic NMVOCs (specifically, light alkanes produced from anthropogenic sources) have declined since the 1970s and 1980s [*Simpson et al.*, 2006, 2012; *Worton et al.*, 2012; *Helmig et al.*, 2014]. The impact of the decline in light alkanes on the global CO levels is explored in section 6.3.5.

The amount of CO produced indirectly from oxidation BVOCs is perhaps the most uncertain part of the atmospheric CO budget. BVOC emissions are temperature dependent and vary widely depending on vegetation type. There are also several classes of BVOCs, including isoprene, monoterpenes, sesquiterpenes, and oxygenated BVOCs. While these compounds may have similar oxidation pathways in the atmosphere, the scavenging of soluble intermediates along the hydrocarbon oxidation pathway can lead to different molar CO yields, resulting in different amounts of CO produced. The treatment of BVOCs (e.g. speciation or climate-sensitivity) in model, will thus impact the atmospheric lifetime of CO and its atmospheric distribution. Historical BVOC emissions during the twentieth century are even less certain, and changes in OH can also impact the rate of oxidation of BVOCs. In the box model, we prescribe fixed CO emissions from global BVOC oxidation equal to 500 Tg CO y^{-1} because there is no information on which to base assumptions about the molar CO yield, specific composition of BVOCs, or changes in historical BVOC emissions.

6.2.3 Model optimization method

The box model is used to derive top-down CO emissions during the twentieth century. Two scenarios are tested, one for anthropogenic emissions and one for biomass burning emissions. The model result is optimized for consistency with the atmospheric CO history for the HSH derived from South Pole firn air (see Chapter 5). We used the MATLAB function "fminsearch"

for the optimization, with tolerances set to 10^{-4}. We calculate a chi-square statistic for decadal time slices between 1900-2010 for the HSH. The box model cost function is given in equation 6.6:

$$\chi^2_{total} = [\chi^2_{HSL}]_{1900-2010} \quad (6.6)$$

where $[\chi^2_{HSL}]$ is the function value that is minimized is the sum of the chi square terms for each decade from 1900-2010. We use σ=1 ppb for the uncertainty in the atmospheric reconstruction for all model years. In the first scenario, anthropogenic CO emissions are optimized, with biomass burning emissions fixed to the ACCMIP inventory [*Lamarque et al.*, 2010]. As a starting condition for the minimization algorithm, historical anthropogenic CO emissions in the box model were set to the ACCMIP emissions for all years, using the sum of CO sources labeled "land anthropogenic" and "anthropogenic NMVOC" sources (using a conversion factor of $(28\ g\ CO\ mol^{-1})/(12\ g\ C\ mol^{-1})$). In the second scenario, biomass burning emissions are optimized. As a starting condition for the model algorithm, the biomass burning emissions were set at the ACCMIP historical emissions. In both scenarios, CO production from oxidation of CH_4 and BVOCs were fixed as described in section 6.2.2.

Table 6.1. CO budget and the fraction of the CO source in the northern hemisphere box (f_N) used in the CO box model. Source fractions are based on Emissions Database for Global Atmospheric Research (EDGAR), except where noted. Modern CO emissions for box model scenario 1 are also listed.

Source	**This study** [a]		***Duncan et al.*, 2007**[b]	***Bergamaschi et al.*, 2000**[c]	**ACCMIP** [d]
	CO (Tg y^{-1})	**f_N**	**CO (Tg y^{-1})**	**CO (Tg y^{-1})**	**CO (Tg y^{-1})**
CH_4 oxidation	747	$f_{N,CH4}$=0.5	778 – 861	830	--
Anthropogenic	*	$f_{N,ff}$=0.95	653-676 [c]	708-1021	910
Biomass burning	*	$f_{N,bb}$=0.58	451 – 573	615-740	459
BVOC Oxidation[c]	500	$f_{N,bvoc}$=0.51	354-379	314-507	
Oceanic	20	$f_{N,oc}$=0.25	--	5-35	--
Total source			2236 – 2489	2867-3009	

[a] In the box model, anthropogenic sources include direct and indirect emissions from fossil fuels and biofuels. Source fractions were used in this study to distribute the CO sources in each hemisphere between the two boxes in the model. The source fraction for BVOC oxidation is based on Guenther et al., [1995]. CO from atmospheric CH_4 oxidation (747 Tg y^{-1}) is based on an atmospheric methane level of 1790 ppb and a CO molar yield (λ) of 0.95.

[b] Overall budget used in the GEOS-Chem model for CO from 1988-1997.

[c] Anthropogenic emissions from *Duncan et al.* [2007] are the sum of CO emission from fossil fuels and biofuels sources, including both direct emissions and photochemical oxidation.

[d] ACCMIP emissions as reported in *Lamarque et al.* [2010]. Anthropogenic emissions include the sum of the Land Anthropogenic source and the anthropogenic NMVOCs, assuming a yield of 1.0 and using $(28\ g\ CO\ mol^{-1})/(12\ g\ C\ mol^{-1})$.

6.2.4 UCI Chemical Transport Modeling Studies

Simulations were carried out using the UCI three-dimensional Chemical Transport Model (UCI CTM) [*Holmes et al.*, 2013] The UCI CTM is a tropospheric CTM, with T42 (~2.8° x 2.8°) horizontal resolution and 57 vertical layers. The model transport is driven by meteorological fields from the European Center for Medium-Range Weather Forecasting (ECMWF). Tropospheric chemistry of the major gas-phase species involved in HO_x, NO_x, O_3, and NMVOC reactions is simulated as described by *Holmes et al.*, [2013]. Surface CO emissions for

anthropogenic sources (road, non-road, and ships) were based on the RCP year 2000 inventory [*Lamarque et al.*, 2010]. Biomass burning emissions were from the Global Fire Emissions Database (GFED3.1, http://www.globalfiredata.org). Biogenic emissions were from the Model of Emissions of Gases and Aerosols from Nature (MEGANv2.1), which estimates the net biogenic volatile organic compound (BVOC) emissions to the atmosphere [*Guenther et al.*, 2012]. In the CTM simulations, the model was run for two years using year 2000 meteorology and results from the second model year were analyzed. Three perturbation experiments were designed with the CTM to study the response of CO levels in each hemisphere and at high latitudes to a small change in CO emissions from biomass burning, anthropogenic sources, or CH_4 oxidation. In addition, a CO tagged tracer run was developed, where CO emissions from major sources were tracked as four separate tracers for biomass burning, anthropogenic, total-VOC, and CH_4 sources. These two methods were employed to relate the mean hemispheric CO level to the high latitudes, as described below.

Relating mean hemispheric CO levels to the high latitudes

A simple two-box model has obvious deficiencies in terms of relating changes in global emissions to tropospheric CO levels at high latitudes because there are large CO gradients in the troposphere today. Two approaches were used to determine how to scale the mean hemispheric CO level to the high latitudes: 1) a perturbation experiment, where each source was perturbed relative to a "base case" and 2) a CO tracer experiment, where the CO emissions from major sources were tagged so the contribution of each source at different latitudes could be quantified. The results from both approaches are described here.

CO perturbation experiments: A combination of 3D model simulations and field observations were used to account for the relative impact of a particular source on the CO level

at high latitudes. Table 6.2 summarizes the 3D perturbation simulations conducted for this study, which included (1) a base case scenario; and three perturbation runs in which one of the following sources was increased by 5%: (2) anthropogenic CO emissions, (3) biomass burning CO emissions, or (4) atmospheric methane abundance. We used a small perturbation approach, where the response of the chemical system is expected to be closer to the "true" impact of changing emissions [*Hoor et al.*, 2009]. For each perturbation run, a high latitude response (HLR) factor was determined for each source, in each hemisphere, as follows:

$$HLR = \frac{([CO_{pert}]-[CO_{base}])_{60-90^\circ}}{([CO_{pert}]-[CO_{base}])_{0-90^\circ}} - 1 \quad (6.7)$$

where $[CO_{pert}]$ is the CO response to the emissions enhancement from one of the perturbation experiments and $[CO_{base}]$ is the CO response to the baseline emissions in the base case scenario. The HLR is computed using the ratio of the annually averaged CO level from the CTM results in the given latitude bands – either at high latitudes (60-90°) or in the entire hemisphere (0-90°). We use the sum of 30 vertical layers from the UCI CTM, representing roughly 150 hPa (Table 6.3 and Table A11). An HLR>0 reflects that the annually averaged response in the 60-90° latitude band is more sensitive than the annually averaged response to the emissions perturbation in the hemisphere average (0-90°). Similarly, an HLR<0 reflects a response where 60-90° latitude band is less sensitive to the emissions perturbation than the hemispheric average (0-90°), and an HLR=0 reflects a response where the high latitudes and the hemispheric mean are equally sensitive to the emissions perturbation. The equations used to calculate the HLRs and the results given below and in Table 6.3.

Sources contribute to the levels of CO in the northern and southern hemispheres and the high latitudes with different efficiencies. The HLR values in Table 6.3 are used in the box model to

obtain a source-weighted estimate of atmospheric CO at high latitudes, as follows:

$$HLR_{HNH} = \frac{S_a * f_{N,ff}}{S_{N,total}} * \left(HLR_{HNH,FF}\right) + \frac{S_{bb} * f_{N,bb}}{S_{N,total}} * \left(HLR_{HNH,BB}\right) + \frac{S_{CH4} * f_{N,CH4}}{S_{N,total}} * \left(HLR_{HNH,CH4}\right) \quad (6.8)$$

$$HLR_{HSH} = \frac{S_a * (1 - f_{N,ff})}{S_{S,total}} * \left(HLR_{HSH,FF}\right) + \frac{S_{bb} * (1 - f_{N,bb})}{S_{S,total}} * \left(HLR_{HSH,BB}\right) + \frac{S_{CH4} * (1 - f_{N,CH4})}{S_{S,total}} * \left(HLR_{HSH,CH4}\right) \quad (6.9)$$

In equations (6.8-6.9), HLR_{HNH} and HLR_{HSH} are the source weighted response factors for the high latitude Northern Hemisphere and the high latitude Southern Hemisphere, $HLR_{HNH,FF}, HLR_{HNH,BB}, HLR_{HNH,CH4}$ are the HLRs for the northern hemisphere from anthropogenic, biomass burning, and CH_4 oxidation, and $S_{N,total}$ and $S_{S,total}$ are the total CO source in the Northern and Southern hemispheres, respectively.

The high-latitude mixing ratio in the box model is computed from the mean hemispheric CO mixing ratio by:

$$CO_{HNL} = CO_N\,(1 + HLR_{HNH}) \quad (6.10)$$

$$CO_{HSL} = CO_S\,(1 + HLR_{HSH}) \quad (6.11)$$

where CO_{HNL} and CO_{HSL} are the CO burdens at high latitudes, and CO_N and CO_s represent the mean hemispheric CO burden in the northern and southern hemispheres, respectively.

The CTM simulations show that perturbations in fossil fuel emissions and biomass burning emissions have similar impacts in the HSH, with an HLR of -0.4 (Table 6.3). The CTM simulations show that the HLR for CH_4 oxidation is -0.16 for the HNH and -0.18 for the HSH, reflecting the larger CH_4 oxidative source in the tropics relative to the poles. The UCI-CTM underestimates CO levels in HNH, like many other chemical transport models (see Appendix Figure A6). Flask observations show that the mean CO level in the HNH is about 20% higher

than the northern hemispheric mean [*Novelli and Masarie*, 2013]. The underestimation could reflect a weaker than observed OH sink in the CTM, (which would contribute to a N/S asymmetry in tropospheric OH). The CO bias could also reflect inaccuracies in the CO budget, related to either the magnitude or latitudinal distribution of anthropogenic CO sources. For example, the CO mixing ratios could also be underestimated in the CTM due to a few small high latitude CO sources missing from the model. However, the data from the poles does not offer sufficient information with which to predict a missing CO source in the HNH. Until this problem is resolved, the CTM results cannot be used to accurately predict an HLR for anthropogenic CO emissions. In this study, we assume that the underestimation of CO levels in the high latitude Northern Hemisphere is entirely due to fossil fuel emissions. Therefore, we conclude that the Northern Hemisphere HLR obtained from the fossil fuel CTM perturbation ($HLR_{HNH,FF}$=0.17) was not realistic based on comparison of the model results to observational flask data in the high latitude Northern Hemisphere. Instead, we used CO flask data [*Novelli and Masarie*, 2013] to estimate a modern day fossil fuel HLR for the HNH ($HLR_{HNH,FF}$=0.46, Table 6.3).

Table 6.2. Summary of simulations carried out with the UCI-CTM. Fossil emissions are based on the RCP60 inventory, biomass burning emissions are based on GFEDv3.1, and biogenic emissions are based on MEGANv2.1.

Simulation Name	Perturbation Type	Simulation Period
Base case	None	2000-2001
1.05*BB	+5% biomass burning	2000-2001
1.05*FF	+5% fossil fuel	2000-2001
1.05*CH_4	+5% methane	2000-2001

Table 6.3: High latitude response factors (HLRs) determined from the UCI CTM. These values are used to estimate levels of carbon monoxide in the HNH and HSH from the two-box model.

	HLR_{HNH}	HLR_{HSH}
CH_4 Oxidation	-0.16	-0.18
Biomass burning	-0.1	-0.4
Anthropogenic fossil fuels	0.1 (0.46)*	-0.4
Biogenic VOCs	0**	0**

* The CO HLR_{HNH} for anthropogenic fossil fuel sources was estimated using observational data.
** The CO emitted from oxidation of BVOCs was not quantified in the perturbation experiments. Instead a scaling factor of 0 was assumed for the box model simulations, assuming that we assume the response of CO levels at high latitudes is equal to the response in the entire hemisphere for BVOC oxidation.

CO Tagged Tracer Simulation: Emissions from major CO sources were tracked in the atmosphere in a tagged tracer run with the UCI CTM. This run was conducted to determine the impact of each source on the CO mixing ratio at high latitudes. Four tracers were tracked, to distinguish between CO emissions from biomass burning, anthropogenic, and oxidative emissions from total-VOCs and CH_4. The tracers were named: CO_{fire}, CO_{anth}, CO_{CH4}, and $CO_{total-VOC}$. The CO_{anth} tracer includes emissions from fossil fuel and biofuel use. Figure 6.1 shows the model result for the high latitude Northern Hemisphere (HNH – 60-90°N) and high latitude Southern Hemisphere (HSL – 60-90°S), compared alongside flask data from Summit, Greenland and the South Pole, respectively. Table 6.4 shows the mean CO levels produced by each source in various model boxes (Global, NH – 0-90°N, SH – 0-90°S, HNH – 60-90°N, and HSH – 60-90°S). The CO response from each tracer was calculated as the average of 10 vertical layers in the model, and the average moles of CO in specified latitudinal range divided by the average moles of air in the same boxes. In the HSH, CH_4 oxidation has the largest impact on annually averaged CO mole fractions (around 50%), followed by total-VOC oxidation (32%), and anthropogenic fossil fuel and biomass burning emissions (about a 7-8%). In the HNH,

anthropogenic fossil fuel sources have the largest impact (41%), followed by CH_4 oxidation (27%), total-VOC oxidation (26%), and biomass burning (7%) (Figure 6.1 and Tables 6.4 and 6.5).

The values reported in Table 6.4 were used to check the box model for consistency with the CTM budget at the South Pole since the CTM results show good agreement with the flask data from south of 40°S. However, CO tracers are not used to evaluate HNL CO mixing ratios because the CTM underestimates CO mole fractions from 60-90°N (Figure 6.1). The CTM results for total-VOC oxidative emissions could not be used to determine HLR factors for BVOCs in the box model because the anthropogenic and biogenic tracers were not tagged separately and they have very different emissions patterns and lifetimes.

Table 6.4: UCI CTM results for a CO tagged tracer run for 10 vertical layers.

	Anthropogenic (FF)	Biomass burning	CH_4 oxidation	total-VOC oxidation	Sum
Global	18.5	7.2	25.8	23.2	74.7
NH	31.4	7.6	26.1	25.2	90.4
SH	5.7	6.8	25.5	21.2	59.3
HNL	37.0	6.1	24.2	23.6	90.9
HSL	3.7	3.3	23.2	14.5	44.7

Table 6.5: Atmospheric CO source contributions in the HNH and HSH based on the UCI-CTM CO tagged tracer run.

	HNH		HSH		Global	
	CO from each source (ppb)	Relative % Contribution	CO from each source (ppb)	Relative % Contribution	CO from each source (ppb)	Relative % Contribution
Anthropogenic (FF)	37	41%	4	9%	19	22%
Methane oxidation	23	27%	23	52%	26	34%
Anth-NMVOC +BVOC oxidation	24	26%	15	32%	23	35%
Biomass burning	6	7%	3	7%	7	9%

6.2.5 ACCMIP inventory

In this study, historical CO emissions from the Atmospheric Chemistry and Climate Modeling Intercomparison Project (ACCMIP) inventory were used to explore the CO trends during the twentieth century. The ACCMIP inventory provides a dataset of historical monthly, sectoral, gridded anthropogenic and biomass burning emissions covering 1850-2000 [*Lamarque et al,* 2010]. Global gridded emissions of CO and NMVOCs from anthropogenic and biomass burning sources are given at decadal time slices. The ACCMIP anthropogenic emissions are derived from a combination of many existing emission inventories, including RETRO [*Schultz et al.*, 2008], EDGAR-HYDE [*van Aardenne et al.*, 2001] and several others (EMEP, EPA, REAS). The ACCMIP biomass burning emissions are derived from the combined results of the GFEDv2, RETRO, and GICC datasets.

For the purpose of the this study, anthropogenic CO emissions from the ACCMIP inventory were modified to include direct and indirect CO emissions, taken as the sum of the total "Land Anthropogenic" emissions (sum of the 12 sectors reported in *Lamarque et al.* [2010]) and "Anthropogenic NMVOCs," assuming a yield λ=1.0 and a ratio of $(28\ g\ CO\ mol^{-1})/(12\ g\ C\ mol^{-1})$ for the production of CO due to oxidation of anthropogenic NMVOCs. The ACCMIP inventory was also extended to 2010 by applying constant emissions between 2000-2010. This was done for consistency of the years of the box model simulations (1900-2010).

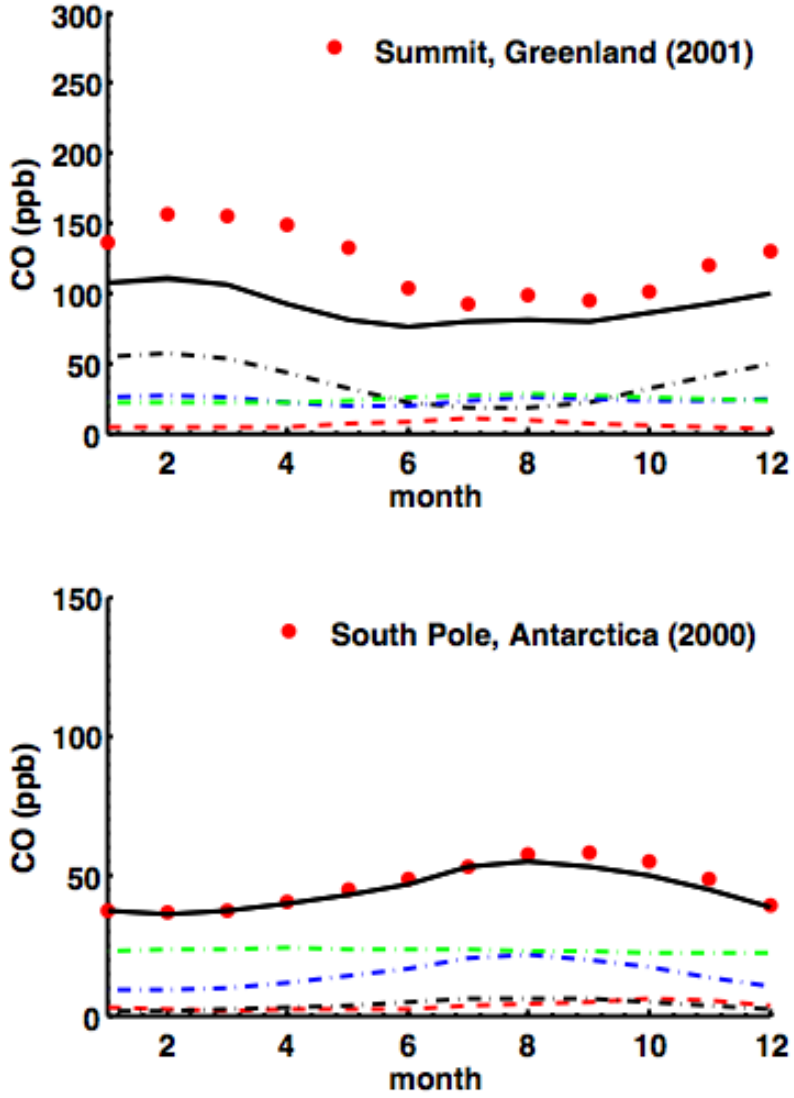

Figure 6.1: CO contributions from various sources to the high latitudes from the UCI Chemical Transport Model. CO levels from are shown from NOAA flask data (red circles) at Summit, Greenland (year 2001) and South Pole (year 2000). High latitude CO levels from the UCI-Chemical Transport Model are shown for the year 2000 (lines). Model results are shown for all CO sources (solid black line) and the relative contribution of CO emissions from biomass burning (red dashed line), anthropogenic (black dashed line), total-VOC oxidation (dashed blue line), and CH_4 oxidation (dashed green line). All model results shown represent the sum of 10 vertical layers in the UCI CTM. The CTM results for the high latitude Northern Hemisphere (60-90°N) are compared alongside the flask data from Summit, Greenland. The results for the high latitude Southern Hemisphere (60-90°S) are compared alongside the flask data from the South Pole.

6.3 Results and Discussion

This section describes the results derived using the box model. In the first model run, historical fossil fuel and biomass burning emissions from the ACCMIP inventory are prescribed in a forward box model run with fixed CH_4 and BVOC oxidative emissions of CO, as described above. Southern Hemisphere CO levels from the box are scaled using the HLR sensitivity factors and the model result was compared to the atmospheric history of CO from the South Pole (Chapter 5). In the next model runs, top-down anthropogenic and biomass burning emissions histories are derived for the Southern Hemisphere based on the South Pole firn air data. The Southern Hemisphere emissions are then scaled to calculate global emissions using the methods described in section 6.2 to derive CO mixing ratios in the high latitude Northern Hemisphere. The results are compared to the CO atmospheric history from Greenland determined by *Petrenko et al.* [2013]. The top-down CO emissions derived with the box model are also compared alongside the ACCMIP inventory.

6.3.1 Forward model run: ACCMIP anthropogenic and biomass burning emissions

We evaluated historical anthropogenic and biomass burning emissions from the ACCMIP inventory in a forward run with the 2-box CO model. Uncertainties in OH and CO oxidative emissions were prescribed as noted in section 6.2.2. Figure 6.2 shows the ACCMIP historical CO emissions for the Southern Hemisphere and the resulting atmospheric CO history for high southern latitudes (60-90°S). CO emissions histories for the Southern Hemisphere were determined using the modern fraction of sources the Southern Hemisphere box (Table 6.1) and the CO mixing ratio in the high latitude Southern Hemisphere (60-90°S) was determined as described in section 6.2.

The ACCMIP inventory shows rising CO emissions from anthropogenic and biomass burning sources during the twentieth century (Figure 6.2, a) [*Lamarque et al.*, 2010]. The results show CO levels from 60-90°S are underestimated during the mid-twentieth century, from about 1940-1980 (Figure 6.2, c). The model-data bias is not explained by the uncertainties in the CO lifetime (Figure 6.2, b) or oxidative CO emissions from CH_4 and BVOCs. This suggests that there are additional uncertainties in the major sources of CO that have not been explored. Anthropogenic and/or biomass burning emissions are the only remaining CO sources that are large enough to drive changes in atmospheric CO levels. In the remainder of this study, we derive top-down anthropogenic and biomass burning CO emissions histories based on the South Pole data.

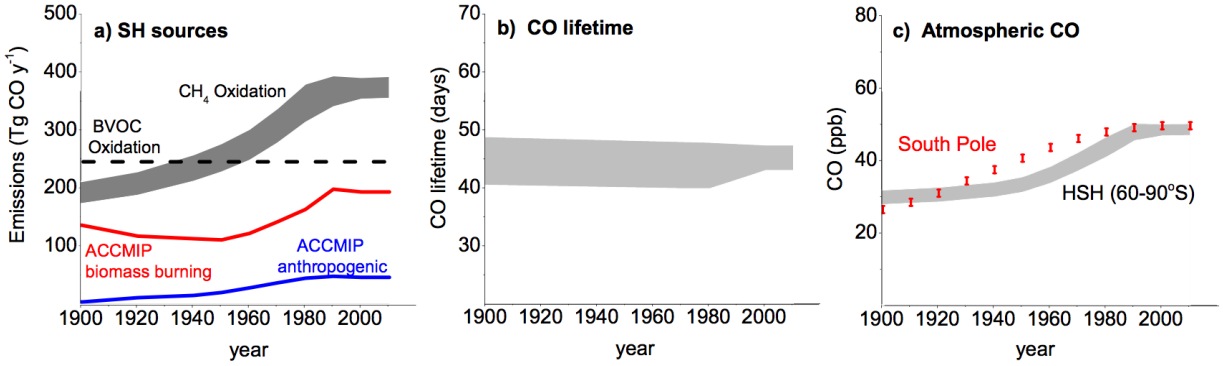

Figure 6.2: Historical ACCMIP CO emissions for the Southern Hemisphere and CO mixing ratios for the high latitude Southern Hemisphere (60-90 °S) compared with the atmospheric CO history derived from South Pole firn. a) CO emissions histories for the Southern Hemisphere: ACCMIP anthropogenic (solid black line) and biomass burning (red line) emissions [*Lamarque et al.*, 2010], prescribed CO emissions from the oxidation of BVOCs (dashed line, 250 Tg y^{-1} in the SH), and CO emissions due to oxidation of atmospheric CH_4 with uncertainties (dark grey band). ACCMIP emissions for the SH were calculated using the source fractions from the CO box model (see text). b) CO lifetime (black line), with uncertainties based on the historical OH trend from *Naik et al.*, [2013] (shaded area, see text). The width of the band reflects the uncertainty in OH. c) Atmospheric CO history over South Pole, Antarctica (red bars) and modeled CO mole fraction from 60-90° S (grey band) based on the source and sink histories and uncertainties shown in panels (a-b). Error bars represent 1 ppb uncertainty in the measured CO level.

6.3.2 Southern Hemisphere CO emissions based on the South Pole firn record

The forward model run with the ACCMIP historical emissions suggests additional anthropogenic fossil fuel and/or biomass burning CO emissions are needed to achieve agreement with the South Pole CO history. In this section, we derive top-down CO emissions consistent with the South Pole CO history. Changes in other CO sources and sinks are identical to those described in Section 6.3.1. The model results are discussed below and are shown in Figure 6.3.

Scenario 1: Optimized anthropogenic emissions - Southern Hemisphere anthropogenic CO emissions were derived based on the South Pole atmospheric history, using a biomass burning source fixed to the ACCMIP inventory (Figure 6.3, a-c). The anthropogenic fossil fuel emissions history for the Southern Hemisphere show a rise from about 10 Tg y^{-1} in 1920, reaching a peak at about 85 Tg y^{-1} between 1960-1970, followed by a decline, reaching roughly constant emissions of 60 Tg y^{-1} between 2000-2010. The peak in the anthropogenic fossil fuel emissions between 1960-1970 is three times larger than the fossil fuel emissions estimate for the ACCMIP inventory during the same period (roughly 30 Tg y^{-1}). The shape of the rise in CO emissions is also very different between the two inventories. The ACCMIP inventory shows a continuous rise beginning in 1900, with emissions peaking and 1990 and stable thereafter (Figure 6.2, *Lamarque et al.*, 2010], while the inventory from this study shows a rise, peak, and decline. The emissions history from this study estimates Southern Hemisphere fossil fuel emissions were about 25 Tg y^{-1} higher from 1990-2010 compared to the ACCMIP inventory.

Scenario 2: Optimized biomass burning emissions - Southern Hemisphere biomass burning emissions were derived based on the South Pole atmospheric history, using anthropogenic fossil fuel emissions fixed to the ACCMIP inventory (Figure 6.3, d-f). The biomass burning emissions

show a rise from 1900-1970, followed by a peak and small decline. The biomass burning emissions history from this study shows about a doubling of emissions from about 100-150 Tg y^{-1} between 1900-1920, reaching a peak of 320 Tg y^{-1} between 1960-1970, followed by a small decline between 1970-1990, with roughly constant emissions at 270 Tg y^{-1} after 1990. This is very different from the ACCMIP biomass burning emissions history, which show a continuous rise in emissions from 1950-1990, with constant emissions after 1990 (Figure 6.2) [*Lamarque et al.*, 2010].

The CTM studies show that anthropogenic fossil fuel and biomass burning emissions both comprise a small fraction of the total CO at high Southern latitudes (Figure 6.1). Relatively, the biomass burning emissions impact the CO mixing ratios at the South Pole is larger than the anthropogenic fossil fuel emissions (on a ppb/Tg basis). Unfortunately, the South Pole atmospheric history of CO cannot differentiate between these two sources. In the next section, we test these model results by comparing to the CO reconstruction for the high latitude Northern Hemisphere, which provides an additional constraint on the CO sources [*Petrenko et al.,* 2013].

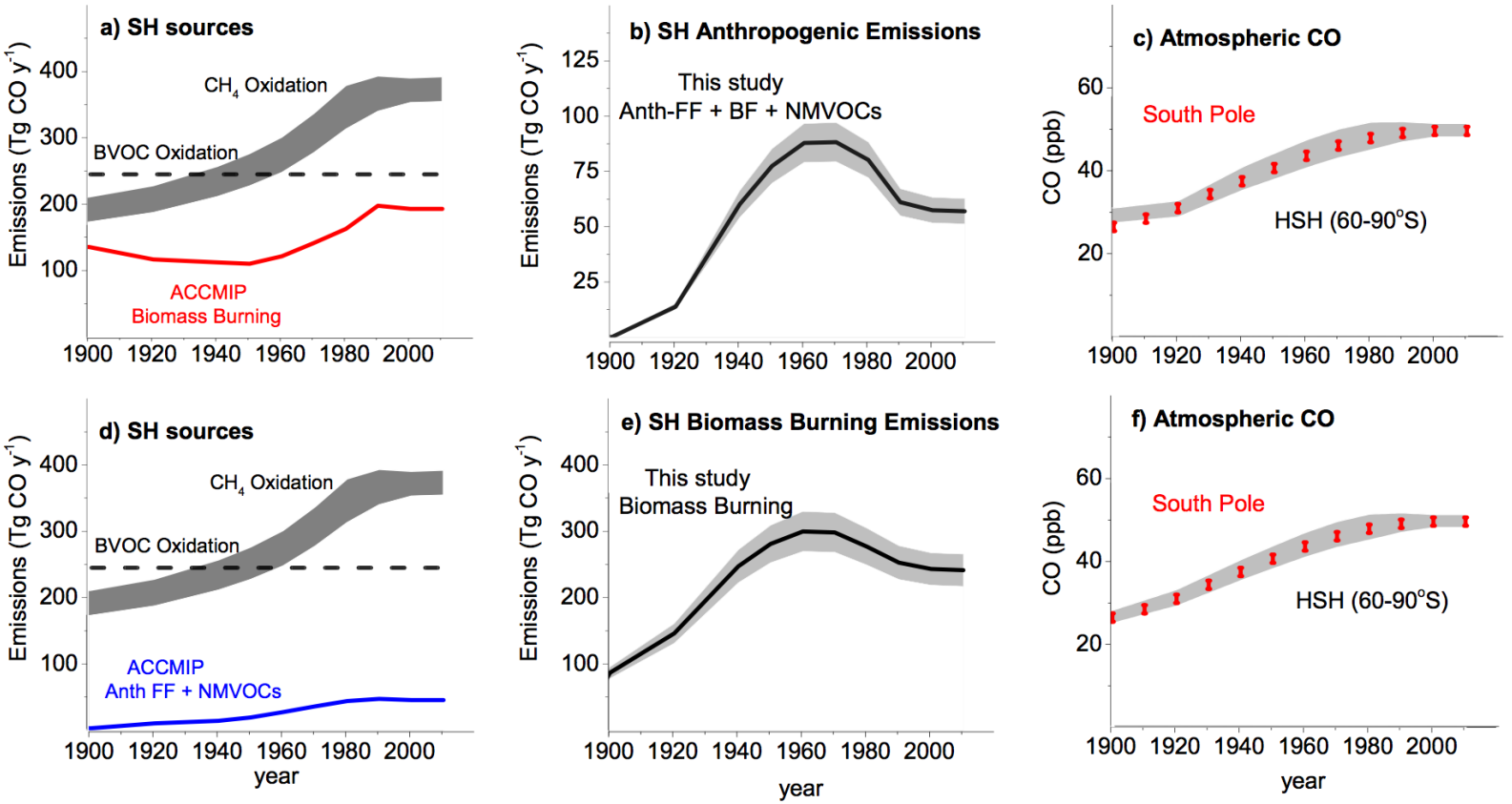

Figure 6.3: Top-down CO emissions histories for the Southern Hemisphere based on the CO atmospheric history derived from South Pole firn air. a) CO emissions histories for the Southern Hemisphere: ACCMIP biomass burning emissions (red line, *Lamarque et al.*, 2010), prescribed CO emissions from the oxidation of BVOCs (dashed lines, ~150-240 Tg y^{-1}), and CO emissions from atmospheric oxidation of CH_4 (dark grey band, see text). ACCMIP emissions for the Southern Hemisphere were calculated using the source fractions from the CO box model (see text). b) Anthropogenic CO emissions, based on fit to the South Pole history (black line) with 10% uncertainty (grey band). c) Atmospheric CO history at South Pole, Antarctica (red bars) and modeled CO mole fractions from 60-90° S (grey band) based on the source histories shown in panels (a-b). Error bars represent the 1ppb uncertainty in the measured CO level. The grey band reflects uncertainties in CO emissions from oxidation of CH_4 and BVOCs, and the OH lifetime of CO (see text and Figure 6.1, b). d) Same as panel (a), except with anthropogenic emissions from the ACCMIP inventory (blue line, *Lamarque et al.*, 2010). e) Biomass burning CO emissions fit to the South Pole history (black line) with 10% uncertainty (grey band) f) Atmospheric CO history over South Pole, Antarctica (red bars) and modeled CO mole fraction from 60-90°S (grey band) based on the source histories shown in panels (d-e) The SH emissions from the ACCMIP inventory were calculated using the source fractions from the CO box model (see text).

6.3.3 Inferring global CO emissions from the South Pole firn record

The two-box model is used to scale the Southern Hemisphere CO emissions histories from Figure 6.3 to the global atmosphere. Global CO emissions are calculated using the source fractions shown in Table 6.1 and the CO levels at high latitudes are determined using the HLRs (Table 6.4). The global emission histories in Figure 6.4 are constrained by the South Pole firn alone and the model result is compared alongside the atmospheric CO history derived from Greenland firn air from 1950-2006 using firn air observations from the Summit, NGRIP, and NEEM in Greenland [*Petrenko et al.,* 2013]. The Greenland atmospheric history is extended from 2006 to 2010 by extrapolating with surface flask data (Figure A5). To do this, we use the zonal mean in the high northern latitudes (30-90°N), based on surface flask observations [*Novelli and Masarie,* 2013].

Scenario 1: Global anthropogenic emissions optimized to South Pole – The box model result shows global anthropogenic fossil fuel CO emissions rising from around 250 Tg y^{-1} in 1910, reaching a peak around 1800 Tg y^{-1} between 1960-1970, followed by a decline from 1970-1990 and stable emissions around 1200 Tg y^{-1} after the 2000 (Figure 6.4b). The model result shows good agreement with the CO histories at both high latitude sites (Figure 6.4c). The model slightly overestimates the CO levels in the HNH in 2010, by roughly 10%. This likely reflects the fact that the model was only constrained to the South Pole firn history, and fossil fuel emissions make up <10% of the atmospheric CO levels at the South Pole. This could also be due to uncertainty in the N/S ratio of CO anthropogenic emissions, which was fixed using $f_{N,ff} = 0.95$. The result for the last 20 years could be improved if the box model result was also forced to fit to the CO levels at high Northern latitudes in 2010, or if larger uncertainties were taken into account in the model result, such as uncertainties in BVOC oxidative emissions.

Scenario 2: Global biomass burning emissions optimized to South Pole – The model result shows global CO biomass burning emissions rising from around 350 Tg y^{-1} in 1920, followed by a peak around 760 Tg y^{-1} between 1960-1970, and a small decline, with emissions stabilizing around 630 Tg y^{-1} in 2000-2010 (Figure 6.4e). The biomass burning emissions history underestimates the CO levels at high Northern latitudes from 1950-2000. The model result reflects the distribution of biomass burning emissions, which impact CO levels similarly in both hemispheres.

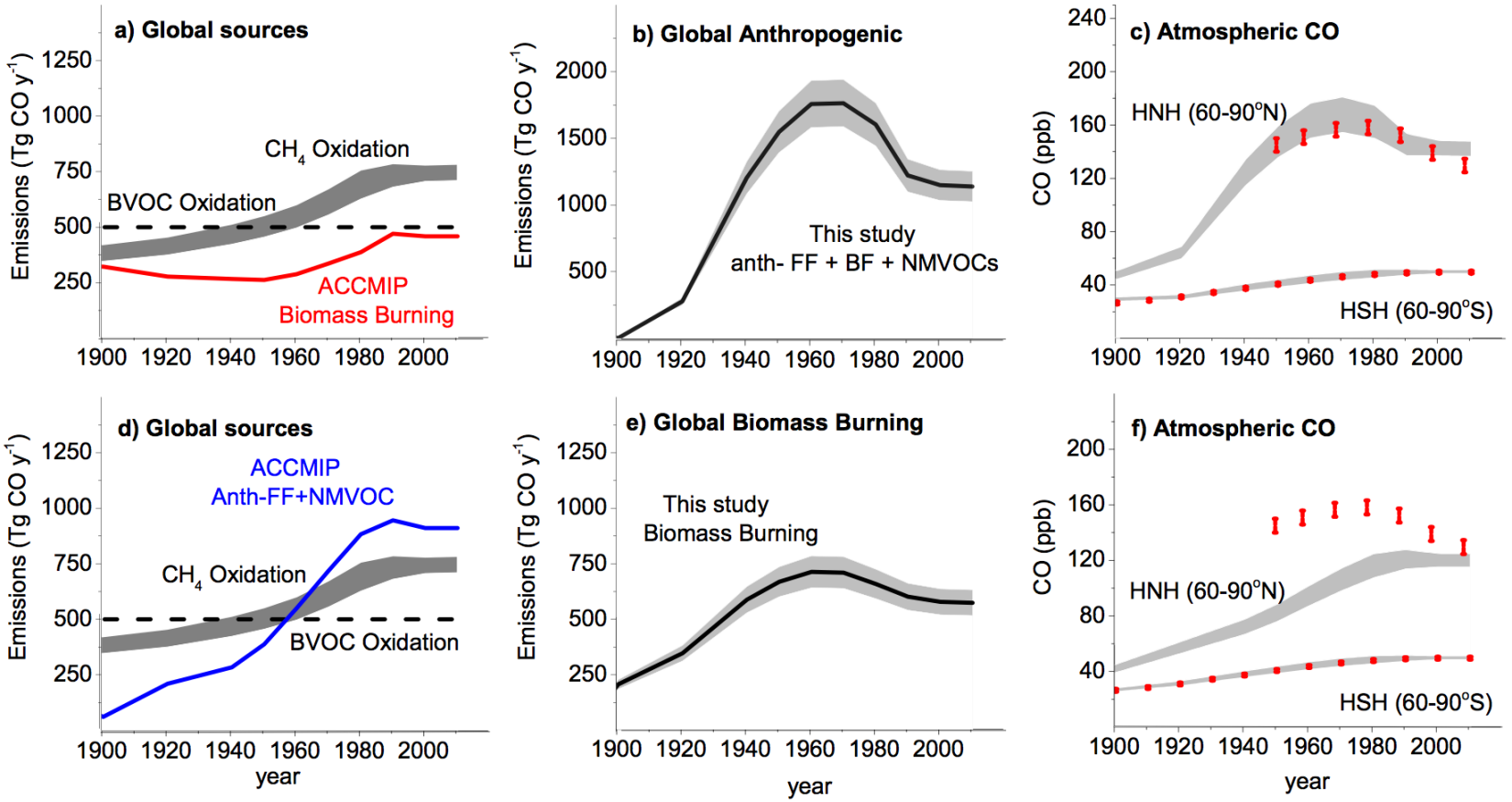

Figure 6.4: Top-down CO emissions histories for the global atmosphere based on the CO atmospheric history derived from South Pole firn air, scaled to the high latitude Northern Hemisphere. a) Global CO emissions histories: ACCMIP biomass burning emissions (red line, *Lamarque et al*., 2010), prescribed CO emissions from the oxidation of BVOCs (dashed lines, 400-600 Tg y^{-1}), and CO emissions from atmospheric oxidation of CH_4 (dark grey band, see text). ACCMIP emissions for the Southern Hemisphere were calculated using the source fractions from the CO box model (see text). b) Anthropogenic CO emissions, based on the South Pole history (black line) with 10% uncertainty (grey band). c) Atmospheric CO history based on the South Pole and Greenland firn air records (red bars, this study and *Petrenko et al*., 2013). Modeled CO mole fractions are shown from 60-90°N and 60-90°S (grey bands) based on the source histories shown in panels (a-b). Error bars represent the uncertainty in the CO atmospheric reconstruction for Greenland [*Petrenko et al*., 2013]. The grey band reflects uncertainties in CO emissions from oxidation of CH_4, and the OH lifetime of CO (see text and Figure 6.1b). d) Same as panel (a), except with anthropogenic emissions from the ACCMIP inventory (blue line, *Lamarque et al*., 2010). e) Biomass burning CO emissions based on the South Pole history (black line) with 10% uncertainty band. f) Same as panel (c), with the modeled CO mole fractions (grey bands) based on the source histories shown in panels (d-e).

6.3.5 CO production from oxidation of anthropogenic NMVOCs

The levels of several light alkanes have decreased globally during the last few decades, including ethane, propane, i/n-butane, and i/n-pentane [*Helmig et al.*, 2014; *Worton et al.*, 2012; *Simpson et al.*, 2012; *Aydin et al.*, 2011]. Oxidation of these anthropogenic NMVOCs indirectly leads to production of CO. Therefore, at least part of the CO decline in the high latitude Northern Hemisphere during the late twentieth century may be due to decreased emissions from NMVOCs. Atmospheric histories of these six NMVOCs have been reconstructed in Arctic firn air and surface air flasks. We estimate the change in CO due to NMVOCs as follows:

$$\Delta\,[\mathrm{CO}]_{1980-2000}^{NMVOC\ Oxid}\ (ppb\ CO) = \gamma\left(\frac{\tau_{CO,OH}}{\tau_{NMVOC,OH}}\right) * (\Delta\,[NMVOC]_{1980-2000})\ \ (ppb\ NMVOC) \qquad (6.12)$$

where $\Delta[\mathrm{CO}]_{1980-2000}^{NMVOC\ Oxid}$ is the change in atmospheric CO levels (in ppb) due to the oxidation of NMVOCs from 1980-2000, $\frac{\tau_{CO,OH}}{\tau_{NMVOC,OH}}$ is the ratio of the tropospheric lifetimes (in years) for the reaction of CO+OH and NMVOC+OH, $\Delta\,[NMVOC]_{1980-2000}$ is the change in the atmospheric levels of NMVOC (in ppb) in the high latitude Northern Hemisphere from 1980 to 2000, based on four independent studies [*Helmig et al.*, 2014; *Worton et al.*, 2012; *Simpson et al.*, 2012; *Aydin et al.*, 2011]. We assume a CO lifetime due to reaction with OH ($\tau_{CO,OH}$) of 0.1315 y and a yield (γ) equal to 1.0 for the conversion of six NMVOCs to CO (ethane, propane, i/n-butane, and i/n-pentane). To simplify the calculation, it is assumed that the levels of these six alkanes peaked in 1980 and declined until 2000, although there may be small differences in the timing of the peak for each compound [*Helmig et al.,* 2014]. Table 6.6 shows the NMVOC lifetimes, ΔNMVOC (based combined results from the independent studies), and estimated ΔCO for each NMVOC.

Petrenko et al. [2013] showed that CO levels in the HNH declined from 158-137 ppb (about 21 ppb CO) from 1980-2000. We estimate oxidation of the six light anthropogenic NMVOCs could be responsible for up to 3 ppb / 21 ppb, or about 15% of the CO decline. The actual amount of CO produced by anthropogenic NMVOC oxidation in the atmosphere depends on the speciation of the NMVOCs and the fraction of carbon molecules in the compound that are oxidized to CO. The global impact of the decline NMVOCs on global atmospheric CO levels is uncertain because: 1) the magnitude of the decline in these six anthropogenic NMVOCs is not well known at mid latitudes, 2) atmospheric trends in other anthropogenic NMVOCs that produce CO are not well known, and 3) the amount of CO produced from these compounds (i.e. the molar yield) is not well constrained.

Table 6.6: Estimated decline in atmospheric CO levels due to reductions in NMVOC levels in the high latitude Northern Hemisphere. NMVOC results are based on firn air and ambient surface flask measurements from four independent studies*. Atmospheric lifetimes are reported based on *Helmig et al.,* [2014]. ΔCO calculated assuming a yield, γ=1.

	Lifetime days	NMVOC (ppb) yr 1980*	NMVOC (ppb) yr 2000*	ΔNMVOC (ppb) 1980-2000	Δ CO (ppb) 1980-2000
Ethane	66	2.0	1.56	-0.44	-0.32
Propane	15	0.76	0.52	-0.24	-0.77
i-butane	7.6	0.14	0.095	-0.05	-0.28
n-butane	7	0.3	0.2	-0.10	-0.69
i-pentane	4.6	0.12	0.07	-0.05	-0.52
n-pentane	4.5	0.1	0.063	-0.04	-0.39
Total					-2.97

* NMVOC trends based on: *Helmig et al.* [2014]; *Worton et al.* [2012]; *Simpson et al.* [2012]*; Aydin et al.* [2011].

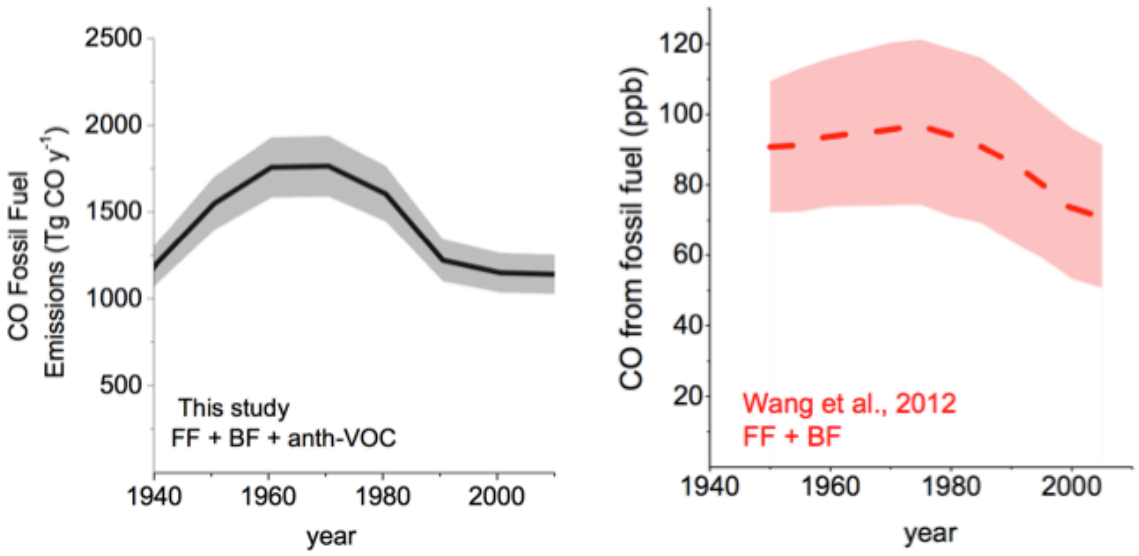

Figure 6.5: Comparison of CO anthropogenic fossil fuel histories from a) this study and b) *Wang et al.* [2012]. a) Global CO anthropogenic fossil fuel emissions from direct and indirect sources (black line, with 10% uncertainty due to OH shown by the grey band). b) Sum of the direct CO (in ppb) from fossil fuels and biofuels sources at high Northern latitudes, based on a mass balance model result constrained by the atmospheric history of CO its stable isotopes from Greenland firn air (dashed red line, with shaded area showing 50% model uncertainty) [*Wang et al.,* 2012].

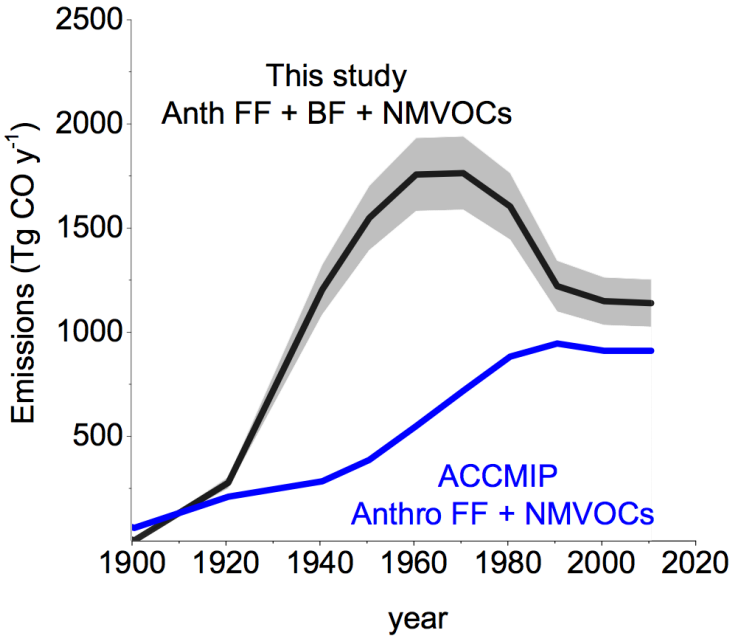

Figure 6.6: Carbon monoxide anthropogenic emissions history from this study compared alongside land anthropogenic emissions of carbon monoxide from the ACCMIP inventory [*Lamarque et al.,* 2010]. Global CO anthropogenic emissions from this study (sum of direct fossil fuel, NMVOC, and biofuels) are shown by the black line and shaded band, indicating 10% uncertainty. The ACCMIP anthropogenic emissions are shown from 1900-2010 by the blue line and include the sum of the land anthropogenic emissions (from 12 sectors reported by *Lamarque et al.* [2010] and anthropogenic NMVOC emissions, assuming a yield of 1 and a ratio of $(28\ g\ CO\ mol^{-1})/(12\ g\ C\ mol^{-1})$.

6.3.3 What caused the CO variability during the 20th century?

The CO atmospheric histories presented here and by *Petrenko et al.* [2013] offer a new constraint on the global emissions of CO during the twentieth century. Surprisingly, CO levels declined in the high latitude Northern Hemisphere after the 1980s [*Petrenko et al.,* 2013] and stabilized in the high latitude Southern Hemisphere over the same period (this study). The strong decline in CO levels in the Northern Hemisphere implies that the changes after 1980 were primarily driven by a source in the Northern Hemisphere, which is where most of the fossil fuel CO emissions are located.

When the Southern Hemisphere CO emissions are scaled to the global atmosphere, the result shows a surprising level of agreement with the CO history from high Northern latitudes based on the Greenland firn air reconstructions and surface flask data [*Novelli and Masarie*, 2013; *Petrenko et al.*, 2013] between 1950-2000. The rise, peak, and decline in anthropogenic fossil fuel emissions are constrained by the South Pole data alone. The largest disagreement for the CO concentration at high Northern latitudes is in 2010. This may reflect the uncertainties in BVOC oxidative emissions, which are not included in the data analysis. The box model result confirms earlier studies that suggest that the Northern Hemisphere CO decline could not have been driven by changes in biomass burning alone [*Wang et al.*, 2012; *Petrenko et al.*, 2013].

The box model results are consistent with a rise in anthropogenic fossil fuel emissions from the early twentieth century until the 1960s and 1970s, followed by about a 30% decline in from 1970-2010 (from 1750 to 1200 Tg y^{-1}). The fossil fuel emissions history from the box model includes direct fossil fuel emissions and oxidative emissions from anthropogenic NMVOCs, which should have roughly the same source distribution as fossil fuels, and thus would impact CO mixing ratios at the poles similar to direct fossil fuels. The calculations in section 6.3.5

suggest that declining emissions of anthropogenic NMVOCs contributed up to (or less than) 15% of the total CO decline. Therefore, we attribute most of the CO decline from 1980-2010 (roughly 15-20%) due to decreases direct fossil fuel CO emissions. The results from this study roughly agree with an earlier CO fossil fuel reconstruction based on the Greenland firn air measurements of [CO] concentrations and ^{18}O isotopes [*Wang et al.*, 2012; *Petrenko et al.*, 2013]. The results from a mass balance model show about a 25-30% decrease in CO from fossil fuels (from roughly 85 to 65 ppb CO) from 1970 to 2005 (Figure 6.5) [*Wang et al.*, 2012]. The model result from this study is within the uncertainty of the *Wang et al.,* [2012] estimate, suggesting the South Pole firn air record provides a new constraint on the magnitude of global anthropogenic fossil fuel emissions during the twentieth century. We attribute most decline in atmospheric CO levels in the Northern Hemisphere after 1980 to changes in direct anthropogenic fossil fuel emissions, as suggested in these earlier studies [*Wang et al.*, 2012; *Petrenko et al.*, 2013].

The anthropogenic fossil fuel emissions history from this study is very different than the ACCMIP fossil fuel emissions (Figure 6.6). The emissions history based on the South Pole firn-air shows a rise in anthropogenic fossil fuel emissions from 1900-1960, with a peak in1960-1970, while the ACCMIP inventory shows a continuous rise beginning in 1900, with emissions peaking and 1990 and stable thereafter (Figure 6.6, *Lamarque et al.*, 2010]. The inventory from this study shows a peak in fossil fuel emissions that is more than double the magnitude of the ACCMIP estimate. In addition, the fossil fuel emissions decline based on the firn air records occurs when the ACCMIP inventory estimates the steepest rise in fossil fuel emissions.

This study highlights the use of firn air records from Greenland and Antarctica as a new constraint on historical anthropogenic CO emissions estimates. In general, bottom up inventories are constrained using knowledge of present-day atmospheric budgets and lifetimes. Historical

emissions are then estimated by scaling the results for present-day and incorporating known changes in emissions activities (or emissions factors) for prior decades. Firn air records allow us to constrain emissions for earlier time periods, for which atmospheric data is not available, and can also be used to test for consistency with bottom-up approaches. Additionally, firn air records can help improve our understanding of how atmospheric CO levels are impacted by different mixtures of emissions and changes in anthropogenic activities.

The CO decline in the high latitude Northern Hemisphere may be associated with reduced emissions from the road transportation sector and the introduction of catalytic converters following implementation of clean air policies in the US and Europe in the 1970s and 1980s [*Petrenko et al.*, 2013; *Wang et al.,* 2012]. The catalytic converter was designed to oxidize partially combusted hydrocarbons and CO from motor vehicle exhaust into CO_2. The catalytic converter was first introduced in cars in the US in 1968, and in Europe in 1975. *Petrenko et al.,* [2013] argue that it is possible that a small (few percent) increase in OH levels may have contributed to the atmospheric CO decrease during the 1980s. Although possible, it appears unlikely that changes in global OH contributed significantly to the atmospheric CO trends throughout the 20th century. Recent studies show that the interannual variations of global OH were less than 10% since the late 1970s and were likely even smaller (less than 5%) during the period 1985-2008 [*Prinn*, 2005; *Montzka et al.*, 2011]. Simulations with 3D coupled chemistry-climate models suggest that global OH levels are relatively well buffered and did not change significantly during the twentieth century [*Lelieveld and Dentener*, 2004; *Naik et al.*, 2013].

6.4 Conclusions

- This study utilized atmospheric CO histories from both poles to investigate CO emissions during the twentieth century. Simulations with a three-dimensional Chemical Transport Model (CTM) were used to investigate the modern day sources of CO. The results from perturbation experiments and tagged tracer runs were used in the parameterization of a simple two-box model of atmospheric CO. The box model was used to optimize the fit to the South Pole CO atmospheric history using various assumptions about anthropogenic and biomass burning emissions during the 20th century.
- A forward run with the CO box model shows that the CO rise at the South Pole requires additional emissions from either biomass burning or anthropogenic fossil fuel sources between 1940-1980. The rise in CO levels at the South Pole was larger than is predicted by the ACCMIP biomass burning and fossil fuel emissions inventories between 1940-1980.
- An inverse modeling technique was used to optimize anthropogenic fossil fuel and biomass burning emissions of CO during the twentieth century based on the South Pole atmospheric history. The box-model derived anthropogenic emissions history produces a CO history for the high latitude Northern Hemisphere that matches the CO reconstruction based on Greenland firn air measurements from *Petrenko et al.,* [2013]. These results suggest that CO levels in the high latitude Southern Hemisphere provide a relatively good constraint on global CO emissions during the twentieth century. This is surprising given that anthropogenic fossil fuels comprise a relatively small part of the atmospheric CO budget in the Southern Hemisphere (about 8%).

- The decline in Northern Hemisphere CO levels is most likely due to a roughly 15-25% reduction in direct fossil fuel emissions of CO, with a smaller contribution from reduced levels of anthropogenic NMVOCs in the Northern Hemisphere since the 1980s. The decline in atmospheric CO levels in the Northern Hemisphere may be related to reduced emissions from the road transportation sector and the introduction of catalytic converters after the implementation of clean air policies in the US and Europe in the 1970s and 1980s, as suggested in earlier studies [*Wang et al.,* 2012; *Petrenko et al.,* 2013]. Reduced emissions of anthropogenically produced NMVOCs may have contributed up to 15% (3 ppb) of the 21 ppb CO decline in the high latitude Northern Hemisphere between 1980-2000.

References

van Aardenne, J. A., F. J. Dentener, J. G. J. Olivier, C. G. M. Klein Goldewijk, and J. Lelieveld (2001), A 1 x 1 degree resolution dataset of historical anthropogenic trace gas emissions for the period 1890-1990, *Global Biogeochem. Cycles*, *15*(4), 909–928.

Aydin, M., K. R. Verhulst, E. S. Saltzman, M. O. Battle, S. A. Montzka, D. R. Blake, Q. Tang, and M. J. Prather (2011), Recent decreases in fossil-fuel emissions of ethane and methane derived from firn air, *Nature*, *476*(7359), 198–201, doi:10.1038/nature10352.

Bergamaschi, P., R. Hein, M. Heimann, and J. Crutzen (2000), Inverse modeling of the global CO cycle 1. Inversion of CO mixing ratios, *J. Geophys. Res.*, *105*(D2), 1909–1927.

Denman, K. L. et al. (2007), *2007: Couplings Between Changes in the Climate System and Biogeochemistry. In: Climate Change 2007: The Physical Science Basis. Contribution of Working Group I to the Fourth Assessment Report of the Intergovernmental Panel on Climate Change*, edited by M. T. and H. L. M. (eds.). Solomon, S., D. Qin, M. Manning, Z. Chen, M. Marquis, K.B. Averyt, Cambridge Univ. Press, Cambridge and New York.

Duncan, B. N., J. A. Logan, I. Bey, I. A. Megretskaia, R. M. Yantosca, P. C. Novelli, N. B. Jones, and C. P. Rinsland (2007), Global budget of CO, 1988–1997: Source estimates and validation with a global model, *J. Geophys. Res.*, *112*(D22), 1–29, doi:10.1029/2007JD008459.

Etheridge, D. M., L. P. Steele, R. J. Francey, and R. L. Langenfelds (1998), Atmospheric methane between 1000 A.D. and present: Evidence of anthropogenic emissions and climatic variability, *J Geophys Res.*, *103*(D13), 15979–15993.

Guenther, A., C. N. Hewitt, D. Erickson, R. Fall, C. Geron, T. Graedel, P. Harley, L. Klinger, M. Lerdau, W. A. McKay, T. Pierce, B. Scholes, R. Steinbrecher, R. Tallamraju, J. Taylor, and P. Zimmerman (1995), A global model of natural volatile organic compound emissions, *J. Geophys. Res.*, 100 (D5), 8873-8892.

Guenther, A. B., X. Jiang, C. L. Heald, T. Sakulyanontvittaya, T. Duhl, L. K. Emmons, and X. Wang (2012), The Model of Emissions of Gases and Aerosols from Nature version 2.1 (MEGAN2.1): an extended and updated framework for modeling biogenic emissions, *Geosci. Model Dev.*, *5*(6), 1471–1492, doi:10.5194/gmd-5-1471-2012.

Helmig D., V. Petrenko, P. Martinerie, E. Witrant, T. Röckmann, A. Zuiderweg, R. Holzinger, J. Hueber, C. Thompson, J. W. C. White, W. Sturges, A. Baker, T. Blunier, D. Etheridge, M. Rubino, and P. Tans (2014), Reconstruction of Northern Hemisphere 1950–2010 atmospheric non-methane hydrocarbons, *Atmos. Chem. Phys.*, *14*(3), 1463–1483, doi:10.5194/acp-14-1463-2014.

Holmes, C. D., M. J. Prather, O. a. Søvde, and G. Myhre (2013), Future methane, hydroxyl, and their uncertainties: key climate and emission parameters for future predictions, *Atmos. Chem. Phys.*, *13*(1), 285–302, doi:10.5194/acp-13-285-2013.

Hoor, P. et al. (2009), The impact of traffic emissions on atmospheric ozone and OH : results from QUANTIFY, *Atmos. Chem. Phys.*, *9*, 3113–3136.

Kanakidou, M., and P. J. Crutzen (1999), The photochemical source of carbon monoxide: Importance, uncertainties and feedbacks, *Chemosph. Glob. Chang. Sci.*, *1*(1), 91–109, doi:10.1016/S1465-9972(99)00022-7.

Lamarque, J.-F. et al. (2010), Historical (1850–2000) gridded anthropogenic and biomass burning emissions of reactive gases and aerosols: methodology and application, *Atmos. Chem. Phys.*, *10*(15), 7017–7039, doi:10.5194/acp-10-7017-2010.

Lelieveld, J., and F. Dentener (2004), On the role of hydroxyl radicals in the self-cleansing capacity of the troposphere, *Atmos. Chem. Phys.*, *4*, 2337–2344.

Montzka, S., M. Krol, E. Dlugokencky, and B. Hall (2011), Small Interannual Variability of Global Atmospheric Hydroxyl, *Science*, 331, 67-69, doi:10.1126/science.1197640.

Naik, V., A. Voulgarakis, A. M. Fiore, L. W. Horowitz, J.-F. Lamarque, M. Lin, M. J. Prather, P. J. Young, D. Bergmann, P. J. Cameron-Smith, I. Cionni, W. J. Collins, S. B. Dalsøren, R. Doherty, V. Eyring, G. Faluvegi, G. A. Folberth, B. Josse, Y. H. Lee, I. A. MacKenzie, T. Nagashima, T. P. C. van Noije, D. A. Plummer, M. Righi, S. T. Rumbold, R.Skeie, D. T. Shindell, D. S. Stevenson, S. Strode, K. Sudo, S. Szopa, and G. Zeng (2013), Preindustrial to present-day changes in tropospheric hydroxyl radical and methane lifetime from the Atmospheric Chemistry and Climate Model Intercomparison Project (ACCMIP), *Atmos. Chem. Phys.*, *13*(10), 5277–5298, doi:10.5194/acp-13-5277-2013.

Novelli, P. C., and K. A. Masarie (2013), Atmospheric Cycle, Carbon Monoxide Dry Air Mole Fractions from the NOAA ESRL Carbon Cooperative Global Air Sampling Network, 1988-2012, Version: 2013-06-18.

Novelli, P. C., K. A. Masarie, P. M. Lang, B. D. Hall, R. C. Myers, and J. W. Elkins (2003), Reanalysis of tropospheric CO trends: Effects of the 1997 – 1998 wildfires, *J. Geophys. Res.*, *108*(D15), 4464, doi:10.1029/2002JD003031.

Petrenko, V. V., P. Martinerie, P. Novelli, D. M. Etheridge, I. Levin, Z. Wang, T. Blunier, J. Chappellaz, J. Kaiser, P. Lang, L. P. Steele, S. Hammer, J. Mak, R. L. Langenfelds, J. Schwander, J. P. Severinghaus, E. Witrant, G. Petron, M. O. Battle, G. Forster, W. T. Sturges, J.-F. Lamarque, K. Steffen, and J. W. C. White (2013), A 60 yr record of atmospheric carbon monoxide reconstructed from Greenland firn air, *Atmos. Chem. Phys.*, *13*, 7567–7585, doi:10.5194/acp-13-7567-2013.

Prinn, R. G. (2005), Evidence for variability of atmospheric hydroxyl radicals over the past quarter century, *Geophys. Res. Lett.*, *32*(7), L07809, doi:10.1029/2004GL022228.

Schultz, M. G., A. Heil, J. J. Hoelzemann, A. Spessa, K. Thonicke, J. G. Goldammer, A. C. Held, J. M. C. Pereira, and M. van het Bolscher (2008), Global wildland fire emissions from 1960 to 2000, *Global Biogeochem. Cycles*, *22*, GB2002, doi:10.1029/2007GB003031.

Simpson, I. J., F. S. Rowland, S. Meinardi, and D. R. Blake (2006), Influence of biomass burning during recent fluctuations in the slow growth of global tropospheric methane, *Geophys. Res. Lett.*, *33*(L22808), 1–5, doi:10.1029/2006GL027330.

Simpson, I. J., M. Andersen, S. Meinardi, L. Bruhwiler, N. J. Blake, D. Helmig, F. S. Rowland, and D. R. Blake (2012), Long-term decline of global atmospheric ethane concentrations and implications for methane, *Nature*, *488*, 490–494, doi:10.1038/nature11342.

Spivakovsky, C. M., J. A. Logan, S. A. Montzka, Y. J. Balkanski, M. Foreman-Fowler, D. B. A. Jones, L. W. Horowitz, A. C. Fusco, C. A. M. Brenninkmeijer, M. J, Prather, S. C. Wofsy, M. B. McElroy (2000), Three-dimensional climatological distribution of tropospheric OH: Update and evaluation, *J. Geophys. Res.,* 105, (D7), 8931-8980.

Wang, Z., J. Chappellaz, P. Martinerie, K. Park, V. Petrenko, E. Witrant, L. K. Emmons, T. Blunier, C. a. M. Brenninkmeijer, and J. E. Mak (2012), The isotopic record of Northern Hemisphere atmospheric carbon monoxide since 1950: implications for the CO budget, *Atmos. Chem. Phys.*, *12*(10), 4365–4377, doi:10.5194/acp-12-4365-2012.

Worton, D. R., W. T. Sturges, C. E. Reeves, M. J. Newland, S. A. Penkett, E. Atlas, V. Stroud, K. Johnson, N. Schmidbauer, S. Solberg, J. Schwander, J.-M. Barnola (2012), Evidence from firn air for recent decreases in non-methane hydrocarbons and a 20th century increase in nitrogen oxides in the northern hemisphere, *Atmos. Environ.*, *54*, 592–602, doi:10.1016/j.atmosenv.2012.02.084.

CHAPTER 7

Conclusions

7.1 Man's impact on ethane and carbon monoxide levels during the 20th century

This dissertation uses surface flask, firn air, and ice core measurements to examine variability in the levels of ethane and carbon monoxide over the past century. The data show that the atmospheric levels of these gases increased dramatically during the first half of the 20th century. The rising levels were likely due to increased anthropogenic fossil fuel use, with smaller contributions from the combustion of biomass and biofuels. In the latter half of the 20th century, atmospheric ethane and carbon monoxide levels declined [*Aydin et al.*, 2011; *Petrenko et al.*, 2013]. This is surprising because fossil fuel use increased dramatically during the last 50 years. The post-1980's decline in atmospheric ethane levels over Greenland is much larger than the decline over Antarctica. Atmospheric carbon monoxide levels over Greenland declined since the 1970s, while levels over Antarctica show slowed growth in the 1980s, and near zero growth after the 1990s. The decline in the levels of both gases is strongest in the Northern Hemisphere, where the majority of fossil fuel emissions are located. This implies that the declining levels of ethane and carbon monoxide were driven by reductions in anthropogenic fossil fuel emissions in the Northern Hemisphere. It is unlikely that these trends were driven by changes in global OH (hydroxyl radicals). Observational and modeling studies suggest that the atmosphere is generally well buffered against large changes in OH over interannual timescales. These studies suggest that

global OH levels have changed relatively little during the last century [*Lelieveld and Dentener*, 2004; *Montzka et al.*, 2011; *Naik et al.*, 2013].

The peak, rollover, and decline in Northern Hemisphere ethane and carbon monoxide levels are surprising. These features are not reflected in bottom-up emissions estimates for these gases. Bottom-up inventories generally suggest that the emissions of both gases rose continuously from 1900-1990 AD, with constant emissions thereafter. This study highlights the value of using atmospheric observations to constrain historical trace gas emissions and to quantify uncertainties in bottom-up emissions inventories.

The ethane and carbon monoxide trends found in this study have been confirmed by recent work [*Assonov et al.*, 2007; *Aydin et al.*, 2011; *Simpson et al.*, 2012; *Worton et al.*, 2012; *Petrenko et al.*, 2013; *Helmig et al.*, 2014]. In the 1970s and 1980s, the US and Europe enacted legislation targeted at reducing air pollution. Air quality management regimes began with the US Clean Air Act of 1963 and its Amendments in 1977 and 1990, and with the EU Directives in 1980. Through these policies, standards were put in place to limit air pollution from various sources, including motor vehicles, power plants, municipal waste incinerators, and many smaller emission sources, to target gases such as carbon monoxide, hydrocarbons, sulfur dioxide, nitrogen oxides, and suspended particulates such as lead. Clean air strategies for motor vehicles included the use of catalytic converters, which effectively decrease emissions from engine exhaust by oxidizing carbon monoxide and partially combusted hydrocarbons to carbon dioxide. Catalytic convertors were first introduced in the US in 1968 and in Europe in 1975, and later became mandatory. As a result, their use led to significant reductions in CO emissions from the transportation sector since the 1970s (in the US) and the 1980s and 1990s (in Europe) [*Parrish*, 2006; *Monks et al.*, 2009].

Ethane emissions from the fossil fuel sector are mainly associated with the production, processing, and/or transmission of natural gas and oil, and not due to combustion processes. The major ethane fossil fuel sources come from so-called "fugitive emissions", which include emissions from vented or flared gas, evaporative losses from oil and gas fields, and leaks from equipment, pipelines, and/or storage tanks [*Simpson et al.*, 2012]. *Stern and Kaufmann* [1996] estimated that the volumes of flared natural gas peaked in the 1970s, declined, and then stabilized during the mid-1990s. The reductions in gas flaring may have been associated with economics, due to the rising cost of natural gas. Unlike carbon monoxide, ethane emissions are fairly insensitive to the effects of catalytic convertors [*Simpson et al.*, 2012]. It is more likely that the ethane decline was due to a reduction in flaring of natural gas or associated gas (i.e. natural gas from oil fields) [*Aydin et al.*, 2011; *Simpson et al.*, 2012].

The atmospheric histories of ethane and carbon monoxide could be used to improve our understanding of man's impact on tropospheric photochemistry and the atmosphere's oxidative capacity. Ethane and carbon monoxide are precursors to tropospheric ozone formation. These gases also impact the atmosphere's oxidative capacity through their reaction with OH, the primary loss pathway. The 20th century trends of these gases could be used to examine changes in global OH and ground-level ozone. Feedbacks between the CO-CH_4-OH-NO_x-VOC system could also be explored using these trends. Although CO itself is not an important greenhouse gas, it indirectly influences the abundance and lifetime of tropospheric ozone and methane (CH_4), and thus impacts earth's radiative budget. Future research questions could address these impacts on tropospheric chemistry, for example:

1) How did rising levels of carbon monoxide and ethane impact OH and tropospheric ozone during the 20th century?

2) Did the changes in these gases impact the atmosphere differently between the pre-industrial period and 1980, and from 1980 -2010?
3) What impact, if any, did these gases have on the lifetime of atmospheric methane? Can this information help reduce uncertainties in future projections of atmospheric methane growth?

7.2 Feasibility of reconstructing a long-term ethane record from polar ice

In the current atmosphere, methane and ethane are co-emitted from fossil fuel, biofuel, and biomass burning sources, with a potentially significant source from geologic seeps [*Rudolph*, 1995; *Xiao et al.*, 2008; *Etiope and Ciccioli*, 2009]. Recently, it has been proposed that geologic emissions constitute a significant fraction of the modern-day budgets of methane and ethane [*Etiope et al.*, 2008; *Etiope and Ciccioli*, 2009]. A pre-industrial ethane record from ice cores could help constrain the magnitude and variability of the natural emissions (biomass burning, and geologic) over long timescales.

This study made progress toward developing a method for reconstructing ethane levels from polar ice cores. The laboratory experiments show that it is possible to extract air from ice core bubbles via wet extraction, with analytical blanks that are smaller than the levels of ethane in the ancient air. The preliminary data suggest that an atmospheric ethane signal is preserved in the Antarctic and Greenland ice core bubbles. The ethane signal in the Antarctic ice core bubbles is small (roughly 140±50 ppt). It appears likely that prior analyses of ethane in Greenland ice cores using dry extraction were contaminated, and it should be possible to reconstruct paleo-atmospheric ethane levels from both hemispheres.

With records of atmospheric ethane from Greenland and Antarctic ice cores, one could determine the north-south interhemispheric gradient of atmospheric ethane in the pre-industrial

atmosphere. Differences in ethane variability between the two hemispheres would provide new information about 1) the relative on the magnitude of ethane emissions from fires and geologic sources in each hemisphere, 2) the relationship between burning and climate, and 3) about the factors controlling changes in atmospheric methane.

Figure 7.1 shows the existing ice core records of methane, ^{13}C-methane isotopes, ethane, and carbon monoxide from 900-1900 AD [*this study, Etheridge et al.*, 1998; *Wang et al.*, 2010; *Mitchell et al.*, 2011; *Sapart et al.*, 2012]. The records of methane, methane isotopes, and carbon monoxide imply significant changes in the biomass burning emissions during the last 1000 years. However, the trends in biomass burning based on the methane and carbon monoxide records are completely different. *Wang et al.* [2010] suggested that CO levels measured in Antarctic ice cores show a biomass burning minimum during the 1600s, and that biomass burning emissions of CO were significantly larger from 1800-1900 AD than at present. However, methane isotopes in Greenland and Antarctic ice cores estimate a minimum in pyrogenic emissions of methane around 1800 AD [*Ferretti et al.*, 2005; *Sapart et al.*, 2012]. A high-resolution ethane record, from both poles, could be compared alongside these and other biomass burning proxies (e.g. charcoal, organic acids) to constrain pre-industrial biomass burning emissions during the last 1000 years [*Etheridge et al.*, 1998; *Marlon et al.*, 2008; *Wang et al.*, 2010; *Mitchell et al.*, 2011; *Sapart et al.*, 2012]

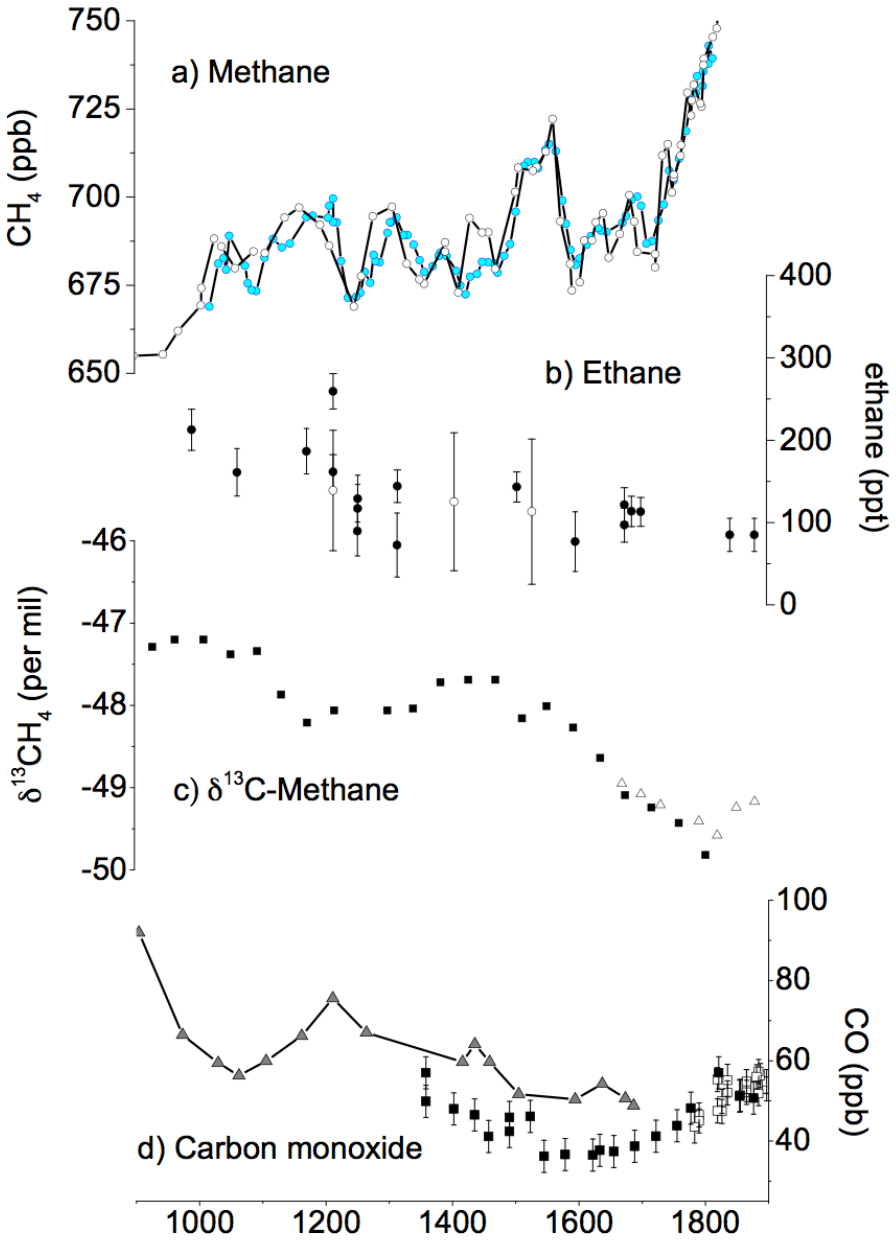

Figure 7.1: Atmospheric CH_4 levels during the last from 900-1900 AD, shown with ice core results for $\delta^{13}CH_4$, CO, and ethane. a) Atmospheric methane concentrations during the last 1000 years from the Law Dome compilation [*Etheridge et al.*, 1998; *MacFarling Meure et al.*, 2006] and the WDC-05A ice cores[*Mitchell et al.*, 2011]. WDC-05A data are plotted on the WDC05A:2 time scale. b) Ethane measurements from WAIS Divide (filled circles) and South Pole (open circles) ice cores using a wet extraction technique (this study). c) $\delta^{13}C$ of methane measurements in Greenland ice cores from the NEEM (squares) and Eurocore (triangles) ice cores [*Sapart et al.*, 2012]. d) Carbon monoxide measurements in Antarctic ice cores from the D47 (white squares) and South Pole (black squares) ice cores [*Wang et al.*, 2010].

References

Assonov, S. S., C. A. M. Brenninkmeijer, P. Jöckel, R. Mulvaney, S. Bernard, and J. Chappellaz (2007), Evidence for a CO increase in the SH during the 20th century based on firn air samples from Berkner Island, Antarctica, *Atmos. Chem. Phys.*, *7*(2), 295–308, doi:10.5194/acp-7-295-2007.

Aydin, M., K. R. Verhulst, E. S. Saltzman, M. O. Battle, S. A. Montzka, D. R. Blake, Q. Tang, and M. J. Prather (2011), Recent decreases in fossil-fuel emissions of ethane and methane derived from firn air, *Nature*, *476*(7359), 198–201, doi:10.1038/nature10352.

Etheridge, D. M., L. P. Steele, R. J. Francey, and R. L. Langenfelds (1998), Atmospheric methane between 1000 A.D. and present: Evidence of anthropogenic emissions and climatic variability, *J Geophys Res.*, *103*(D13), 15979–15993.

Etiope, G., and P. Ciccioli (2009), Earth's degassing: A missing ethane and propane source, *Science*, *323*, 4000.

Etiope, G., K. R. Lassey, R. W. Klusman, and E. Boschi (2008), Reappraisal of the fossil methane budget and related emission from geologic sources, *Geophys. Res. Lett.*, *35*(9), L09307, doi:10.1029/2008GL033623.

Ferretti, D. F, J. B. Miller, J. W. C. White, D. M. Etheridge, K. R. Lassey, D. C. Lowe, C. M. MacFarling Meure, M. F. Dreier, C. M. Trudinger, T. D. van Ommen, R. L. Langenfelds (2005), Unexpected changes to the global methane budget over the past 2000 years, *Science*, *309*(5741), 1714–7, doi:10.1126/science.1115193.

Helmig D., V. Petrenko, P. Martinerie, E. Witrant, T. Röckmann, A. Zuiderweg, R. Holzinger, J. Hueber, C. Thompson, J. W. C. White, W. Sturges, A. Baker, T. Blunier, D. Etheridge, M. Rubino, and P. Tans (2014), Reconstruction of Northern Hemisphere 1950–2010 atmospheric non-methane hydrocarbons, *Atmos. Chem. Phys.*, *14*(3), 1463–1483, doi:10.5194/acp-14-1463-2014.

Lelieveld, J., and F. Dentener (2004), On the role of hydroxyl radicals in the self-cleansing capacity of the troposphere, *Atmos. Chem. Phys.*, *4*, 2337–2344.

MacFarling Meure, C., D. Etheridge, C. Trudinger, P. Steele, R. Langenfelds, T. van Ommen, A. Smith, and J. Elkins (2006), Law Dome CO2, CH4 and N2O ice core records extended to 2000 years BP, *Geophys. Res. Lett.*, *33*(14), L14810, doi:10.1029/2006GL026152.

Marlon, J. R., P. J. Bartlein, C. Carcaillet, D. G. Gavin, S. P. Harrison, P. E. Higuera, F. Joos, M. J. Power, and I. C. Prentice (2008), Climate and human influences on global biomass burning over the past two millennia, *Nat. Geosci.*, *1*(10), 697–702, doi:10.1038/ngeo313.

Mitchell, L. E., E. J. Brook, T. Sowers, J. R. McConnell, and K. Taylor (2011), Multidecadal variability of atmospheric methane, 1000–1800 C.E., *J. Geophys. Res.*, *116*(G2), G02007, doi:10.1029/2010JG001441.

Monks, P. S. et al. (2009), Atmospheric composition change – global and regional air quality, *Atmos. Environ.*, *43*(33), 5268–5350, doi:10.1016/j.atmosenv.2009.08.021.

Montzka, S., M. Krol, E. Dlugokencky, and B. Hall (2011), Small Interannual Variability of Global Atmospheric Hydroxyl, *Science*, 331, 67-69, doi:10.1126/science.1197640.

Naik, V., A. Voulgarakis, A. M. Fiore, L. W. Horowitz, J.-F. Lamarque, M. Lin, M. J. Prather, P. J. Young, D. Bergmann, P. J. Cameron-Smith, I. Cionni, W. J. Collins, S. B. Dalsøren, R. Doherty, V. Eyring, G. Faluvegi, G. A. Folberth, B. Josse, Y. H. Lee, I. A. MacKenzie, T. Nagashima, T. P. C. van Noije, D. A. Plummer, M. Righi, S. T. Rumbold, R.Skeie, D. T. Shindell, D. S. Stevenson, S. Strode, K. Sudo, S. Szopa, and G. Zeng (2013), Preindustrial to present-day changes in tropospheric hydroxyl radical and methane lifetime from the Atmospheric Chemistry and Climate Model Intercomparison Project (ACCMIP), *Atmos. Chem. Phys.*, *13*(10), 5277–5298, doi:10.5194/acp-13-5277-2013.

Parrish, D. D. (2006), Critical evaluation of US on-road vehicle emission inventories, *40*, 2288–2300, doi:10.1016/j.atmosenv.2005.11.033.

Petrenko, V. V., P. Martinerie, P. Novelli, D. M. Etheridge, I. Levin, Z. Wang, T. Blunier, J. Chappellaz, J. Kaiser, P. Lang, L. P. Steele, S. Hammer, J. Mak, R. L. Langenfelds, J. Schwander, J. P. Severinghaus, E. Witrant, G. Petron, M. O. Battle, G. Forster, W. T. Sturges, J.-F. Lamarque, K. Steffen, and J. W. C. White (2013), A 60 yr record of atmospheric carbon monoxide reconstructed from Greenland firn air, *Atmos. Chem. Phys.*, *13*, 7567–7585, doi:10.5194/acp-13-7567-2013.

Rudolph, J. (1995), The tropospheric distribution and budget of ethane, *J. Geophys. Res.*, *100*(D6), 11369–11381.

Sapart, C. J. et al. (2012), Natural and anthropogenic variations in methane sources during the past two millennia., *Nature*, *490*(7418), 85–8, doi:10.1038/nature11461.

Simpson, I. J., M. Andersen, S. Meinardi, L. Bruhwiler, N. J. Blake, D. Helmig, F. S. Rowland, and D. R. Blake (2012), Long-term decline of global atmospheric ethane concentrations and implications for methane, *Nature*, *488*, 490–494, doi:10.1038/nature11342.

Stern, D. I., and R. K. Kaufmann (1996), Estimates of global anthropogenic methane emissions 1860-1993, *Chemosphere*, *33*(1), 159–176.

Wang, Z., J. Chappellaz, K. Park, and J. E. Mak (2010), Large variations in Southern Hemisphere biomass burning during the last 650 years, *Science*, *330*(6011), 1663–1666, doi:10.1126/science.1197257.

Worton, D. et al. (2012), Evidence from firn air for recent decreases in non-methane hydrocarbons and a 20th century increase in nitrogen oxides in the northern hemisphere, *Atmos. Environ.*, *54*, 592–602, doi:10.1016/j.atmosenv.2012.02.084.

Xiao, Y., J. A. Logan, D. J. Jacob, R. C. Hudman, R. Yantosca, and D. R. Blake (2008), Global budget of ethane and regional constraints on U.S. sources, *J. Geophys. Res.*, *113*(D21), D21306, doi:10.1029/2007JD009415.

Appendix A: Physical properties of South Pole firn

Table A1: Physical properties used in the 1D firn air advection-diffusion model for the South Pole firn air site.

Layer #	Depth (mbs)	Density	Open porosity	Diffusivity	Closed porosity
1	0.794309716	311.9297247	0.662219604	1.39E-05	1.65E-21
2	1.54203345	329.5948462	0.643090514	1.35E-05	7.61E-21
3	2.252777445	345.3718783	0.626005986	1.31E-05	2.98E-20
4	2.933315683	359.6046662	0.610593679	1.27E-05	1.02E-19
5	3.58863267	372.5468371	0.596578946	1.24E-05	3.14E-19
6	4.222519377	384.3917925	0.583752359	1.21E-05	8.74E-19
7	4.837938801	395.2911192	0.571949768	1.19E-05	2.24E-18
8	5.437255742	405.3661657	0.561039769	1.16E-05	5.36E-18
9	6.022393316	414.7159334	0.550915154	1.14E-05	1.20E-17
10	6.594938648	423.422408	0.541487145	1.12E-05	2.55E-17
11	7.156219727	431.5544393	0.532681184	1.10E-05	5.14E-17
12	7.707359542	439.1704735	0.524433984	1.08E-05	9.92E-17
13	8.249317637	446.3206541	0.516691243	1.07E-05	1.84E-16
14	8.782920296	453.0483471	0.509406004	1.05E-05	3.28E-16
15	9.308886228	459.3914397	0.502537238	1.04E-05	5.67E-16
16	9.82784259	465.3831519	0.496048972	1.02E-05	9.51E-16
17	10.34034206	471.0528995	0.489909353	1.01E-05	1.55E-15
18	10.84687247	476.4267829	0.484090118	9.95E-06	2.46E-15
19	11.3478686	481.5281836	0.478565947	9.83E-06	3.82E-15
20	11.84371775	486.3780474	0.473314158	9.71E-06	5.80E-15
21	12.33476764	490.9952843	0.468314276	9.60E-06	8.62E-15
22	12.82133113	495.397006	0.463547768	9.50E-06	1.26E-14
23	13.30369023	499.5987345	0.458997828	9.40E-06	1.81E-14
24	13.78210109	503.6146484	0.454649102	9.30E-06	2.55E-14
25	14.25679576	507.4576773	0.450487588	9.20E-06	3.55E-14
26	14.72798598	511.1396899	0.446500435	9.11E-06	4.87E-14
27	15.19586466	514.6715738	0.442675852	9.02E-06	6.60E-14
28	15.66060875	518.0633758	0.43900296	8.93E-06	8.83E-14
29	16.12237979	521.3243365	0.435471752	8.85E-06	1.17E-13
30	16.58132687	524.4630308	0.432072944	8.77E-06	1.53E-13
31	17.03758662	527.4873775	0.428797959	8.70E-06	1.98E-13
32	17.49128531	530.4047383	0.425638827	8.62E-06	2.55E-13
33	17.94253915	533.2219386	0.422588156	8.55E-06	3.24E-13
34	18.39145585	535.9453415	0.419639055	8.48E-06	4.10E-13
35	18.83813483	538.5808623	0.41678512	8.42E-06	5.14E-13
36	19.28266832	541.1340234	0.414020369	8.35E-06	6.39E-13
37	19.72514188	543.6099781	0.411339224	8.29E-06	7.90E-13

Layer #	Depth (mbs)	Density	Open porosity	Diffusivity	Closed porosity
38	20.16563494	546.013542	0.408736469	8.23E-06	9.71E-13
39	20.60422129	548.3492155	0.40620723	8.17E-06	1.19E-12
40	21.04096968	550.6212131	0.403746944	8.11E-06	1.44E-12
41	21.47594382	552.8334712	0.401351349	8.06E-06	1.74E-12
42	21.90920359	554.9896943	0.399016432	8.00E-06	2.10E-12
43	22.34080434	557.0933377	0.396738453	7.95E-06	2.51E-12
44	22.77079803	559.1476509	0.394513892	7.90E-06	2.99E-12
45	23.1992331	561.1556796	0.392339451	7.85E-06	3.55E-12
46	23.62615477	563.1202791	0.390212038	7.80E-06	4.20E-12
47	24.05160559	565.0441357	0.388128745	7.75E-06	4.95E-12
48	24.47562502	566.9297606	0.386086852	7.70E-06	5.82E-12
49	24.89825036	568.7795205	0.384083797	7.65E-06	6.82E-12
50	25.31951635	570.59563	0.38211718	7.61E-06	7.96E-12
51	25.73945561	572.3801693	0.38018475	7.56E-06	9.28E-12
52	26.15809878	574.1350916	0.378284391	7.52E-06	1.08E-11
53	26.57547469	575.8622303	0.376414119	7.47E-06	1.25E-11
54	26.99161047	577.5633061	0.374572069	7.43E-06	1.44E-11
55	27.40653141	579.2399285	0.372756499	7.39E-06	1.67E-11
56	27.82026166	580.8936127	0.370965768	7.35E-06	1.92E-11
57	28.23282354	582.5257715	0.369198347	7.30E-06	2.21E-11
58	28.64423851	584.1377356	0.367452794	7.26E-06	2.53E-11
59	29.05452661	585.7307476	0.365727764	7.22E-06	2.90E-11
60	29.46370678	587.3059707	0.364021997	7.18E-06	3.32E-11
61	29.87179697	588.8644935	0.362334314	7.14E-06	3.79E-11
62	30.2788141	590.4073325	0.360663615	7.11E-06	4.33E-11
63	30.68477418	591.9354372	0.359008871	7.07E-06	4.93E-11
64	31.08969261	593.4496968	0.357369119	7.03E-06	5.61E-11
65	31.49358361	594.9509349	0.355743468	6.99E-06	6.38E-11
66	31.89646111	596.4399246	0.354131081	6.95E-06	7.24E-11
67	32.29833813	597.9173824	0.352531181	6.91E-06	8.21E-11
68	32.69922708	599.3839747	0.350943048	6.88E-06	9.30E-11
69	33.09913984	600.8403205	0.349366009	6.84E-06	1.05E-10
70	33.49808774	602.2869943	0.347799445	6.80E-06	1.19E-10
71	33.89608164	603.7245284	0.346242778	6.77E-06	1.35E-10
72	34.29313197	605.1534152	0.344695474	6.73E-06	1.52E-10
73	34.6892487	606.5741093	0.343157042	6.69E-06	1.72E-10
74	35.08444126	607.9870288	0.341627029	6.66E-06	1.94E-10
75	35.47871904	609.3925611	0.340105016	6.62E-06	2.18E-10
76	35.87209079	610.7910593	0.338590619	6.59E-06	2.46E-10
77	36.26456509	612.1828488	0.337083487	6.55E-06	2.77E-10

Layer #	Depth (mbs)	Density	Open porosity	Diffusivity	Closed porosity
78	36.65615026	613.5682269	0.335583298	6.51E-06	3.11E-10
79	37.04685429	614.9474646	0.334089758	6.48E-06	3.50E-10
80	37.43668492	616.3208085	0.332602601	6.45E-06	3.94E-10
81	37.82564969	617.6884824	0.331121583	6.41E-06	4.42E-10
82	38.21375597	619.0506886	0.329646486	6.38E-06	4.97E-10
83	38.6010109	620.4076094	0.328177113	6.34E-06	5.57E-10
84	38.98742134	621.7594079	0.326713286	6.31E-06	6.25E-10
85	39.3729942	623.1062303	0.325254848	6.27E-06	7.01E-10
86	39.7577361	624.4482063	0.323801658	6.24E-06	7.86E-10
87	40.14165356	625.7854503	0.322353592	6.20E-06	8.80E-10
88	40.52475291	627.1180622	0.320910542	6.17E-06	9.86E-10
89	40.90704051	628.4461299	0.319472412	6.14E-06	1.10E-09
90	41.2885225	629.7697283	0.318039123	6.10E-06	1.23E-09
91	41.66920492	631.088921	0.316610604	6.07E-06	1.38E-09
92	42.04909375	632.4037616	0.315186798	6.04E-06	1.54E-09
93	42.42819487	633.7142943	0.313767657	6.00E-06	1.73E-09
94	42.80651411	635.0205543	0.312353142	5.97E-06	1.93E-09
95	43.18405725	636.3225691	0.310943225	5.94E-06	2.15E-09
96	43.56083	637.620359	0.309537882	5.90E-06	2.40E-09
97	43.93683785	638.9139367	0.308137101	5.87E-06	2.68E-09
98	44.31208651	640.2033104	0.306740873	5.84E-06	2.99E-09
99	44.6865814	641.4884819	0.305349194	5.80E-06	3.34E-09
100	45.06032809	642.7694488	0.303962069	5.77E-06	3.72E-09
101	45.43333184	644.0462033	0.302579505	5.74E-06	4.15E-09
102	45.80559817	645.3187354	0.301201513	5.71E-06	4.62E-09
103	46.17713241	646.5870309	0.299828109	5.67E-06	5.14E-09
104	46.54793984	647.8510725	0.298459312	5.64E-06	5.72E-09
105	46.91802572	649.1108409	0.297095141	5.61E-06	6.37E-09
106	47.28739529	650.3663145	0.295735622	5.58E-06	7.08E-09
107	47.65605376	651.6174702	0.294380778	5.55E-06	7.88E-09
108	48.02400633	652.8642834	0.293030636	5.51E-06	8.75E-09
109	48.39125816	654.1067287	0.291685224	5.48E-06	9.72E-09
110	48.75781428	655.3447793	0.290344571	5.45E-06	1.08E-08
111	49.12367985	656.5784087	0.289008705	5.42E-06	1.20E-08
112	49.48885995	657.8075902	0.287677656	5.39E-06	1.33E-08
113	49.85335953	659.0322961	0.286351453	5.36E-06	1.47E-08
114	50.21718368	660.2525006	0.285030125	5.33E-06	1.64E-08
115	50.58033738	661.4681773	0.283713699	5.29E-06	1.81E-08
116	50.94282547	662.6793001	0.282402205	5.26E-06	2.01E-08
117	51.30465299	663.8858449	0.281095667	5.23E-06	2.22E-08

Layer #	Depth (mbs)	Density	Open porosity	Diffusivity	Closed porosity
118	51.66582482	665.0877882	0.279794112	5.20E-06	2.46E-08
119	52.02634581	666.2851073	0.278497565	5.17E-06	2.72E-08
120	52.38622081	667.4777811	0.277206047	5.14E-06	3.01E-08
121	52.74545464	668.6657898	0.275919581	5.11E-06	3.33E-08
122	53.10405207	669.8491152	0.274638186	5.08E-06	3.68E-08
123	53.46201789	671.0277408	0.27336188	5.05E-06	4.06E-08
124	53.81935681	672.2016517	0.272090679	5.02E-06	4.49E-08
125	54.17607344	673.3708342	0.270824597	4.99E-06	4.95E-08
126	54.53217259	674.5352782	0.269563647	4.96E-06	5.46E-08
127	54.8876588	675.6949735	0.268307838	4.93E-06	6.02E-08
128	55.2425367	676.8499132	0.267057178	4.90E-06	6.64E-08
129	55.59681084	678.0000919	0.265811674	4.87E-06	7.31E-08
130	55.95048581	679.1455066	0.264571327	4.84E-06	8.05E-08
131	56.30356599	680.2861552	0.263336141	4.82E-06	8.87E-08
132	56.65605595	681.4220395	0.262106113	4.79E-06	9.76E-08
133	57.00796011	682.5531624	0.260881241	4.76E-06	1.07E-07
134	57.35928283	683.6795288	0.259661518	4.73E-06	1.18E-07
135	57.71002848	684.801146	0.258446937	4.70E-06	1.30E-07
136	58.06020134	685.9180231	0.257237488	4.67E-06	1.42E-07
137	58.40980573	687.0301717	0.256033157	4.64E-06	1.56E-07
138	58.75884585	688.1376053	0.254833932	4.62E-06	1.72E-07
139	59.10732593	689.2403394	0.253639794	4.59E-06	1.88E-07
140	59.45525013	690.3383919	0.252450724	4.56E-06	2.07E-07
141	59.8026226	691.4317824	0.2512667	4.53E-06	2.26E-07
142	60.1494474	692.5205325	0.2500877	4.51E-06	2.48E-07
143	60.49572848	693.604665	0.248913698	4.48E-06	2.72E-07
144	60.84146998	694.6842065	0.247744666	4.45E-06	2.98E-07
145	61.18667573	695.7591834	0.246580574	4.42E-06	3.26E-07
146	61.53134974	696.8296255	0.24542139	4.40E-06	3.56E-07
147	61.87549577	697.895563	0.244267081	4.37E-06	3.90E-07
148	62.21911776	698.9570294	0.243117611	4.34E-06	4.26E-07
149	62.56221938	700.0140579	0.241972944	4.31E-06	4.65E-07
150	62.90480441	701.0666851	0.240833039	4.29E-06	5.08E-07
151	63.24687656	702.1149484	0.239697856	4.26E-06	5.55E-07
152	63.58843948	703.1588867	0.238567352	4.23E-06	6.06E-07
153	63.92949675	704.1985403	0.237441483	4.21E-06	6.61E-07
154	64.2700519	705.2339508	0.236320205	4.18E-06	7.21E-07
155	64.61010847	706.2651614	0.23520347	4.15E-06	7.86E-07
156	64.9496699	707.2922163	0.234091229	4.13E-06	8.57E-07
157	65.28873962	708.315161	0.232983432	4.10E-06	9.33E-07

Layer #	Depth (mbs)	Density	Open porosity	Diffusivity	Closed porosity
158	65.62732102	709.3340422	0.23188003	4.08E-06	1.02E-06
159	65.96541741	710.3489077	0.230780969	4.05E-06	1.11E-06
160	66.30303212	711.3598062	0.229686196	4.03E-06	1.20E-06
161	66.64016837	712.3667874	0.228595658	4.00E-06	1.31E-06
162	66.97682925	713.3699007	0.227509298	3.97E-06	1.42E-06
163	67.31301804	714.3691985	0.226427061	3.95E-06	1.55E-06
164	67.64873781	715.3647324	0.22534889	3.92E-06	1.68E-06
165	67.98399154	716.3565545	0.224274727	3.90E-06	1.83E-06
166	68.31878237	717.3447188	0.223204513	3.86E-06	1.98E-06
167	68.65311314	718.3292781	0.22213819	3.83E-06	2.15E-06
168	68.98698686	719.310287	0.221075697	3.80E-06	2.34E-06
169	69.32040642	720.2878003	0.220016976	3.77E-06	2.54E-06
170	69.65337454	721.2618718	0.218961965	3.74E-06	2.75E-06
171	69.98589413	722.2325574	0.217910603	3.70E-06	2.98E-06
172	70.31796792	723.1999122	0.21686283	3.67E-06	3.23E-06
173	70.64959861	724.1639914	0.215818583	3.64E-06	3.51E-06
174	70.98078882	725.1248502	0.214777803	3.61E-06	3.80E-06
175	71.3115412	726.0825442	0.213740426	3.58E-06	4.11E-06
176	71.64185835	727.0371285	0.212706392	3.55E-06	4.45E-06
177	71.97174281	727.9886585	0.211675639	3.52E-06	4.82E-06
178	72.30119707	728.9371889	0.210648104	3.49E-06	5.22E-06
179	72.6302236	729.8827746	0.209623728	3.46E-06	5.64E-06
180	72.95882479	730.8254695	0.208602449	3.43E-06	6.10E-06
181	73.28700303	731.7653278	0.207584205	3.39E-06	6.60E-06
182	73.61476071	732.7024031	0.206568937	3.36E-06	7.13E-06
183	73.94210012	733.6367484	0.205556583	3.33E-06	7.71E-06
184	74.26902352	734.5684162	0.204547085	3.30E-06	8.33E-06
185	74.5955331	735.4974579	0.203540382	3.27E-06	9.00E-06
186	74.92163115	736.4239253	0.202536416	3.24E-06	9.72E-06
187	75.24731974	737.3478684	0.201535129	3.21E-06	1.05E-05
188	75.57260107	738.2693372	0.200536461	3.18E-06	1.13E-05
189	75.8974772	739.1883805	0.199540357	3.15E-06	1.22E-05
190	76.2219502	740.1050463	0.198546759	3.12E-06	1.32E-05
191	76.54602207	741.0193818	0.197555611	3.09E-06	1.42E-05
192	76.86969489	741.9314335	0.196566858	3.06E-06	1.53E-05
193	77.1929705	742.8412459	0.195580446	3.03E-06	1.65E-05
194	77.51585093	743.7488638	0.19459632	3.00E-06	1.78E-05
195	77.83833809	744.6543302	0.193614427	2.97E-06	1.92E-05
196	78.16043383	745.5576871	0.192634715	2.94E-06	2.07E-05
197	78.48213996	746.458975	0.191657131	2.91E-06	2.23E-05

Layer #	Depth (mbs)	Density	Open porosity	Diffusivity	Closed porosity
198	78.80345835	747.3582341	0.190681625	2.88E-06	2.40E-05
199	79.1243908	748.2555028	0.189708147	2.85E-06	2.59E-05
200	79.44493906	749.1508182	0.188736646	2.83E-06	2.79E-05
201	79.76510489	750.0442165	0.187767075	2.80E-06	3.00E-05
202	80.08489	750.9357323	0.186799384	2.77E-06	3.23E-05
203	80.4042961	751.8253989	0.185833527	2.74E-06	3.48E-05
204	80.72332485	752.7132486	0.184869457	2.71E-06	3.74E-05
205	81.04197792	753.5993119	0.183907127	2.68E-06	4.02E-05
206	81.36025694	754.4836182	0.182946492	2.65E-06	4.33E-05
207	81.67816346	755.3661953	0.181987508	2.62E-06	4.65E-05
208	81.99569913	756.2470697	0.18103013	2.60E-06	5.00E-05
209	82.31286554	757.1262668	0.180074313	2.57E-06	5.38E-05
210	82.62966424	758.0038102	0.179120014	2.54E-06	5.78E-05
211	82.94609667	758.8797216	0.178167191	2.51E-06	6.22E-05
212	83.26216449	759.7540223	0.1772158	2.48E-06	6.68E-05
213	83.57786912	760.6267315	0.176265798	2.45E-06	7.18E-05
214	83.89321205	761.4978669	0.175317143	2.42E-06	7.71E-05
215	84.20819481	762.367445	0.174369792	2.39E-06	8.28E-05
216	84.5228188	763.2354807	0.173423702	2.37E-06	8.89E-05
217	84.8370855	764.1019874	0.172478831	2.34E-06	9.55E-05
218	85.15099636	764.9669773	0.171535135	2.31E-06	0.000102486
219	85.46455273	765.8304606	0.170592571	2.28E-06	0.000110007
220	85.77775612	766.6924469	0.169651094	2.25E-06	0.000118062
221	86.0906079	767.5529436	0.16871066	2.22E-06	0.000126687
222	86.40310941	768.411957	0.167771223	2.19E-06	0.000135922
223	86.71526209	769.2694921	0.166832735	2.16E-06	0.000145808
224	87.02706732	770.1255524	0.165895149	2.14E-06	0.000156389
225	87.33852645	770.9801401	0.164958415	2.11E-06	0.000167712
226	87.64964086	771.833256	0.164022482	2.08E-06	0.000179829
227	87.96041186	772.6848995	0.163087298	2.05E-06	0.000192791
228	88.27084082	773.5350688	0.162152807	2.02E-06	0.000206656
229	88.5809291	774.383761	0.161218953	2.00E-06	0.000221484
230	88.89067803	775.2309718	0.160285675	1.97E-06	0.00023734
231	89.20008894	776.0766956	0.159352911	1.94E-06	0.000254292
232	89.50916315	776.9209259	0.158420596	1.91E-06	0.000272413
233	89.81790199	777.7636547	0.157488661	1.88E-06	0.000291779
234	90.1263068	778.6048734	0.156557034	1.86E-06	0.000312473
235	90.4343789	779.4445719	0.155625637	1.83E-06	0.000334583
236	90.74211963	780.2827395	0.154694391	1.80E-06	0.0003582
237	91.04953027	781.1193642	0.153763209	1.77E-06	0.000383422

Layer #	Depth (mbs)	Density	Open porosity	Diffusivity	Closed porosity
238	91.35661211	781.9544328	0.152832003	1.74E-06	0.000410355
239	91.66336652	782.7879321	0.151900676	1.71E-06	0.000439108
240	91.96979484	783.6198475	0.150969125	1.69E-06	0.000469799
241	92.27589826	784.4501634	0.150037245	1.66E-06	0.000502553
242	92.58167824	785.2788642	0.14910492	1.63E-06	0.0005375
243	92.88713599	786.105933	0.148172029	1.60E-06	0.00057478
244	93.19227289	786.9313528	0.147238442	1.57E-06	0.000614542
245	93.49709021	787.7551054	0.146304022	1.54E-06	0.000656942
246	93.80158931	788.577173	0.145368623	1.52E-06	0.000702146
247	94.10577145	789.3975364	0.144432091	1.49E-06	0.000750328
248	94.40963804	790.2161772	0.143494259	1.46E-06	0.000801676
249	94.71319027	791.0330753	0.142554953	1.43E-06	0.000856384
250	95.01642956	791.8482118	0.141613987	1.40E-06	0.000914661
251	95.31935723	792.6615671	0.140671161	1.37E-06	0.000976726
252	95.62197454	793.4731208	0.139726267	1.34E-06	0.00104281
253	95.92428285	794.2828537	0.13877908	1.31E-06	0.001113159
254	96.22628351	795.0907462	0.137829363	1.28E-06	0.001188031
255	96.52797783	795.8967788	0.136876864	1.25E-06	0.001267699
256	96.82936715	796.7009323	0.135921316	1.22E-06	0.001352451
257	97.13045276	797.5031876	0.134962435	1.19E-06	0.00144259
258	97.43123601	798.3035265	0.133999922	1.16E-06	0.001538438
259	97.73171823	799.101931	0.133033456	1.14E-06	0.001640332
260	98.03190077	799.8983839	0.132062702	1.11E-06	0.001748629
261	98.33178495	800.6928685	0.1310873	1.08E-06	0.001863705
262	98.63137211	801.485369	0.130106873	1.05E-06	0.001985954
263	98.93066357	802.2758703	0.12912102	1.02E-06	0.002115794
264	99.22966067	803.0643585	0.128129318	9.85E-07	0.002253664
265	99.5283647	803.8508206	0.127131317	9.54E-07	0.002400026
266	99.82677703	804.6352449	0.126126544	9.23E-07	0.002555366
267	100.124899	805.417621	0.125114499	8.92E-07	0.002720198
268	100.4227319	806.1979399	0.124094651	8.74E-07	0.002895059
269	100.7202771	806.9761941	0.123066442	8.51E-07	0.003080516
270	101.0175358	807.752377	0.122029284	8.22E-07	0.003277167
271	101.3145094	808.526485	0.120982551	7.89E-07	0.003485639
272	101.6111992	809.2985156	0.119925588	7.51E-07	0.003706591
273	101.9076066	810.0684678	0.1188577	7.10E-07	0.003940718
274	102.2037327	810.8363436	0.117778157	6.67E-07	0.004188749
275	102.4995789	811.6021468	0.116686187	6.22E-07	0.004451451
276	102.7951465	812.3658826	0.115580977	5.76E-07	0.004729632
277	103.0904367	813.1275606	0.114461668	5.29E-07	0.005024139

Layer #	Depth (mbs)	Density	Open porosity	Diffusivity	Closed porosity
278	103.3854508	813.8871905	0.113327359	4.83E-07	0.005335866
279	103.6801901	814.6447871	0.112177095	4.39E-07	0.005665749
280	103.9746558	815.4003656	0.111009872	3.95E-07	0.006014775
281	104.2688491	816.1539464	0.109824632	3.54E-07	0.006383983
282	104.5627713	816.9055511	0.10862026	3.14E-07	0.006774462
283	104.8564236	817.6552055	0.10739558	2.77E-07	0.007187362
284	105.1498071	818.4029388	0.106149351	2.43E-07	0.00762389
285	105.442923	819.1487824	0.104880269	2.12E-07	0.008085318
286	105.7357725	819.8927728	0.103586954	1.84E-07	0.008572986
287	106.0283567	820.6349497	0.102267954	1.58E-07	0.009088302
288	106.3206768	821.3753564	0.100921737	1.35E-07	0.009632752
289	106.6127338	822.11404	0.099546687	1.15E-07	0.010207901
290	106.9045287	822.8510526	0.098141097	9.68E-08	0.0108154
291	107.1960628	823.5864501	0.096703167	8.11E-08	0.011456987
292	107.4873369	824.3202928	0.095230995	6.76E-08	0.012134501
293	107.7783522	825.0526457	0.093722572	5.60E-08	0.012849879
294	108.0691095	825.7835785	0.092175774	4.61E-08	0.013605168
295	108.3596098	826.5131658	0.090588358	3.77E-08	0.014402534
296	108.649854	827.2414874	0.088957949	3.07E-08	0.015244264
297	108.9398429	827.9686281	0.087282032	2.48E-08	0.016132779
298	109.2295776	828.6946783	0.085557947	1.99E-08	0.017070643
299	109.5190586	829.4197337	0.083782874	1.59E-08	0.018060573
300	109.8082869	830.143896	0.081953821	1.26E-08	0.01910545
301	110.0972631	830.8672724	0.080067618	9.95E-09	0.020208328
302	110.385988	831.5899765	0.078120896	7.80E-09	0.021372453
303	110.6744622	832.3121276	0.076110077	6.08E-09	0.022601274
304	110.9626863	833.0338519	0.074031357	4.72E-09	0.023898458
305	111.2506608	833.7552817	0.071880688	3.63E-09	0.025267909
306	111.5383863	834.4765562	0.069653762	2.78E-09	0.026713786
307	111.8258632	835.1978213	0.067345986	2.12E-09	0.028240524
308	112.1130919	835.9192301	0.064952462	1.61E-09	0.029852854
309	112.4000728	836.6409427	0.062467963	1.21E-09	0.03155583
310	112.6868062	837.363127	0.059886903	9.07E-10	0.033354855
311	112.9732923	838.0859578	0.057203312	6.76E-10	0.035255712
312	113.2595312	838.8096179	0.054410801	5.00E-10	0.03726459
313	113.5455231	839.5342986	0.051502525	3.69E-10	0.039388129
314	113.8312681	840.260198	0.04847115	2.70E-10	0.041633447
315	114.1167661	840.9875237	0.045308801	1.97E-10	0.044008195
316	114.402017	841.7164908	0.042007026	1.43E-10	0.04652059
317	114.6870206	842.4473236	0.038556738	1.03E-10	0.049179479

Layer #	Depth (mbs)	Density	Open porosity	Diffusivity	Closed porosity
318	114.9717768	843.1802547	0.03494816	7.37E-11	0.051994385
319	115.2562851	843.9155263	0.031170763	5.25E-11	0.054975576
320	115.5405452	844.6533884	0.027213202	3.73E-11	0.058134126
321	115.8245566	845.3941025	0.023063228	2.63E-11	0.061482
322	116.1083188	846.1379369	0.018707627	0	0.065032123
323	116.391831	846.8851716	0.014132107	0	0.068798483
324	116.6750925	847.6360958	0.009321208	0	0.072796225
325	116.9581025	848.3910077	0.0042582	0	0.07704176
326	117.2408601	849.150217	0	0	0.080477832
327	117.5233642	849.9140438	0	0	0.079650704
328	117.8056137	850.6828171	0	0	0.07881822
329	118.0876073	851.4568774	0	0	0.077980011
330	118.3693438	852.2365762	0	0	0.077135696
331	118.6508216	853.0222764	0	0	0.076284882
332	118.9320391	853.8143514	0	0	0.075427165
333	119.2129947	854.6131852	0	0	0.074562129
334	119.4936867	855.4191739	0	0	0.073689345
335	119.774113	856.232725	0	0	0.072808373
336	120.0542717	857.0542578	0	0	0.071918757
337	120.3341605	857.8842032	0	0	0.071020031
338	120.6137772	858.7230041	0	0	0.070111716
339	120.8931194	859.5711153	0	0	0.069193319
340	121.1721845	860.4290039	0	0	0.068264334
341	121.4509697	861.2971489	0	0	0.067324243
342	121.7294723	862.1760426	0	0	0.066372512
343	122.0076893	863.06619	0	0	0.065408595
344	122.2856175	863.9681062	0	0	0.064431934
345	122.5632537	864.88232	0	0	0.063441956
346	122.8405945	865.8093729	0	0	0.062438076
347	123.1176363	866.749823	0	0	0.061419687
348	123.3943753	867.7042349	0	0	0.06038618
349	123.6708078	868.673187	0	0	0.059336927
350	123.9469295	869.6572775	0	0	0.058271282

Appendix B: Selected ice core data

Table A2: Ethane dry extraction results (in ppt) measured in the WAIS-Divide ice core samples reported in this study. Ethane mixing ratios were calculated by subtracting the average of the two stationary clean N_2 blanks, taken before and after each sample.

TD	BD	Approx Gas Age	Can	Ethane
m	m	AD	#	ppt
78.5	78.6	1940.9	3	1128.1
82.738	82.888	1923.1	3	1163.6
84.69	84.79	1915.1	5	548.3
84.69	84.79	1915.1	5	856.3
87.7	87.8	1902.1	4	1276.2
87.8	88	1901.5	3	908.0
91.3	91.4	1885.8	4	552.7
95	95.1	1869.0	3	325.4
99.4	99.5	1852.4	2	694.6
99.5	99.7	1851.6	2	658.9
101.9	102	1841.4	8	800.2
102.9	103	1837.2	5	806.7
103.3	103.4	1835.7	3	1009.9
107.45	107.55	1817.9	4	938.6
107.8	107.9	1816.6	2	712.0
111.3	111.4	1802.2	4	757.9
123.8	123.9	1746.8	2	669.7
126.83	126.93	1733.3	3	414.4
127.4	127.5	1730.9	4	774.7
130.9	131.1	1714.7	1	464.5
133.2	133.3	1704.0	5	197.6
133.3	133.4	1703.6	5	356.7
135.7	135.9	1693.8	2	795.1
143.4	143.6	1663.5	2	599.9
147.4	147.6	1641.6	4	776.6
154.8	155	1610.0	1	596.4
158.1	158.2	1596.2	6	453.0
158.7	158.8	1593.9	3	397.0
159.1	159.2	1592.2	1	1004.8
159.1	159.2	1592.2	5	427.5
162.4	162.6	1576.9	1	423.3
166.6	166.8	1560.4	2	613.2
174.8	175	1524.7	2	740.7
178.6	178.8	1507.4	1	451.0
181.9	182.1	1491.4	3	1019.2
185.9	186	1473.9	1	570.6
190.7	190.8	1452.6	2	558.0
195.3	195.4	1432.8	2	532.1
199.1	199.2	1415.8	3	924.9
199.2	199.3	1415.3	1	338.5
202.6	202.8	1400.3	4	626.6
210.8	211	1363.6	1	359.4
214.7	214.8	1344.9	4	1082.6
222.2	222.3	1314.5	7	916.9
222.2	222.3	1314.5	5	360.4

TD	BD	Approx Gas Age	Can	Ethane
222.3	222.5	1313.6	3	712.3
226.4	226.6	1294.9	2	641.0
229.5	229.8	1278.9	2	510.0
231.8	232	1269.9	2	543.0
234.9	235.1	1256.8	3	1415.1
239.2	239.3	1239.9	4	776.0
243.8	244	1220.9	3	623.7
247.5	247.6	1207.2	2	613.0
258	258.2	1161.6	2	881.2
262.8	262.9	1141.1	1	839.8
266.5	266.6	1126.2	4	1374.8
266.5	266.6	1126.2	4	689.2
271.3	271.4	1105.9	3	676.8
277.4	277.5	1080.5	3	733.2
283.3	283.4	1055.6	2	658.5
287.3	287.4	1034.8	1	1087.4
290.2	290.4	1022.4	4	528.9
293	293.2	1010.8	3	881.2
294.2	294.3	1006.2	3	525.3
297.1	297.3	993.3	3	617.3
297.3	297.4	992.8	1	512.3

Table A3: Ethane levels (in pmol) measured in WAIS-Divide ice core samples analyzed in 2011 and 2012.

	BD	**Dry N_2 blank**	**Exploding N_2 blank**	**Sample (uncorr)**	**1st melt N_2 blank**	**2nd melt N_2 blank**	**3rd melt N_2 blank**
2011	**m**	**pmol C_2H_6**	**pmol C_2H_6**	**pmol C_2H_6**	**pmol C_2H_6**	**pmol C_2H_6**	**pmol C_2H_6**
	85.2	0.068592		0.404898	0.130877	0.120805	0.091801
	85.2	0.101989	0.0394337	0.370577	0.133480	0.131504	
	134.3	0.105129		0.331682	0.174242	0.152637	
	138.4	0.121014	0.0329631	0.324374	0.152825		
	141.0	0.119075		0.316782	0.185734	0.149221	
	141.0	0.095009		0.285263	0.164959	0.171034	
	179.6	0.089628		0.367644	0.122892	0.163568	0.158160
	222.2	0.101297		0.353323	0.173023	0.157263	
	246.0	0.124450		0.481555	0.210186		
	246.0	0.153349		0.363794	0.155151	0.206783	0.139061
	298.1	0.160056		0.385559	0.179572	0.176150	
2012	255.8		0.151892	0.352688	0.150974		
	236.34		0.075469	0.223647	0.079123		
	236.16			0.277371	0.121734		
	236.16		0.072715	0.258823	0.117603		
	222.3		0.080343	0.186817	0.121589		
	158.2		0.060734	0.195443	0.093608		
	282.3		0.077545	0.313929	0.180390		
2011	Mean ± 2*s.e.	0.113 ± 0.016	0.100 ± 0.007	0.362 ± 0.031	0.162 ± 0.016	0.159 ± 0.017	0.130 ± 0.039
2012	Mean ± 2*s.e.		0.086 ± 0.027	0.258 ± 0.046	0.124 ± 0.026		

Table A4: Ethane, propane, and n-butane mixing ratios (in ppt) measured in WAIS-Divide ice core samples analyzed by wet extraction in 2011 and 2012. Ethane, propane and n-butane levels measured in the WAIS-Divide samples were corrected for the mean blank (in pmol) measured during the period when the sample was analyzed (either 2011 or 2012).

Bottom Depth	Sample mass	Sample size	Approx Gas Age	C_2H_6 Sample	C_2H_6 error	C_3H_8 Sample	C_3H_8 error	C_4H_{10} Sample	C_4H_{10} error
m	g	mb	AD	ppt	ppt	ppt	ppt	ppt	ppt
85.2	304	112.86	1913.3	183.5	19.9	90	11.1	49.9	9.1
85.2	299.3	98.17	1913.3	181.1	22.8	93.1	12.8	44.2	10.5
134.3	239.4	127.94	1699.8	113.0	17.5	66.1	9.8	31.8	8.1
138.4	362.8	122.29	1685.0	113.5	18.4	63.7	10.3	38.8	8.5
141	306.8	108.51	1673.8	121.6	20.7	76.5	11.6	32.1	9.5
141	291.7	108.64	1673.8	96.8	20.7	90.5	11.6	77.3	9.5
179.6	315.5	122.39	1503.8	143.2	18.3	44.6	10.3	24.7	8.4
222.2	310.7	113.35	1315.0	144.2	19.8	43.9	11.1	22.3	9.1
246	316.8	105.01	1213.1	259.4	21.4	126.7	12.0	66.5	9.8
246	286.1	106.59	1213.1	161.5	21.1	42.1	11.8	18.9	9.7
298.1	295.9	89.67	989.5	212.6	25.0	101.4	14.0	57.7	11.5
2011 samples (mean ± 1σ)				157.3±48.9	20.5±2.1	76.2±27.1	11.5±1.2	42.4±19.0	9.4±1.0
158.2	208	105.01	1596.2	76.7	36.2	96.5	15.2	61.7	9.8
222.3	197	95.30	1314.5	72.6	38.9	45.8	16.4	23.9	10.6
236.2	257.3	101.74	1252.3	117.0	29.3	52.0	12.0	28.1	7.7
236.2	252.9	98.61	1252.3	129.0	28.4	62.6	12.4	29.6	8.0
236.3	250.1	74.42	1251.7	89.6	30.3	47.7	12.8	12.7	8.2
255.8	337.8	79.95	1171.1	186.5	27.6	86.0	11.6	41.4	7.5
282.3	274.4	100.90	1061.2	161.0	28.7	68.8	12.1	45.4	7.8
2012 samples (mean ± 1σ)				118.9±43.3	31.4±4.4	65.6±19.5	13.2±1.8	34.7±16.1	8.5±1.2

Table A5: Propane levels measured in WAIS-Divide ice cores analyzed by wet extraction in 2011 and 2012.

	BD	Dry N_2 blank	Exploding N_2 blank	Sample (uncorr)	1st melt N_2 blank	2nd melt N_2 blank	3rd melt N_2 blank
	m	pmol C_3H_8	pmol C_3H_8	pmol C_3H_8	pmol C_3H_8	pmol C_3H_8	pmol C_3H_8
2011	85.2	0.0209246		0.1719282	0.0534749	0.0370348	0.0308331
	85.2	0.0359326	0.0394337	0.1600834	0.0440805	0.0409600	
	134.3	0.0166072		0.1521640	0.0581836	0.0539312	
	138.4	0.0173177	0.0329631	0.1440003	0.0649942		
	141.0	0.0335232		0.150236	0.0676136	0.0532803	
	141.0	0.0194977		0.1679922	0.038025	0.0262206	
	179.6	0.0143427		0.1168361	0.0433010	0.0409797	0.0515062
	222.2	0.0156207		0.1111428	0.0423139	0.0433771	
	246.0	0.0283018		0.2089700	0.0824697		
	246.0	0.0186444		0.1055393	0.0329715	0.0271418	0.0256036
	298.1	0.0225485		0.1594407	0.0546057	0.0457296	
2012	255.8		0.050282	0.155289	0.048837		
	236.34		0.023413	0.082959	0.029642		
	236.16			0.118507	0.056540		
	236.16		0.026873	0.123079	0.050759		
	222.3		0.032202	0.096379	0.063516		
	158.2		0.020564	0.134316	0.043931		
	282.3		0.020097	0.155610	0.074297		
2011	Mean ± 2*s.e.	0.022 ± 0.004	0.036 ± 0.006	0.150 ± 0.018	0.053 ± 0.009	0.041 ± 0.007	0.036 ± 0.016
2012	Mean ± 2*s.e.		0.029 ± 0.009	0.124 ± 0.021	0.053 ± 0.011		

Table A6: Butane levels measurements in WAIS-Divide ice cores analyzed by wet extraction in 2011 and 2012.

	BD	**Dry N_2 blank**	**Exploding N_2 blank**	**Sample (uncorr)**	**1st melt N_2 blank**	**2nd melt N_2 blank**	**3rd melt N_2 blank**
	m	**pmol n-C_4H_{10}**	**pmol n-C_4H_{10}**	**pmol n-C_4H_{10}**	**pmol n-C_4H_{10}**	**pmol n-C_4H_{10}**	**pmol n-C_4H_{10}**
2011	85.2	0.0130589		0.1018689	0.0373267	0.0202976	0.0178941
	85.2	0.0217478	0.0216751	0.0867345	0.0297251	0.0226858	
	134.3	0.0106149		0.0835798	0.0425971	0.0297646	
	138.4	0.0094112	0.0199813	0.0912940	0.0465061		
	141.0	0.0175853		0.0766156	0.0540374	0.0414120	
	141.0	0.0097234		0.1341305	0.0279346	0.0130406	
	179.6	0.0108425		0.0712589	0.021439	0.0195676	0.0257150
	222.2	0.0096039		0.0653677	0.0296988	0.0319432	
	246.0	0.0151068		0.1176999	0.053725		
	246.0	0.0094562		0.0594149	0.018683	0.0203647	0.017499
	298.1	0.0094313		0.0964476	0.0323603	0.0268247	
2012	255.8		0.027332	0.080428	0.023923		
	236.34		0.012655	0.043750	0.015527		
	236.16			0.063090	0.033802		
	236.16		0.013271	0.063835	0.028927		
	222.3		0.016421	0.050397	0.036046		
	158.2		0.012907	0.087378	0.025165		
	282.3		0.011980	0.083200	0.043683		
2011	Mean ± 2*s.e.	0.012 ± 0.002	0.021 ± 0.002	0.089 ± 0.014	0.036 ± 0.007	0.025 ± 0.006	0.020 ± 0.005
2012	Mean ± 2*s.e.		0.016 ± 0.005	0.067 ± 0.013	0.030 ± 0.007		

Table A7: Measurements of ethane, propane, and n-butane in Greenland (GISP2 B) ice cores analyzed by dry extraction [*Aydin et al.,* 2007].

Tube	Bottom	Can	Published data				
			Ethane			CFC-12	
#	Depth	#	pmol	ppt	err	ppt	err
135	134.42	1	1.67026	1155.4	16.9	0.7	0.7
134	134.69	1	2.06742	1249.7	26.5	0.8	0.7
104	104.855	1	1.84986	1135.9	14.9	0.8	0.7
111	111.35	1	1.91523	1100.8	20.9	0.2	0.3
119	118.55	1	1.96153	1257.9	10.9	6.2	1.0
98	98.81	1	1.7417	1221.7	24.8	6.6	1.1
107	107.49	2	4.36112	2153.9	18.7	0.0	0.0
114	114.955	2	2.21089	1952.1	31.5	0.0	0.0
101	101.845	2	3.39455	2526.4	25.5	0.2	0.4
123	122.2	2	2.67388	1579.4	26.4	0.1	0.2
124	123.9	2	2.72318	2121.2	18.4	7.1	1.2
138	137.17	2	2.78366	1822.1	35.4	2.1	0.9

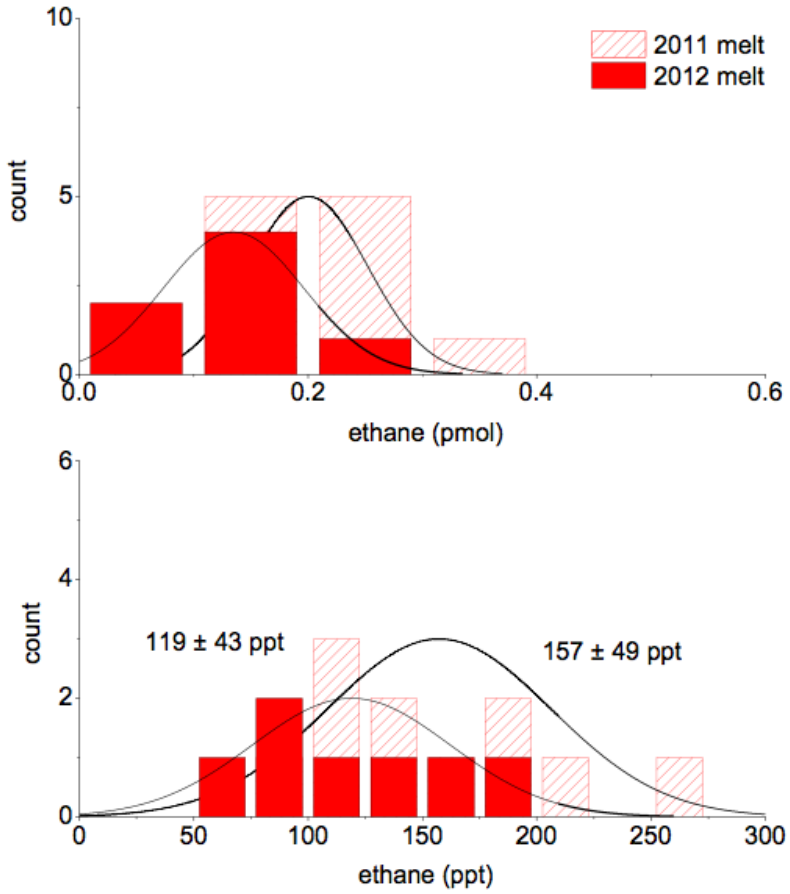

Figure A1: Histogram of ethane levels measured by wet extraction in 2011 (hatched red bars) and 2012 (solid red bars).

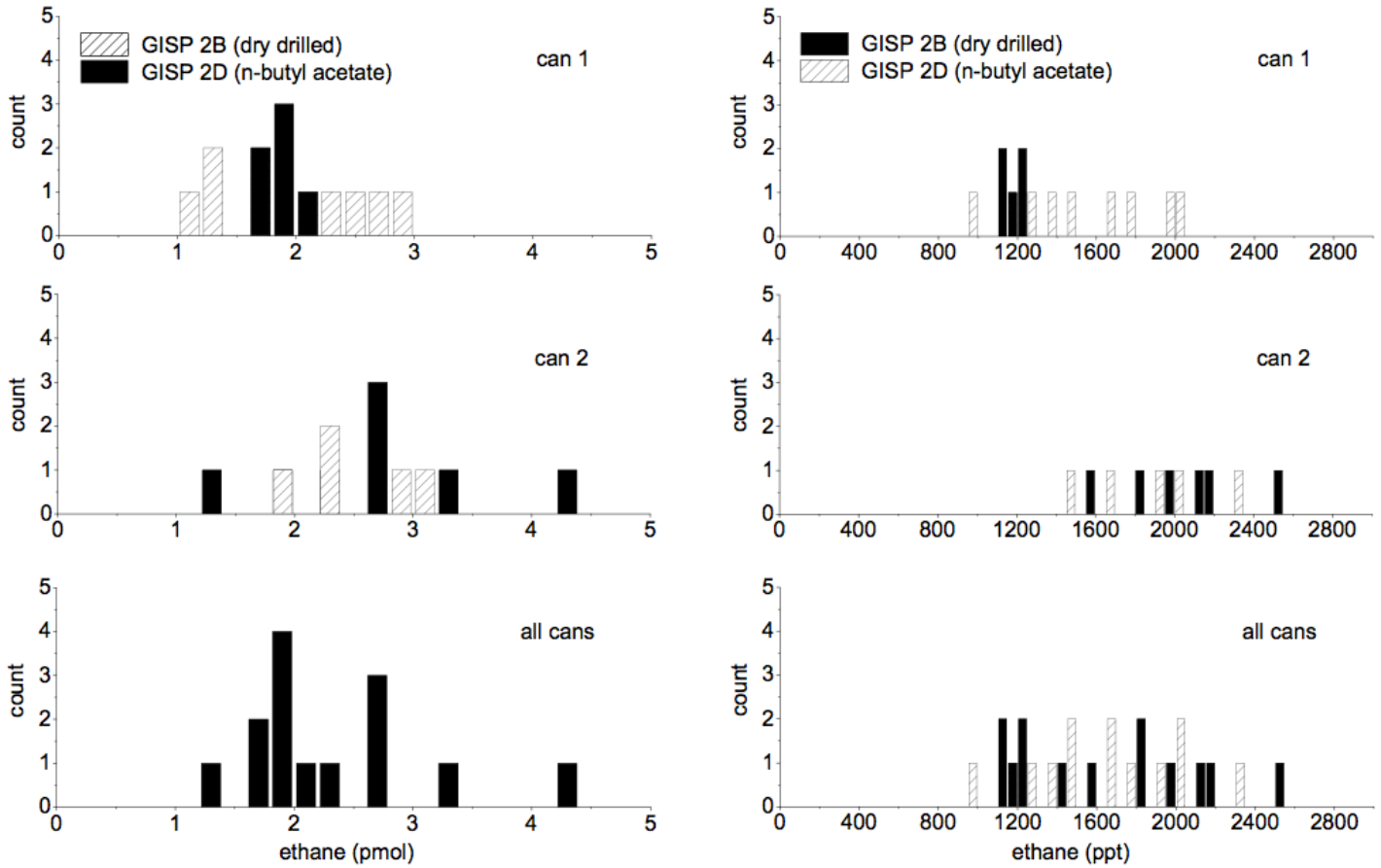

Figure A2: Histograms showing ethane levels (in pmol, left panels) and mixing ratios (in ppt, right panels) measured in Greenland (GISP2 B and GISP2 D) ice core air. The GISP2 B ice cores were dry-drilled and the GISP2 D ice cores were fluid-drilled with n-butyl acetate drilling fluid. Results are shown for two stainless steel chambers used in the analysis (cans 1 and 2). These cans were also used for analysis of ethane in Antarctic ice cores from WAIS Divide (Chapter 4). Bin sizes for ethane 0.2 pmol in the left panels and 50 ppt in the right panels.

Appendix C: Carbon monoxide data

Table A8: Carbon monoxide levels measured in the South Pole firn flasks. Flasks with suspected contamination are marked with an asterisk. The criteria for contamination was determined as follows: * = high CO_2 measured in the flask, ** = high COS and CS_2 levels measured in the flask.

Flask	firn hole	depth (m)	CO (ppb)	Contaminated?
UCI-08-06	green	0.0	44.48	
6572-66	green	0.0	43.62	
6055-66	green	10.01	50.59	
6342-66	red	19.73	53.87	
6301-66	green	30.04	52.08	
6421-66	red	39.94	68.99	*
UCI-05-23	red	39.94	52.27	
6038-66	green	50.09	51.79	
6052-66	red	60.14	52.12	
6071-66	red	60.14	51.72	
6119-66	green	64.87	52.62	
6826-66	red	75.0	52.42	
6037-66	green	79.62	51.59	
6453-66	red	85.01	52.07	
6258-66	green	91.16	51.92	
6056-66	red	95.08	51.84	
6571-66	green	100.72	81.23	*
6120-66	green	104.94	76.87	*
6366-66	red	106.85	52.28	
6339-66	green	109.08	50.95	
6072-66	red	111.05	50.9	
UCI-08-04	red	112.05	49.76	
6250-66	red	112.05	50.03	
6835-66	red	113.07	49.27	
UCI-06-13	red	113.07	48.96	
6422-66	green	113.14	61.86	*
6138-66	red	114.06	46.74	
6138-66	red	114.06	47.36	
UCI-06-09	red	114.06	46.22	
6365-66	red	115.08	79.95	*
6365-66	red	115.08	46.82	
UCI-06-01	red	115.08	46.92	
6249-66	red	115.66	106.38	*
6249-66	red	115.66	45.21	
UCI-06-15	red	115.66	44.27	
6825-66	green	116.01	45.47	*
6638-66	red	116.34	40.85	
6638-66	red	116.34	41.38	
UCI-06-07	red	116.34	41.59	
6330-66	red	116.9	43.56	**
6330-66	red	116.9	43.87	**
UCI-06-04	red	116.9	42.64	**
6195-66	green	117.57	40.23	*
6664-66	green	118.95	57.24	*
6765-66	green	118.95	56.98	*

Table A9: Depth averaged carbon monoxide levels measured in the South Pole firn flasks. Corrections applied to the data are also shown.

depth (m)	CO (ppb)	Grav corr CO (ppb)	Blank corr + Grav corr CO (ppb)
0	44.05	44.05	41.14
10.01	50.59	50.59	47.68
19.73	53.87	53.88	50.96
30.04	52.08	52.09	49.17
39.94	52.27	52.28	49.37
50.09	51.79	51.80	48.89
60.14	51.92	51.94	49.02
64.87	52.62	52.64	49.72
75.00	52.42	52.44	49.53
79.62	51.59	51.61	48.70
85.01	52.07	52.09	49.18
91.16	51.92	51.95	49.03
95.08	51.84	51.87	48.95
106.85	52.28	52.31	49.40
109.08	50.95	50.98	48.07
111.05	50.90	50.93	48.02
112.05	49.90	49.93	47.02
113.07	49.12	49.15	46.24
114.06	46.77	46.80	43.88
115.08	46.87	46.90	43.98
115.66	44.74	44.77	41.85
116.34	41.27	41.30	38.38

Table A10: Comparison of carbon monoxide levels measured in NOAA/CCG flasks at sampling stations in the high latitude Southern Hemisphere. Average and monthly offsets were calculated for the overlapping periods of the records from each site compared to South Pole, using data downloaded from ftp://ftp.cmdl.noaa.gov/ccg. Stations: SPO= South Pole Observatory, SYO=Syowa Station, PSA=Palmer Station, CGO=Cape Grim Observatory.

	SPO - SYO	**SPO - PSA**	**SPO - CGO**
Period of overlap	**1994-2008**	**1995-2008**	**1994-2008**
Jan	-2.8	-5.4	-5.5
Feb	-1.6	-2.4	-2.8
Mar	-0.1	0.0	-1.2
Apr	0.5	0.1	-1.6
May	0.4	0.1	-2.1
Jun	0.6	0.6	-1.9
Jul	0.7	0.6	-0.9
Aug	0.7	0.7	-0.3
Sept	1.2	0.6	-0.9
Oct	0.8	-0.6	-2.6
Nov	-1.5	-3.5	-5.0
Dec	-2.9	-5.7	-6.5
Mean offset	-0.3	-1.2	-2.6

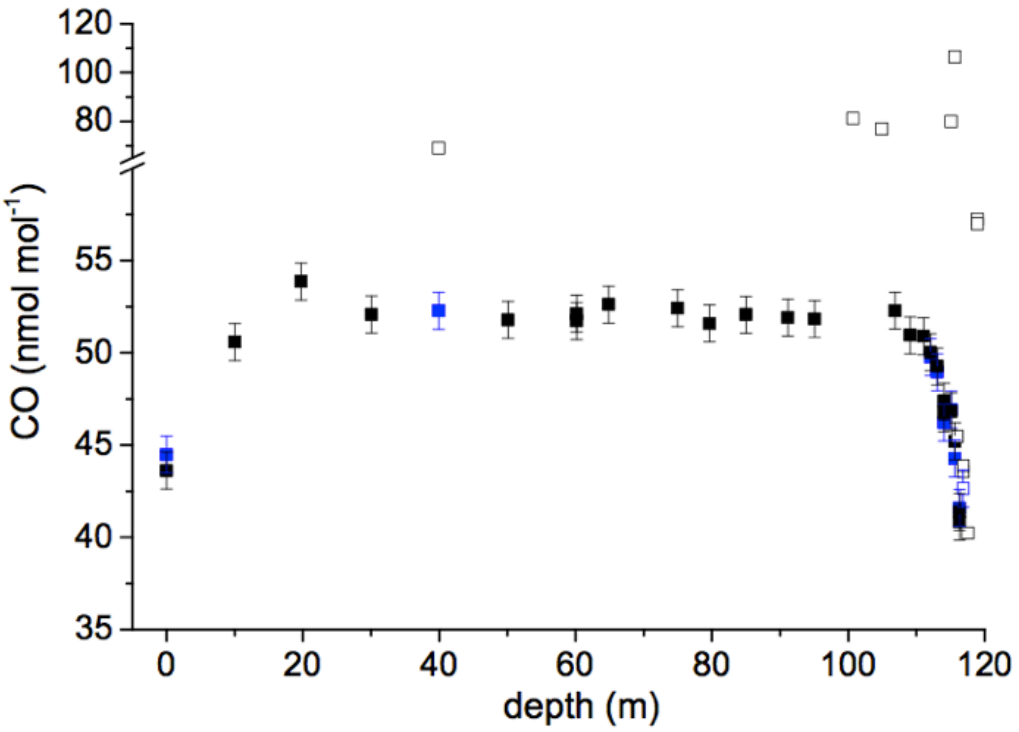

Figure A3: All carbon monoxide observations from South Pole firn flasks. Black squares – NOAA/CCG, blue squares – UCI, open squares – sample contamination, as described in the text (Chapter 5). Note, break in y-axis from 60-65 ppb.

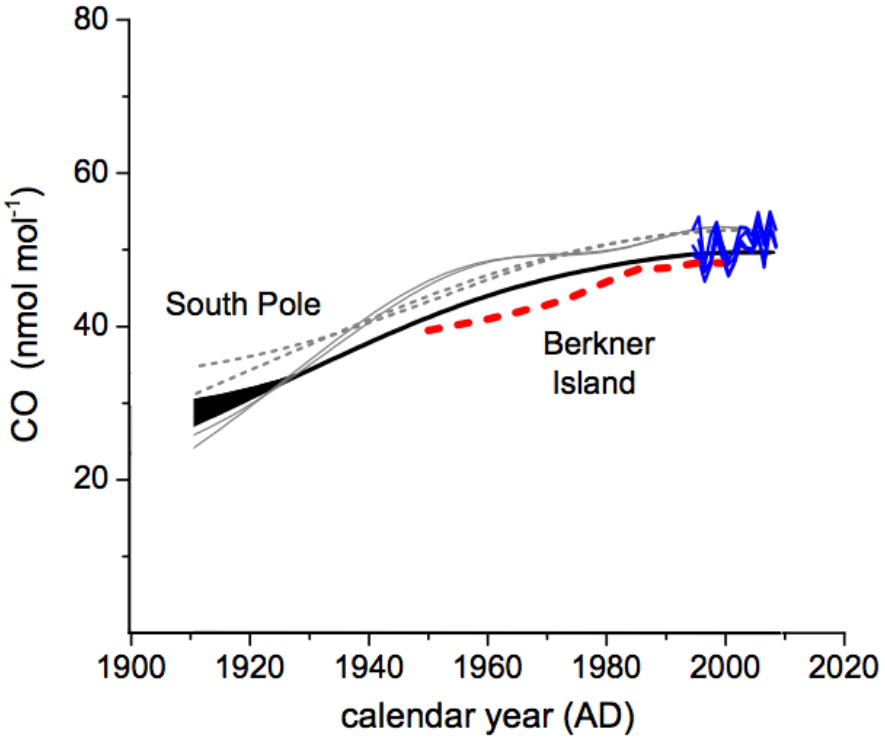

Figure A4: Comparison of 20th century atmospheric CO histories based on the blank corrected and uncorrected Antarctic firn air data. Atmospheric CO levels reconstructed from the corrected South Pole firn data (thick black line, identical to colored lines in Figure 1b). Carbon monoxide levels reconstructed from the uncorrected South Pole firn data are also shown by the grey lines (dashed line, α=30 and solid line, α=1). Dashed red line shows an independent atmospheric CO reconstruction derived from Berkner Island firn air samples [*Assonov et al.,* 2007]. The Berkner Island CO reconstruction was shifted by the scale coefficient (1.08) to account for known difference between the two laboratory scales, as reported in *Assonov et al.,* [2007]. Berkner Island firn air samples constrain the Antarctic CO history to approximately 1950. Solid blue lines show annually averaged CO concentrations at four high southern latitude sites in the NOAA global flask sampling network (see Chapter 5).

Appendix D: Selected data from the UCI Chemical Transport Modeling studies

Table A11: Carbon monoxide response ratios calculated for the three perturbation experiments tested with the UCI CTM (Chapter 6). Results are shown for the global atmosphere, Southern Hemisphere (SH=0-90°S), high southern latitudes (HSL=60-90°S), and at South Pole (SPO=90°S). SPO/SH indicates the ratio of change (in ppb/ppb) at South Pole compared to the Southern Hemisphere and HSL/SH indicates the ratio of change (in ppb/ppb) in the high southern latitudes compared to the southern hemisphere. Mixing ratios were calculated as the sum of 3, 10, 30, and 57 vertical layers in the model.

	# of vertical layers	Global CO (ppb)	SH CO (ppb)	HSL CO (ppb)	SPO CO (ppb)	SPO/SH	HSL/SH	total mol air
5% BB pert	3	0.4508	0.462	0.2393	0.2375	0.51	0.52	2.01E+17
	10	0.4233	0.4391	0.241	0.2378	0.54	0.55	9.95E+17
	30	0.3648	0.3968	0.2272	0.2177	0.55	0.57	4.37E+18
tot col	57	0.3176	0.3452	0.1918	0.1776	0.51	0.56	5.11E+18
5% FF pert	3	1.2396	0.3707	0.2457	0.2434	0.66	0.66	
	10	1.1011	0.3581	0.2466	0.2431	0.68	0.69	
	30	0.9055	0.3794	0.2249	0.2145	0.57	0.59	
tot col	57	0.7917	0.3362	0.1899	0.1749	0.52	0.56	
5% CH_4 pert	3	1.8726	1.7632	1.6101	1.5926	0.90	0.91	
	10	1.891	1.7799	1.6132	1.5908	0.89	0.91	
	30	1.7676	1.6833	1.3857	1.3191	0.78	0.82	
tot col	57	1.5499	1.4752	1.1718	1.0614	0.72	0.79	

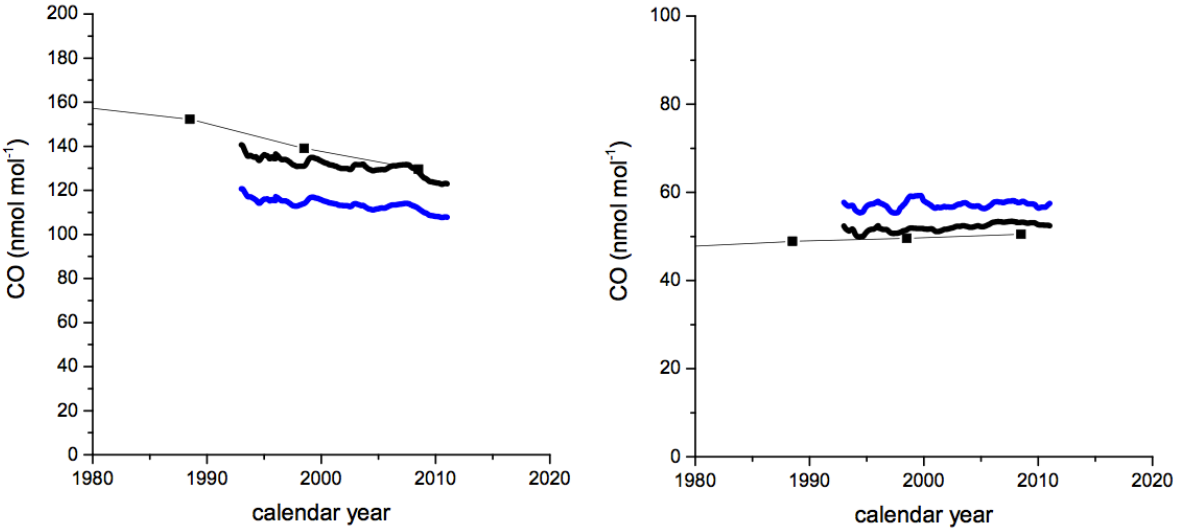

Figure A5: Carbon monoxide atmospheric histories from Greenland (left) [*Petrenko et al.,* 2013] and Antarctica (right, this study) after 1980, plotted with zonally averaged flask measurements from the NOAA/CCG network from 1991-2010 [*Novelli and Masarie*, 2013]. Hemispheric means are based on the average of zonal flask measurements from 0-30° and 30-90°. Zonal averages are plotted as the two year running average to smooth seasonal and inter-annual variability in the CO signal. a) Zonally averaged CO flask measurements from the HNH (black line) and Northern hemisphere mean (blue line) plotted with the history of CO from Greenland firn [*Petrenko et al.,* 2013]. b) Zonal average of CO flask measurements from the High latitude Southern Hemisphere (black line) and the Southern Hemisphere mean (blue line), plotted with the history of CO from South Pole firn air (this study). Latitude bands are define as follows: High latitude Northern Hemisphere, HNH=30-90° N, High latitude Southern Hemisphere, HSH=30-90° S.

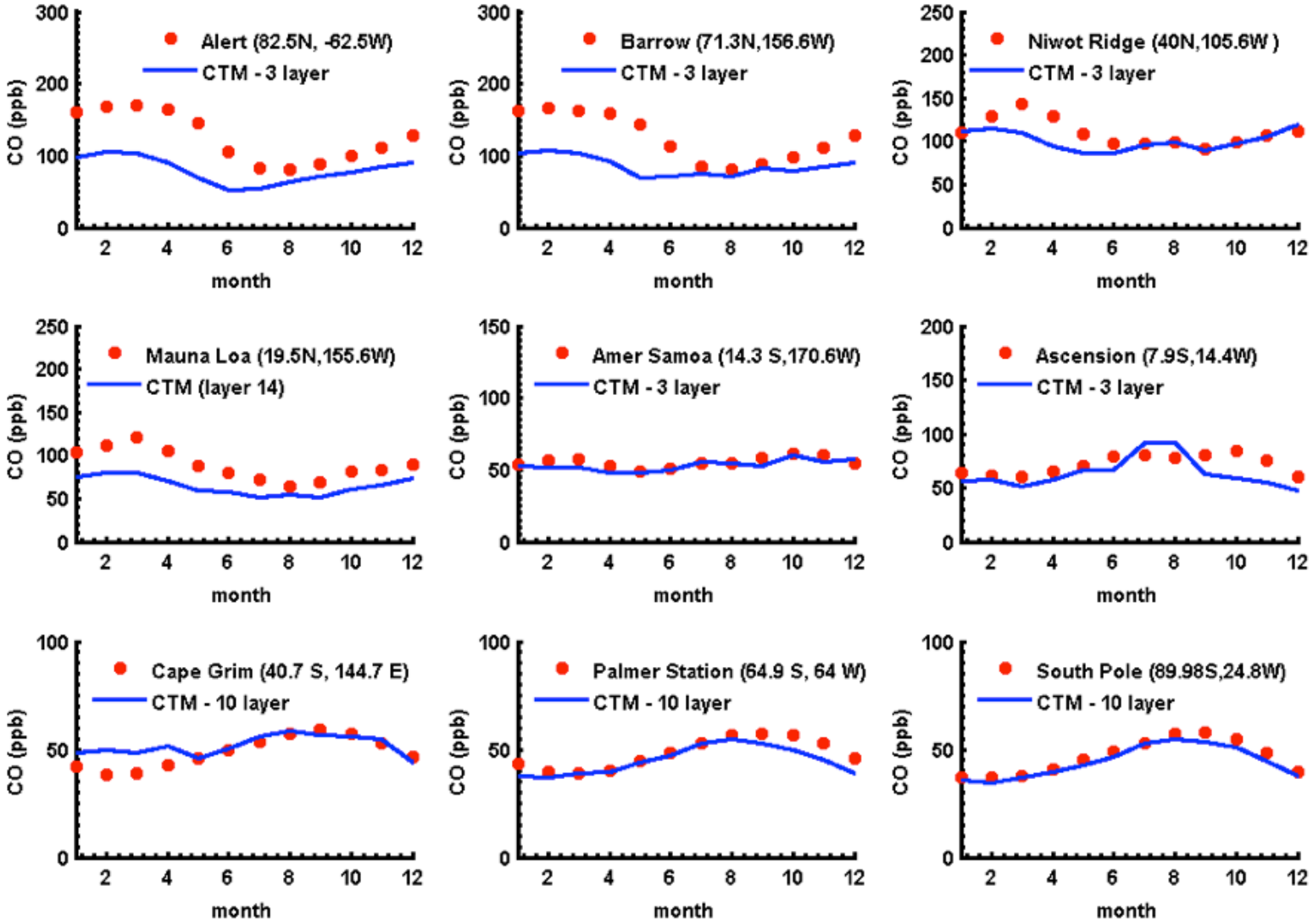

Figure A6: Results from the UCI Chemical Transport Model for CO mixing ratios (blue lines) calculated in the model box closest to the NOAA/ESRL flask station for the year 2000. The NOAA flask observations are shown for various sites (red circles) for the year 2000 for comparison to the model result.

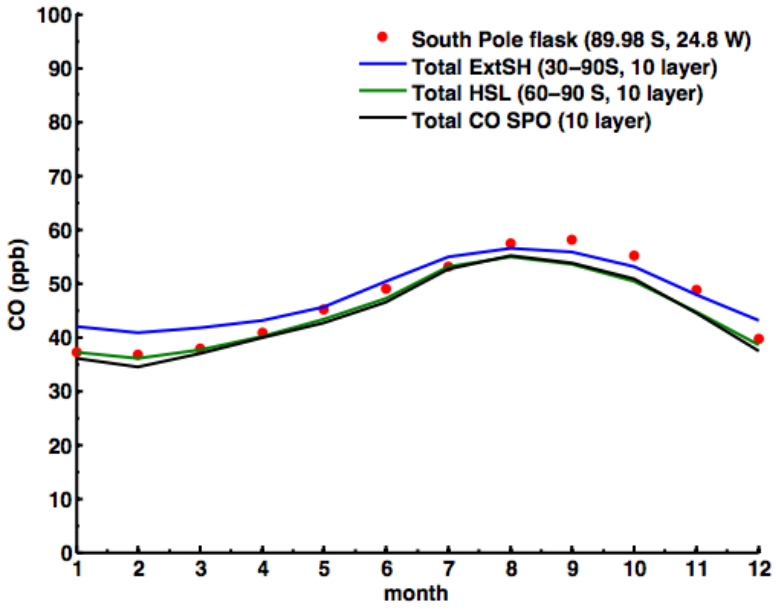

Figure A7: Comparison of CO levels in the high latitude Southern Hemisphere from the UCI-CTM. The CTM results are shown for the year 2000 as the average CO mole fraction in the extra-tropical SH (Total ExtSH, blue line, sum of model boxes from 30-90°S, 10 vertical layers), the high latitude Southern Hemisphere (Total HSL, green line, sum of model boxes from 60-90°S, 10 vertical layers) and at the South Pole (Total SPO, black line, sum of 10 vertical layers for a single box closest to 90°S). Model results are compared to NOAA flask data from the South Pole (red circles) for the year 2000.